X-RAY ABSORPTION FINE STRUCTURE STUDIES OF SOLID STATE MATERIALS OF CURRENT TECHNOLOGICAL IMPORTANCE

By

SOHINI BASU

PHYS 01200904015

Bhabha Atomic Research Centre

A thesis submitted to the

Board of Studies in Physical Sciences

In partial fulfillment of requirements

for the Degree of

DOCTOR OF PHILOSOPHY

of

HOMI BHABHA NATIONAL INSTITUTE

August, 2014

Homi Bhabha National Institute

Recommendations of the Viva Voce Committee

As members of the Viva Voce committee, we certify that we have read the dissertation prepared by Ms. Sohini Basu entitled “X-ray Absorption Fine Structure studies of solid state materials of current technological importance” and recommend that it may be accepted as fulfilling the thesis requirement for award of the Degree of Doctor of Philosophy.

Name	Designation	Signature	Date
Dr. B. S. Tomar	Chairman		11.03.2015
Prof. A. K. Pal	External Examiner		11.03.2015
Dr. N.K. Sahoo	Member		11.03.2015
Dr. D.K. Aswal	Member		11.03.2015
Prof. S. Mahamuni	Member	SRMahamuni	11.03.2015
Dr. D.Bhattacharyya	Guide / Convener		11.03.2015

Final approval and acceptance of this thesis is contingent upon the candidate’s submission of the final copies of the thesis to HBNI.

I hereby certify that I have read this thesis prepared under my direction and recommend that it may be accepted as fulfilling the thesis requirement.

Date: March 11th, 2015
Place: Mumbai

(Dr. D. Bhattacharyya)

STATEMENT BY AUTHOR

This dissertation has been submitted in partial fulfilment of requirements for an advanced degree at Homi Bhabha National Institute (HBNI) and is deposited in the Library to be made available to borrowers under rules of the HBNI.

Brief quotations from this dissertation are allowable without special permission, provided that accurate acknowledgement of source is made. Requests for permission for extended quotation from or reproduction of this manuscript in whole or in part may be granted by the Competent Authority of HBNI when in his or her judgment the proposed use of the material is in the interests of scholarship. In all other instances, however, permission must be obtained from the author.

Sohini Basu

SOHINI BASU

DECLARATION

I, hereby declare that the investigation presented in the thesis has been carried out by me. The work is original and has not been submitted earlier as a whole or in part for a degree / diploma at this or any other Institution / University.

Sohini Basu

SOHINI BASU

PUBLICATIONS

Journals:

Publications arising from the Thesis

1. *X-ray Absorption Spectroscopy of doped ZrO_2 systems.*
   S. Basu, S.Varma, A. N. Shirsat, B. N. Wani, S. R. Bharadwaj, A. Chakrabarti, S. N. Jha, and D. Bhattacharyya, *J. Appl . Phys.*, **2012**, *111*, 053532-1-9.

2. *Eu^{3+} assisted structural collapse of GaOOH nanorods: Probed through EXAFS and vibrational techniques.*
   S. Basu, S. N. Jha, D. Bhattacharyya, S. Naidu, M. Pandey, V. Sudarsan, R. K. Vatsa and R. J. Shirsagar, *Chem. Phys. Lett.,* **2012**, *528*, 21–25.

3. *Probing local environments in Eu^{3+} doped SrSnO3 nano-rods by luminescence and Sr K-edge EXAFS techniques.*
   S. Basu, D. K. Patel, J. Nuwad, V. Sudarsan, S.N. Jha, D. Bhattacharyya, R.K. Vatsa, S. K. Kulshreshtha, *Chem. Phys. Lett*., **2013**, *561–562*, 82-86.

4. *Extended X-ray Absorption Fine Structure (EXAFS) Study of Gd doped ZrO_2 systems.*
   S. Basu, Salil Varma, A. N. Shirsat, B.N. Wani, S. R. Bharadwaj, Aparna Chakrabarti, S.N. Jha and D. Bhattacharyya, *J. App. Phys*., **2013**, *113*, 043508-1-4.

5. *Nature of WO_4 tetrahedra in blue light emitting $CaWO_4$ particles: Probed through EXAFS technique.*
   S. Basu, B. S. Naidu, B. Viswanadh, V. Sudarsan, S.N. Jha, D. Bhattacharyya and R. K. Vatsa, *RSC Advances,* **2014**, *4*, 15606-15612.

6. *Local Structure Investigation of Co and Mn Doped ZnO Nanocrystals and its Correlation with Magnetic Properties.*
   S. Basu, D. Y. Inamdar, Shailaja Mahamuni, Aparna Chakrabarti, C. Kamal, G. Ravi Kumar, S.N. Jha and D.Bhattacharyya, *J. Phys. Chem. C*., **2014**, *118 (17)*, 9154–9164.

7. *Temperature dependent EXAFS Study of Cr doped $GaFeO_3$ at Ga and Fe edges.*
   S. Basu, Ripandeep Singh, A. Das, T. Roy, A. Chakrabarti, A.K. Nigam, S.N. Jha and D. Bhattacharyya
   J. Phys. Chem. C., **2015**, *119*, 2029-2037.

Other

8. *Chemical shifts of K-X-ray absorption edges of copper in different compounds by X-ray absorption spectroscopy (XAS) with Synchrotron Radiation.*
   D. Joseph, S. Basu, S.N. Jha and D. Bhattacharyya, *Nucl. Instrum. Meth. B*, **2012**, *274*, 126–128.

9. *One-pot thioetherification of aryl halides with thiourea and benzyl bromide in water catalyzed by Cu-grafted furfural imine functionalized mesoporous SBA-15.*
   J. Mondal, A. Modak, A. Dutta, S. Basu, S. N. Jha, D. Bhattacharyya and A. Bhaumik, *Chem. Comm.*, **2012**, *48,* 8000-8002.

10. *Spectrally selective CrMoN/CrON tandem absorber for mid-temperature solar thermal applications.*
    N. Selvakumar, S. Santhoshkumar, S. Basu, A. Biswas, Harish C.Barshilia, *Solar Energy Materials & Solar Cells*, **2013**, *109*, 97–103.

11. *Structural, optical and magnetic properties of sol–gel derived ZnO:Co diluted magnetic semiconductor nanocrystals: an EXAFS study.*
    S. Kumar, S. Basu, B. Rana, A. Barman, S. Chatterjee, S. N. Jha, D. Bhattacharyya, N. K. Sahoo and A. K. Ghosh, *J. Mater. Chem. C*, **2014**, *2*, 481–495.

12. *Correlation of structural and magnetic properties of Ni-doped ZnO nanocrystals.*
    D. More, C. Phadnis, S. Basu, A. Pathak, I. Dubenko, N. Ali, S N Jha, D Bhattachryya and S. Mahamuni, *J. Phys. D: Appl. Phys.*, **2014**, *47*, 045308-1-7.

13. *Effect of size and aspect ratio on structural parameters and evidence of shape transition in zinc oxide nanostructures.*
    M. Ghosh, D. Karmakar, S. C. Gadkari, S. K. Gupta, S. Basu, S.N. Jha, and D. Bhattacharyya, *J. Phys. Chem. Solids,* **2014**, *75*, 543–549.

14. *An Experimental and Computational Study to Understand Lithium Storage Mechanism in Molybdenum Disulphide.*
    Uttam Kumar Sen, Priya Johari, Sohini Basu, Chandrani Nayak, and Sagar Mitra, *Nanoscale,* **2014,** DOI: 10.1039/C4NR02480J.

15. *A New type of phase separation in Ga doped $Ce_{75}Al_{25}$ glassy alloy with delocalization of Cerium 4f electrons.*
    Radhey Shyam Tiwari, Dharmendra Singh, Sohini Basu, Rajiv Kumar Mandal, O.N. Srivastava.
    (Communicated)

Conference publications

1. *X-Ray absorption spectroscopy of Fe_2O_3-based catalysts using Synchrotron Radiation.*
   S. Basu, A. M. Banerjee, M.R. Pai, A.K. Tripathi, S.N. Jha, D.Bhattacharyya and S.R. Bharadwaj
   3rd DAE-BRNS International Symposium on Materials Chemistry, Mumbai, Dec 7-11, 2010.

2. *X-ray Absorption Near Edge Structure (XANES) Study of $YBaCo_{4-x}Fe_xO_7$ (x = 0.2, 0.4, 0.5, 0.6, 0.8) using Synchrotron Radiation.*
   S.Basu, A.K.Bera, D.Bhattacharyya, S.N. Jha and S.M. Yusuf
   3rd DAE-BRNS International Symposium on Materials Chemistry, Mumbai, Dec 7-11, 2010.

3. *In-situ EXAFS study of ZnO nanoparticles in different gaseous environments.*
   S.Basu, M. Ghosh, A.K. Singh, S.N. Jha and D.Bhattacharyya
   56th DAE-Solid State Physics Symposium, Kattankulathur, December 19-23, 2011, AIP Conf. Proc.1447 (2012) 497.

4. *X-ray Absorption Spectroscopy of Doped $BaCeO_3$-$BaZrO_3$ Systems.*
   S. Basu, P. Sawant, S. Verma, B.N. Wani, S.R. Bharadwaj, S.N.Jha and D. Bhattacharyya, 56th DAE-Solid State Physics Symposium, Kattankulathur, December 19-23, 2011.

5. *Local structure investigation of Eu doped $SrSnO_3$ samples surrounding Sr site.*
   S. Basu, D. K. Patel, V.Sudarsan, S.K.Kulshreshtha, S. N. Jha and D.Bhattacharyya
   57th DAE-Solid State Physics Symposium, IIT Bombay, Powai, Dec. 3–7, 2012.
   AIP Conf. Proc. 1512 (2013) 472.

6. *Local Structure Investigation of Co & Mn doped Zinc Oxide Nanoparticles.*
   S. Basu, D. Inamdar, S. Mahamuni, S.N. Jha and D. Bhattacharyya
   DAE-BRNS 4th Interdisciplinary Symposium on Materials Chemistry, Mumbai, Dec. 11-15, 2012. (First prize in poster presentation).

7. *GdSZ as an electrolyte material for intermediate temperature solid oxide fuel cell.*
   S. Varma, S. Basu, A. N. Shirsat, D. Bhattacharyya, B. N. Wani, S. N. Jha, Fuel Cells 2012 Science & Technology: A grove Fuel Cell Event, Berlin, Germany, April 11-12, 2012, P-54.

8. *Preliminary Experiments at the Dispersive EXAFS beamline at INDUS-2 Synchrotron Source, Indore, INDIA.*
   D. Bhattacharyya, S. N. Jha, A. K. Poswal, S. Basu and A.K.Yadav, 15th International Conference on X-ray Absorption Fine Structure, Beijing (China) 22-28 July 2012.

9. *Correlation of structural, optical and magnetic properties of Co doped ZnO Nanocrystals.*
   D. Y. Inamdar, A. K. Pathak, I. Dubenko, N. Ali, S. Basu, S. N. Jha, D. Bhattacharyya and S. Mahamuni, The International Conference on Nanoscience and Technology (ICONSAT) Hyderabad, January 20-23, 2012.

10. *A comprehensive facility for EXAFS measurements at the INDUS-2 synchrotron source at RRCAT, Indore, India.*
    S. Basu, C. Nayak, A. K. Yadav, A. Agrawal, A. K. Poswal, D. Bhattacharyya, S. N. Jha and N. K. Sahoo, The 17th Pan-American Synchrotron Radiation Instrumentation Conference (SRI-2013) NIST, Gaithersburg, USA, June 17-21, 2013. J. Phys.: Conf. Ser. 493 012032 (2014).

11. *Temperature Dependant X-ray Absorption Spectroscopy Study of $GaFeO_3$.*
    S. Basu, R. Singh, A. Das, S.N. Jha and D. Bhattacharyya
    58th DAE-Solid State Physics Symposium, Thapar University, Punjab, Dec. 17–21, 2013. (Selected for oral presentation)

12. *Physico-Chemical Characterization of Novel Matrix by FT-IR, SEM and EXAFS.*
    Sangita Pal, D. Goswami, S. Basu, S. Roychowdhury, M. Ali , P. K. Tewari.
    58th DAE-Solid State Physics Symposium, Thapar University, Punjab, Dec. 17–21, 2013.

13. *Commissioning and first results of scanning type EXAFS beamline (BL-09) at INDUS-2 synchrotron source*
    A. K. Poswal, A. Agrawal, A. K. Yadav, C. Nayak, S. Basu, S. R. Kane, C. K. Garg, D. Bhattachryya, S. N. Jha, and N. K. Sahoo
    58th DAE-Solid State Physics Symposium, Thapar University, Punjab, Dec. 17–21, 2013.

ACKNOWLEDGEMENTS

I would like to gratefully and sincerely thank my supervisor Dr. Dibyendu Bhattacharyya for his guidance, understanding and patience during my doctoral studies at Bhabha Atomic Research Centre, Mumbai. His mentorship was paramount in providing a well rounded experience consistent with my long-term career goals. He encouraged me to not only grow as an experimentalist and a physicist but also as an instructor and an independent thinker. I am also thankful to Dr. Shambhu Nath Jha, who has been very supportive and encouraging during the course of my research work. I would like to thank all of the members of the XAFS research group, Shri Ashok kumar Yadav, Kum. Chandrani Nayak, Shri Ashwini Poswal, Shri Ankur Agrawal and Dr. Parasmani Rajput, my friends and endearing colleagues who have helped me in every possible way. A special mention for Ashok and Chandrani, who made long working hours worthwhile and for the stimulating discussions on XAFS. I am grateful to Dr. N. K. Sahoo, Head, A&MPD, BARC for his guidance and support in every way possible. I would also like to thank members of my doctoral committee for their input and valuable discussions. I am also thankful to my principal collaborators, Dr. S. Varma, Dr. V. Sudarsan, Prof. (Smt.) S. M. Mahamuni, Dr. A. Das, Prof. S. S. Major and Dr. (Smt.) A. Chakrabarti.

Last but not least, I thank Dr. S. K. Deb, former Head, ISUD, RRCAT and Dr. G. S. Lodha, Head, ISUD, RRCAT along with the INDUS-2 control room members for their unrelenting support and for honouring our beamtime requests at odd hours despite many inconveniences. This work would not have been completed without their support.

CONTENTS

Page No.

LIST OF FIGURES

LIST OF TABLES

Homi Bhabha National Institute

Ph. D. PROGRAMME

1. **Name of the Student:** Sohini Basu
2. **Name of the Constituent Institution:** Bhabha Atomic Research Centre
3. **Enrolment No. :** PHYS01200904015
4. **Title of the Thesis:** X-Ray Absorption Fine Structure Studies of Solid State Materials of Current Technological Importance
5. **Board of Studies:** Physical Sciences

SYNOPSIS

X-ray as a spectroscopic tool is of vital importance with a wavelength of ~ 1- 100 Å, comparable to the length scale of atoms. Thus it is a powerful probe to determine the electronic structure of atoms, molecules, clusters and condensed matter in general. X-ray absorption fine structure (XAFS) is a technique that involves measurement of fine structure in the X-ray absorption spectrum of an atom at energies near and above the core-level binding energies of that atom. Because each element has a specific but different set of binding energies, the X-ray source can be tuned to the corresponding absorption energy to probe a particular element, thus making it an element specific technique. Since crystallinity is not a prerequisite, this technique is particularly well suited to investigate materials that lack long-range order like nanomatrials, amorphous and disordered solids, liquids, gels, molecular solutions, liquid crystals, macromolecules containing metallic or large atoms (polymers, bio molecules) etc. XAFS is thus routinely used in a wide range of scientific fields, including biology, environmental science, catalysts research and materials science. X-ray absorption measurements require an intense and energy-tuneable X-ray source like a synchrotron accelerator. The specifications of synchrotron sources, beamline optics and experimental station define the energy ranges, beam sizes, and intensities available, and dictate the practical experimental limits on the XAFS measurements that can be performed.

Chapter 1 of my thesis addresses my motivation for undertaking this work and elaborates on the choice of the XAFS technique. It describes the requirements of investigating local structures around specific elements in certain samples to explain their macroscopic properties and also justifies the choice of the XAFS technique for these investigations. In order to fully exploit the benefits of a recently commissioned beamline at INDUS-2 Synchrotron source dedicated completely to XAFS spectroscopy, samples of diverse nature with potential applications in varied fields have been studied as described in this work. The contents of this chapter thus, provide both inspiration and the basis for the work presented in subsequent chapters.

Chapter-2 is devoted to the theory of XAFS technique and its physical interpretation, both near (XANES region) and far (EXAFS region) from the absorption edge. It also includes a comprehensive account of the experimental methods followed in this work, including detailed description of the beamline and the experimental station. My work has been carried out at the Energy Dispersive EXAFS beamline (BL-08) at INDUS-2 Synchrotron radiation source at Raja Ramanna Centre for Advanced Technology, Indore, India [1, 2]. INDUS-2 is a 2.5 GeV synchrotron source operating at 120mA with a critical wavelength of ~2.0 Å. This beamline works in energy dispersive mode which uses a bent Si (111) crystal as the dispersing-cum-focusing element and a CCD detector as the position sensitive detector to collect the spatially dispersed transmitted beam. The beamline is designed to cover the photon energy range of 5– 20 keV. The working principle of the beamline including different modes of data collection with their merits and demerits has been thoroughly discussed in this chapter. Sample preparation method has also been described since it dictates the quality of spectrum obtained, specifically for measurements in transmission mode. Finally the data analysis procedure is described elaborately which involves extensive use of the IFEFFIT software package including ATHENA and ARTEMIS subroutines [3]. This chapter has been divided into four subsections covering the entire theory and experimental basis for the XAFS technique.

Chapter-3 onwards deals with different genres of samples, possessing definite properties that have been characterized by the XAFS technique during my PhD programme. This particular chapter deals with EXAFS measurements on doped zirconium oxide samples. It has catalytic applications, either as supports or as electrolytes, especially in solid oxide fuel cells (SOFCs). Pure ZrO_2 is monoclinic from room temperature to 1440 K, tetragonal between 1440 and 2650 K and cubic up to its melting point of 2950 K [4]. It exhibits high anionic conductivity when doped with aliovalent cations which facilitates the generation of oxygen ion vacancies for charge compensation [5]. There are contradictions in the literature regarding the possible positions of oxygen vacancies created in ZrO_2 matrix when doped with trivalent ions. We have looked into the above issue using EXAFS measurements supported by X-ray diffraction data and also by theoretical simulations to some extent. The rare earth substituted ZrO_2 samples discussed in this study were prepared by co-precipitation route with 11% doping of Nd and La and with 7, 9, 11, and 13% doping of Gd. Data analysis from EXAFS measurements confirm the tetragonal structure for Gd and Nd doped ZrO_2 samples and monoclinic structure for La doped samples. It was further concluded that maximum oxygen vacancies in ZrO_2 host matrix are created near the Zr site for Gd doping. Nd and La dopant atoms having relatively larger ionic radii compared to Zr ion, generate lesser number of oxygen vacancies that are located near the dopant cations. First principle calculations have confirmed that for La-doped ZrO_2 systems, oxygen ion vacancies at the nearest neighbor sites leave the system in a more stable state, supporting our experimental findings. It has been further observed that ~9% Gd doping is optimum for creation of vacancies near the Zr sites and hence for increasing its ionic conductivity. Thus by employing EXAFS technique, we could identify the most effective dopant in ZrO_2 system and its optimum concentration for creation of sufficient oxygen vacancies near the dopant site.

In chapter-4 we explore luminescent nano-materials. The chapter is divided into three subsections, each of them concerned with a different luminescent nanomaterial. The first system is Eu doped gallium oxy-hydroxide (GaOOH). It has been observed by XRD measurements that layered structures of highly crystalline orthorhombic GaOOH nanorods undergo significant lattice distortions leading to amorphisation even when very small amounts of Eu^{3+} ions (1 at.% or more) are present during its synthesis. However, interestingly EXAFS spectra of these samples indicate that the local short range order around Ga^{3+} is unaffected by the incorporation of Eu^{3+} ions in the sample. Analysis of EXAFS data indicates that Eu^{3+} do not replace Ga^{3+} in GaOOH lattice, but the disorder factor increases appreciably even with the introduction of a small amount of Eu^{3+} (0.5%) and reaches a maximum for 1 at.% Eu^{3+} doping. Supporting information from vibrational studies reveal systematic appearance of new peaks which can be attributed to the bending vibrations of the OH groups associated with $Ga(OH)_3$ and $Eu(OH)_3$ phase [6]. This further suggests that Eu^{3+} affects the lattice structure through the OH linkages existing at the GaOOH inter layer spacing by forming europium hydroxide species thus destabilizing the layered structure of GaOOH.

The second luminescent material studied is Eu doped $SrSnO_3$. It has been observed that with the increase in Eu doping concentration in $SrSnO_3$ there is a change in luminescent pattern of $SrSnO_3$ viz., the otherwise forbidden electric dipole transition ($^5D_0$ to $^7F_2$) gets enhanced giving rise to significant asymmetry in the luminescence spectra due to possible distorted environment around Sr sites in the sample. In the present study, EXAFS measurements have been carried out on a series of $Sr_{1-x}Eu_xSnO_3$ (x = 0, 0.01, 0.02, 0.03, 0.04) samples at Sr K-edge (16105 eV) to see if Eu goes to Sr site (symmetric environment) or precipitates as separate phase/cluster (distorted environment) in $SrSnO_3$. There exists some ambiguity in the literature regarding the space group of $SrSnO_3$. So we have investigated both the possibilities (*Pbnm* and *I4/mcm*) to determine the appropriate structure for modeling and observed that better fitting of the data (lower χ^2 values) were obtained with the space group of *I4/mcm*. EXAFS data analysis further shows that the average Sr-O bond distance is higher for Eu^{3+} containing sample compared to the undoped $SrSnO_3$ which clearly establishes substitution of a larger cation (Sr^{2+}) by a smaller one (Eu^{3+}).

The third luminescent material which has been probed is $CaWO_4$ nanoparticles having different average crystallite sizes in the range of 5-10 nm synthesized at room temperature. These samples were subsequently heated at different temperatures (300°C, 500°C, 700°C and 900°C) in air for 5 hours each and luminescence measurements have shown significant improvement in luminescence intensity and lifetime with increase in annealing temperature. This has been attributed in the literature to localized bands arising due to oxygen vacancy complexes or distorted WO_4 tetrahedra. To investigate it further both W L_1 edge XANES and W L_3 edge EXAFS measurements have been employed in this study. XANES measurements at W L_1 edge (12100 eV) shows the presence of the pre-edge peaks of considerable intensity in all the samples which further confirms that W in $CaWO_4$ exists as WO_4 tetrahedra that remains unaffected by annealing. EXAFS data analysis further shows that oxygen coordination around W decreases gradually with increase in annealing temperatures. Hence, EXAFS measurements could clearly establish that creation of oxygen vacancies is responsible for the increase in luminescence intensity and associated increase in the lifetime values. This chapter provides insight to structural information of luminescent materials and helps to understand their macroscopic properties in the light of this information.

Chapter-5 explores the origin of magnetic properties in transition metal (TM) doped dilute magnetic semiconductor (DMS) nanoparticles. The reported results pertaining to the magnetic behavior (T_c, magnetic moment etc.) of these DMSs vary greatly ranging from room temperature ferromagnetism (RTFM) to no magnetic ordering at all [7-9]. Thus origin of FM in TM doped ZnO is still a fairly unresolved question.

In the present study, we put forward a systematic local structure investigation of Co and Mn doped ZnO nanocrystals (NCs) by synchrotron-based EXAFS measurements at both Zn K edge and dopant (Co, Mn) K edges. The measurements have been carried out on samples prepared by different methods, viz., high temperature wet chemical method (WC), sol-gel route (SG) and the microwave-assisted (MW) method with TM dopant concentrations varying from 0-15% by weight. The EXAFS results presented here have been supported by XRD measurements, magnetization measurements and are also confirmed by first principle calculation results. The findings indicate that doping levels of $\leq$ 10% of Co is optimum for efficient doping in ZnO lattice. XANES measurements at Co K-edge confirmed presence of Co^{2+} state in the lattice. Similarly, the XANES region of the Mn edge XAFS spectrum revealed that Mn in WC samples are in +3 state whereas it is in +2 state for MW and SG samples. Doping concentrations of ~10% for WC samples and 7% for MW samples are found to be optimum beyond which Mn clustering sets in.

The magnetic measurements indicate that, while WC Co doped samples show ferromagnetism which increases with increase in Co concentration, MW Co doped samples are not ferromagnetic. WC Mn doped samples, on the other hand, show ferromagnetism which decreases with increase in Mn concentration and MW Mn doped samples demonstrate anti-ferromagnetic ordering. For SG samples the magnetization decreases with an increase in the field for 0% and 1% Co doped ZnO whereas it increases with the increase in the magnetic field for 2% and 4% Co doped ZnO samples. The observed M-H behaviour reveals that the 0% and 1% Co doped samples comprise a mixture of ferromagnetic (FM) and diamagnetic (DM) phases (where DM dominates) and the 2% and 4% Co doped samples are in weak ferromagnetic phase. First principle calculations indicate that at high concentration, the dopants tend to cluster together to lower the energy or to increase the stability of the system. In case of Co clustering the system can either be ferromagnetic or anti-ferromagnetic. However, Mn clusters preferentially assume anti-ferromagnetic ordering.

In conclusion, WC Co doped samples show RTFM which may be a consequence of charge redistribution due to the presence of organic capping molecules during synthesis. On the other hand, a secondary Mn_2O_3 phase is detected in WC Mn doped samples which might be the cause of its ferromagnetism. The MW Mn and Co doped samples do not show any ferromagnetism. The SG Co doped samples exhibit weak ferromagnetism and we suggest that oxygen vacancy assisted BMPs are responsible for the RTFM in this system. Hence this comprehensive study has been able to throw some light regarding the magnetic properties of TM doped DMSs and the different mechanisms (substitution and site-disorder) for the origin of magnetic properties.

Chapter-6 considers the problem of magnetic transition in Cr doped $GaFeO_3$ which demonstrates piezoelectricity and ferrimagnetism. It has been reported that the magnetic properties of $GaFeO_3$ at low temperature is associated with cation site disorder, i.e. the presence of octahedral Fe ions predominantly in octahedral Ga sites [10]. Such site disorders can be best probed by an element specific local structure measurement tool such as EXAFS which has not been reported so far in the literature. Further, Cr is doped in $GaFeO_3$ to explore the possibility of manipulating the magneto-electric effect of the system favourably [11]. In the present study a systematic investigation has been conducted on the undoped, 10% and 20% Cr doped multiferroic $GaFeO_3$ by EXAFS technique both at Ga K-edge (10367 eV) and Fe K-edge (7112 eV) over a wide temperature range from 300 K to 25 K. The samples were synthesized by solid state reaction method. Magnetization measurements revealed that the undoped compound undergoes a ferrimagnetic transition at 210K. With doping of Cr the T_C reduces to 160K and 100K for x=0.1, and 0.2, respectively. Analysis of EXAFS spectra at Ga edge shows a decrease in bond distance values around Ga and increase in the bond length values at the Fe sites near the magnetic transition temperature with increase in Cr doping concentration. This result unambiguously establishes that cation site disorder i.e., occupancy of Fe ions at Ga site as the reason for magnetic transition in $GaFeO_3$ systems.

Chapter-7 presents a study involving local structure investigation of $GaAs_{1-x}N_x$ thin films prepared by reactive rf sputtering of GaAs targets in the presence of Ar and N_2 atmospheres [12]. The arsenic to nitrogen ratio in the films was varied by changing the relative percentage of nitrogen in the argon–nitrogen sputtering atmosphere, from 0% to 100%. We have probed the changes in the local structures in these alloy films as a function of nitrogen percentage by EXAFS measurements carried out both at Ga and As edges. This particular experiment was performed in a slightly modified experimental arrangement called TURBO-EXAFS to enable measurements on thin film samples in fluorescence mode using a energy dispersive set up, the details of which has been described in Chapter-2.

XANES spectra at Ga K-edge, show that there is a clear shift in the position of absorption edge towards higher energy with increase in nitrogen concentration. This shift in the absorption edge position has been explained to be due to higher effective positive charge on Ga atom in case of GaN compared to that in GaAs. EXAFS spectra also depict gradual transformation from GaAs-like to GaN-like spectra as nitrogen concentration in the films increases from 8-50%. Detail analysis of the EXAFS spectra assuming a mixed structure of GaAs and GaN shows that As co-ordination decreases rapidly while N coordination increases around Ga atoms as the nitrogen concentration is increased beyond 8% in the sputtering atmosphere. The EXAFS spectra at As K edge have also been fitted assuming possible contribution from both GaAs and GaN structures (by replacing the N atom in GaN by As atom, in the latter case) in the theoretical modeling and it has been found that for samples prepared with 5% and 8% nitrogen concentration, there is a contribution from the latter structure which increases rapidly as the nitrogen concentration is increased beyond 8% in the sputtering atmosphere. The above observations support our earlier findings on this system [12] that the properties of the films, preapred with more than 12% nitrogen in the sputtering ambient, are GaN-like, with their refractive index, extinction coefficient and band gap values resembling that of hexagonal GaN, while for nitrogen concentration in the range of <10%, $GaAs_xN_{1-x}$ alloy films are realized.

Finally, in chapter-8 the conclusions drawn from each of the studies presented in previous chapters are summarized, while stressing on the versatility and effectiveness of XAFS as a powerful characterization technique. Future scope of work, including beamline augmentation programmes, and application of this technique in new fields in terms of sample forms (solutions, biomolecules etc.), sample environments (extreme conditions such as high pressure, high temperature), in-situ and time resolved studies etc. are also discussed.

REFERENCES

1. S Basu, C Nayak, A K Yadav, A Agrawal, A K Poswal, D Bhattacharyya, S N Jha and N K Sahoo, *Journal of Physics: Conference Series* **493** (2014) 012032.
2. D. Bhattacharyya, A.K. Poswal, S.N. Jha, Sangeeta and S.C. Sabharwal, *Nuclear Instruments Method. in Phys. Res.* **A 609** (2009) 286.
3. M. Newville, B.Ravel, D. Haskel, J.J. Rehr, E.A. Stern and Y. Yacoby, *Physica* **B 154** (1995) 208.
4. C. J. Howard, R. J. Hill and B. E. Reichert, *Acta Cryst.* **B44** (1988) 116.
5. M. O. Zacate, L. Minervini, D. J. Bradfield, R. W. Grimes and K. E. Sickafus, *Sol. St. Ionics* **128** (2000) 243.
6. S. Wang, Y. Zhao, J. Chen, R. Xu, L. Luo and S. Zhong, *Superlatt. Microstr.* **47** (2010) 597.
7. D. Y. Inamdar, A. D. Lad, A. K. Pathak, I. Dubenko, N. Ali and S. Mahamuni, *J. Phys. Chem.* **C 114** (2010) 1451.
8. C. N. R. Rao and F. L. Deepak, *J. Mater. Chem.* **15** (2005) 573.
9. C. Guglieri, M. A. Laguna-Marco, M. A. García, N. Carmona, E. Céspedes, M. García Hernández, A. Espinosa and J. Chaboy, *J. Phys. Chem.* ***C*** **116** (2012) 6608.
10. K Sharma, V R Reddy, D Kothari, A Gupta, A Banerjee and V G Sathe, *J. Phys.: Condens. Matter* **22** (2010) 146005.
11. R. Saha, A. Shireen, S. N. Shirodkar, U. V.Waghmare, A. Sundaresan and C. N. R. Rao, *Journal Solid State Chemistry* **184** (2011) 2353.
12. A. Biswas, B.S. Yadav, D. Bhattacharyya, N.K. Sahoo, S.S. Major and R.S. Srinivasa, *Journal of Non-Crystalline Solids* **357** (2011) 3293.

Chapter 1

INTRODUCTION

X-ray as a spectroscopic tool is of vital importance with a wavelength of ~ 1-100Å, comparable to the length scale of atoms and is a powerful probe to determine the electronic structure of atoms, molecules, clusters and condensed matter in general. X-ray absorption spectroscopy (XAS) is a technique that generally deals with measurement of absorption coefficient as a function of X-ray photon energy around an X-ray absorption edge of an element in a material. X-ray absorption spectrum consists of two parts: (i) The spectrum near the absorption edge (viz., the X-ray near edge structure or the XANES part) gives information about the external perturbations in the valence states to which electrons make transitions from core levels upon absorption of X-ray photon energy. Hence XANES can yield information regarding hybridization of orbitals in case of molecule or long range order existing in a crystalline sample apart from the oxidation states of the absorbing atom in the material. (ii) The second part of the spectrum which extends from 50 eV to ~700 eV above the absorption edge is generally called the Extended X-ray absorption fine structure (EXAFS) part which is characterized by the presence of fine structure oscillations arising due to back scattering of outgoing photo-electron by neighboring atoms, and can give precise information regarding the short range order and local structure around the particular atomic species in the material.

Though the appearance of fine structure oscillations in X-ray absorption spectrum of an element, which is a constituent of a material or a molecule, was noticed by scientists way back in 1930s [1]–[3], it was in 1971 only that a robust theoretical formulation was established by Sayers et al. [4], [5] for this phenomenon which also provides a rather straightforward way to derive meaningful parameters from the EXAFS oscillations.

The bond length determination by EXAFS is confined to a distance given by the mean free path of the photoelectron in the condensed matter, which is within a 5-7 Å radius from the core atom. Because each element has a specific but different set of binding energies, the X-ray source can be tuned to the corresponding absorption energy to probe a particular element thus making it an element specific technique. Additionally, since crystallinity is not a prerequisite, this technique is particularly well suited to investigate materials that lack long-range order like nanomaterials, amorphous and disordered solids, liquids, gels, molecular solutions, liquid crystals, macromolecules containing metallic or heavy atoms (polymers, bio molecules) etc. EXAFS can therefore be used in a variety of systems and many experimental techniques are available, including very fast measurements of in-situ chemical processes, and measurements under extreme conditions of temperature and pressure. Thus EXAFS is routinely used in a wide range of scientific fields, including biology, environmental science, catalysts research and material science. The above characteristics along with the fact that EXAFS is an element specific tool, makes EXAFS a powerful local structural probe.

However, X-ray absorption spectroscopy, as the name suggests, requires an intense and energy-tunable X-ray source. The background radiation from a laboratory based X-ray tube source offers a very weak tunable X-ray continuum and this had been a serious limitation in obtaining EXAFS spectrum of reasonable quality till a long time. The availability of modern bright Synchrotron radiation sources since 1970's, has removed this experimental difficulty and since then EXAFS has emerged out to be one of the most powerful tool for local structure determination. A synchrotron light source is a combination of different particle accelerators, including a storage ring in which the desired electromagnetic radiation is generated and stored at a constant energy. Apart from the storage ring, a synchrotron light source usually also contains another accelerator (linear accelerator abbreviated as *linac* or microtron) and another synchrotron which is sometimes called *booster*. The microtron/linac and the booster are used to successively accelerate the electrons to their final energy before they are magnetically "kicked" into the storage ring. This radiation from the storage ring is brought to the experimental station by a set of optical components integrated and aligned in series in a vacuum line, generally known as a beamline. The specifications of synchrotron sources, beamline optics and experimental station define the energy ranges, beam sizes and intensities available and dictate the practical experimental limits on the EXAFS measurements that can be performed.

The evolution of Synchrotron sources as dedicated and independent research facilities for the materials science community has been quite fascinating [6]. After the discovery of X-rays in 1895 by Röentgen, which earned him the first ever Nobel prize in Physics in 1901, Larmor derived an expression for the instantaneous total power radiated by an accelerated charged particle in 1897. The following year Liénard extended the above result to the case of a relativistic particle undergoing centripetal acceleration in circular trajectory. Much later in the 1940s, Ivanenko and Pomeranchuk showed that energy losses due to radiating electrons would set a limit on the energy obtainable in an accelerator. In 1945, Shwinger worked out the classical (non-quantum) theory of radiation from accelerated relativistic electrons, including warping of globular non-relativistic dipole radiation pattern into a strongly forward peaked distribution (for circular trajectories) that gives Synchrotron radiation its highly collimated property. First visual observation of Synchrotron radiation was made accidentally in 1947 at GE at a 70-MeV electron synchrotron that was built to test the idea of phase-stability principle for RF accelerators. In 1956, Tomboulian and Hartman confirmed the spectral and angular distribution of the radiation and performed soft X-ray spectroscopy experiments for the first time with Synchrotron radiation. First generation synchrotron facilities, known as parasitic facilities, as their main objective was high energy physics experiments, were built in the 1960s with NIST modifying its 180 MeV electron Synchrotron to allow access to the radiation via a tangent section into the machine's vacuum system.

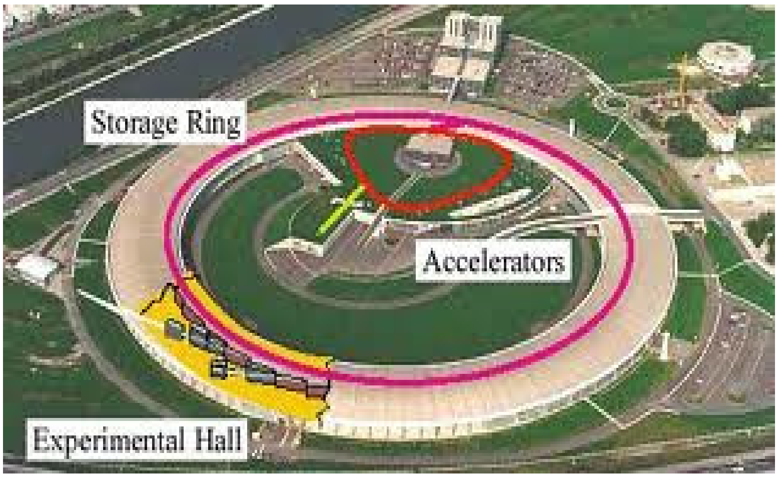

Figure 1.1 A typical Synchrotron facility

The 6 GeV DESY source in Hamburg began operating for both high energy physics and the earliest model for today's multi user Synchrotron facilities. During the next two decades several storage rings were built dedicated to Synchrotron radiation research known as *second generation sources*.

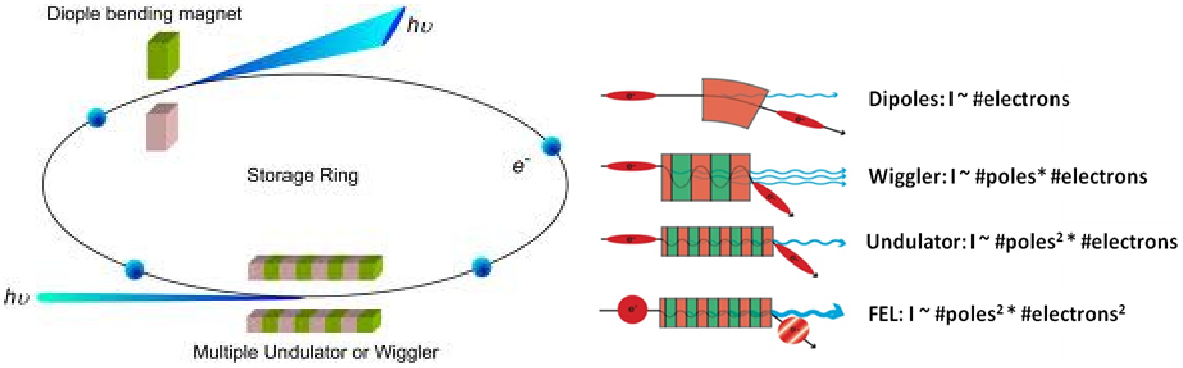

Figure 1.2 Schematic of a Synchrotron radiation source

Many of these facilities were upgraded and new sources were developed, which are known as *third generation sources*. These sources employ insertion devices such as undulators and wigglers. An *insertion device* (ID) is a component in modern synchrotron light sources, so called because they are "inserted" into accelerator track. They are periodic magnetic structures that stimulate highly brilliant, forward-directed synchrotron radiation emission by forcing a stored charged particle beam to perform wiggles, or undulations, as they pass through the device. Presently efforts are being made to develop a new generation of synchrotron radiation sources, namely the *fourth generation sources*, with vastly enhanced performance, even as the third-generation facilities enter their prime. The most promising candidate at the moment for a fourth-generation source is the hard x-ray (wavelength less than 1Å) free-electron laser (FEL) based on a very long undulator in a high energy electron linear accelerator. Such a device has a peak brightness many orders of magnitude beyond that of the third- generation sources, as well as pulse lengths of 100 fs or shorter, and would be fully coherent. Only five FEL sources are currently operating in the ultraviolet and soft x-ray range worldwide and quite a few are expected to be operational within the next few years [7]**.** For example, SPring-8 Angstrom Compact Free Electron Laser (SACLA), in Japan, is the most compact X-ray Free Electron Laser (XFEL) facility in the world, and is also now the only XFEL operating below 1 Å wavelength. The Linac Coherent Light Source (LCLS) at SLAC National Accelerator Laboratory, which is presently the world's most powerful X-ray laser, is also operational. FERMI is the new seeded free electron laser (FEL) facility in operation next to the third-generation synchrotron radiation facility Elettra, Italy while the European X-ray Free-Electron Laser is a 3.4-kilometer-long research facility currently under construction in the Hamburg area, Germany, which will be operational since 2015.

India has its own Synchrotron radiation research facility at Raja Ramanna Centre for Advanced Technology, Indore, Madhya Pradesh. The first Indian synchrotron source INDUS-1, a 450 MeV electron storage ring, was commissioned in early 1999 [8]. It provides a broad electromagnetic spectrum extending from far infrared to soft X-ray region. The second synchrotron source INDUS-2 was commissioned in 2005 and is presently being operated with 2.5 GeV electron energy at 200 mA beam current and a critical wavelength of about 2Å, providing a spectrum in the hard X-ray regime. The nominal specifications of the INDUS-2 source have been given in Table 1.1. INDUS-2 lattice is designed to give low beam emittance and high brightness. The storage ring of INDUS-2 consists of 8 unit cells each providing a 4.5 m long straight section. Each of the eight super periods has two dipole bending magnets, four focusing and five defocusing quadrupoles and six sextupoles.

Figure 1.3 INDUS 2 Synchrotron radiation source in RRCAT, Indore, India

Of the eight long straight sections, three are used for injection and RF cavities respectively. The remaining five can be used for insertion devices. The unit cell has two 22.5º bending magnets, a triplet of quadrupoles for the control of dispersion in the achromat section, two quadrupole triplets for the adjustment of beam sizes in the long straight sections and four sextupoles in the achromat section for the correction of chromaticities. An advantage of this lattice is that the two 2 m long gaps between the focussing and defocusing quadrupoles in the achromat section provide a lot of space for accommodating beam diagnostic and vacuum devices.

Table 1.1 Design parameters for INDUS-2 SRS

Energy		2.5 GeV
Current		200 mA
Bending Field		1.502 T
Critical Wavelength (l_c)		1.986Å (BM)
Circumference		172.4 m
Typical tune point		9.2, 5.2
Beam emittance	X	5.81x10^{-8}m.rad
	Y	5.81x10^{-9}m.rad
Momentum compaction factor a		0.0052
Natural chromaticities	x_x, x_y	-19.05, -12.01
Electron beam size and divergence		
Centre of bending magnet	x, y	0.234, 0.237 mm
	x', y'	0.359, 0.062 mrad
Centre of insertion section	x, y	0.903, 0.108 mm
	x', y'	0.064, 0.054 mrad
Bunch length		2.23 cm
Beam lifetime (1% coupling)		18 hours
Energy spread		9.0 x 10^{-4}
Damping times (t_x, t_y, t_e)		4.74, 4.62, 2.28 ms
Revolution frequency		1.738 MHz
RF frequency		505.812 MHz
Harmonic number		291
Power loss		186.6 kW(BM)

To be able to meet the future aspirations and to keep pace with new developments, new insertion devices has also been planned to be set up in the straight sections of INDUS-2. The insertion devices which are going to be installed on INDUS-2 in near future include two planar undulators, one APPLE type undulator and one super conducting wavelength shifter.

It is possible to operate INDUS-2 at any energy between 600 MeV and 2.5 GeV. At lower energies, the emittance of the ring will be much lower and source can be used to produce radiation of much higher brightness. The electron beam extracted from the booster synchrotron is injected into INDUS-2 in the horizontal plane via two septum magnets (one thick and another thin one) by a multi-turn injection process in one of the 4.5 m long straight section by employing a compensated bump which will be produced by means of four kickers. The booster synchrotron provides two bunches each around 1 ns long separated from each other by nearly 30 ns at the required energy at a repetition rate of 1-2 Hz. After injecting several pulses at 600-700 MeV to accumulate 200 mA, the beam is accelerated to 2.5 GeV. To fill a current of 200 mA in INDUS-2 at the repetition rate of 1-2 Hz, a beam lifetime of at least half an hour is required. At the peak energy, beam lifetime of several hours is required for synchrotron radiation experiments. The beam lifetime is mainly decided by two processes, Coulomb scattering within the electron bunch (Touschek scattering) and scattering of electrons with the residual gas molecules. Assuming that the beam circulates in an ultrahigh vacuum environment having vacuum better than 10^{-9} mbar consisting of nitrogen gas and the limiting acceptance from both the transverse planes, the total beam lifetime is around 12 hours which is adequate for all the applications. At 2.5 GeV the beam lifetime is ~ 18 hours. An RF voltage of 1.5 MV is required to achieve this lifetime at 2.5 GeV. The cavity peak voltage is ramped in order to capture the maximum beam. During the voltage ramp, the synchrotron tune is kept constant. The required voltage is generated at the frequency of 505.812 MHz by employing four RF cavities.

An extended X-ray absorption fine structure (EXAFS) beamline based on the Energy Dispersive geometry using a bent crystal polychromator and a position sensitive detector had been developed and installed at a bending magnet port of INDUS-2 SRS for X-ray absorption studies. This is one of the earliest beamlines to be commissioned at INDUS-2 SRS and is open to users from different universities and institutes across India and abroad since 2009. The present thesis work involves collaborative work with different user groups to demonstrate the utility of the EXAFS technique in explaining the macroscopic behaviours of various types of samples of current technological importance, including ionic conductors, luminescent materials, dilute magnetic semiconductors, multiferroics and opto-electronic materials. In all the cases the EXAFS data have been measured at the Energy Dispersive EXAFS beamline (BL-08) at INSUS-2 SRS, the data had been analysed and were also interpreted in the light of the existing information available on the particular sample from other experimental results or from relevant literatures. It should be noted that only in one case (as-deposited and heat-treated $CaWO_4$ nanoparticles) the data have been measured at the Energy Scanning EXAFS beamline (BL-09) at INDUS-2 SRS which had been available to the users from the later part of 2013.

This thesis is divided into eight chapters with the first two chapters being introductory in nature. The remaining six chapters describe different problems that have been addressed by XAS measurements including XANES and EXAFS. Apart from XAS, other characterization methods and first principle calculations have been employed, wherever necessary, to confirm and establish our findings.

Chapter 2

XAFS THEORY, EXPERIMENTATION AND DATA ANALYSIS

The basic physical quantity that is measured in X-ray Absorption Fine Structure (XAFS) spectrocopy is the X-ray absorption coefficient $\mu(E)$, which describes the probability of X-rays being absorbed as a function of incident X-ray energy E. Generally $\mu(E)$ smoothly decreases as the energy increases (approximately as $1/E^3$), i.e. the X-rays become more penetrating. However, at specific energies that are characteristic of the atoms in a material, the absorption co-efficient increases rapidly and these discontinuities are called *X-ray absorption edges*. These occur when the incident X-ray photon has sufficient energy to knock out electrons from the low-energy bound states in the atoms. The X-ray absorption cross section, a quantity that is proportional to $\mu(E)$, is shown in Fig. 2.1 for different elements.

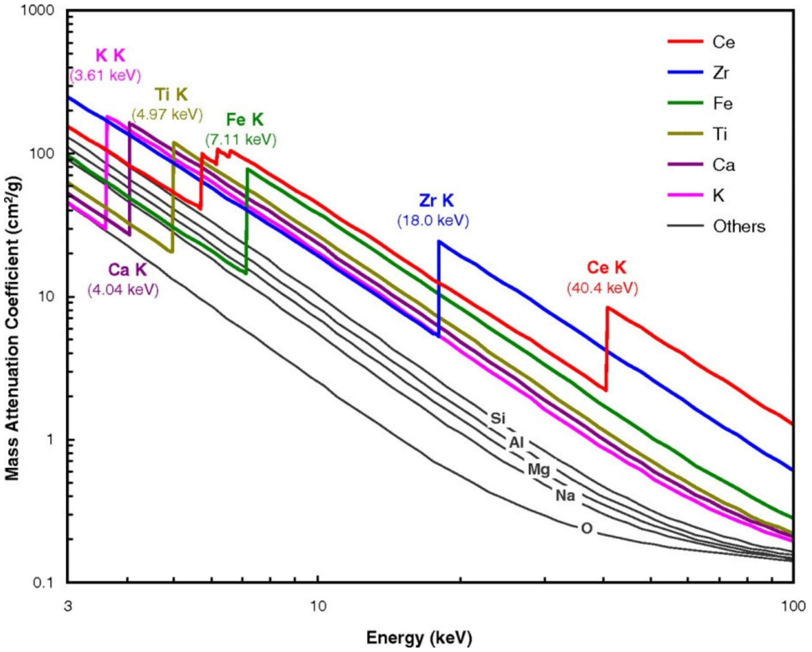

Figure 2.1 Variation of X-ray absorption cross section with incident photon energy.

Absorption edges were first measured in 1913 by Maurice De Broglie. In 1920, using M. Siegbahn's vacuum spectrograph, Hugo Fricke first observed the "fine structure"– energy-dependent variations in the $\mu(E)$ – in the vicinity of the X-ray absorption edges of a number of elements. An example is shown in Fig. 2.2.

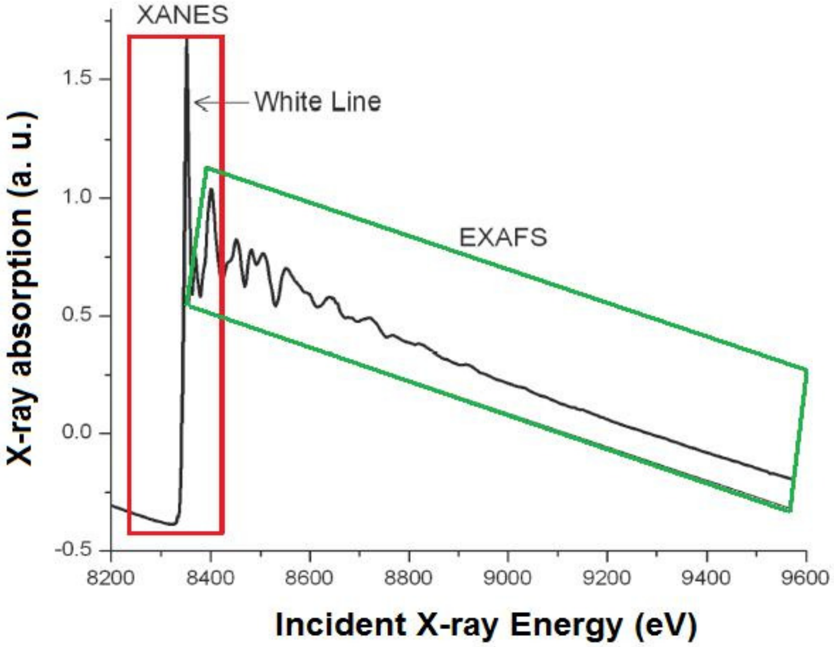

Figure 2.2 X-ray Absorption fine structure spectrum.

Despite some early successes and intermittent progress, the correct theoretical explanation of XAFS eluded researchers for another five decades. In particular, a controversy existed as to whether a model based on the long-range order (LRO) or short-range order (SRO) in the sample was more accurate. This confusion was removed around 1970 when Stern, Sayers, and Lytle [4], [5], [9], [10] formulated a viable theory of XAFS, and further demonstrated that XAFS could be a practical tool for local structure determination.

The term "XAFS" is a broad one that comprises several different techniques: EXAFS (Extended X-ray Absorption Fine Structure); XANES (X-ray Absorption Near Edge Structure); NEXAFS (Near Edge XAFS, which is basically XANES in the soft X-ray regime); and SEXAFS (Surface EXAFS). Although the basic physics of these techniques is fundamentally the same, different approximations, techniques, terminology, and theoretical approaches are employed in different situations, particularly in the low-energy (soft X-ray) and high-energy (hard X-ray) regimes.

2.1 Development of EXAFS equation

In 1931-32, Kronig [1]–[3] first attempted to explain EXAFS and germinated the idea of a short range theory for diatomic molecules which came to be known as short range order (SRO) theory. It had the basic physics of the modern theory of EXAFS i.e. the final state energy spectrum is that of a free electron and the EXAFS is due to the modulations of the final state wave function of the photoelectron caused by the backscattering from the surrounding atoms. In 1941, Kostarev [11] concluded that the SRO theory is accurate for both molecules and matter in the condensed state. The lifetime of the excited photoelectron and the corresponding core-hole state was first calculated by Sawada *et. al.* [12] in terms of a mean free path. Further correction to the theory was introduced by Schmidt [13] who pointed out that the interference of the backscattered waves from atoms at a given average distance will not all be in phase due to the disorder in the distances of the backscattering atoms, as a consequence of structural or thermal vibrations. Hence a Debye-Waller factor was incorporated based on the Debye theory of lattice vibrations. In the period of 1971-75, E. A. Stern and D. Sayers [4], [5], [9], [10] postulated that the photoelectron wavefunction would be modified by the scattering from its nearest neighbour atoms and the interference between the backscattered and outgoing waves would modulate the absorption matrix elements. They had further suggested that a Fourier transform of EXAFS spectrum with respect to the photoelectron wavenumber would peak at distances corresponding to nearest neighbour coordination shells of atoms. In 1975, Lee and Pendry [14] gave first reasonable quantitative theory for calculating EXAFS including multiple scattering effects. A significant progress towards computation was achieved when Rehr and his collaborators [15] developed a computer code called *FEFF* in 1991 that allowed rapid calculations of EXAFS theoretical spectra. The straightforward form of the EXAFS equation has been used in this thesis for theoretical modelling of the data and the corresponding theory is explained in the next sub-section along with inherent assumptions. Detailed mathematical derivation has been omitted here which can be obtained from any standard text [16], [17].

2.1.1 Single Scattering EXAFS

XAFS which is intrinsically a quantum mechanical phenomenon does not occur for isolated atoms and is only observed in condensed matter. In this work the non-relativistic approximations have been assumed unless stated otherwise. The relativistic effects are important mostly for heavy atoms. Interaction of X-rays with matter, in the photon energy range of upto 40 keV, is dominated by photoelectric absorption where the incident photon is completely absorbed, transferring its energy to eject an excited photoelectron and leaving a core-hole in the atom. When the kinetic energy of the ejected photoelectron is about 15eV or greater, this energy is large compared to the interaction energy (~3 eV) with the surrounding atoms. Hence the interaction with the surrounding atom can be treated as a perturbation about an isolated atom. A useful approximation is to treat the behavior of electrons in a many-electron system as that of a single electron moving in the average field of the other electrons. We are interested in the transition rate between a core level (e.g. 1*s*) and final states that is induced by a weak time-dependent perturbation such as an electromagnetic wave. Time-dependent perturbation theory tells us that the transition rate, to first order in the perturbation, is proportional to the squared modulus of the transition amplitude (matrix element), also known as the Fermi's Golden rule:

$$\frac{2\pi}{\hbar}\ |<\boldsymbol{\psi}_f|\boldsymbol{H}|\boldsymbol{\psi}_i>|^2 \qquad (2.1)$$

where $|\psi_i >$ and $|\psi_f >$ are respectively the initial and final electron states, of energy E_f and E_i, ρ is the density of states, and H is the interaction Hamiltonian between the electromagnetic field and the electrons. In the case of excitation by electromagnetic waves, to first order in the field (which, in quantized field picture, corresponds to single photon interactions)

$$\boldsymbol{H} \propto \vec{\boldsymbol{A}}.\vec{\boldsymbol{p}} \tag{2.2}$$

where $\vec{A}$ is the vector potential of the wave and $\vec{p}$ is the momentum operator of the electron. Using commutation relations with the Hamiltonian this can be written as

$$\boldsymbol{\mu} \propto \left|< \boldsymbol{\psi}_f \left|\boldsymbol{\varepsilon}.\vec{\boldsymbol{r}}\, \boldsymbol{e}^{i\vec{k}.\vec{r}}\right|\boldsymbol{\psi}_i > \right|^2 \boldsymbol{\rho}(\boldsymbol{E}_f - \boldsymbol{E}_i - \hbar\boldsymbol{\omega}) \tag{2.3}$$

and ε, $\hbar k$ and $\hbar\omega$ are the X-ray's electric polarization vector, momentum, and energy.

It is useful to express the total absorption coefficient $\mu(E)$ as the isolated atom absorption $\mu_0(E)$ times a correction factor χ:

$$\mu(E) = \mu_0(E)(1+\chi)$$

$$\text{or, } \boldsymbol{\chi}(\boldsymbol{E}) = (\boldsymbol{\mu}(\boldsymbol{E}) - \boldsymbol{\mu}_0\,(\boldsymbol{E}))/\boldsymbol{\mu}_0(\boldsymbol{E}). \tag{2.4}$$

This says that χ is the fractional change in absorption coefficient that is induced by the presence of neighbouring atoms. Within the context of the single scattering approximation (and others discussed below), Stern, Sayers and Lytle [5] derived a simple and extremely useful expression for χ, which has come to be called the standard EXAFS equation. According to this theory, for *K*-edge (and *L*1) excitations, an atom (index *i*) at relative distance r_i makes the following contribution to the EXAFS

$$\boldsymbol{\chi}(\boldsymbol{k}) = \boldsymbol{S}_0^2\, \boldsymbol{\Sigma}_i \frac{3\cos^2\theta_i}{kr_i^2}|\boldsymbol{f}_i(\boldsymbol{k})|\boldsymbol{e}^{-2r_i/\lambda_e} \,\mathbf{sin}\,(2\boldsymbol{kr}_i + 2\boldsymbol{\delta}_1(\boldsymbol{k}) + \mathbf{arg}\,(\boldsymbol{f}_i(\boldsymbol{k})) \tag{2.5}$$

where $k = \sqrt{\frac{2m(E-E_0)}{\hbar^2}} \approx \sqrt{.2625(E - E_0)}$ in eV, Å units), θ is the angle between the X-ray polarization vector ε and the vector $\vec{r_i}$ connecting the central atom with the atom in question. Here, $|f_i\,(k)|$ and arg ($f_i\,(k)$) are the modulus and phase of the complex electron scattering amplitude for each atom: $\delta_1(k)$ is the $l = 1$ partial wave phase shift; and S_0^2 and the photoelectron mean free path λ_e account for losses of coherence due to multi-electron excitations. The $1/r^2$ factor accounts for the $1/r$ decrease in intensity of the photoelectron wave propagating out to the scatterer and then back to the central atom. The overall structure of the simple equation is that of a sum of damped sine waves: a k-dependent amplitude pre-factor times the sine of a phase which is approximately linear in k. In other words, each atom contributes a sinusoidal signal which, when plotted as a function of k, oscillates more rapidly if the distance is larger, thus rapid oscillations in the EXAFS mean long distances. Stronger scattering amplitude generates a larger signal and in an oriented sample, the signal from a given atom is largest when its radius vector lies along the direction of the X-ray polarization vector.

In an experiment one effectively averages over many sites in the sample, and the instantaneous positions of atoms may vary because of thermal and quantum zero point motion and structural heterogeneity. XAFS essentially takes a snapshot of the instantaneous configurations of atoms, because the lifetime of the excited state is limited by the lifetime of the core hole (i.e. the vacancy in the initial 1*s* state), and core-hole level widths ΔE usually are 1 eV or greater, corresponding to time scales of $\tau = \hbar/\Delta E < 10^{-15}$ sec. Because of the rapid spatial variation of the phase factor $\sin(2kr + \delta)$ compared to other r-dependent factors, often the variation of the latter is neglected. The configurational disorder is manifested in the spectra mainly through variations in total path length. The average of the phase factor $<eikr>$ is 1 at $k = 0$ (if the distribution is normalized to 1), so evidently we can expand $\ln <eikr>$ in a Taylor series about $k = 0$ as $\ln <eikr> = ika + (ik)^2 b + \ldots$ where a and b are some constants. Exponentiating both sides we have $<eikr> \approx e^{ika} e^{-bk^2}$. The first term gives an oscillatory contribution while the second term provides a Gaussian damping factor of the sort generally found in the averaged EXAFS equations. The damping occurs because the EXAFS is a superposition of oscillations of different wavelengths. At low *k* the wavelengths are long, so all the contributions add together in phase. As *k* increases, however, the wavelengths become shorter, and the signals of slightly different path length destructively interfere with each other. These damping factors are called EXAFS Debye-Waller factors in analogy with similar quantities in diffraction theory. For randomly oriented polycrystalline or solution samples an isotropic average over angles must be performed. In this case, the contributions from atoms of the same atomic number and at similar distances from the absorbing atom may not be resolvable from each other, and the atoms must be conceptually grouped together into "coordination shells". For small variations in distance within a shell, the equation becomes:

$$\chi(k) = \sum_j \frac{S_0^2 N_j}{kR_j^2} \left|f_j(k)\right| e^{-2R_j/\lambda_e} \, \mathrm{e}^{-2\mathrm{k}^2\sigma_j^2} \sin\left(2kR_j + \delta_j(k)\right) \qquad (2.6)$$

where N_j is the number of atoms in the coordination shell, and σ_j^2 is the mean square variation of distances about the average R_j to atoms in the *j*th shell. This is the classic EXAFS equation of Stern, Sayers, and Lytle [4],[5] for an un-oriented sample with Gaussian disorder with corrections for many body effects incorporated. This equation has been employed for all the theoretical fitting in the present thesis.

2.1.2 Approximations

- *Dipole approximation*

The exponential in the matrix element in Equation 2.3 can be expanded as

$$< \psi_f \left| \varepsilon . e^{i\vec{k}.\vec{r}} \right| \psi_i > \approx \; < \psi_f | \varepsilon . \vec{r} | \psi_i > + \, i < \psi_f \left| (\varepsilon . \vec{r}) (\overrightarrow{k . \vec{r}}) \right| \psi_i > + \cdots$$

The first term is the dipole term; the second term is the quadrupole term. The ratio of the quadrupole to dipole matrix elements for Fe, $Z = 26$, is about 10%, and the ratio of the transition probability is about 1%, for *K*-edges. This shows that dipole approximation is good, but that quadrupole transitions are not always negligible. They can be readily observed in some situations when not masked by allowed dipole transitions, for example in the pre-edge region of transition metal complexes. The quadrupole/dipole ratio grows quadratically with *Z*, so that it can be expected to be substantial for heavier atoms, and for *L*-edges because of size of the initial state wavefunction. Multipoles of higher order than quadrupole are usually negligible.

- *Orientation dependence*

Summing over final states of different energies, in the dipole approximation we can rewrite the expression for the absorption probability as $\mu \propto \varepsilon . M . \varepsilon = \sum_{j,k} M_{jk} \, \varepsilon_j \, \varepsilon_k$

where $\varepsilon = (\sin\theta\cos\phi,\ \sin\theta\sin\phi, \cos\theta)$ is the X-ray polarization vector expressed in spherical coordinates θ, φ. Although the tensor can be diagonalized by choosing an appropriate coordinate system at one energy, it is not generally possible to do this at all energies. However, when the sample itself has certain symmetries the form simplifies considerably. An important special case is if the sample is isotropic (e.g. solution or randomly oriented polycrystalline, or is of cubic symmetry) the absorption tensor is proportional to the identity matrix – it may as well be taken as a scalar. Now suppose that we have a pair of atoms aligned along the z axis, and we excite them with X-rays. Evidently we can expect both $\cos^2\theta$ and $\sin^2\theta$ angle dependencies, where θ is the angle between the polarization vector and the vector connecting the atoms. Calculation shows that in *K*-edges the $\sin^2\theta$ contribution dies off rapidly with energy above the edge, leaving only the $\cos^2\theta$ dependence. However, it must be remembered that the $\sin^2\theta$ term is generally present in the near-edge region, as it is for *L*-edges [18], [19].

- *Selection rules*

The core state from which the electron is removed, is deeply bound, and the dominant interaction of the electron is with the nucleus and electrons of the central (photo absorbing) atom. As a consequence, the initial state is well approximated as an atomic-like state of angular momentum quantum numbers l and m. The transition operator in the dipole approximation is proportional to the vector $\vec{r}$. The final-state wavefunction can be expressed as a linear combination of functions with specific *l, m,* which are eigenfunctions of the operators L^2 and L_z. Because of the orthogonality of spherical harmonics, the transition matrix element projects out only the part of the final-state wavefunction that has the appropriate symmetry for an allowed transition. Electric dipole selection rules tell us that $\Delta l = \pm 1$, and quadrupole selection rules $\Delta l = \pm 2, 0$. Dipole selection rules therefore imply that for *K*- and *L*1-edges, allowed transitions are to states containing *p* symmetry. For *L*2- and *L*3-edges, allowed transitions are to final states containing *d* and *s* symmetry.

- *Small atom approximation*

In this approximation the spherical wave incident on a backscattering atom is approximated by a plane wave. It is only valid when the effective size of the backscattering atom is small compared to the distance between the atom and the central atom, which is true for a photoelectron with high k-value. At low k values, this approximation breaks down.

2.1.3 Corrections

- *Many body effects*

(a) Passive electron effect: As a consequence of absorption of the incident photon, a core electron is knocked out from the excited atom. The atomic electrons of this excited atom perceive a modified potential, which can be approximated by that of an atom with its Z increased by 1. Thus the nucleus attracts the other electrons more, pulling in the wave functions of the original atom and relaxing them to a lower energy. These are called *passive electrons* because they are not directly excited by the x-ray, in contrast to the core electron. In the independent particle model, the wave function of the atom is a product of the wave functions of each electron. If relaxation is neglected, the passive electron states do not change as the atom is excited by the incident photon, and their contribution to the matrix element consists of the product of their overlaps before and after excitation as below:

$$\prod_i |<p_i|p_i>|^2 = 1$$

where $|p_i>$ is the wave function of the ith passive electron. However, if this electron relaxes to some other state $|p_i'>$ in the excited atom, the overlap contribution of the passive electron becomes

$$S_0^2 = \prod_i |<p_i|p_i'>|^2 < 1$$

The product S_0^2 is less than 1 because $|p_i'>$ is normalized and its overlap with $|p_i>$ can be 1 at the most when $|p_i'> = |p_i>$. Hence, S_0^2 is a parameter slightly less than unity that accounts for the less overlap between the wave functions of the passive electrons in the initial and final states. Thus the many body relaxation effect reduces the value of μ by the factor S_0^2 which is in the range of 0.7 – 0.9 in typical cases.

(b) Mean free path: Another key ingredient for accurate calculations at high energies is to account for the fact that the photoelectron interacts dynamically with the gas of other electrons in the material, and its behaviour is substantially modified by these many-body effects. The "leaking away" of probability from the wavefunction effectively introduces a mean free path into the formalism, which means a loss of coherence as the electron propagates through the material. Probability is lost from the main single electron (quasiparticle) channel into a large number of multi-electron channels that need not be explicitly calculated. The effect limits the range of the photoelectron, so the spectra are sensitive only to the short range order in the sample. The electron mean free path is energy dependent, of magnitude ~ 5-10 Å, which limits the sensitivity of XAFS to regions of about nanometer scale or less.

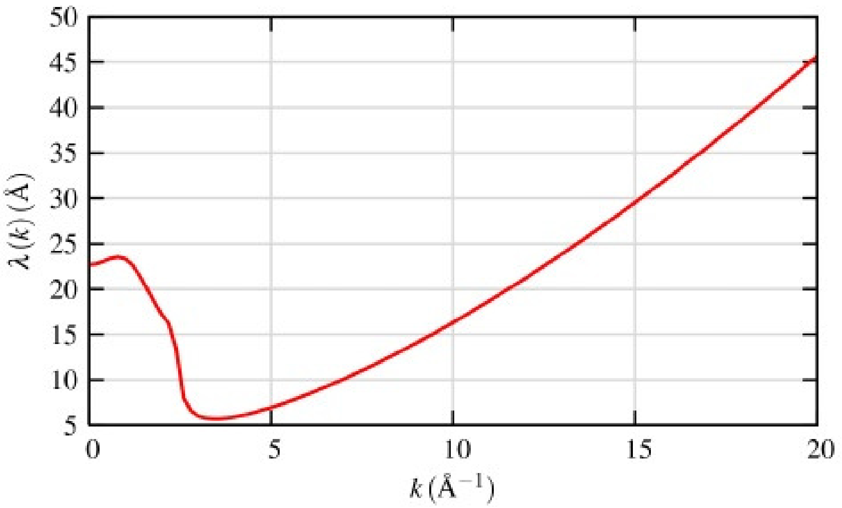

Figure 2.3 Variation of photoelectron mean free path.

(Ref. http://xafs.org/Tutorials; Fundamentals of XAFS, Matthew Newville, Consortium for Advanced Radiation Sources, University of Chicago, Chicago, IL)

- *Multiple Scattering*

The neglect of multiple scattering in the simple equation implies that the total $\chi(k)$ is a simple linear sum of contributions from backscattering atoms. This is a useful first approximation, but it is well known that multiple scattering is often important in EXAFS, particularly when the absorbing atom and scatterers are collinear as shown below.

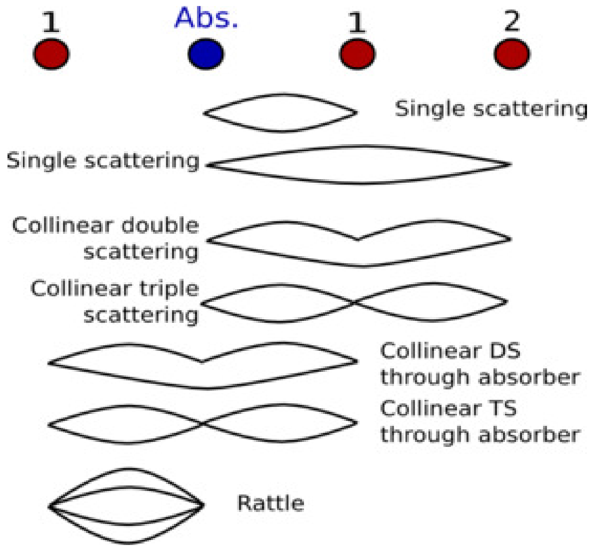

Figure 2.4 Possible nearest neighbour (NN) and next nearest neighbour (NNN) scattering paths.

Most multiple scattering approaches currently employ the “muffin-tin” approximation, in which the atomic potentials are approximated as spherically symmetric out to a finite radius, and the interstitial potential between the atomic sphere is approximated as a constant. This approximation tends to work well for close-packed structures, but is less successful with open structures. A muffin-tin potential is sketched in Fig. 2.5. Typically the muffin-tin radii are chosen so that the charge inside equals that of the atom (*Norman criterion*). In practice the muffin-tin radii often are scaled up so that they overlap slightly, which experience has shown partially makes up for deficiencies in the muffin tin approximation. In the EXAFS region, the kinetic energy of the electron is large enough that small variations in the interstitial potential do not make much difference, and the muffin-tin approximation works well.

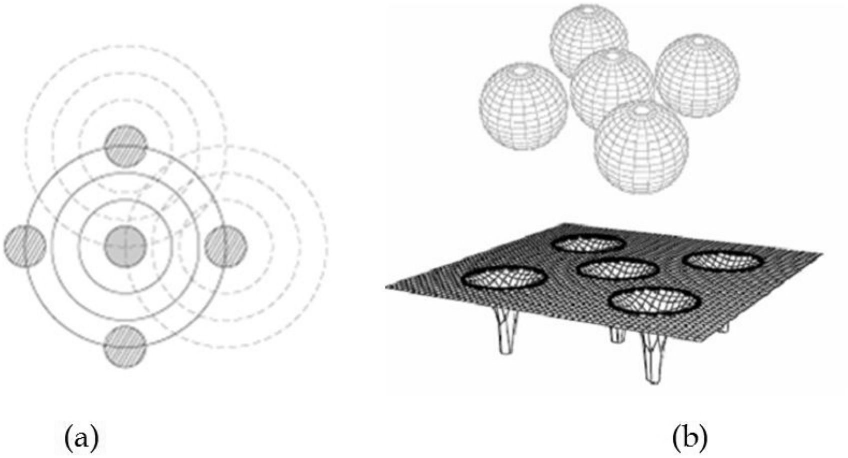

$$\begin{aligned} V(\boldsymbol{r}) &= V_T(\boldsymbol{r}) - V_{MTZ} \quad \text{for } \boldsymbol{r} < \boldsymbol{r}_{MT} \\ &= 0 \qquad\qquad\qquad\quad \text{for } \boldsymbol{r} \geq \boldsymbol{r}_{MT} \end{aligned}$$

Figure 2.5 Schematic of muffin-tin (MT) potential.

- *Anharmonicity*

If the disorder is too large for the Gaussian Debye-Waller factor to suffice, additional terms must be included in the exponential and new terms are introduced into the phase. If these terms are substantial, but are ignored, serious errors in the interatomic distance and other parameters can occur. The cumulant expansion is particularly useful for describing anharmonic systems and thermal expansion.

It is remarkable that, when spherical wave effects, many body interactions, etc. are included, the basic structure of the original EXAFS equation is preserved as long as the plane wave scattering amplitude $f(k)$ is replaced by an *effective* scattering amplitude f_{eff} (k; r): the scattering amplitude acquires a weak r dependence.

2.2 XANES interpretation

In the vicinity of the absorption edge, the interaction of the ejected photoelectron with the potential of the neighbouring atoms is still strong so the simplifying single scattering assumption leading to EXAFS is not possible. The EXAFS equation breaks down at low-k, due to the 1/k term and the increase in the mean-free-path at very low-k. In the near-edge (XANES) region the muffin-tin approximation is less satisfactory for quantitative analysis and the interpretation of XANES is complicated since there is no simple analytic description of XANES. However, useful information regarding the chemical environment can be obtained from the XANES region. The absorption edge position and shape is sensitive to formal valence state, ligand type, coordination geometry and can be used as a fingerprint to identify phases.

The final states of K and L1 edges are *p*-states, and the final states in L2 and L3 edges are a mixture of *d* and *s* character. The *p* final states of K and L1 edges are more diffuse than the localized *d* final state of L2 and L3 edges. All of these edges may show strong peaks at the top of the edge (the “principal maximum”). Historically these were called “white lines,” because that was how they appeared on photographic plates. For K shell absorption, where the core-level is a *1s* state, the photo-electron has to end up in a *p* state according to the selection rules of transition. Thus, even if there are available states with the right energy, there might be no *1s* absorption if there are no available *p* states. For EXAFS, where the energies are well-above the threshold energy, this is rarely an important concern. For XANES, on the other hand, this can play a very important role. From a molecular orbital point of view, the bound states in the pre-edge region consist of linear combinations of orbitals that have specific symmetry properties. If the Hamiltonian is symmetric under inversion, states of opposite parity cannot mix to make an eigenstate of the Hamiltonian. This implies that *p* states (odd parity) can only mix with *d* or *s* states (located at the central atom) if the Hamiltonian (and therefore the local environment) is not totally symmetrical under inversion. Since the final state in *K*- and *L*1-edges are of *p* symmetry (by dipole selection rules), any strong transition near the energy of the metal 3*d* orbitals indicates a breaking of inversion symmetry. Transition metal oxides, for example, usually have many unfilled *3d* electrons near the Fermi level, and a filled *3p* band. There are empty *2p* electron states from the oxygen, but these are too far away to appreciably over-lap with the metal *1s* band. Therefore, the metal *3d* electrons do not normally participate in the absorption process unless there is a strong hybridization of the O *2p* and metal *3d* levels. The XANES spectra are especially sensitive to such hybridization. For ions with unfilled *d*-electron bands, the *pd* hybridization is dramatically altered depending on the coordination environment, with much stronger hybridization for tetrahedral coordination than for octahedral coordination. Since the photo-electron created due to a *1s* core level (a K-shell) must have *p*-like symmetry, the amount of overlap with the *d*-electron orbitals near the Fermi level can dramatically alter the number of available states to the *p*-electron, causing significant changes in the XANES spectrum. This argument would suggest that the pre-edge transition strength should be identically zero for inversion symmetric sites. However, quadrupole transitions can be weakly present because the transition Hamiltonian contains small terms that are non dipolar as previously discussed in *section 2.1.2.* Such terms can be observed in the pre-edge of most transition metal complexes.

Another important and common application of XANES is to use the shift of the edge position to determine the valence state. Fig. 2.6 shows the valence dependence of Fe metal and oxides of Fe^{2+} and Fe^{3+} (and a mixture of these two). With good model spectra, Fe^{3+}/Fe^{2+} ratios can be determined with very good precision and reliability. The heights and positions of pre-edge peaks can also be reliably used to empirically determine oxidation states and coordination chemistry.

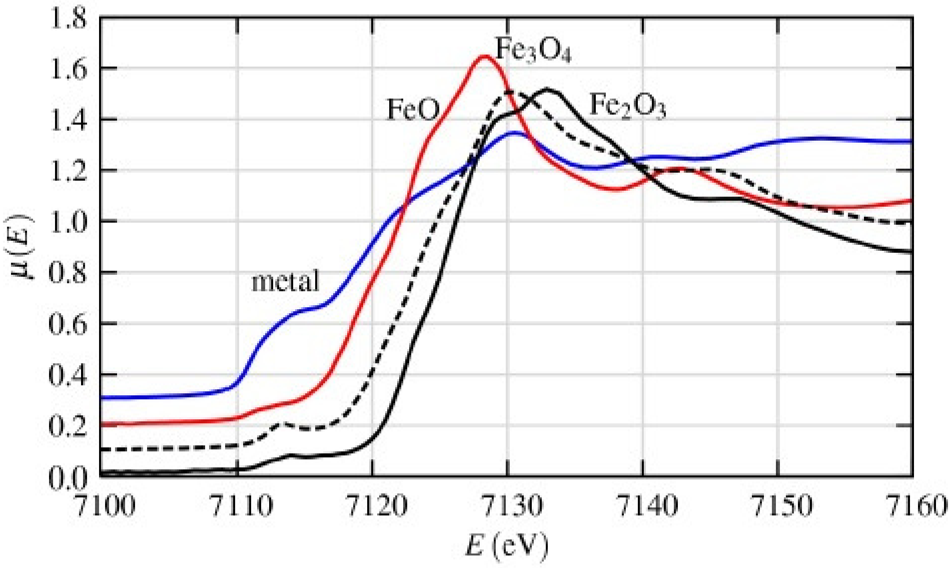

Figure 2.6 XANES spectra of standard Fe metal and oxides.

(Ref. http://xafs.org/Tutorials; Fundamentals of XAFS, Matthew Newville, Consortium for Advanced Radiation Sources, University of Chicago, Chicago, IL)

For many systems, XANES analysis based on linear combinations of known spectra from "model compounds" is sufficient to estimate the ratios of valence states and/or phases. More sophisticated linear algebra techniques such as Principle Component Analysis and Factor Analysis can also be applied to XANES spectra. Some materials, such as the spinel and inverse spinel structures have metal ions in nonequivalent sites: 2/3 of the sites are octahedral, and 1/3 of them are tetrahedral. Despite the dilution due to octahedral sites, the 3*d* pre-edge peaks are noticeably larger than the pure octahedral case. In some cases the states associated with pre-edge transitions are full ($3d^{10}$ configuration) in one charge state, but have a hole ($3d^9$) in another charge state. For example, the presence or absence of the 3*d* pre-edge transition can be used to detect the difference between Cu^+ and Cu^{2+}. Correlating formal charge state with absorption edge shifts is obvious from simple physical arguments that shifts of a few eV can indeed occur by transferring charge.

2.3 XAFS Experimental Technique

2.3.1 Data Collection (TM, FL, TURBO)

EXAFS measurements with synchrotron radiation are generally carried out in two different modes. In the more conventional one the beamline uses a double-crystal monochromator (DCM) to select a particular energy from the incoming synchrotron beam, which is incident on the sample and the intensity of the transmitted beam passing through the sample or that of the fluorescence beam emerging out of the sample is recorded along with the incident intensity at each energy. The absorption data of the sample are then recorded by scanning the monochromator over the whole energy range of interest and hence this is called the *Energy Scanning* EXAFS mode.

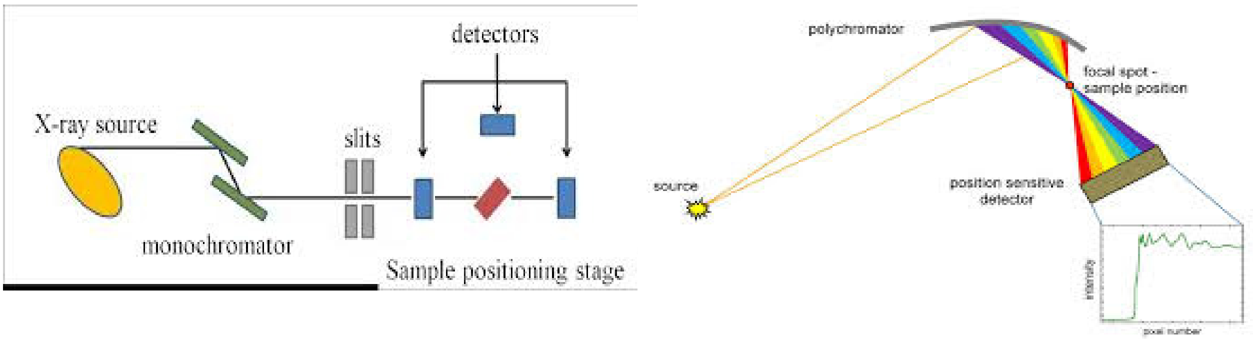

Figure 2.7 (a) Energy Scanning and (b) Energy Dispersive EXAFS modes.

However, it takes several tens of minutes to measure an EXAFS spectrum for dispersed species by the conventional energy scanning XAFS technique and thus it cannot monitor time-dependent structures during dynamic chemical processes. Rapid scanning monochromators have subsequently been developed that permit spectra to be collected in less than a minute [20] and much smaller energy ranges can be scanned at 10 Hz by use of a vibrating monochromator [21]. However, despite these advances, it is clear that energy scanning EXAFS mode is not yet suitable to monitor dynamic change of structures in msec time scale which is required for in situ monitoring of fast kinetics e.g., reaction processes of catalytic materials.

In the other mode of measurement, viz., the *Energy dispersive* EXAFS (EDXAS) mode, on the other hand, a bent crystal polychromator is used to select a band of energy from the white synchrotron beam horizontally dispersed and focused on the sample. The transmitted beam from the sample is recorded on a position sensitive CCD detector, thus enabling recording of the whole EXAFS spectrum around an absorption edge in a single shot. As no mechanical motion for monochromatizing X-rays is required in this technique, EXAFS spectra can be measured in 1s or even less. The EDXAS technique is applied for the elucidation of structural changes during catalyst preparation, chemical treatment, catalytic reaction, study of transient and short-lived species, phase transition under high pressure, etc. [22] [23]. The two experimental modes of EXAFS measurement are illustrated in Fig. 2.7.

XAFS can be measured either in transmission or fluorescence geometries. Transmission mode simply involves measuring the X-ray flux before and after the beam is passed through a homogeneous sample. Under these conditions, the transmitted flux I is related to the incident flux I_0 by:

$$\boldsymbol{I/I_0 = \exp(-\mu(E)x), \text{ or } \mu(E)x = \ln(I_0/I).} \tag{2.7}$$

Transmitted mode measurements are useful for uniformly thick bulk samples having optimum concentration of the absorbing species.

In X-ray fluorescence, a higher energy core-level electron fills the deeper core hole, ejecting an x-ray of well-defined energy. The fluorescence energies emitted in this way are characteristic of the atom, and can be used to identify the atoms in a system, and to quantify their concentrations. For example, an L shell electron dropping into the K level gives the K_α fluorescence line. Since the fluorescence process is a secondary process of photoelectric absorption, all the features of the absorption spectra of a sample get reflected in its fluorescence spectra also and hence fluorescence spectra can also be used to study the EXAFS oscillations. In fluorescence mode one measures the incident flux I_0 and the fluorescence X-rays I_f that are emitted following the X-ray absorption event and follows the relation:

$$\mu(E) \propto I_f / I_0 \tag{2.8}$$

In EXAFS measurements, usually the fluorescence detector is placed at 90° to the incident beam in the horizontal plane, with the sample at an angle (usually 45°) with respect to the beam. This mode is suitable for dilute samples, liquid samples, thin films on thick substrates etc. Fluctuations in the number of elastically scattered X-rays are a significant source of noise in fluorescence XAFS, so the position of the detector is selected to minimize the elastically scattered radiation by exploiting the polarization of the X-ray beam. There are two main considerations for making good fluorescence XAFS measurements: solid angle and energy resolution. The fluorescence is emitted isotropically, and every effort is made to collect as much of the available signal as possible. The scatter is actually not emitted isotropically because the x-rays from a synchrotron are polarized in the plane of the synchrotron. It means that elastic scatter is greatly suppressed at 90 degrees to the incident beam, in the horizontal plane. Therefore, fluorescence detectors are normally placed at a right angle to the incident beam. Energy discrimination is important because it can potentially allow us to completely suppress the scatter peak and other fluorescence lines, and collect only the intensity of the fluorescence lines of interest. This would greatly suppress the background intensity, and increase the signal-to-noise level. Energy discrimination can be accomplished either physically, by filtering out unwanted emission before it gets to the detector by using a Z-1 filter, or electronically after it is detected as shown in Fig. 2.8. To avoid re-radiation from the filter itself, a set of slits (Soller slits) is often used to preferentially collect emission from the sample and block the emission from the filter. Since we know which element is to be probed, we know the energy of the expected x-ray photon and we can establish a band of channels in the solid state detector. These spectra are useful in their own right for being able to identify and quantify the concentrations of other elements in the sample.

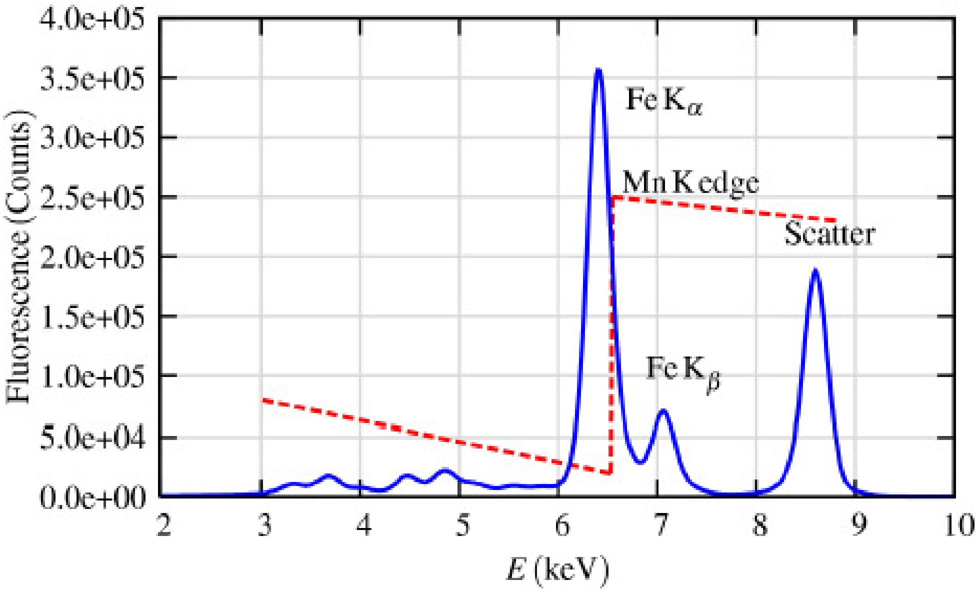

Figure 2.8 The effect of "Z-1" filter on a measured fluorescence spectra.

However, unwanted portions of the fluorescence spectra can also be completely rejected and thus these detectors can be used for XAFS measurements with concentrations down to ppm levels. This band of channels is referred to as a “window” and when we select this window to determine a specific absorption edge, the window is referred to as a “Region of Interest,” or

ROI. The two configurations (transmission and fluorescence) of EXAFS measurements are shown schematically in Fig. 2.9.

In principle, as per the optical layout of an Energy Dispersive set up as shown in Fig. 2.7(b), measurement is only possible is transmission geometry, which poses a problem for measurements on dilute samples and samples deposited on thin films. However, with a slight modification, an Energy Dispersive set up can also be used for EXAFS measurements in fluorescence based geometry which allows good data quality, offering a correct normalization due to the simultaneous recording of I_0 and I_t.

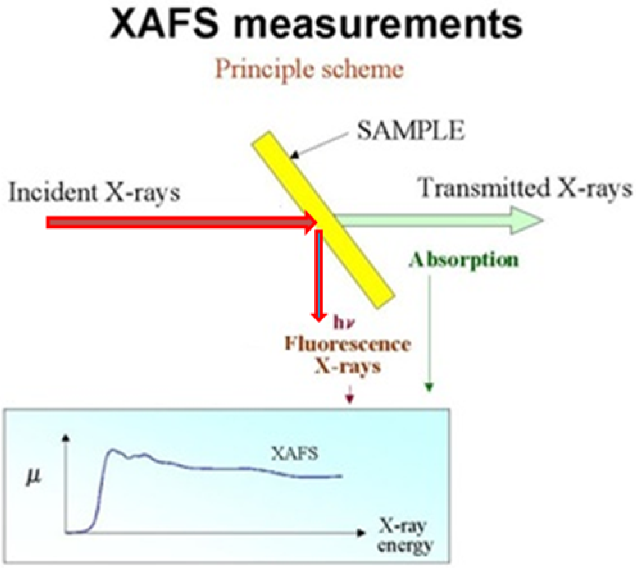

Figure 2.9 Transmission and Fluorescence mode of data collection.

In this modified configuration, first proposed by Pascarelli et al. [24] and known as turbo-XAS (T-XAS) a monochromatic beam is obtained at the sample (focus) position by placing a narrow slit in the energy-dispersed fan of radiation immediately before the polychromator set up as shown in Fig. 2.10. The incident signal is measured in a gas detector positioned before the focal point (D_1) while the fluorescence signal from the sample is detected by a a fluorescence detector D_2 (Lytle-type of a Silicon drift detector-type). The whole EXAFS spectrum is recorded by scanning the slit precisely across the fan of beam. The simultaneous recording of I_0 and I_t implies that the experimental set-up is intrinsically less sensitive to beam instabilities. The experimental setup also profits from the small and stable horizontal focal point and high energy scale stability and reproducibility of the dispersive optics thanks to the decoupling of the monochromatization and of the focusing action. Finally, T-XAS also enables detection of decay channels, allowing time-resolved studies of surfaces and dilute samples or growth of nanoparticles using dispersive optics, in the transmission mode as well as in the fluorescence mode. Due to the possibility of obtaining a correct normalization of the data, T-XAS is also widely employed for the large number of static XAS experiments which need dispersive optics because of the small and stable focal spot, such as high-pressure experiments or which need a high stability of the energy scale, such as XMCD measurements.

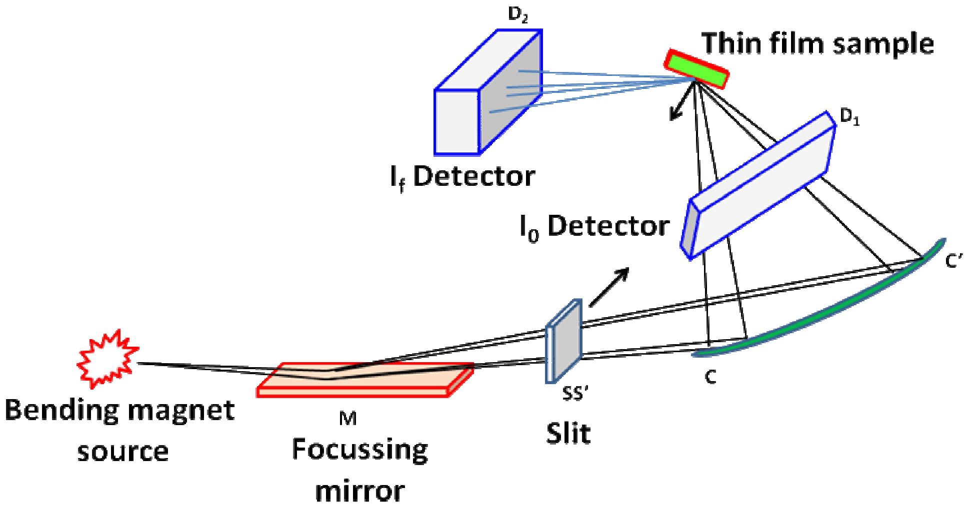

Figure 2.10 A schematic diagram of the TURBO-XAFS experimental set up in an energy dispersive EXAFS beamline.

The EXAFS data presented in this thesis have been measured at the INDUS-2 synchrotron radiation source at RRCAT, Indore, India where a comprehensive EXAFS measurement facility, consisting of two beamlines, has been developed in recent years which facilitate the two modes of XAFS measurements as described above viz., energy dispersive mode and energy scanning mode.[25] Both the beamlines are described briefly in the following section.

2.3.2 Energy Dispersive EXAFS beamline (BL-08)

A energy dispersive extended X-ray absorption fine structure (EXAFS) beamline using a bent crystal and position sensitive detector has been developed and installed at a bending magnet port of INDUS-2 for X-ray absorption studies in the energy dispersive geometry [26].

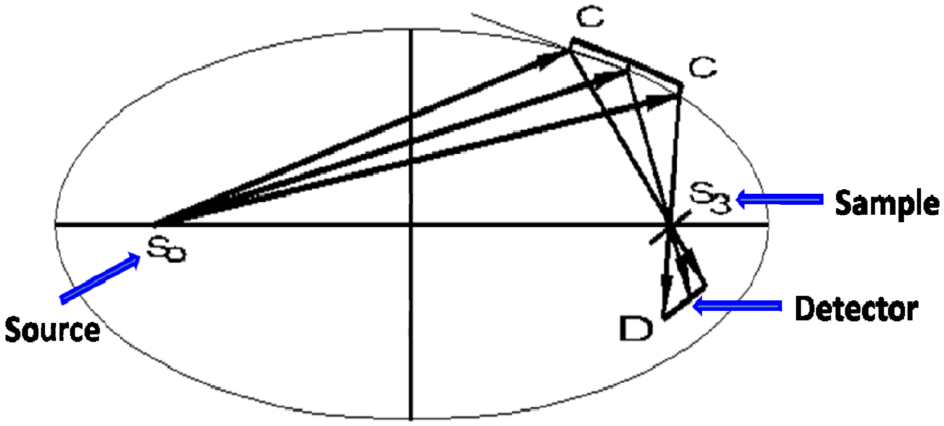

Figure 2.11 Working principle of the Energy Dispersive EXAFS beamline (BL-08) at INDUS-2 SRS

The beamline works in the dispersive mode using a 460-mm-long Si (111) crystal mounted on an elliptical bender and a position-sensitive CCD detector having 2048×2048 pixels. The beamline is designed to cover the photon energy range of 5 – 20 keV providing energy bandwidths of 0.3, 1.0 and 2.0 keV and with resolution of ~ 0.5, 1 and 2eV per pixels at photon energies of 5, 10 and 20 keV, respectively. The optical layout of the beamline is shown in Fig. 2.11. Here, a bent single crystal (C,C) forms part of an ellipse such that the source (S0) and the sample positions (S3) are situated at two focii of the ellipse. The elliptical optics ensures all radiation emerging from one focus (S0) reach the other focus (S3) after reflection from the crystal and offers minimum aberration.

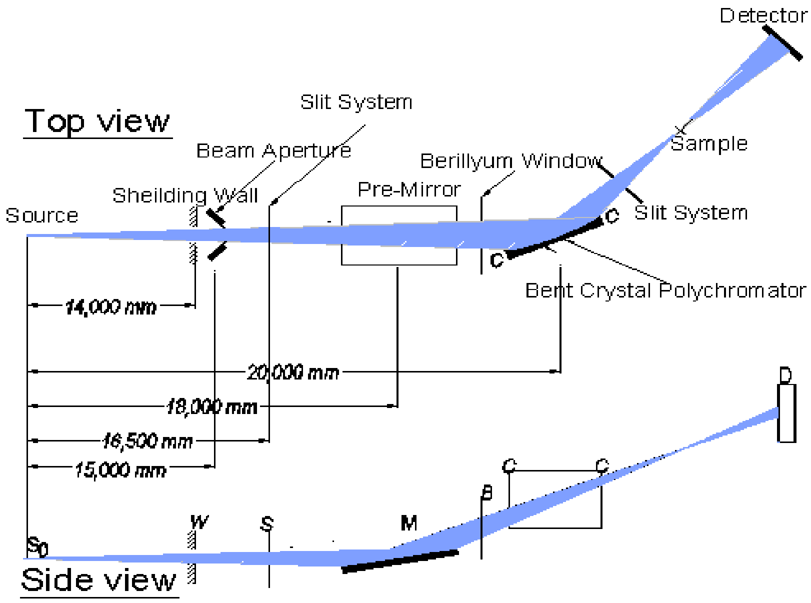

Figure 2.12 Optical layout of BL-08.

The emission from the synchrotron source is first passed through a Be window (B) of suitable thickness to cut off the unwanted low-energy part from the continuum and then through the beam aperture system consisting of two copper blocks (K,K) positioned at an angle of 15° to the beam path for collimation. The collimated beam with horizontal divergence of 1.5 mrad is then made to fall on the slit system (S,S) which defines the final horizontal and vertical divergence of the synchrotron beam using two sets of water-cooled tantalum jaws. The beam emerging from the slit system with required vertical and horizontal divergences falls on a vertically focusing mirror (M, M) at a grazing angle of incidence ~ 0.2°, which cuts off the higher energy part of the synchrotron beam. After reflection from the mirror, the beam falls on silicon crystal (C, C) mounted on a bender. Depending on the angle of incidence of the beam and its radius of curvature, the crystal reflects a particular central energy (E_0) with a certain band-width (ΔE) and this spatially dispersed polychromatic radiation is focused at the sample position (S3). The transmitted radiation from a sample diverges further and is detected by a position- sensitive detector (D,D). Thus, the energy dispersed absorption spectra of the sample over the whole bandwidth (ΔE) around the central energy (E_0) can be simultaneously recorded by the detector.

A <111> oriented (2d = 6.2709 Å) Si single crystal has been chosen as the polychromator consequent to its narrow Darwin width, low thermal expansion coefficient and high thermal conductivity. The source to Si crystal distance (p) is fixed based on practical considerations is 20,000 mm. The horizontal beam divergence (U_m) is chosen to be 1.5 mrad taking into consideration the detector and crystal sizes and heat flux falling on different beamline components. The energy bandwidths (ΔE) sought for meaningful EXAFS studies at different central energies within the energy regime of 5–20 keV have been decided considering practical values of the radius of curvature (R) of the crystal achievable by the crystal bender.

The values of other beamline parameters have been determined as follows. The Bragg angle θ_0 for the central ray at the pole of the crystal is obtained from the central photon energy E_0 or wavelength λ_0 from the Bragg relation:

$$\sin\theta_0 = \frac{\lambda_0}{2d} \tag{2.9}$$

Since the source to crystal distance (p) and horizontal divergence (U_m) are fixed, the length of the illuminated portion of the crystal (l) corresponding to the central energy E_0 is then determined by the simple geometrical relation:

$$U_m = \left(\frac{l}{p}\right)\sin\theta_0 \tag{2.10}$$

For simplification of calculations, initially we have assumed the elliptical crystal to be a spherical cylinder having a uniform radius of curvature (R_0). Since l is known, the radius of curvature (R_0) can be determined by the following relation for a pre-specified value of the energy bandwidth (ΔE) for all values of E_0. [27]

$$\Delta E = E_0 l \cot\theta_0 \left(\frac{1}{R_0} - \frac{\sin\theta_0}{p}\right) \qquad (2.11)$$

Since the values of p, θ_0 and R_0 are known, the crystal to sample distance (q) is then determined from the equation below

$$\frac{1}{\sin\theta_0} = \frac{R_0}{2}\left(\frac{1}{p} + \frac{1}{q}\right) \qquad (2.12)$$

The above calculations have been done for various photon energies between 5 and 20 keV.

It should be noted here that, following eqn. 2.11, the band width obtained at a particular central energy in such a set up is limited by the minimum radius of curvature attainable on the crystal by a mechanical crystal bender within the elastic limit of silicon. Thus in the energy dispersive EXAFS beamline described here, though one can get reasonlably good band width of ~1000 eV at central energy of 10 keV, it reduces significantly in lower energy range with only ~400 eV of available band width at 6 keV. This poses a major limitation in utilization of the present enrgy dispersive beamline for probing elements whose X-ray absorption edges lie below 7 keV.

The CCD at BL-08 is an ANDOR make, Model no. DW 436-F0 Sr No.: CCD-3320 area detector with 2048 × 2048 pixels each having a width of 13.5 μm. It has a theoretical resolution of 1eV/pixel, though this can be increased or decreased depending on the experimental requirements. Each element interacts with light to build up a charge – the brighter the light, and/or the longer the interaction, the more charge is registered. At the end of the measurement read out electronics pull the charge from the elements, at which point each individual charge reading is measured. A schematic diagram depicting the principle of action is shown in Fig. 2.13**.** CCDs require some degree of cooling to make them suitable for high grade spectroscopy. Typically this is done using either water cooling, peltier cooling (suitable for temperatures down to -90^{o}C), and liquid nitrogen cryogenic cooling. We have a water cooling system that maintains the detector temperature at –35^{o}C.

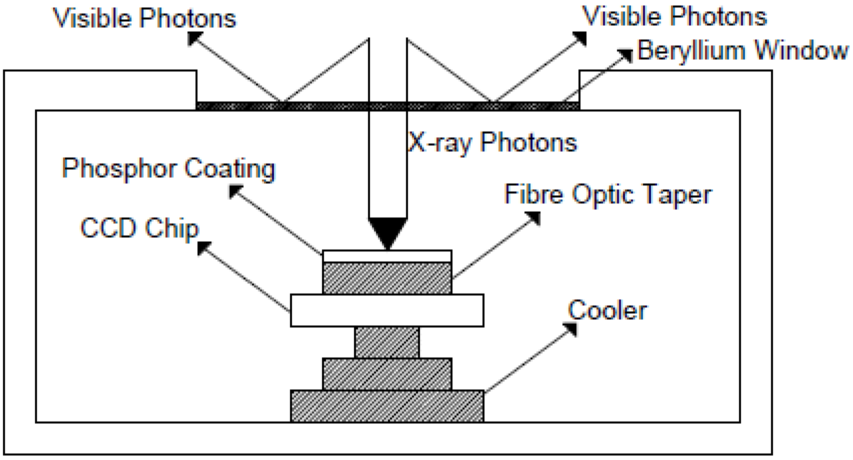

Figure 2.13 Schematic diagram of the working principle of a CCD.

A photograph of the beamline after final installation is shown in Fig. 2.14.

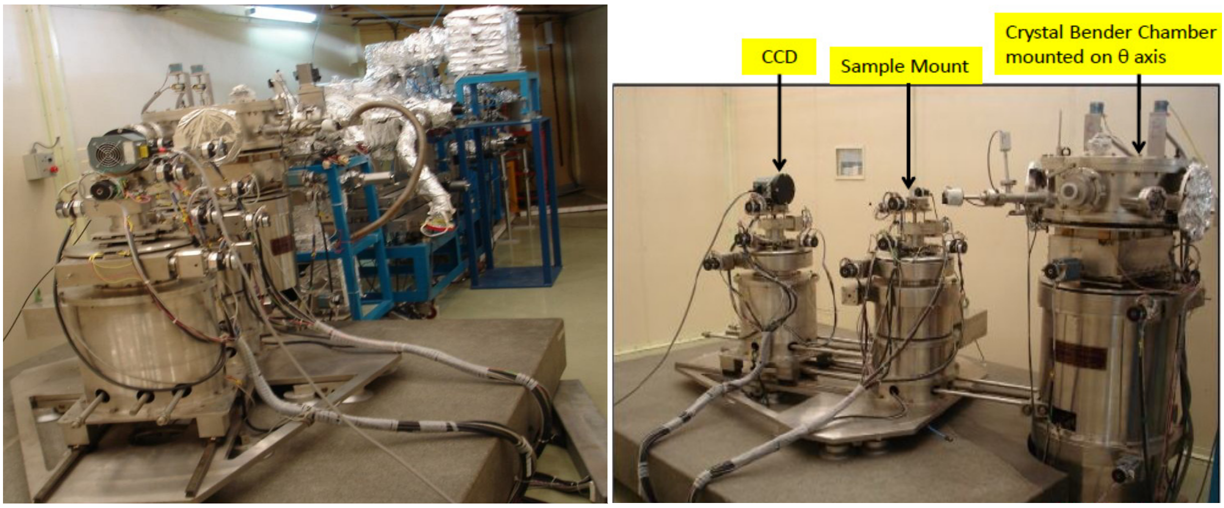

Figure 2.14 Photograph of the Energy Dispersive EXAFS beamline (BL-08).

Fig. 2.15 shows the synchrotron beam spot on a CCD screen focused horizontally by the crystal bender and vertically by the mirror at the sample position for 20,000eV setting of the crystal. It should be noted that prior to the EXAFS measurement at any particular energy edge in this Energy Dispersive set up, the uniformity of the focal spot at the sample position has been carefully checked. This has been done by illuminating different regions of the bent crystal sequentially by scanning a fine slit at the polychromator entrance and observing the intensity distribution of the focal spot recorded on a CCD screen kept at the sample position. Aberrations in the focal spot, if any is corrected by precisely adjusting the two stepper motors connected to the crystal bender.

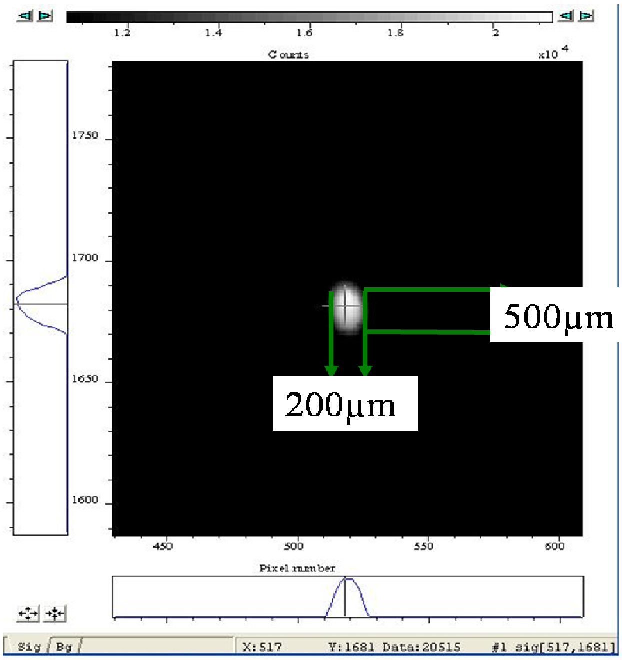

Figure 2.15 Focussed beam spot at the sample position at 20 keV.

In some of the studies in the present thesis a closed cycle cryostat has been used to carry out temperature dependent EXAFS measurements. The major components of the closed cycle cryostat are the expander, compressor, vacuum shroud, and radiation shield. The expander, commonly referred to as the coldhead or cold finger, is where the refrigeration cycle takes place. It is connected to a compressor by two gas lines and an electrical power cable. One of the gas lines supplies high pressure helium gas to the expander, the other gas line returns low pressure helium gas from the expander. The compressor provides the necessary helium gas flow rate at the high and low pressure for the expander to convert into the desired refrigeration capacity. The vacuum shroud surrounds the cold end of the expander in vacuum limiting the heat load on the expander caused by conduction and convection. The radiation shield is actively cooled by the first stage of the expander and insulates the second stage from the room temperature thermal radiation being emitted from the vacuum shroud. A schematic of the cryostat is shown in Fig. 2.16.

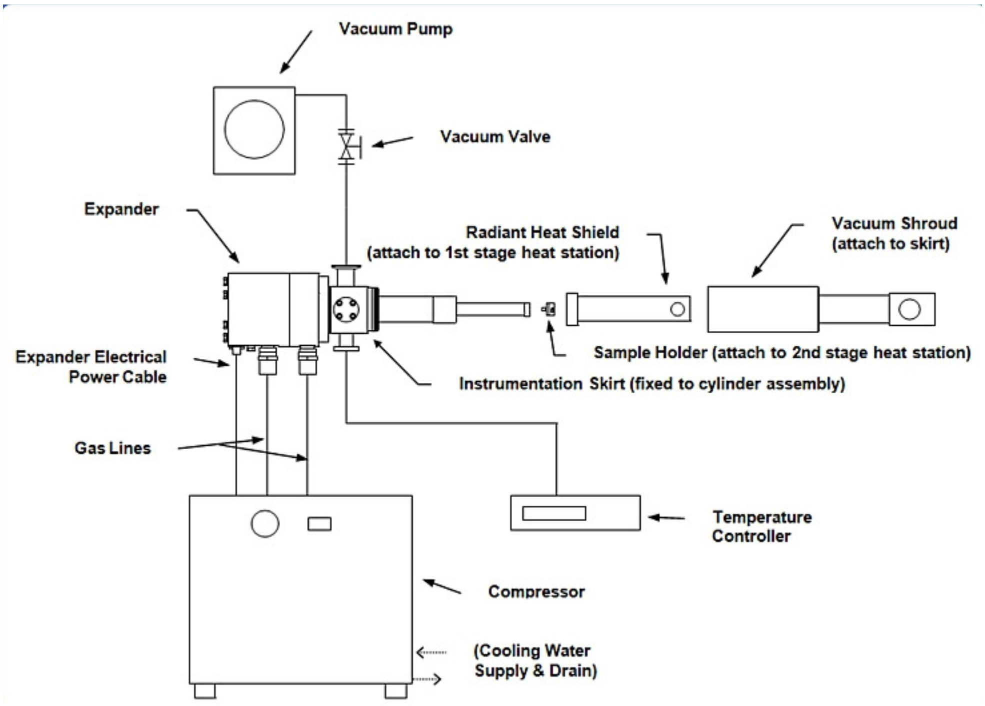

Figure 2.16 A schematic diagram of the closed cycle cryostat.

In addition to these major components the closed cycle cryo-cooler is accompanied by several support systems like a vacuum port and electrical feedthroughs, as well as a temperature controller to measure and adjust the sample temperature. The system also requires cooling water for the compressor and a vacuum pump for the sample space.

2.3.3 Energy Scanning EXAFS beamline (BL-09)

An Energy Scanning type EXAFS beamline has also been developed at BL-09 port of INDUS-2 synchrotron source and has been commissioned recently [28]**.** The beamline uses a

1.3 m long meridonial cylindrical mirror with radius of curvature 11.2 Kms for vertical collimation of the beam. This mirror is followed by a fixed exit type double crystal monochromator (DCM). The DCM consists of two Si (111) crystals with 2d=6.2709Å and narrow Darwin widths. The fixed exit is realized by varying relative lateral and vertical distances between the two crystals at each energy setting, maintaining parallelism between them. The second crystal of the DCM is a saggital cylinder with variable radius of curvature in the range 1.2 m to flat, which provides horizontal focusing to the beam. A post mirror with meridonial curvature is used upside-down for bending the beam path to horizontal direction again as well as for vertical focusing of the beam at the sample position. Higher harmonics are rejected by changing the angle of incidence at the second mirror. Each of the two cylindrical mirrors has two coating strips, viz., of Platinum (Pt) and Rhodium (Rh). Rhodium has the absorption edge at 23.2 KeV (K-edge) and Pt has L1, L2 and L3 absorption edges between 11.5 KeV to 13.9 KeV. So to cover the energy range of 4-25 keV, coatings of Rh and Pt are used. The optical layout of the beamline is given in Fig. 2.17(a), while the photograph is shown in Fig. 2.17(b).

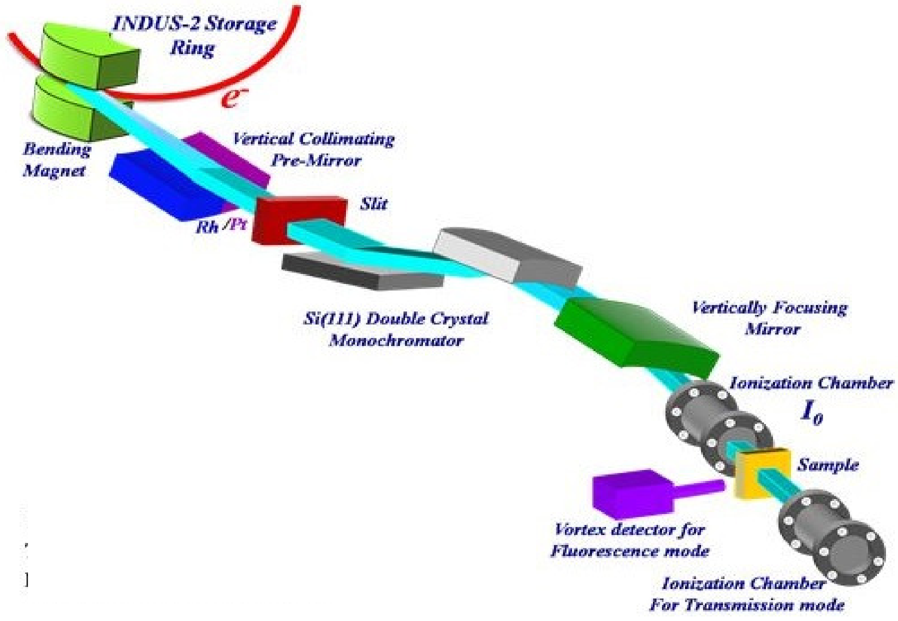

(a)

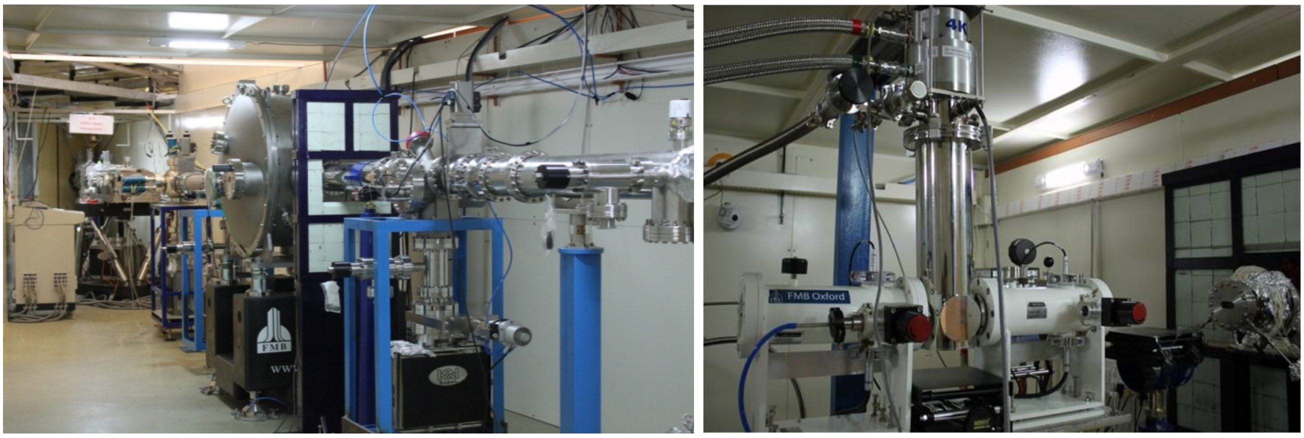

(b)

Figure 2.17 (a) Optical layout of BL-09 (b) Photographs of the optics hutch (below-left) and the experimental hutch (below-right) at BL-09.

The beamline has been installed with two separate sections namely the optics hutch and the experimental hutch. The optics hutch consists of the optical components e.g., slit system, grazing incidence X-ray mirrors, beam viewer, double crystal monochromator (DCM) and Beryllium window. The components in the optics hutch are at 10^{-9} torr vacuum and separated by front end and experimental hutch using 200μm beryllium windows. The experimental hutch is equipped to record EXAFS spectra of the samples both in transmission and fluorescence mode,. In the transmission mode of measurement, the sample is placed between two ionization chamber detectors. The first ionization chamber measures the incident flux (I_0) and the second ionization chamber measures the transmitted intensity (I_t). A third ionization chamber is also used where reference metal foils are measured for energy calibration. The IC Spec ionisation chamber (Make: FMB Oxford) has been specially designed for high precision X-ray intensity measurements at Synchrotrons and is particularly suited for transmission X-ray absorption spectroscopy measurements. It has a large installed base and has been shown that it is capable of measuring EXAFS spectra with signal to noise of the order 10^5. The operating voltage of these ionization chambers are 200 kV and a pressure of 100-1000 mbar is maintained at each of these detectors depending on the available flux and the absorption edge being probed. For dilute and thin film samples, measurements are done in fluorescence mode using a silicon drift detector, which is placed in front of the sample in 45º degree geometry. The Si drift detector (Model no. Vortex-60EX®, Make: Hitachi-High Technologies Science America, Inc.) which is generally produced from high purity silicon, feature excellent energy resolution (<133 eV FWHM at Mn K_α is typical) and a high count rate capability (input rate >1 Mcps). At a very short peaking time of 0.25 µs, an output count rate of 600 kcps is achieved. A unique feature of these detectors is their ability to process high count rates with virtually zero loss in energy resolution and no peak shift with count rate. This detector is operated at room temperature and cooled by a thermoelectric cooler (TEC) and can be cycled as frequently as needed without any degradation in detector performance. Cool down times are typically less than 3 minutes. The detector spectroscopy system includes a detector unit and control box, which includes power supplies for the detector and TEC, a digital pulse processor with PI-SPEC Software. The complete detector also contains a charge-sensitive preamplifier and temperature stabilization system, which eliminates concerns of varying ambient temperature.

It is to be noted here that while the energy dispesive beamline (BL-08) is operational since 2009, the energy scanning beamine (BL-09) has only been in operation since 2014 and hence most of the studies presented in this thesis have been carried out in the energy dispersive beamline. However in my future course of work, the energy scanning beamline (BL-09) will be used in most of my studies particularly for doped, dilute and thin film systems, since it offers better signal to noise ratio, larger band width even for low energy edges and ease in measurement both in transmission and flouresecence mode, while the energy dispersive beamline (BL-08) will be used mostly for time-resolved in-situ studies for its short (msec) time scale of measurement.

2.3.4 Sample Preparation

In the transmission mode of measurement, ideally the sample should be homogeneous so that every ray of light interacts identically with every part of the sample. It should be uniform, of appropriate sample thickness of ~2 absorption lengths and it should be free from pinholes. In case of powder, the grains should be very fine grained (particle size should be comparable to less than one absorption length) and uniform. If the sample particles are large compared to an absorption length it implies some regions are very thick, while other regions have gaps (or leakage). The leakage problem distorts the data by decreasing white line height and altering the measured σ^2 of the EXAFS. In transmission experiments it has been observed that, if samples are too thick, most photons don't get through and if it is too thin, most photons don't interact. These thickness effects are particularly serious in the near-edge region where large amplitude, high-contrast structure may be found. A symptom of thickness effects is that the XAFS oscillations are compressed ‑ they have reduced amplitudes, which has the effect of erroneously reducing the estimated coordination numbers that are obtained in data analysis. It is best to keep the sample edge step $\Delta\mu x$ to about 1.0 or less, and the total sample absorption μx to less than 3 or so, preferably less. The exact amount of the sample required for a particular transmission EXAFS measurement can be estimated from:

$$Weight = \text{Surface} * \frac{\mu \text{x}}{\sum_{\text{i}} \text{g}_{\text{i}} \left(\mu/\rho \right)_i} \tag{2.9}$$

It turns out that for majority standard samples to satisfy the above conditions, the amount of sample required is generally not more than about 20-25 mg/square cm. For 12 or 15 mm diameter pellets, this is a very small amount. Hence, binders of very light non-reactive elements viz., Boron Nitride, graphite, zeolites, cellulose etc. are used to make self supporting pellets that will not crack.

For thick samples or lower concentrations (down to the ppm level and lower), monitoring the x-ray fluorescence is the preferred technique. However, a self absorption correction has to be applied to equation 2.8. The term self-absorption usually refers to the case where the penetration depth into the sample is dominated by the element of interest. Since all matter attenuates x-rays, the fluorescence intensity, and therefore the XAFS oscillations, can be damped due to this self absorption effect. In the worst case for self absorption (a thick sample of a pure element), the XAFS simply changes the peneteration depth into the sample, but essentially all the x-rays are absorbed by the element of interest. The escape depth for the fluoresced x-ray is generally much longer than the penetration depth, so that essentially all absorbed x-rays cause a fluoresced x-ray. This severely dampens the XAFS oscillations. The two limits (very thin or thick, dilute samples) are the best cases for fluorescence measurements.

2.4 Data Analysis

The standard sequence of operations in EXAFS data analysis consists of the following steps: normalization of the data to unit edge step; background subtraction, conversion from energy to k-space; Fourier transformation to R-space and generation of experimental $\chi(R)$ vs. R spectra; windowing and inverse transformation; generation of theoretical $\chi(R)$ vs. R spectra using a crystallographic/amorphous model and fitting of the experimental spectra with the theoretical spectra by nonlinear least squares fitting. The normalization procedure, by which the data are divided by the size of the edge step, compensates for the uncertainties in the concentration and sample thickness. A common method of determining the edge step is to fit the data within a few hundred eV below the edge, and also above the edge, with low order polynomials (linear or quadratic), and then extrapolate them to the edge. The difference between the pre-edge and post-edge fits extrapolated to the edge energy is the edge step. To convert to k-space, the value of E_0, the threshold energy (muffin tin zero level in the theory) must be specified. Fortunately the precise value is immaterial as long as it is within a rydberg or so of the edge, and that it is consistent for standard and unknown. Typically the half-maximum point on the edge is taken, or the first maxima of the derivative of the EXAFS signal. In the next step, background subtraction is performed, to isolate the oscillations in EXAFS from the atomic part of the absorption $\mu_0(E)$, and the background absorption or scatter from other elements in the beam path. In principle, the isolated atom absorption $\mu_0(E)$ (which is generally unknown) is subtracted from the absorption of the atom in condensed matter $\mu(E)$, and the result is divided by $\mu_0(E)$, which is a slow function of energy in the EXAFS region. Background subtraction is accomplished by ordinary linear least squares fitting, typically using cubic spline functions. Subsequently the data is converted to k space and is generally weighted by an increasing function of k (such as k^3) so that the data at high k (which are of small amplitude) becomes significant. At this point, the data consist of sums of damped sine waves corresponding to the different shells of atoms and hence Fourier transformation is carried out to generate the radial distribution function. The region below k = 2 $Å^{-1}$ is excluded because of possible complications from multiple scattering etc. The transformed data (χ(R) vs. R) actually consist of a complex function, which has real and imaginary parts, or alternatively a modulus and phase. The modulus is the most frequently used quantity, but the real and imaginary parts are also useful. They exhibit significantly more structure than the modulus does, and they don't suffer from nonlinear interference and hence in all the cases discussed in this thesis the data fitting has been carried out on the modulus as well as separately on the real and imaginary parts.

2.4.1 Data Processing and Analysis using IFEFFIT software package

A collection of computer codes have been developed by Dr. Bruce Ravel and co-workers [29], [30] providing a rich graphical interface to the extensive analytical and numerical capabilities of the popular IFEFFIT library [31]. It includes the four sub-routines: (i) ATOMS, a program to generate input data for the *ab initio*, multiple scattering, x-ray absorption spectroscopy code FEFF, (ii) ATHENA, a program for XAS data processing, (iii) ARTEMIS, a program for analysis of extended X-ray absorption fine structure (EXAFS) data using theoretical standards computed by the FEFF program [32], [33] and (iv) HEPHAESTUS, a collection of beamline utilities based on tables of atomic absorption data.

The raw experimental EXAFS data needs some pre-processing before a meaningful data analysis can be carried out to extract relevant information. The data processing includes such steps as conversion of raw data to $\mu(E)$ spectra, background subtraction, energy calibration of spectra, alignment of data, use of reference spectra, deglitching (i.e. the removal of spurious points from spectra), merging of data by calculating the average and standard deviation at each point in a set of spectra and finally Fourier transforming and plotting. The above steps are carried out in the ATHENA subroutine. Once the raw data has been processed appropriately, it is used in ARTEMIS for theoretical modelling and fitting.

ARTEMIS includes access to the functionality of the ATOMS program, which converts crystallographic data into a format suitable for FEFF. This interface can read crystallographic data either in the form of an ATOMS input file or a crystallographic information file (CIF). These data are then converted into a FEFF input file or can be converted into a form suitable for export to a molecule viewer. ATOMS was originally conceived as a tool for generating input files of the form needed by FEFF, an *ab initio* multiple scattering code used to generate theoretical fitting standards for EXAFS analysis and simulation of XANES spectra. FEFF performs its calculation in real-space on a specified cluster of atoms and so requires a list of Cartesian coordinates of each atom in the cluster. The original purpose of ATOMS is to generate such a list from crystallographic structure data. The central algorithms in ATOMS are for interpreting space group symbols and constructing a description of a unit cell using space group symmetries and the input crystallographic data.

HEPHAESTUS is basically an application for several small utilities based on the periodic table of elements and on a database of absorption cross sections and other data for the elements. All calculations made by HEPHAESTUS use one of several published compilations of atomic cross sections. It provides relevant information regarding absorption and fluorescence line energies of the elements using a periodic table interface, computes the absorption length and quantity of sample required for measurement given the chemical formula and density of a material, displays chemical data such as melting point and electronegativity of the elements, computes the ideal gas mixture for ion chambers of various lengths and internal pressures, finds all absorption edges in the vicinity of a given energy etc.

In XAFS analysis, a theoretical model of the data is constructed containing unknown parameters and their values are determined by fitting. Parts of the theoretical model are well established, such as the basic theory of EXAFS. Other aspects of the model have been well tested, such as the electron scattering contributions in EXAFS that are computed by FEFF. The remaining parts of the model are less well established that must be defined by the data analyst and its accuracy depends on understanding of the problem. In particular, it is crucial to describe the distribution of atoms and the disorder in the structure most usefully and economically in terms of number of parameters. Formulation of these aspects of the model is the most subtle and tricky part of data analysis.

Each scattering path has a degeneracy N (the number of equivalent atoms in single scattering paths), an effective distance R (half path-length), and a mean square variation parameter σ^2, as mentioned in the canonical EXAFS (equation 2.6). Once calculated, each of these paths can be easily modified to give a different N, R, σ^2, and even E_0 (if that is necessary). Of the remaining parameters in equation 2.6, $f(k)$ and $\delta(k)$ (the scattering amplitude and phase shift due to the neighbouring backscattering atom respectively) and the photoelectron mean free path $\lambda(k)$ are calculated theoretically. In the past decade or so, calculations of these factors have become more accurate and readily available from the program FEFF and they have been shown to be accurate enough to be used in real analysis. In addition, the calculated factors are not restricted to the first shell and can account for multiple-scattering of the photo-electron. The parameters that are often determined from a fit to the EXAFS spectrum affect either the amplitude of the EXAFS oscillations (N, S_0^2, σ^2) or the phase of the oscillations (ΔE_0 and ΔR, the energy shift and the change in half path length respectively.)

The spectrum for a structure that is close to the reference structure can be computed without re-running FEFF, which makes it fast to do within a fitting loop. This is similar to the classical approach in which the spectrum of a standard compound was modified to fit a similar material of unknown structure. Artemis/IFEFFIT [31] works in this way where, the user needs to devise a set of fitting parameters that are adjusted by IFEFFIT to give the best fit to the data (usually over a selected region in *r*-space). This approach is particularly good for analyzing simple structures in which only a few paths (mostly single scattering) are important, and also for refining complex structures that are pretty much known, except for a few details. Hence this approach of data fitting has been taken for all the studies described in the present thesis. Although reasonable ad hoc assumptions or constraints can be made to limit the degrees of freedom, it seems more defensible to calculate the DWFs, validate them, and then use them as supplementary information in the fitting process. It is always good to first do a rough analysis of the data to get an overview, and then refine the analysis in later steps. The fitting algorithms are intended to find a global minimum but it can get trapped in one of the numerous local minima and give misleading results. To verify the true minima, parallel minimizations using Levenberg-Marquardt with many random starting points must be performed, in order to find all the multiple minima. It is also best to start with the simplest hypothetical structure while modelling, and if the fit is inadequate for all rational choices of the parameters, further complexity can be introduced into the model.

In case of an unknown structure, it is a better methodology to model the data shell by shell. The first shell of the FT EXAFS signal is generally dominated by single scattering, even though the tails of multiple scattering contributions at larger r may leak in. However, they have very trivial contributions and initially can be neglected. After approximate solutions are obtained, it is a good idea to fit the whole spectrum together as a unit, in order to account for residual overlap between the shells.

Some of the fitting parameters are correlated. For example, changing the coordination number affects the amplitude parameter uniformly as a function of k. Varying σ^2 also affects the amplitude, but it has a greater effect at high k than at low k. Hence, if one of the correlated parameter is perturbed, the other will adjust accordingly to partially make up for it. A similar correlation is observed between ΔE_0 and the distance R. Both affect the slope of the phase, but in different ways. The shorter the range of data in k space, the more highly they will be correlated. The fitting problem becomes poorly determined and numerically unstable and introduces large error in parameter values. To avoid this problem one of the correlated parameters should be fixed during a fit. Adding unnecessary parameters may introduce correlations that will cause the error bars to inflate, so the information about the original parameters is masked. This raises the question: how many parameters can be reasonably fit? EXAFS data exist over a finite range in both k-space and r-space, and therefore they have limited information content. It is known from a Fourier series expansion that only a finite number of coefficients are needed to represent a signal of fixed bandwidth. All of the data in the FT exist on an array of N points in size. If we assume that the k window width is Δk wide, and the r-space data are contained in total width ΔR, the grid spacings respectively are δk and δr where $\delta r = \pi/(N\delta k)$. The maximum r value in the r space is $(N/2)\delta r = \pi/(2\delta k)$, where the factor of two comes in because half the space is allocated to negative frequencies which offer no new information. The fraction of the total information contained within ΔR is then $2\delta k\Delta R$. The number of k-space data points in the window is (about) $\Delta k/\delta k$. But most of these data points actually carry no information, because the signal can be accurately represented within only a fraction of the total r-space. Therefore the actual information content in the data is number of k-space points $\Delta k/\delta k$ times the compression factor $2\delta k\Delta R$. This gives a total "independent point" count of $N_{\mathrm{ind}} = 2\Delta k\Delta R/\pi$. Stern [34] has argued that a more precise value is $N_{\mathrm{ind}} = 2\Delta k\Delta R/\pi + 2$.

A simple flow chart depicting the data analysis methodology is given below:

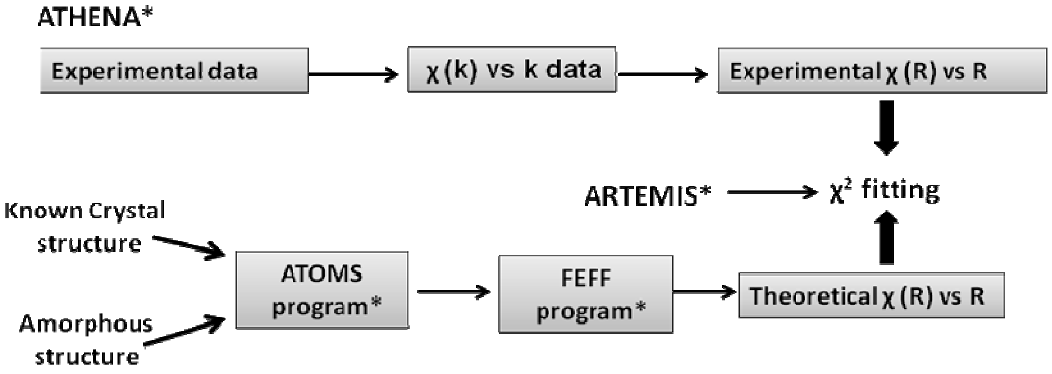

*All the programs come within IFEFFIT software package. It is free and can be downloaded from the following links : http://cars9.uchicago.edu/ifeffit/; http://sourceforge.net/projects/ifeffit/

2.4.2 ATHENA

The normal view of the ATHENA window is shown in Fig. 2.18. Data conversion from its raw form is executed, creating $\mu(E)$ spectra from transmission or fluorescence experiments. ATHENA also supports powerful pre processing of data as it is imported, including automated deglitching, truncation, alignment and constraint of analysis parameters. Background subtraction is performed using the AUTOBK algorithm [35] which determines an empirical background spline based on a distinction between data and background in terms of Fourier components. Edge-step normalization of the data is determined by a linear pre-edge subtraction and regression of a quadratic polynomial beyond the edge. The difference between these two polynomials extrapolated to the edge energy E_0 is used as the normalization constant in the definition of:

$$\chi(E) = \frac{\mu(E) - \mu(E_0)}{\mu_0(E_0)} \tag{2.10}$$

Normalized data are typically presented after subtracting the curvature of the regressed quadratic and the difference in slope between the post- and pre-edge polynomials after the edge.

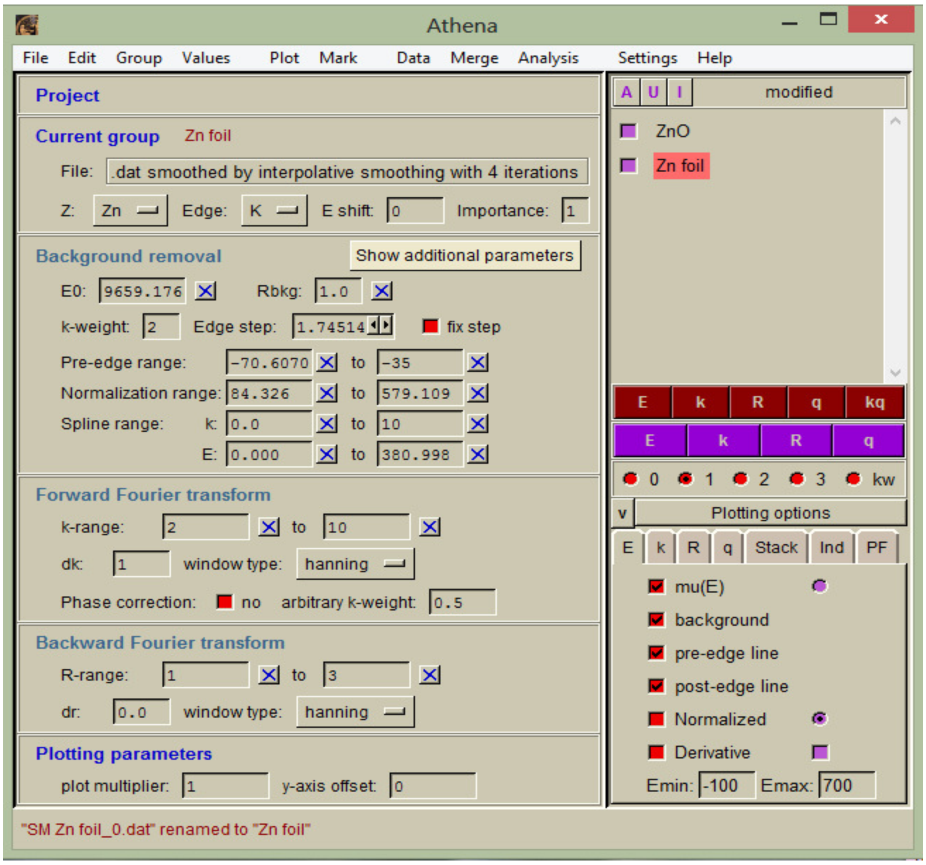

Project

Current group Zn foil

File: .dat smoothed by interpolative smoothing with 4 iterations

Z: Zn Edge: K E shift: 0 Importance: 1

Background removal

E0: 9659.176 ☒ Rbkg: 1.0 ☒

k-weight: 2 Edge step: 1.74514 ☑ fix step

Pre-edge range: -70.6070 ☒ to -35 ☒

Normalization range: 84.326 ☒ to 579.109 ☒

Spline range: k: 0.0 ☒ to 10 ☒

E: 0.000 ☒ to 380.998 ☒

Forward Fourier transform

k-range: 2 ☒ to 10 ☒

dk: 1 window type: hanning

Phase correction: ☐ no arbitrary k-weight: 0.5

Backward Fourier transform

R-range: 1 ☒ to 3 ☒

dr: 0.0 window type: hanning

Plotting parameters

plot multiplier: 1 y-axis offset: 0

☑ mu(E) ○

☑ background

☑ pre-edge line

☑ post-edge line

☐ Normalized ●

☐ Derivative ☐

Emin: -100 Emax: 700

"SM Zn foil_0.dat" renamed to "Zn foil"

Figure 2.18 The main window of ATHENA program.

The data in E-space is converted to k-space and $\chi(k)$ is obtained by the formula

$$k = \sqrt{\frac{2m(E-E_0)}{\hbar^2}} \qquad (2.11)$$

The absorption edge E_0 is determined automatically as the data is imported by finding the first large peak in the first derivative of the $\mu_0(E)$ spectrum, but can also be set interactively. ATHENA provides utilities for most common chores involved in the preparation of EXAFS data for analysis such as energy calibration, alignment of data, use of reference spectra, deglitching and merging of data etc. ATHENA provides tools for the analysis of near-edge spectra as well. There are utilities for calculation of difference spectra, for fitting line shapes (arctangent, Gaussian, Lorentzian) to spectra, and for fitting linear combinations of standard spectra to unknown spectra. ATHENA can also import and display the results of FEFF8 calculations [33] for comparison with measured data. A significant feature of ATHENA is that processing and displaying many data sets simultaneously is as simple as for a single data set. The parameters controlling background removal and Fourier transforms can be adjusted for each data set individually or constrained in a flexible manner between data sets. Additional features include principle component analysis and self-absorption corrections for fluorescence data.

2.4.3 ARTEMIS

ARTEMIS works within the framework of FEFF's multiple-scattering path expansion [15], [32]. In ARTEMIS the values of the parametric terms in the EXAFS equation, N, S_0^2, E_0, ΔR and σ^2 must be specified for each path included in the fit. The path expansion and how it is parameterized and used in a fit is described elsewhere [36], [37]. EXAFS analysis can be quite subtle and complicated. By providing a graphical forms-based mechanism ARTEMIS makes basic analysis chores simple and sophisticated analysis problems easy to handle. Shown in Fig. 2.19 is the ARTEMIS window in its data view.

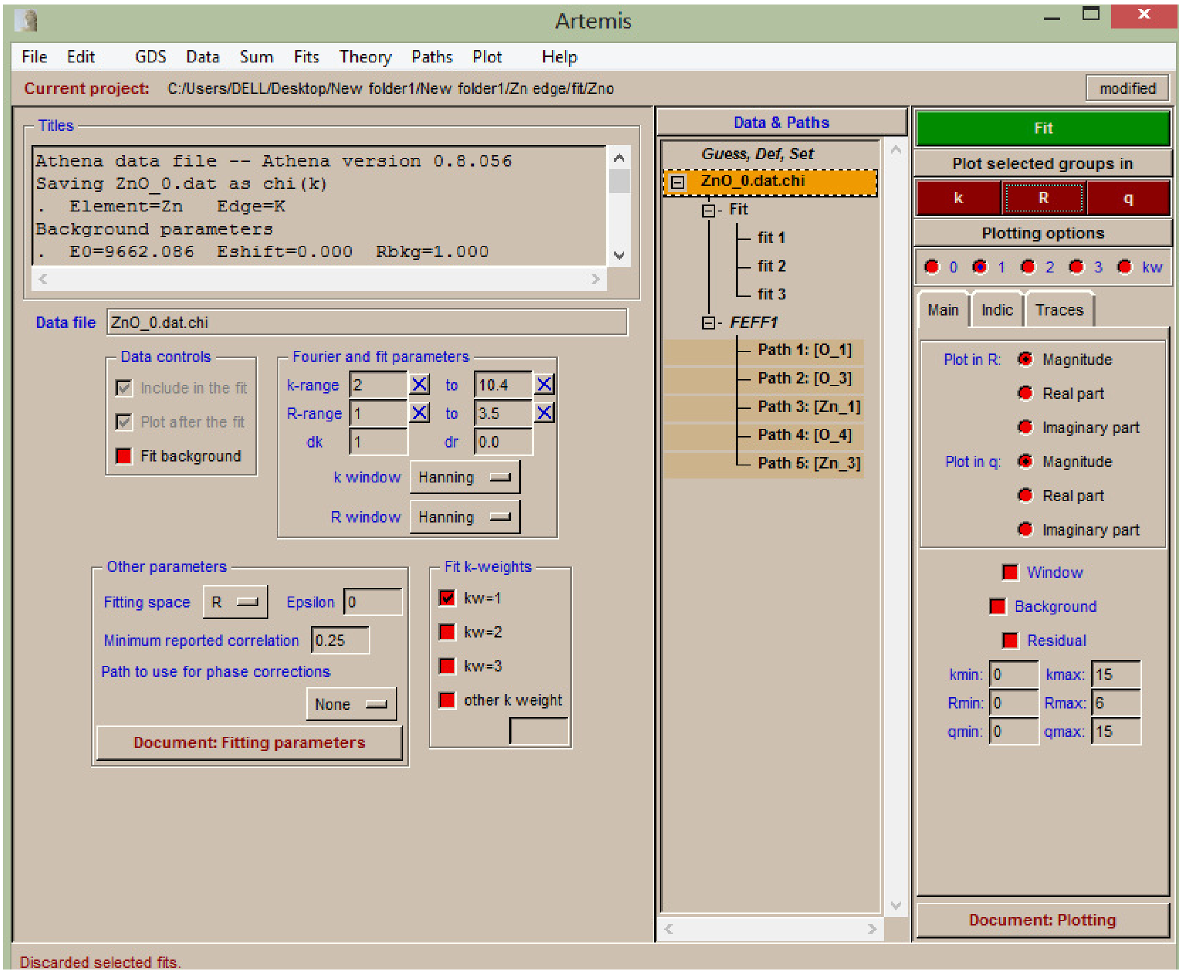

Current project: C:/Users/DELL/Desktop/New folder1/New folder1/Zn edge/fit/Zno

```
Athena data file -- Athena version 0.8.056
Saving ZnO_0.dat as chi(k)
.  Element=Zn    Edge=K
Background parameters
.  E0=9662.086  Eshift=0.000  Rbkg=1.000
```

Data file ZnO_0.dat.chi

k-range 2 to 10.4
R-range 1 to 3.5
dk 1 dr 0.0
k window Hanning
R window Hanning

Fitting space R Epsilon 0
Minimum reported correlation 0.25
Path to use for phase corrections None

kmin: 0 kmax: 15
Rmin: 0 Rmax: 6
qmin: 0 qmax: 15

Discarded selected fits.

Figure 2.19 Main window of ARTEMIS program.

The data processing parameters, including the range of the Fourier transform from k-space and the fitting range in R-space, are set in the main window. The far right panel is used to control how plots are displayed. The middle panel is a list of all data sets, FEFF calculations and paths used in the fit. ARTEMIS includes access to the functionality of the ATOMS program, which converts crystallographic data into a format suitable for FEFF. These data are then converted into a FEFF input file or can be converted into a form suitable for export to a molecule viewer. For materials that are not crystalline or do not have a crystalline analogue, FEFF input files prepared in some other way can be imported directly into ARTEMIS. A simple interface to FEFF is included in ARTEMIS for altering the contents of the input file as needed and a button for launching an external instance of FEFF. After the FEFF run, ARTEMIS displays a page containing a concise interpretation of the paths computed by FEFF including the path distances, degeneracy, atomic species in the path, whether the path is single or multiple-scattering, and estimated importance of the path. ARTEMIS has tools for organizing and plotting the results of the calculation, including plotting the individual contributions of each path in both k- and R-space. ARTEMIS has several features which facilitate the creation and examination of fitting models. One such is the automated generation of parameters appropriate for a first-shell fit. On conducting or importing a FEFF calculation, a set of fitting parameters are automatically generated. In many cases, a fit can be run immediately which will give a physically reasonable result. Because all fitting problems are unique, this fully automated fit is usually inadequate, but it provides a sensible starting point for almost any fitting problem from which the fitting model can be further refined. ARTEMIS provides convenient plotting in k-, R- or back-transformed k-space of the data, the fit and any number of the individual paths used in the fit. Numerous tools are available to check the consistency and sensibility of the parameters used in the fit and to evaluate the results of the fit. An extensive log file is presented upon completion of the fit, allowing the user to evaluate the quality of the fit, the reasonableness of the fitting parameters and the effects of the fitting parameters on the FEFF paths used in the fit. The major fitting statistics, including the reduced χ^2 fitting metric and the R-factor are displayed along with uncertainties and correlations between all fitting parameters. ARTEMIS is equally well suited to simple first-shell analysis of single data sets as well as the most challenging fitting models. Among its advanced features are:

(i) Simultaneous refinement of multiple data sets.

(ii) Refinement using multiple k-weightings for any data set.

(iii) Use of multiple FEFF calculations in a single fit.

(iv) Co-refinement of a background spline to reveal correlations between the spline and the fitting parameters.

(v) Arbitrary constraints between and restraints on parameters.

2.4.4 Goodness of Fit

The experimental data fitting process based on some theoretical modelling invariably includes some presumably known or determinable experimental uncertainties from random noise and other influences. These can be divided into random noise (such as photon counting) and non-random (systematic) errors. It is important to track and eliminate the systematic errors, but they cannot be completely eliminated. While fitting data we systematically vary the hypothetical values of the “unknown” (i.e. only partially known) parameters to give the best agreement with the experimental data. We will not achieve perfect agreement with the data, because of the noise and other uncertainties (“errors”), but we can determine how far we can vary the parameters around the best-fit values while still getting an acceptable fit to within the experimental (and theoretical) errors. The quality of a fit can be quantified by a comparison between the experimental data and the theoretical fit. The simplest approach is to calculate the squared deviation between the data and theory. The deviation (“residual”) is squared so that both positive and negative deviations contribute positively to the error statistic. If there are many data points the squared deviations are summed:

$$\chi^2 = \sum_{i=min}^{max} [(\chi_d(r_i) - \chi_t(r_i))^2]$$

where $\chi_d(r_i)$ is the *i*th measured data point, $\chi_t(r_i)$ represents the theory function, which depends on the independent variable r_i. For EXAFS fitting the goodness of fit can be determined by the following quantities:

- **Chi-square**:

$$\chi^2 = \frac{N_{idp}}{\varepsilon N_{data}} \sum_{i=min}^{max} [Re(\chi_d(r_i) - \chi_t(r_i))^2 + \mathrm{Im}(\chi_d(r_i) - \chi_t(r_i))^2]$$

Where *$\chi(r)$* is the FT EXAFS data (which is a complex quantity) and the subscripts *d* and *t* denote data and theory respectively and ε = measurement uncertainty

- **Reduced chi-square:**

Chi square scaled by degrees of freedom *v*

$$\chi_v^2 = \frac{\chi^2}{v}$$

where

$$v = N_{idp} - N_{var}$$

The values of $\chi_v^2 \sim 10$ or higher typically for good quality EXAFS data.

- **R-factor:**

It is the fractional misfit between experimental data and the theoretical fit.

$$R\ factor = \frac{\sum_{i=min}^{max}[Re(\chi_d(r_i) - \chi_t(r_i))^2 + \mathrm{Im}(\chi_d(r_i) - \chi_t(r_i))^2]}{\sum_{i=min}^{max}[Re(\chi_d(r_i))^2 + \mathrm{Im}(\chi_d(r_i))^2]}$$

. In all the EXAFS fittings presented in this thesis, uncertainties in the fitting parameters have been estimated and typical values are ±0.05 Å in R, ± 10% in CN and ±0.001 in DW factor (σ^2).

Chapter 3

EXAFS MEASUREMENTS ON SOLID STATE ELECTROLYTES

(Gd^{3+}, Nd^{3+} and La^{3+} doped ZrO_2)

A fuel cell is an energy conversion device that converts the chemical energy of a fuel gas directly to electrical energy and heat without the need for direct combustion as an intermediate step, giving much higher conversion efficiencies than conventional thermo-mechanical methods. The operating principles of fuel cells involves electrochemical combination of reactants to generate electricity, a combination made of a gaseous fuel (hydrogen) and an oxidant gas (oxygen from the air) through electrodes and via an ion conducting electrolyte. In a SOFC, oxygen becomes ionized in the cathode triple-phase boundary (TPB) (where the ionic conductor, electronic conductor, and the gas species meet). The O^{2-} ions flow through the electrolyte to the anode TPB and react electrochemically with the fuel. If the fuel is H_2 (CO), steam (CO_2) is generated and electrons are released.

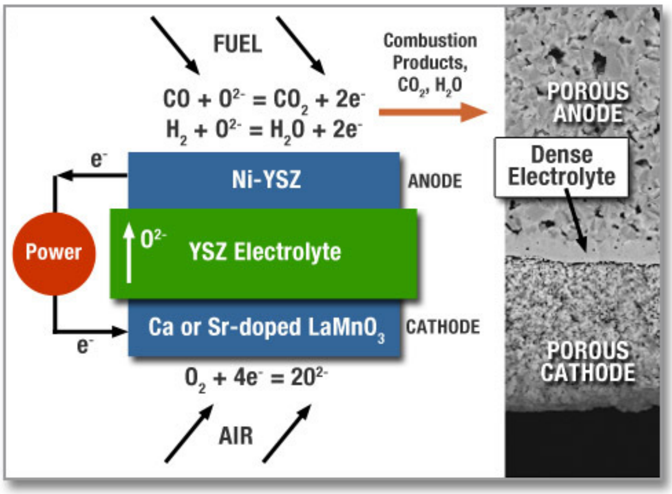

Figure 3.1 Schematic of a fuel cell cycle.

(Ref. http://www.grc.nasa.gov/WWW/StructuresMaterials/Ceramics/research_solid.htm)

The electrons flow through the external circuit to the cathode, generating power. A fuel cell operates as long as both fuel and oxidant are supplied to the electrodes and the influence it exerts on the surrounding environment is negligible. The operating principle of a SOFC with an oxide ion conductor is schematically shown in Fig. 3.1. When an external load is applied to the cell, oxygen is reduced at the porous air electrode to produce oxide ions. These ions migrate through the solid electrolyte to the fuel electrode, and they react with the fuel, H_2 or CO, to produce H_2O or CO_2. The following electrochemical reactions occur in the SOFC:

$$\text{At the anode:} \quad H_2 + O^{2-} \rightarrow H_2O + 2e^-$$

$$\text{At the cathode:} \quad \tfrac{1}{2} O_2 + 2e^- \rightarrow O^{2-}$$

Zirconium oxide or Zirconia powders find significance in catalytic applications, either as supports or as electrolytes, in solid oxide fuel cells (SOFCs) [38], [39]. Pure ZrO_2 is monoclinic from room temperature to 1440 K, tetragonal between 1440 and 2650 K and cubic up to its melting point of 2950 K. [40] It exhibits high anionic conductivity when doped with aliovalent cations which facilitates the generation of oxygen ion vacancies for charge compensation. [41] Doping in this manner also stabilizes the cubic fluorite phase of zirconia, having considerable ionic conductivity as a solid electrolyte, at the operating temperatures of the solid oxide fuel cell. Yttria-stabilized zirconia (YSZ) typically with 8 mol% Y doped in ZrO_2, is the most common material used as an electrolyte in SOFCs as shown in Fig. 3.1. The major limitation to the use of YSZ arises from the need to operate the fuel cell at relatively high temperatures of ~1100–1300 K to achieve adequate ionic conduction. Other materials like scandium stabilized zirconia (ScSZ) and gadolinium doped ceria (GDC) also have their operating temperatures in the range of 1000 – 1200 K and < 1000K respectively [42]. The high temperatures of operation lead to material stability and compatibility issues. This has prompted the search for alternate materials with equivalent ionic conductivity at lower temperature to enable operation of SOFCs at intermediate temperatures of ~700–800K.

There have been a few studies on the X-ray absorption spectroscopy of doped ZrO_2 systems to have insight into the mechanism of creation of oxygen vacancies and on their locations within the ZrO_2 matrix, though there is contradictory information in the literature regarding the same. Sadykov *et al.* [43] have observed for their Gd/La doped CeO_2- ZrO_2 nanocrystalline systems that with the increase in Gd concentration, the oxygen coordination around Zr/Ce increases while disorder at oxygen sites decrease. This implies that with Gd doping oxygen vacancies are mainly created near the dopant site. However, with La doping Zr-O bonds get contracted and oxygen coordination decreases around Zr atoms indicating presence of oxygen vacancies near Zr sites. Zacate *et al.* [41] have estimated the binding energies of the oxygen vacancies with the cations in doped ZrO_2 systems by atomistic simulation where they have found that for dopants with size smaller than the host atom, binding energies of oxygen vacancy is higher for a nearest neighbour configuration of the dopant and for dopants with size larger than the host atom, the binding energy is higher for next nearest neighbour configuration. Li and Chen [44] have also investigated the changes in Zr-O environment by EXAFS measurements on Gd, Y, Fe, and Ga doped systems and concluded the same. However, for cryochemically-prepared doped ZrO_2 systems Cole *et al.* [45] have observed that the Zr-Zr peak intensity increases and the disorder term decreases as the dopant cation changes from Er to Gd to La which suggests that the central Zr atoms has less perturbation for doping with larger sized atoms. They have concluded that when the dopant size is close to that of Zr, oxygen vacancies prefer to be located in the vicinity of Zr sites while for larger sized dopants the oxygen vacancies lie close to the dopant site. Thus, the above discussion highlights the contradictions in the literature regarding the possible positions of oxygen vacancies created in ZrO_2 matrix when doped with different trivalent ions. We have looked into the above issue using the results of synchrotron based EXAFS measurements, further confirmed by X-ray diffraction data and also by theoretical simulations to some extent. By analyzing the EXAFS data, we seek the effect of size and concentrations of the dopant on the local structure around the Zr sites.

The rare earth substituted ZrO_2 samples discussed in this study were prepared by co-precipitation route. In the above process, a stoichiometric solution was first prepared by mixing appropriate concentrations of $ZrO(NO_3)_2$ and the nitrate of the dopant metal (viz., $Gd(NO_3)_3$ for Gd doped samples). This solution was then added directly to ammonia solution with constant stirring. The precipitate, which consists of homogenous mixture of hydroxides of Zr and the dopant metal, was allowed to settle down and was subsequently filtered and washed with distilled water. The precipitate was dried at 100°C and the samples were prepared by calcining the dried powder at 1100°C for 24 h, to test the stability of the samples at higher operating temperature of SOFC devices. ZrO_2 samples have been prepared with 11% doping of Gd, Nd and La.

3.1 ZrO_2 doped with different cations (Gd^{3+}, Nd^{3+}, La^{3+})

Fig. 3.2(a) and (b) show the X-ray diffraction spectra of ZrO_2 samples with 11 mol% doping of La, Gd, Nd and sintered at 700°C and 1100°C.

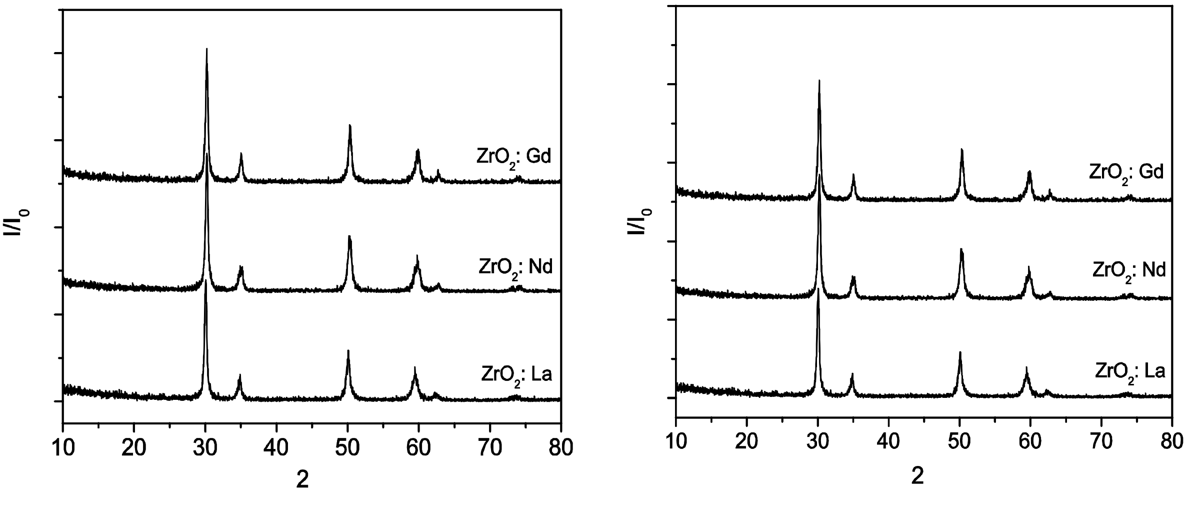

(a) (b)

Figure 3.2 XRD spectra for rare earth doped zirconia samples after sintering at (a) 700°C and (b) 1100°C

XRD peaks for all the samples can be identified with the cubic phase of yttria stabilized zirconia (JCPDS 30-1468). Crystallite sizes in the samples have been estimated from the broadening of the XRD peaks using the Scherrer equation and are shown in Table 3.1. The samples are found to have 22-25 nm particle size. The Gd doped sample retains the distorted cubic phase with slight broadening of XRD peaks at ~35° and ~60° 2θ value while Nd and La substituted samples exhibit partial transition to tetragonal and monoclinic phases, respectively which is evident from the splitting of these peaks. The overall data for the phases present in the three types of samples

after sintering are summarized in Table 3.1.

Table. 3.1 Crystallite size and phase identification after sintering at different temperatures.

	700 °C		**1100 °C**	
Sample	Particle size	symmetry	Particle size	Symmetry
ZrO_2 : Gd (11%)	22 nm	C	38 nm	C + T
ZrO_2 : Nd (11%)	23 nm	C	45 nm	C + T
ZrO_2 : La (11%)	25 nm	C	48 nm	M

C = Cubic, T = Tetragonal, M = Monoclinic

It should be noted that trace amounts of monoclinic phase of ZrO_2 is also present in the Gd and Nd doped samples characterized by the presence of small peaks at 2θ ~ 28.2° and ~31.5° in their XRD spectra (Fig. 3.2). Thus, low temperature synthesized rare earth substituted zirconia showed cubic phase which on heating above 1100°C get converted to tetragonal and/or monoclinic phase. In case of Gd doped sample, cubic phase could be stabilized to a greater extent as compared to other two substituted samples. This could be due to identical ionic radii of Y^{3+} (1.02 Å) and Gd^{3+} (1.05 Å), which also displays similar behaviour. The ionic size of La^{3+} (1.16 Å) and Nd^{3+} (1.11 Å) being higher, stabilization of cubic phase was not possible at sintering temperatures in excess of 1100°C. The appearance of different phases in samples sintered at 1100°C has been further investigated by EXAFS measurements. Sample pellets were prepared and EXAFS measurements were performed in the transmission mode at the Energy Dispersive EXAFS beamline (BL-08) at INDUS-2 as described in *Chapter-2*. EXAFS spectrum of a commercial YSZ sample has been used for calibration of the CCD channels, where both the Zr and Y edges appeared in the same spectrum at CCD channel nos. 253 and 460, respectively, and assuming the reported values of Y K-edge of 17046 eV and Zr K edge of 18014 eV in YSZ, the CCD channels were calibrated in energy scale. Fig. 3.3 shows a representative experimental EXAFS ($\mu\ (E)$ versus E) spectrum of ZrO_2 sample doped with 11 mol% of La and sintered at 1100°C. The data in k-space is shown in Fig. 3.4 for all the samples.

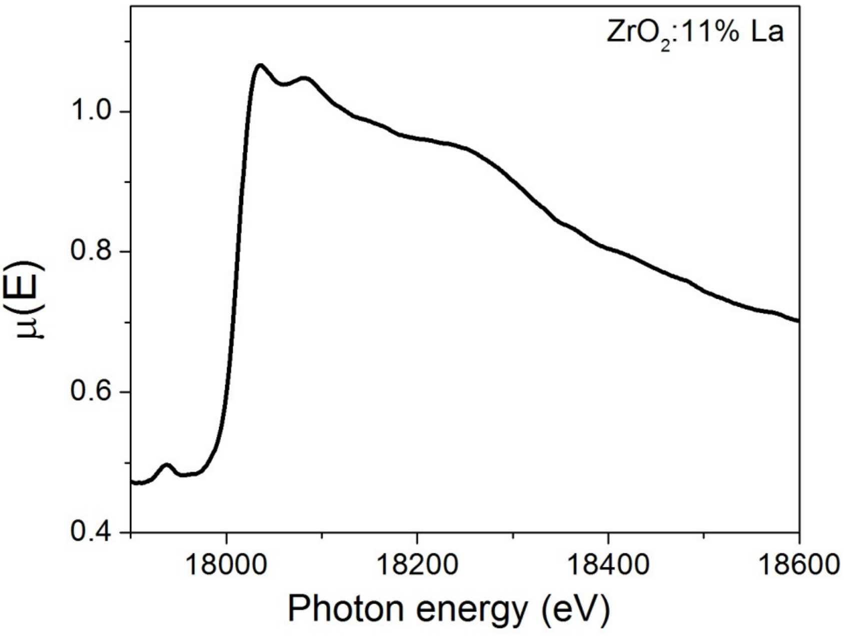

Figure 3.3 Representative $\mu(E)$ *vs* E spectrum of ZrO_2 doped with La.

Fig. 3.5 shows the experimental $\chi(R)$ versus R spectrum along with the best theoretical fit of the ZrO_2 samples doped with 11 mol% of Gd, Nd, and La, respectively. The first two peaks in the range of 1-2 Å represents Zr-O bonds while the more distant peaks in the range of 3.5-

4 Å are attributed to the Zr-Zr bonds. It should be noted that the theoretical FT-EXAFS spectrum of cubic ZrO_2 is characterized by only one peak in the 1-2Å range, while in case of tetragonal ZrO_2, the first peak is split into two.

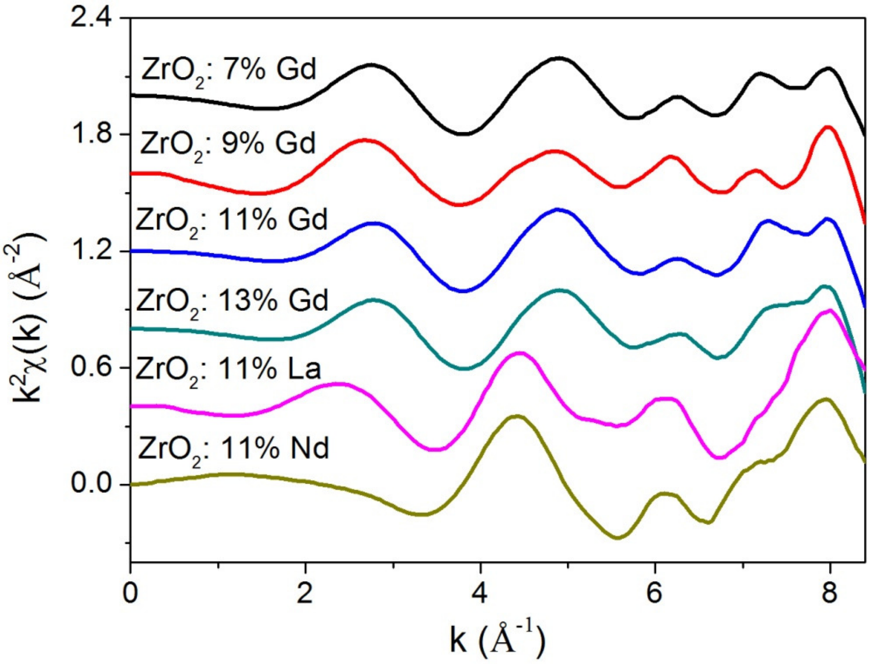

Figure 3.4 Exprimental $k^2\chi(k)$ *vs* k data for doped ZrO_2 samples at Zr K edge.

The first Zr-O peaks in the FT-EXAFS spectra of Gd and Nd doped ZrO_2 samples in the present case have also been found to split into two peaks and hence have been fitted assuming tetragonal structure of ZrO_2. Though it was apparent from the XRD spectra that the Gd doped samples have been stabilized in cubic fluorite structure with a trace of tetragonal phase, however, EXAFS spectra reveal the tetragonal structure of the samples with certainty. However, for the La doped ZrO_2 sample, reasonable theoretical fitting of the FT-EXAFS spectrum could be achieved assuming a monoclinic structure in accordance with the XRD spectrum of these samples.

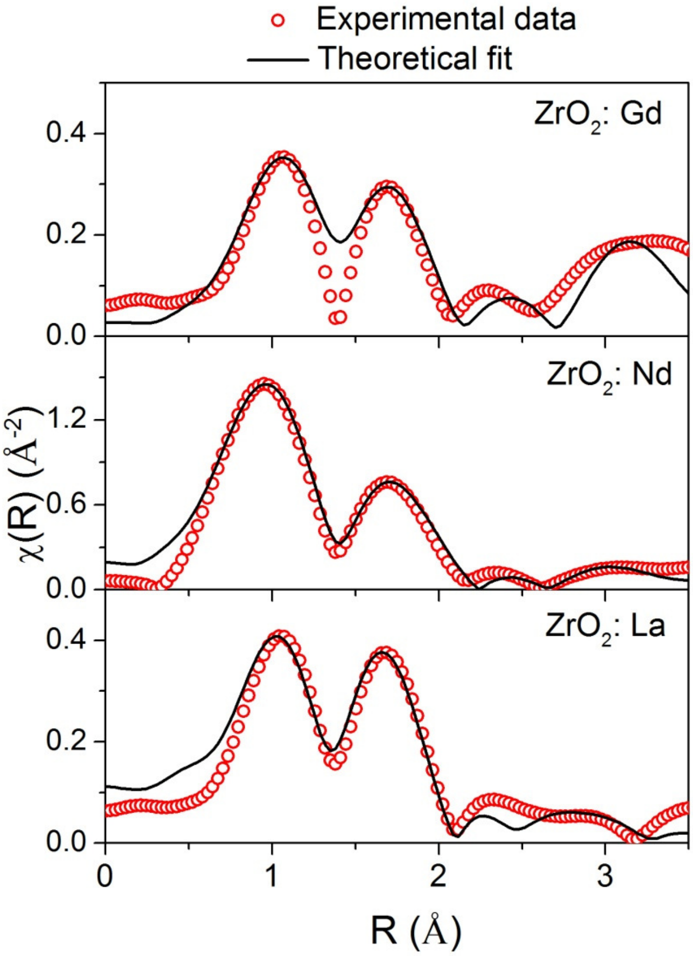

Figure 3.5 Experimental *χ(R) vs R* spectra with best-fit theoretical plots for ZrO_2 doped with 11 mol% of (a) Gd, (b) Nd, and (c) La.

To support our experimental results, relativistic spin polarized first principle calculations of the La-doped ZrO_2 samples were performed using the full potential linearized augmented plane wave code [46] with the generalized gradient correction (GGA) of local density approximation for exchange correlation function [47]. The muffin-tin radii of Zr and La have been taken as 2.05 a.u. and for O it has been taken as 1.8 a.u. The convergence criterion for the total energy E has been taken to be about 0.1 mRy per atom and the charge convergence has been set to 0.001. The calculations have been performed with lattice parameters of a, b, and c = 5.145, 5.2075, and 5.3107 Å, $\alpha = \gamma = 90^\circ$ and $\beta = 99.233^\circ$ for the monoclinic phase and with a = b = 3.64, c = 5.27 Å, and a = b = c = 90° for the tetragonal phase. The number of k-points for self-consistent field cycles in the reducible (irreducible) Brillouin zone are about 4000 (270) for the tetragonal phase and about 2000 (430) for the monoclinic phase. Fig. 3.6 shows a representative 2×2×4 supercell used in the above calculations for the 12.5% La-doped ZrO_2 sample having monoclinic structure.

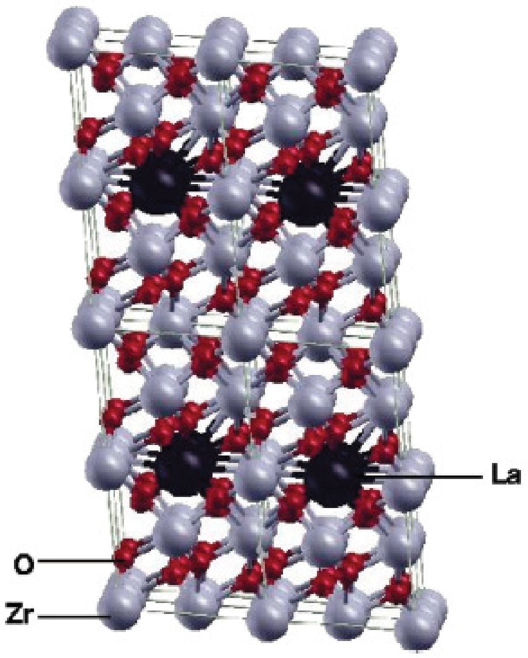

Figure 3.6 A 2×2×4 supercell in monoclinic symmetry for the 12.5% La-doped ZrO_2. (The largest spheres correspond to La, second largest to Zr and smallest spheres correspond to O.)

The ab-initio calculations reveal that the undoped zirconia in the ground state has a monoclinic symmetry with the tetragonal phase being higher in energy by 114.682 meV/f.u. (formula unit). La-doped ZrO_2 is observed to retain the ground state monoclinic symmetry with its energy less than that of the tetragonal phase by 13.729 meV/f.u. The above results agree well with the experimental findings. It should be mentioned here that we have carried out the calculations with 12.5% doping by La which is very close to the sample subjected to our EXAFS measurements, which is having 11% doping.

To investigate the local structure around the Zr atoms more quantitatively, we have analyzed the best fit parameters obtained from the fitting of the experimental $\chi(R)$ versus R spectra following the methodology described in *Chapter 2*. The best fit theoretical $\chi(R)$ versus R spectra of the samples have been shown in Fig. 3.5. The structural parameters for the tetragonal and monoclinic ZrO_2 used for simulation of theoretical EXAFS spectra of the samples have been obtained from reported values in the literature.[48], [49] The first two peaks in the range 1-2 Å have been attributed to two Zr-O shells with a total of eightfold coordination while the more distant peaks in the range of 3.5-4 Å are attributed to two Zr-Zr bonds having a total of 12-fold coordination. The bond distances, coordination numbers (including scattering amplitudes) and disorder (Debye-Waller) factors (σ^2), which give the mean-square fluctuations in the distances, have been used as fitting parameters and the best fit results of the above parameters have been summarized in Figs 3.7 and 3.8.

Fig. 3.7 shows the variation in average Zr-O bond length for the two shells, (r_{Zr-O}), total oxygen coordination (N_{Zr-O}) and average disorder parameter (σ^2) of the Zr-O shells for different dopant cations. It can be seen that for the Gd dopant, oxygen coordination near Zr site is significantly less indicating that in this case oxygen vacancies are created near Zr site. However, as the size of the dopant cation is increased from Gd to La, the bond length and disorder parameters decrease while the oxygen coordination increases. This implies that with larger sized dopants, the oxygen vacancy near Zr site decreases or in other words the oxygen vacancies are created near the dopant site leaving the host sites unperturbed. As the dopant size increases from Gd to La, the average Zr-Zr bond lengths (r_{Zr-Zr}) gets contracted while the total Zr-Zr coordination number (N_{Zr-Zr}) and average disorder parameters (σ^2_{Zr-Zr}) decrease as in Fig. 3.8.

The decrease in the disorder term as the dopant ion changes from Gd to La also confirms that with increase in the size of the dopant cation the disorder near the host Zr cation is decreased. However, in case of doping with Nd and La, due to accommodation of larger size ions in the lattice, the Zr-Zr bonds contract. The slight opposite trend in the variations of the different parameters from Nd-doped samples to La-doped samples can be ignored since the values of the parameters for La-doped samples have been obtained assuming a monoclinic structure while the other two systems have been fitted assuming tetragonal structure.

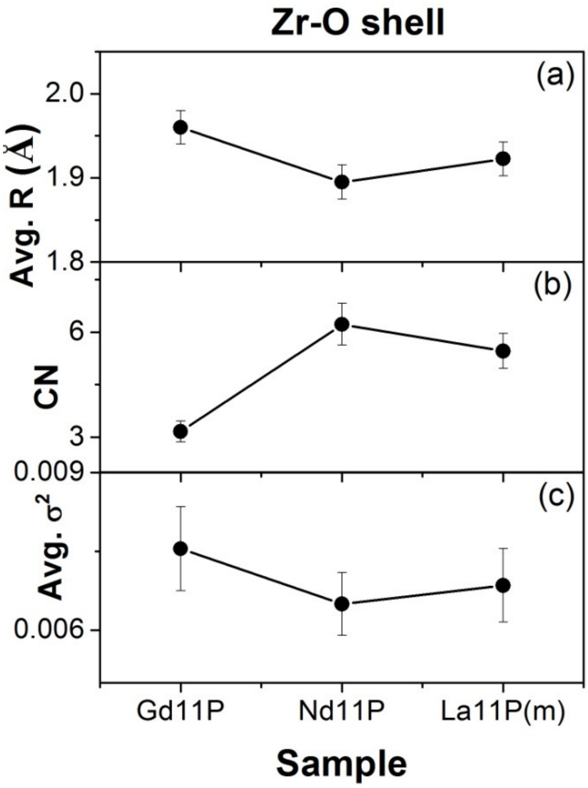

Figure 3.7 Variation of (a) average first shell distances, Zr-O, (b) total oxygen coordination numbers, CN, (c) average Debye Waller factors.

In order to have a further insight into the above issue regarding the location of oxygen vacancies in doped ZrO_2 system, *ab initio* calculations have also been performed for La-doped ZrO_2 assuming oxygen vacancies at the near neighbour (NN) and next near neighbour (NNN) sites of the dopant La. For the calculations with oxygen vacancies, the k-points in the irreducible Brillouin zone are about 690 in number. From the energetics, it has been clearly observed that the oxygen vacancies are created near the dopant sites leaving the host sites unperturbed as is observed from our experimental results also. Oxygen ion vacancies at the near neighbour (NN) sites of the dopant leave the system in a more stable state with an energy difference of 10.633 meV/f.u. in comparison to vacancies at further sites.

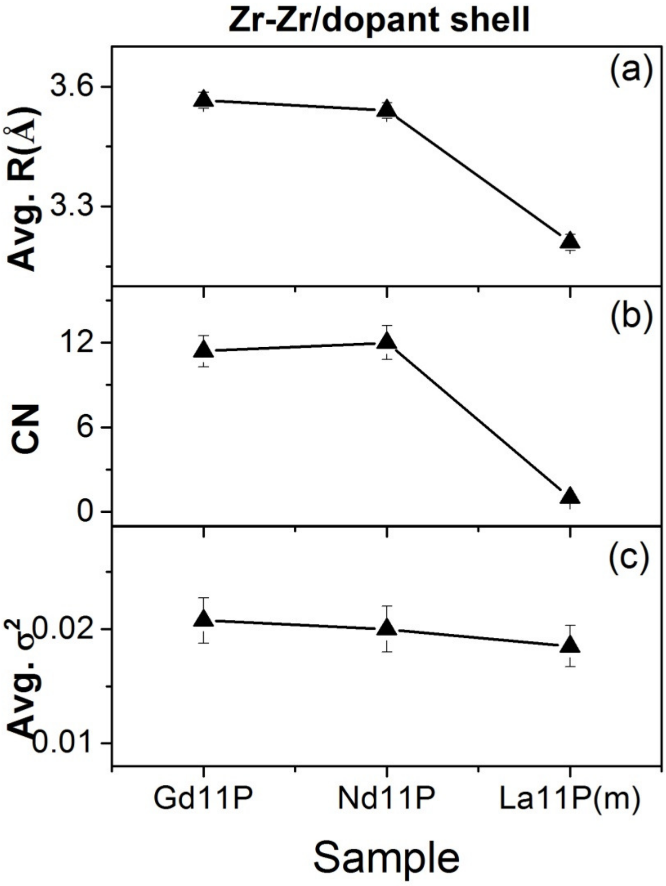

Figure 3.8 Variation of (a) average second shell distances, Zr-Zr/dopant, (b) total Zr/dopant coordination number, CN, and (c) average Debye Waller factors.

From the above studies, since it is observed that Gd-doped samples have the minimum oxygen coordination, it can be concluded that Gd doping is most effective in generating oxygen vacancies near Zr sites among the three dopants studied, which is favourable for enhancing ionic conductivity of ZrO_2. Thus a more exhaustive study has been carried out with different doping concentrations of Gd in ZrO_2 with 7, 9, 11, and 13% doping of Gd.

3.2 ZrO_2 doped with different concentrations of Gd^{3+}

XRD spectra of Gd doped ZrO_2 samples with varying concentration of gadolinium (7–13 at. %) sintered at 1100°C, for longer period of 48 h, have been shown in Fig. 3.9. The sintering time has been increased to explore the genesis for the peak broadening observed in case of Gd doped samples. All the samples exhibit phases similar to distorted cubic phase (tetragonal) as evident from splitting of XRD peaks at ~35° and ~60° 2θ value. The data obtained for different samples have been summarized in Table 3.2 and have also been shown in Fig. 3.10 as a function of Gd doping concentration.

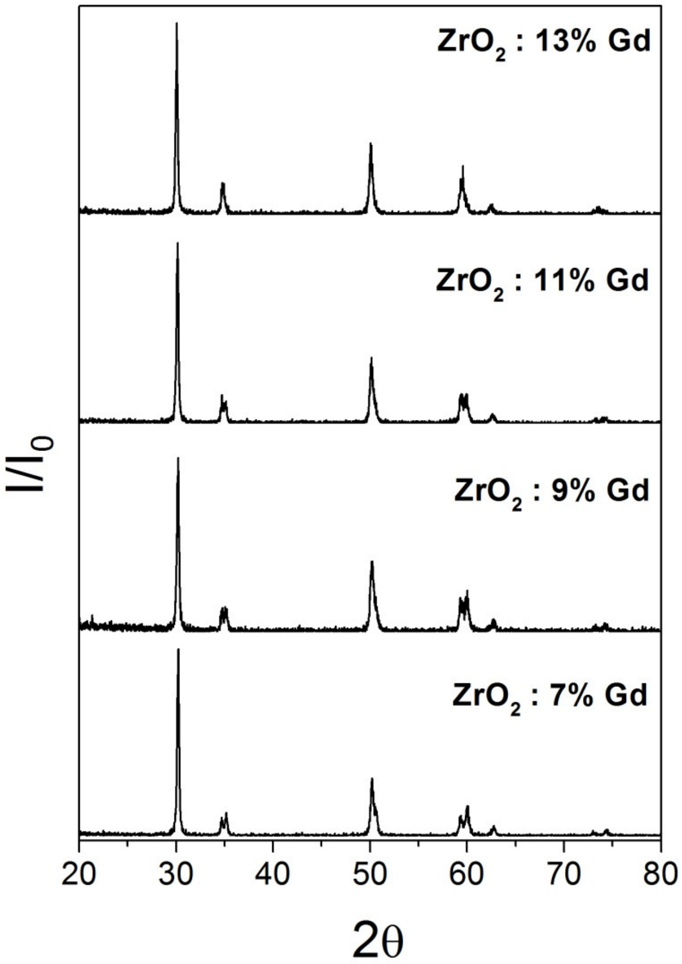

Figure 3.9 XRD spectra for Gd_2O_3 doped zirconia samples after sintering at 1100°C.

Table 3.2 Cell parameters for generated after indexing and refinement of XRD patterns for GdSZ samples.

Sl. no.	Sample	Symmetry	a_0 (Å)	c_0 (Å)	Volume (Å^3)
1.	ZrO_2 : Gd (7%)	Tetragonal	3.602 ± 0.002	5.176 ± 0.001	67.17 ± 0.04
2.	ZrO_2 : Gd (9%)	Tetragonal	3.607 ± 0.003	5.171 ± 0.001	67.29 ± 0.07
3.	ZrO_2 : Gd (11%)	Tetragonal	3.609 ± 0.002	5.176 ± 0.001	67.41 ± 0.06
4.	ZrO_2 : Gd (13%)	Tetragonal	3.629 ± 0.002	5.159 ± 0.001	67.94 ± 0.04

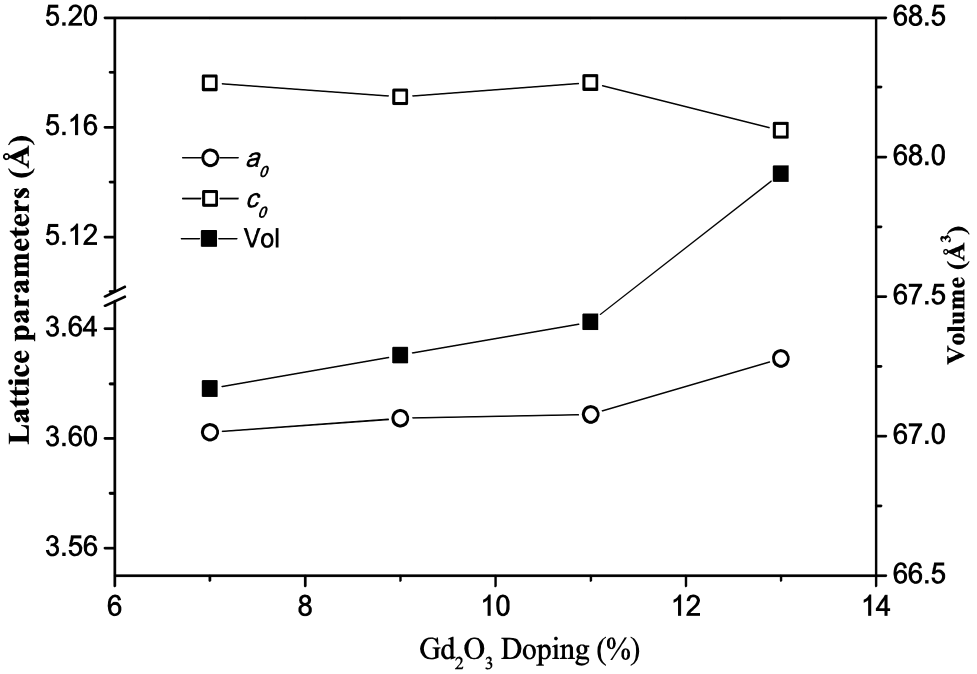

Figure 3.10 Variation in lattice parameters and cell volume with extent of gadolinium oxide doping.

Lattice parameter a_0 is found to increase with increasing concentration of Gd, while c_0 remains constant around 5.17 Å for doping up to 11% of Gd and reduces to 5.16 Å for 13% of Gd doping. The cell volume increases monotonically with increase in Gd concentration of up to 11% Gd followed by a sharp increase for 13% of Gd. The sharp increase in a_0 and cell volume and abrupt decrease in c_0 value for 13% Gd doping suggests a shift in stabilization of lattice symmetry to cubic phase for higher doping percentage. Thus, the XRD spectrum of

13% doped sample has been indexed and refined again with cubic symmetry (JCPDS 30-1468) having a_0 value of 5.1513 ± 0.0033, though with lower Fig. of merit implying the presence of mixed phases.

Fig. 3.11 shows a representative experimental EXAFS ($\mu(E)$ versus E) spectrum of ZrO_2 sample doped with 13% Gd and the χ (R) versus R spectra for ZrO_2 samples doped with different (7, 9, 11, and 13%) concentrations of Gd are shown in Fig. 3.12. The χ(k) data of the samples are shown in Fig. 3.4. All the FT-EXAFS spectra are characterized by two peaks in the range 1-2 Å corresponding to the Zr-O bonds and two peaks in the range 3-4 Å corresponding to Zr-Zr bonds. The experimental spectra have been fitted with theoretical EXAFS spectra simulated assuming tetragonal structure of ZrO_2 as discussed earlier.

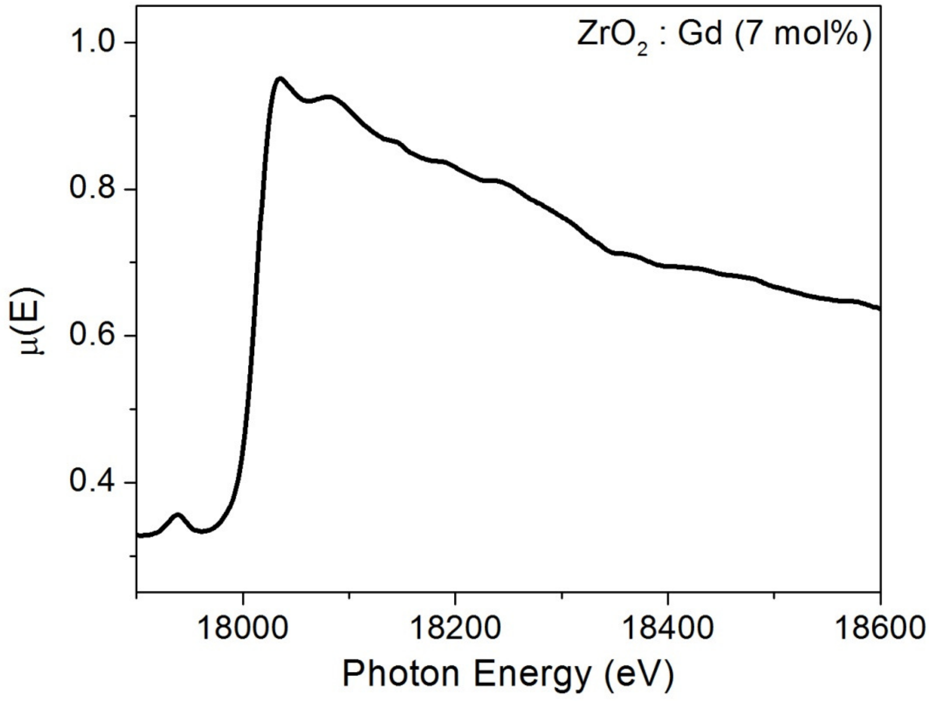

Figure 3.11 Representative $\mu(E)$ vs E spectrum of ZrO_2 doped with 7% Gd concentration.

The best fit theoretical spectra are also shown in Fig. 3.12 along with the experimental spectra and the best fit results have been summarized in Fig. 3.13. It is observed that with increase in Gd concentration from 7% to 9%, the average Zr-O bond distance decreases while the average disorder parameter at the O site increases whereas the total oxygen coordination decreases upto a doping concentration of 11% of Gd.

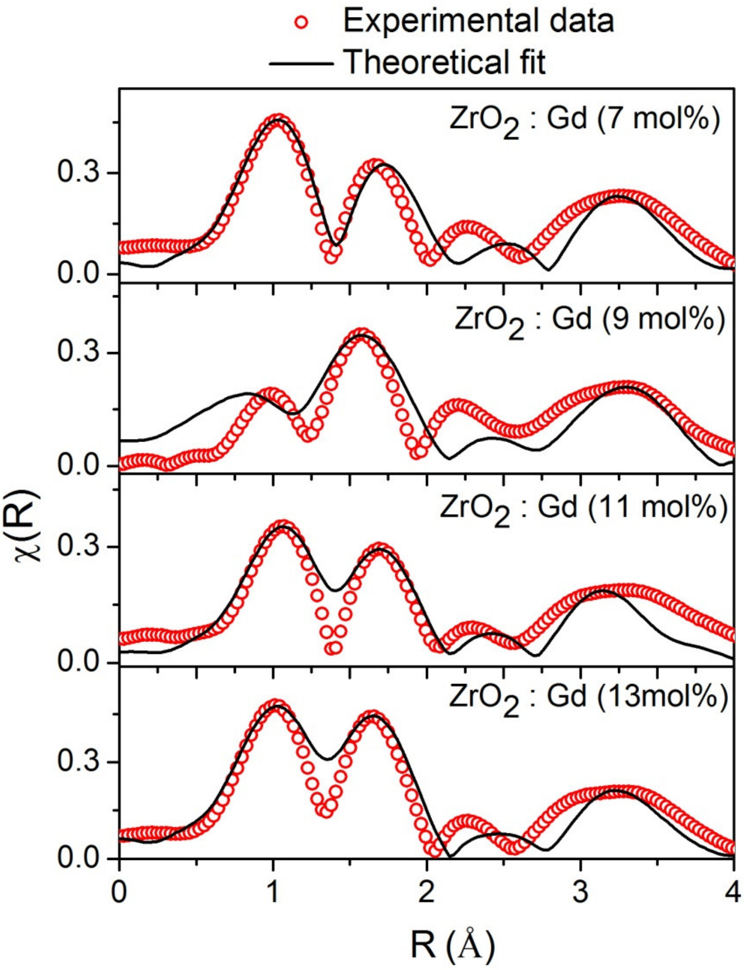

Figure 3.12 Experimental $\chi(R)$ *vs* R spectra with best-fit theoretical plots for ZrO_2 doped with different Gd_2O_3 concentrations.

However, for doping concentration of more than 11%, Zr-O bond distance increases with a decrease in the disorder factor while oxygen coordination increases beyond a doping concentartion of 11%. Hence, it is observed that maximum number of oxygen vacancies is created for an optimum Gd doping of 9-11% and the reduced effect of Gd doping on the Zr-O shell with higher concentration of dopants maybe because of clustering of Gd ions inside ZrO_2 lattice.

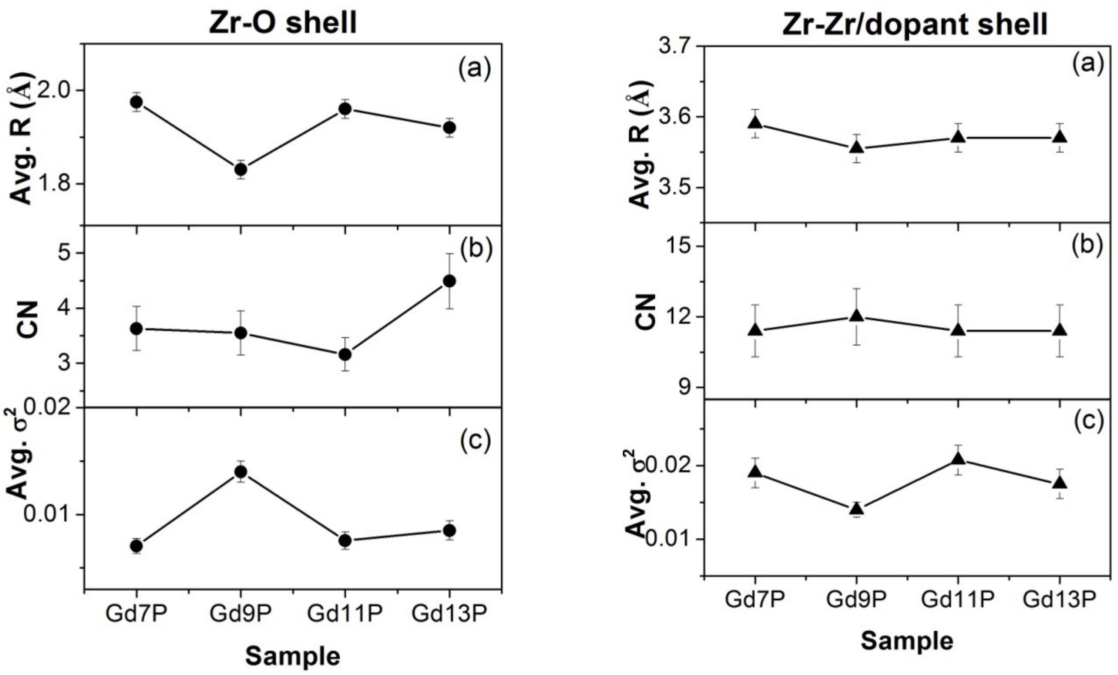

Figure 3.13 Variation of (a) average first shell distances, (b) total oxygen coordination numbers, CN, and (c) average Debye Waller factors for the nearest Zr-O and next nearest Zr-Zr/dopant shells.

The above postulate is also supported by the results obtained for Zr-Zr/cation shells, as shown in Fig. 3.13(b), which indicates that the Zr coordination and the bond distances are affected most by a Gd doping concentration of 9%. The reduced effect on the Zr-O shell with increase in concentration of Gd dopants has also been observed by Sadykov *et al.* [43] for their CeO_2–ZrO_2 sample.

In order to have more information on the mechanism of creation of oxygen vacancies in the Gd doped system, we have carried out EXAFS measurements of the 7, 9, 11 and 13 mol % Gd^{3+} doped ZrO_2 samples at the Gd L_3-edge also. For the present measurement carried out at the Energy Dispersive EXAFS beamline (BL-08) at INDUS-2 SRS, the bent crystal polychromator of the beamline has been set at the proper Bragg angle so that a band of energy is obtained around Gd L_3 edge of ~ 7243 eV. EXAFS spectra of a commercial Fe metal foil and pellet made from commercial Gd_2O_3 powder have been used for calibration of the CCD channels. Under the above experimental setting, Gd and Fe edges of the respective standard samples appeared at CCD channel nos. 875 and 475 respectively and assuming the reported values of Fe K-edge of 7112 eV and Gd L_3 edge of 7243 eV in Gd_2O_3, the CCD channels were calibrated in energy scale. Fig. 3.14(a) shows the experimental EXAFS ($\mu(E)$ versus E) spectrum of a representative ZrO_2 sample with 13 mol% of Gd doping measured at Gd edge. Fig. 3.14(b) shows the experimental $\chi(R)$ versus R spectrum for the representative sample of 13 mol% Gd doping.

The experimental $\chi(R)$ versus R spectra of the samples have subsequently been fitted with the theoretical spectra generated assuming a cubic Gd_2O_3 structure of the Gd environment. It is justified since incorporation of Gd^{3+} in the ZrO_2 lattice is carried out by adding Gd_2O_3 during the synthesis of the samples. Such an approach to modeling has been reported by other authors as well [44]. The best fit theoretical $\chi(R)$ versus R spectrum of the representative sample has been shown in Fig. 3.14(b) along with the experimental spectrum. The structural parameters for cubic Gd_2O_3 used for simulation of theoretical EXAFS spectra of the samples have been obtained from reported values in the literature [50].

The fitting has been carried out in the R-range of 1- 4 Å. The first prominent peak at ~ 2 Å is attributed to nearest oxygen shell with an ideal coordination number of 6 while the second conspicuous peak at ~ 3.6 Å corresponds to the next nearest gadolinium shell with 6 coordination number, all values representing the cubic Gd_2O_3 structure. The bond distances, co-ordination numbers (including scattering amplitudes) and disorder (Debye-Waller) factors (σ^2), which give the mean-square fluctuations in the distances, have been used as fitting parameters and the best fit results of the above parameters for all the samples have been summarized in Table 3.3.

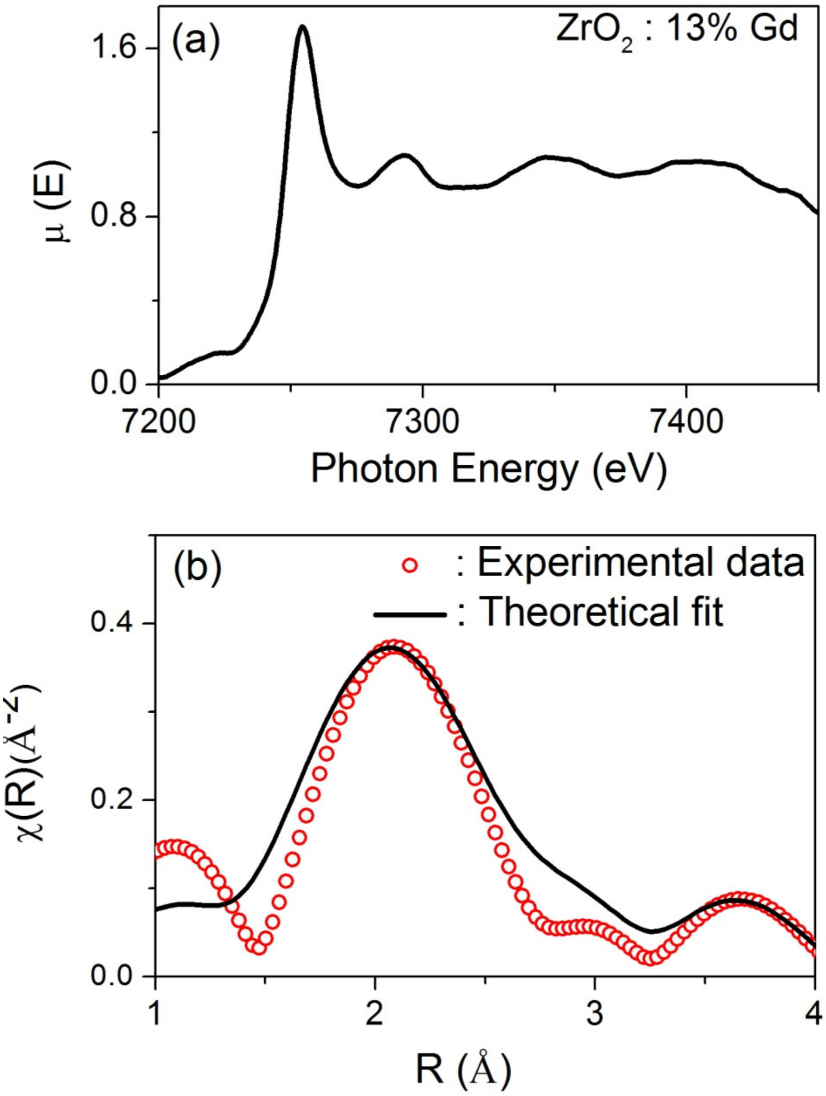

Figure 3.14 (a). X-ray absorption coefficient (μ) versus photon energy (E) of a representative ZrO_2 sample with 13 mol% of Gd doping. (b). FT-EXAFS χ(R) versus (R) spectra for a representative ZrO_2 sample with 13 mol% of Gd doping along with the best fit.

The bond distances of the Gd-O shell as well as the Gd-Gd/Zr shell are higher than the respective values in the Gd_2O_3 compound. This is expected since in the present samples Gd resides in the distorted cubic or tetragonal lattice of ZrO_2 instead of the cubic lattice of Gd_2O_3. Even the coordination number of the first two shells (8 for O coordination and 12 for Gd/Zr coordination) do not agree with expected coordination of values for Gd_2O_3 (6 coordinations for both the shells), but rather agree with the expected values for the Zr-O and

Zr-Zr shells of tetragonal ZrO_2 matrix. This clearly establishes the fact that in the present samples, Gd replaces Zr and gets incorporated in the lattice, which has tetragonal structure with 8 coordination for oxygen. It also establishes the fact that the oxygen vacancies due to Gd doping are created near the host Zr atoms since the oxygen coordination near the Gd sites remain close to its expected values of 8. This is in accordance with the results reported by us earlier [51]. This is further strengthened by the fact that the disorder or Debye-Waller factors (σ^2) for the nearest neighbour oxygen shells of the first two samples are quite low, implying a stable Gd neighbourhood since distortions due to Gd doping are created near the Zr sites as has been observed by our earlier studies.

The third sample (Gd11P), however, shows a very high Debye-Waller factor which indicates increased disorder in the system. The last sample of the series Gd13P shows even higher coordination numbers though the bond length values are comparable to the other samples. The latter observations can be attributed to the fact that Gd_2O_3 doping beyond 9% increases instability and the possibility of Gd clustering in the ZrO_2 matrix instead of substitutional replacement of Zr atoms, which are in agreement with the findings of our previous report [51].

Table 3.3 Best fit parameters for Gd doped ZrO_2 samples at Gd L3-edge.

		Gd7P	Gd9P	Gd11P	Gd13P
Gd-O	R	2.48	2.39	2.45	2.46
(2.3 Å; 6)	CN	8	8	8	10.24
	σ^2	0.003	0.003	0.014	0.003
Gd-Gd	R	3.66	3.61	3.68	3.67
	CN	12	12	12	12.6
(3.58 Å; 6)	σ^2	0.008	0.017	0.015	0.007

Typical error bars involved are ±0.02 Å in R and ±10% in CN and σ^2

To support our experimental results on the position of the oxygen vacancies near the Zr sites, first principle calculations of the Gd-doped ZrO_2 system with 6.25, 12.5 and 25% Gd doping in the ZrO_2 system have been performed. In each case, calculations have been carried out on oxygen vacancies created near and far from the dopant atom, Gd. In Fig. 3.15, a typical structure with an oxygen vacancy near the Zr site and far from the dopant site has been shown. We have employed the Vienna Ab Initio Simulation Package (VASP) [52]–[54] in combination with the projector augmented wave (PAW) [55] method and the generalized gradient approximation (GGA) over the local density approximation for the exchange-correlation functional [47]**.** GGA is used because it accounts for the density gradients, and hence, for most of the systems, provides better agreement with experiment compared to local-density approximation. An energy cutoff of 500 eV for the planewave has been used. The final energies have been calculated with a k mesh consisting of about 300 K-points and the k-mesh convergence has been tested. The energy and force tolerance for our calculations were 10 μeV and 10 meV/Å, respectively. To study the stability of the system under different conditions, we have calculated the formation energy in each case. The formation energy (E_{mix}) can be obtained by subtracting the total sum of the bulk energy of all the material components, E_i weighted by its concentration c_i from the ground state energy of the total alloy system, E_{tot}:

$$E_{mix} = E_{tot} - \sum_i c_i E_i \tag{3.1}$$

where, a more negative mixing energy of a system indicates that it is more stable.

We have optimized the geometries of each system, with and without oxygen vacancies, and with different doping concentration. The system has shown a tendency towards a transition of crystal symmetry from tetrahedral to cubic above 13% Gd-doping. Hence we have carried out calculations on both cubic and tetragonal symmetry for each case.

However, though the formation energy decreases for the tetragonal phase, upto 25% doping the structure with tetragonal symmetry has the lower total energy in each doping. The formation energies for all the doping concentrations up to 25% and different positions of oxygen vacancies have been plotted in Fig 3.16. It is clearly seen from this Fig. that beyond about 7% Gd doping, the system is more stable when the oxygen vacancies are created far from the dopant site i.e., near the Zr site. However, the stability of systems with increasing doping tends to decrease as the doping concentration increases. Hence a doping concentration of 7-10% is optimum for the ZrO_2 system for creation of optimum oxygen vacancies as well as for stability of the system.

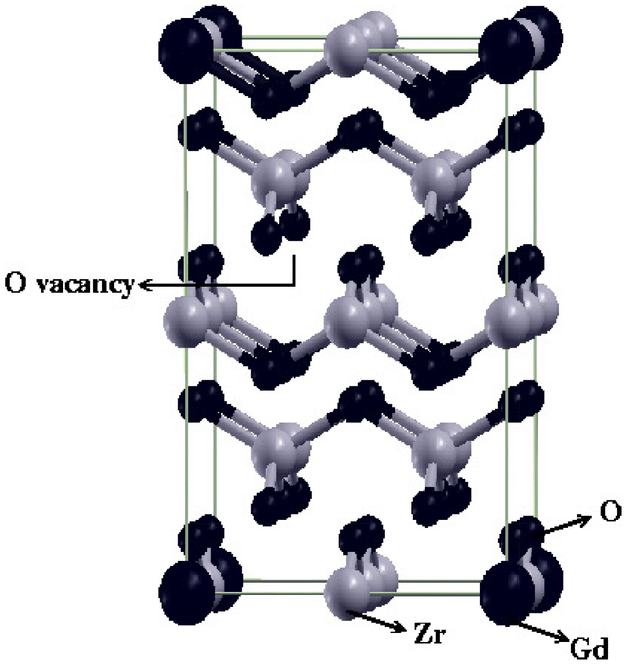

Figure 3.15 Model ZrO_2 structure with an oxygen vacancy near the Zr site and another far from the dopant site.

Conclusion

EXAFS measurements have been carried out on Gd, Nd and La doped ZrO_2 samples at Zr K edge to investigate the mechanism of creation of oxygen vacancies in these systems. It has been observed from X-ray diffraction measurements that Gd and Nd doped samples show appearance of tetragonal structure and La doped samples attain monoclinic structure, when sintered at 1100°C.

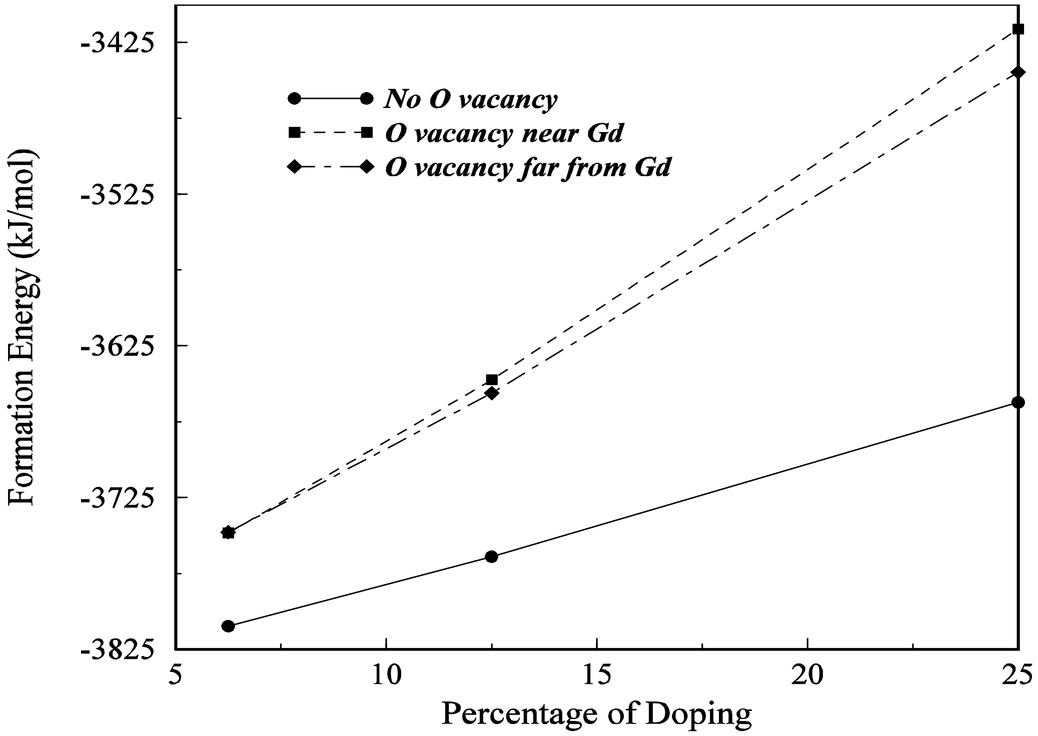

Figure 3.16 Variation of formation energies as a function of Gd doping concentrations upto 25% for different positions of oxygen vacancies in ZrO_2 matrix.

This has been confirmed by EXAFS measurements which clearly reveal splitting of the first Zr-O shell into two sub-shells for the samples sintered at 1100°C which is a characteristic of tetragonal and monoclinic phases. Ab-inito first principle calculations show that La-doped ZrO_2 has lower ground state energy in the monoclinic symmetry than in the tetragonal phase. The EXAFS data have been analyzed to find out relevant local structure parameters of the Zr-O and Zr-Zr shells, viz., bond distances, coordinations, and disorder parameters. It was concluded that oxygen vacancies in ZrO_2 host matrix are created near the Zr site for Gd doping, whereas, for Nd and La dopant atoms having relatively larger ionic radii, the Zr-O shell remains more or less unperturbed and the oxygen vacancies are located near the dopant cations. First principle calculations have confirmed that for La-doped ZrO_2 systems oxygen ion vacancies at the nearest neighbour sites of the dopant leave the system in a more stable state in comparison to oxygen vacancies at further sites, supporting of our experimental findings. From EXAFS measurements on 7%-13% Gd doped samples, it had been further concluded that 9% Gd doping is optimum for creation of vacancies near the Zr sites and hence for increasing its ionic conductivity. A further increase in Gd dopant concentration decreases the number of oxygen vacancies possibly due to the clustering of Gd dopants at higher concentration. All the above inferences made from Zr edge EXAFS measurements on the samples have also been supported by the findings of EXAFS measurements on the samples at Gd L3 edge.

Chapter 4

EXAFS MEASUREMENTS ON LUMINISCENT MATERIALS

4.1 Eu doped GaOOH

Gallium oxyhydroxide (GaOOH) and lanthanide ions (Ln^{3+}) containing GaOOH ($GaOOH:Ln^{3+}$) are the precursor materials for the synthesis of Gallium oxide based luminescent materials and devices [56], [57]. A number of studies are available regarding the preparation and characterization of both undoped and lanthanide ions doped GaOOH and Ga_2O_3 nanomaterials [58], [59]**.** Different types of linkages are present in GaOOH which has a layered structure stabilized by hydrogen bonds. However, the extent of the effect of doping on these linkages is not clearly understood. It has been observed that layered structure of highly crystalline orthorhombic GaOOH nanorods undergo significant lattice distortions leading to amorphisation even when very small amounts of Eu^{3+} ions (1 at.% or more) are present during its synthesis [60]**.** As the ionic radii of Ln^{3+} and Ga^{3+} are significantly different, it is quite interesting to know precisely where the lanthanide ions are getting incorporated and what structural modification it makes to the GaOOH lattice during doping. Such studies are essential for understanding the mechanism of lanthanide ion incorporation in different structural modifications of Ga_2O_3 hosts which are obtained by the decomposition of lanthanide ions containing GaOOH phase. Chemical and structural changes can be either associated with changes in the local short range order around gallium or with the changes in the hydroxyl linkages in GaOOH lattice. EXAFS characterization can give valuable information regarding this aspect. Hence in the present study, changes in both local environments around Ga and hydroxyl linkages present in GaOOH nanorods brought about by the presence of Eu^{3+} ions during its synthesis, is probed using EXAFS technique.

The GaOOH nanorods samples discussed in the present study have been prepared as follows. Around 1 g of $Ga(NO_3)_3.xH_2O$ was dissolved in 20 ml H_2O in a 100 ml round bottom flask. The solution was slowly heated up to 70˚C on silicon oil bath while stirring followed by addition of 5 g of urea. Temperature was then raised to 98˚C and refluxed till a slightly turbid solution was obtained. The temperature was maintained at this value for 2 h. After the reaction, the precipitate was collected by centrifugation and then washed two times with ethyl alcohol and three times with acetone followed by drying under ambient conditions. For Eu^{3+} containing samples, the same procedure was used except that, $Eu(NO_3)_3.5H_2O$ was used along with 1g of $Ga(NO_3)_3.xH_2O$ and 5 g of urea as the starting materials.

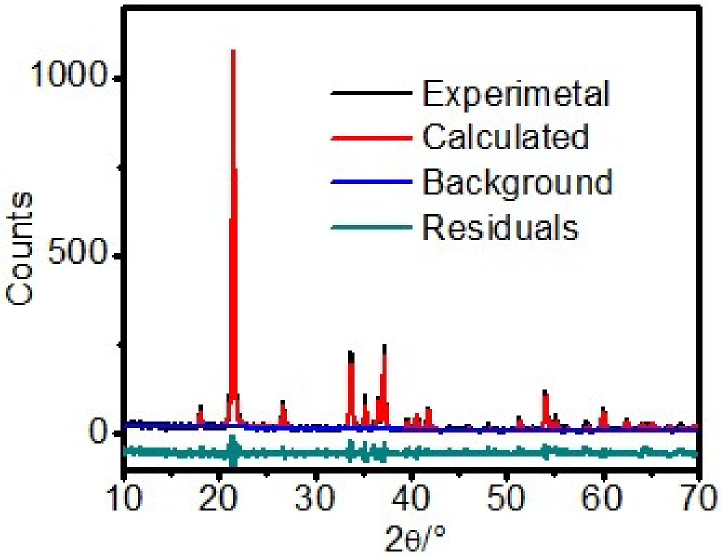

Figure 4.1 XRD pattern of as prepared GaOOH sample.

Initial structural characterization has been accomplished by XRD. Fig. 4.1 shows the Rietveld refined XRD pattern of as-prepared GaOOH sample. The pattern is a characteristic of well crystalline orthorhombic GaOOH phase with lattice parameters of a = 4.546(2) Å, b = 9.797(2) Å and c = 2.972(3) Å. As-prepared GaOOH sample is found to have rod shaped morphology as can be seen from the representative SEM image shown in Fig. 4.2. The rods have length around 2.5–3 µm and width around 300–400 nm.

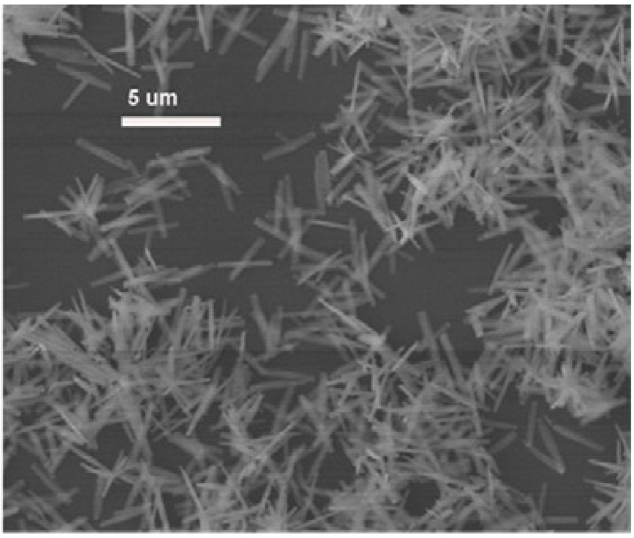

Figure 4.2 SEM image of as prepared GaOOH sample.

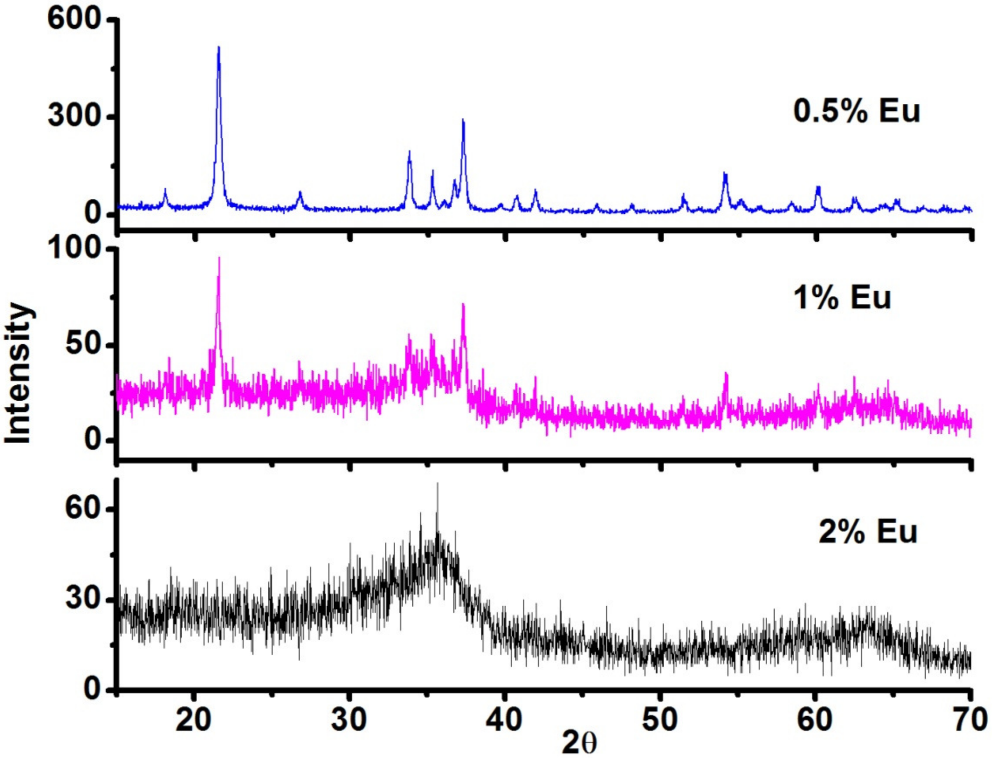

Figure 4.3 XRD patterns of GaOOH samples prepared in presence of different amounts of Eu^{3+} ions.

Fig. 4.3 shows the XRD patterns of GaOOH samples prepared in the presence of different amounts of Eu^{3+} ions. With increase in Eu^{3+} concentration, there is an increase in line width of the different diffraction peaks and for samples prepared in the presence of more than 1 at.% Eu^{3+}, no sharp peak characteristic of crystalline materials is observed and instead a broad peak characteristic of an amorphous phase appeared. The lattice parameters have been calculated for the crystalline samples based on least square fitting of the diffraction peaks and are found to be the same as that of the as-prepared GaOOH sample within experimental errors. Broadening of peaks and conversion of crystalline GaOOH to an amorphous phase with increase in Eu^{3+} concentration suggests that the GaOOH lattice is getting affected by the presence of Eu^{3+} in the reaction medium. The fact that even the presence of around 1 at.% Eu^{3+} during the precipitation process of GaOOH can significantly affect its crystallinity prompted us to investigate the changes in the structural environment around Ga^{3+} in GaOOH nanorods brought about by the lanthanide ions. Hence detailed Ga–K edge EXAFS studies were carried out on the samples and are described below.

EXAS measurements on these samples have been carried out at the Energy Dispersive EXAFS beamline (BL-08) described in *Chapter-2*. For the present measurement, the bent crystal polychromator of the beamline was set at the proper Bragg angle so that a band of energy is obtained around Ga–K edge of ~10367 eV. EXAFS spectra of a Ga_2O_3 foil and a Lu_2O_3 pellet measured under the same configuration of the polychromator, the sample and detector positions, were used for calibration of the CCD channels in terms of energy assuming the reported values of Ga–K edge of 10367 eV and Lu–L_2 edge of 10349 eV. Fig. 4.4(a) shows the representative experimental EXAFS ($\mu(E)$ versus E) spectra of all the samples. $\chi(k)$ is weighted by k^2 to amplify the oscillation at high k and the $k^2\chi(k)$ functions are Fourier transformed in R space to generate the $\chi(R)$ versus R (or FT-EXAFS) spectra in terms of the real distances from the centre of the absorbing atom and it is shown in Fig. 4.4(b).

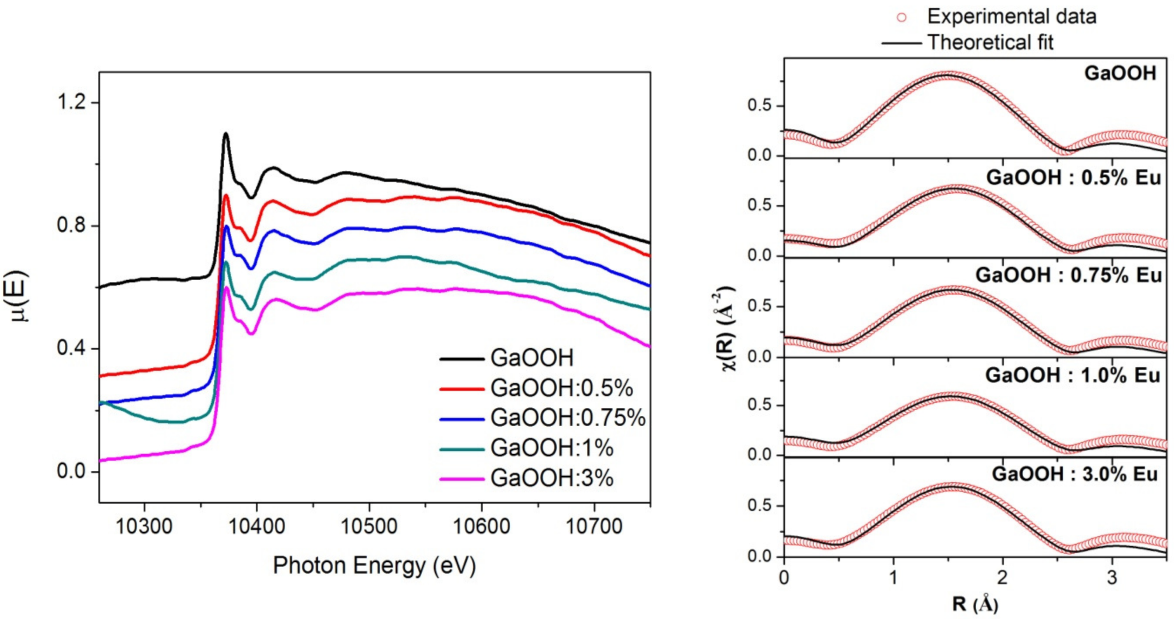

(a)

(b)

Figure 4.4 (a) Experimental EXAFS ($\mu(E)$ versus E) spectra (b) FT-EXAFS $\chi(R)$ versus R spectra

Subsequently, theoretical χ(R) versus R spectra have been simulated based on the information available on the structural features of GaOOH lattice. In order to do this, it is necessary to understand the nature of the coordination polyhedra and the different types of linkages existing in GaOOH lattice, which is briefly described below. GaOOH is iso-structural with α-AlOOH (the mineral diaspore) [61] and has a layered structure made up of distorted GaO_6 octahedra stabilized by the hydrogen bonding between the OH groups existing at the inter layer space of GaOOH lattice. A schematic representation of a fragment of GaOOH lattice, depicting GaO_6 unit, O tetrahedral and H atoms attached with oxygen atoms is shown in Fig. 4.5. The unit cell is shown within the rectangle drawn with light black line. This structure consists of two non-equivalent axial oxygen atoms namely Oa and Ob which are indicated in Fig. 4.5.

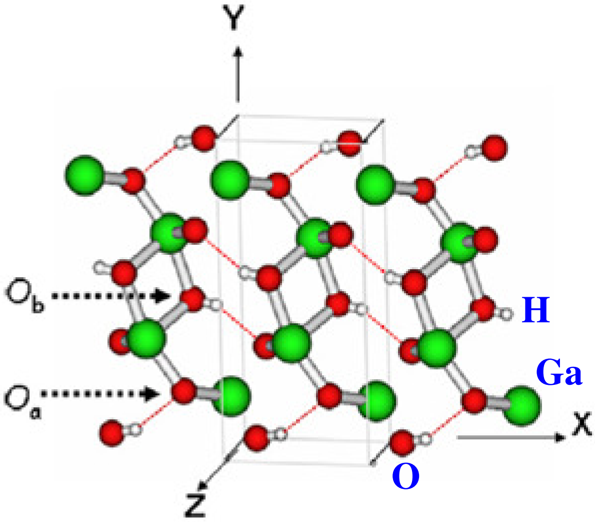

Figure 4.5 Schematic representation of a fragment of GaOOH lattice.

One of the octahedral axes i.e. GaOa is almost normal to the equatorial plane with Ga at the centre, while the other octahedral axis formed with GaOb is slightly tilted from the normal. These non-equivalent oxygen atoms (Oa and Ob) form two different kinds of OH linkages in the GaOOH structure, with one of the axial oxygen atoms (Ob) bonded directly to hydrogen, while another oxygen atom (Oa) is hydrogen bonded (represented as dotted line) with hydrogen of the neighbouring octahedron. These hydrogen bonds between the OH groups stabilize the layered structure of GaOOH. The structural parameters reported for α-AlOOH have been used for simulation of theoretical EXAFS spectra of the samples assuming the model described in [62] according to which each Al atom is surrounded by six oxygen atoms forming an irregular octahedron. The two types of non-equivalent atoms form two oxygen shells. The first oxygen shell (Al-O_a: R1) at 1.852 Å and second oxygen shell (Al-O_b: R2) at 1.975 Å, each shell having 3 oxygen atoms. We have also taken into account the 3 hydrogens (attached to O atoms) present at a distance of 2.513 Å from the Al atom. This structure was used to fit the first few peaks (up to 3.5 Å) obtained in the $\chi(R)$ versus R spectra of the samples. The fitting of Eu^{3+} containing samples has been done keeping the coordination numbers of different atoms constant with values obtained from the fitting result of the starting material i.e. as prepared GaOOH without any Eu^{3+}. The best fit theoretical plots have been shown along with the experimentally derived $\chi(R)$ versus R spectra in Fig. 4.4(b) where the bond distances (R), coordination numbers (including scattering amplitudes) (N) and disorder (Debye–Waller) factors (σ^2), which give the mean-square fluctuations in the distances, have been used as fitting parameters and the best fit results of the above parameters have been summarized in Table 4.1.

Table 4.1 Best fit parameters for GaOOH nanorods in presence of different amounts of Eu^{3+} ions at Ga K edge.

		GaOOH	0.5 at.% Eu^{3+}	0.75 at.% Eu^{3+}	1.0 at.% Eu^{3+}	3.0 at.% Eu^{3+}
Ga-O1 (1.852 Å; 3)	R1	2.05	2.12	2.07	2.06	2.06
	N1	3	3	3	3	3
	σ_1^2	0.008	0.012	0.014	0.017	0.011
Ga-O2 (1.975 Å; 3)	R2	2.18	2.22	2.20	2.19	2.20
	N2	3	3	3	3	3
	σ_2^2	0.006	0.008	0.006	0.008	0.005
Ga-H (2.513 Å; 3)	R3	2.51	2.51	2.51	2.51	2.51
	N3	3	3	3	3	3
	σ_3^2	0.003	0.003	0.003	0.003	0.003

Typical error bars involved are ±0.02 Å in R and ±10% in N and σ^2

It is clear from Table 4.1 that the GaOOH sample has bond distances slightly higher than that reported for the AlOOH system which is expected considering Ga^{3+} (0.62 Å) has higher ionic radius than Al^{3+} (0.54 Å). The bond length values of the Eu^{3+} containing samples do not vary much from that prepared without Eu^{3+} and are within the experimental error except for 0.5 at.% Eu^{3+} containing sample which shows a slightly larger deviation. These results establish the fact that the local short range order around Ga^{3+} is unaffected by the incorporation of Eu^{3+} ions in the sample. The results also indicate that Eu^{3+} do not replace

Ga^{3+} because the introduction of a foreign atom with much larger radius (0.95 Å) in the lattice would have been reflected by a decrease in the Ga-O bond distances. The inability of Eu^{3+} replacing Ga^{3+} has also been suggested by a significantly large difference in the solubility products of $Eu(OH)_3$, $Ga(OH)_3$ and GaOOH as reported in [63]. The change in amplitudes of the $\chi(R)$ versus R spectra could only be explained in terms of change in the disorder factor. It has been found that the disorder increases appreciably even with the introduction of a small amount of Eu^{3+} (0.5%) and reaches a maximum for 1 at.% Eu^{3+} doping. This agrees with the fact that even a small amount of lanthanide ion doping disrupts the structure of GaOOH. The hydrogen atoms are indirectly bonded to the Ga atom via an oxygen atom and no change is observed either in their position or coordination. Our EXAFS studies confirm the fact that the local short range order around Ga^{3+} is unaffected, whereas the disorder in the lattice increases with increase in Eu^{3+} content in the sample which is in agreement with our earlier results on vibrational studies of the samples [60]. It has been observed that even with 1 at.% Eu^{3+} doping the IR spectrum of GaOOH undergo considerable changes with disappearance of number of peaks at various frequencies (~385, 526, 2975 and 3250 cm^{-1}) which are characteristics of undoped GaOOH and the spectrum resembling that of amorphous $Ga(OH)_3$. The vibrational studies also reveal systematic appearance of new peaks at ~1490 and 1635 cm^{-1} which can be attributed to the bending vibrations of the OH groups associated with $Ga(OH)_3$ and $Eu(OH)_3$ phases [64]. This further suggests that Eu^{3+} is affecting the lattice structure through the OH linkages existing at the inter layer spacing. Due to the smaller ionic radius of Eu^{3+} compared to GaOOH-inter layer spacing (~2.5 Å) [65], Eu^{3+} ions/species have a tendency to get incorporated at the interlayer and preferentially interact with OH groups to form europium hydroxide species. Formation of such hydroxide species destabilizes the layered structure of GaOOH. Since each Eu^{3+} ions can react with three OH groups, small amounts of Eu^{3+} in GaOOH is sufficient to create significant structural destabilization leading to the formation of finely mixed amorphous $Ga(OH)_3$ and $Eu(OH)_3$. The collapse of GaOOH structure assisted by the Eu^{3+} ions and formation of amorphous phase is schematically shown in Fig. 4.6.

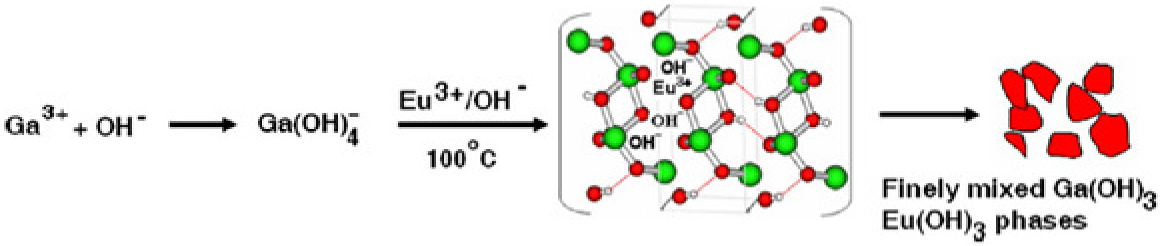

Figure 4.6 Schematics of collapse of Eu doped GaOOH structure.

Conclusions

Based on XRD, EXAFS and vibrational studies it is concluded that the lattice of GaOOH undergoes considerable extent of distortion followed by amorphisation, even when very small amount of Eu^{3+} ions (1 at.% and more) are present during its synthesis. The local short range order around Ga is unaffected by the amorphisation process as confirmed by the EXAFS studies. Incorporation of Eu^{3+} ions (lanthanide ions) at the interlayer spacing of GaOOH and its reaction with structure stabilizing OH groups to form finely mixed amorphous europium and gallium hydroxide is the reason for the collapse of the layered structure.

4.2 Eu doped $SrSnO_3$

Alkaline earth stannates have gained considerable interest recently, due to their luminescence and photo-catalytic properties [66]–[70]**.** Lanthanide ion doping in such materials is an option for making efficient luminescent materials**.** Usually lanthanide ions in the above compounds occupy the alkaline earth metal ion site in the lattice due to their comparable ionic radii. For example, previous studies on Eu^{3+} doped $BaSnO_3$ and $SrSnO_3$ samples [71], [72] indicated that europium ions occupy Ba^{2+}/Sr^{2+} site in the lattice. However, from these studies it is not clear how the local environment around lanthanide ions as well as Ba^{2+}/Sr^{2+} ions get affected due to such doping. Understanding this aspect is quite important for visualizing the overall changes in the host lattice and the luminescent properties of the doped samples/nano-material and Eu^{3+} can be used as a representative lanthanide ion to probe this. Though quite a few studies address the structural aspects of $SrSnO_3$ and lanthanide ions doped $SrSnO_3$, [67], [68] [71]–[73] nature of electronic environment around lanthanide ions (Eu^{3+}) in the lattice and its variation with doping concentration is not known. In the present study, we address this problem by preparing a series of $Sr_{1-x}Eu_xSnO_3$ (x = 0, 0.01, 0.02, 0.03, 0.04) samples and characterizing them by XRD, luminescence and Sr K-edge (16105 eV) EXAFS techniques.

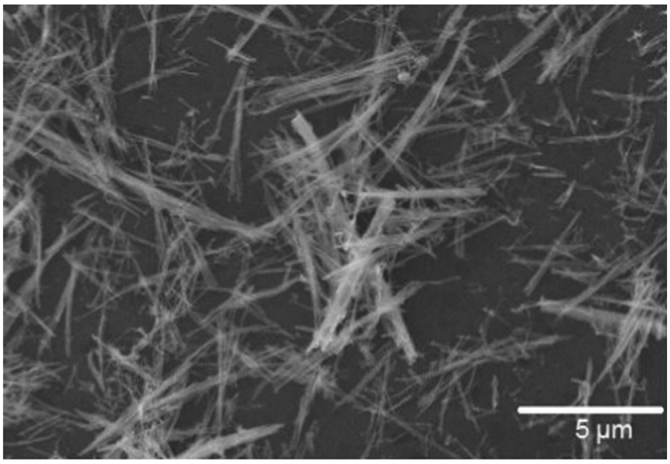

Figure 4.7 SEM image of 1 at % Eu^{3+} doped $SrSnO_3$ sample.

Samples for the present study were prepared by the reaction of sodium stannate and $SrCl_2$ in aqueous solution in presence of required amounts of Eu^{3+} ions. The precipitate obtained at room temperature was heated at 900°C to get $SrSnO_3$ samples doped with different amounts of Eu^{3+} ions. Representative SEM image of 1 at % Eu^{3+} doped sample is shown in Fig. 4.7. The image consists of rods having length around 5-10 μm and diameter in the range of 100-300 nm. Energy Dispersive X-ray (EDX) analysis carried out for the samples has confirmed that relative concentration of lanthanide ions and Sr^{2+} are in good agreement with the initial amounts taken prior to the reaction.

Fig. 4.8 shows the Rietveld refined XRD patterns of $SrSnO_3$ samples containing different amounts of Eu^{3+} ions and Table 4.2 gives the Sr-O and Sn-O bond lengths. All the patterns are characteristic of body centered tetragonal structure of $SrSnO_3$ phase. For samples containing more than 2 at % Eu^{3+} ions, additional diffraction peaks characteristic of $Eu_2Sn_2O_7$ phase started appearing as can be seen from Fig. 4.8. The lattice parameters obtained from the refinement of the diffraction patterns are found to remain unchanged (within experimental errors) with variation in the Eu^{3+} concentration in the lattice. As above 2 at% doping leads to phase separation, all the remaining studies were mainly carried out with samples containing only up to 2 at% Eu^{3+} ions. To confirm the incorporation of Eu^{3+} at Sr^{2+} site in the lattice and subsequent changes in the electronic environment around Eu^{3+} ions, detailed luminescence studies have been carried out and are described below.

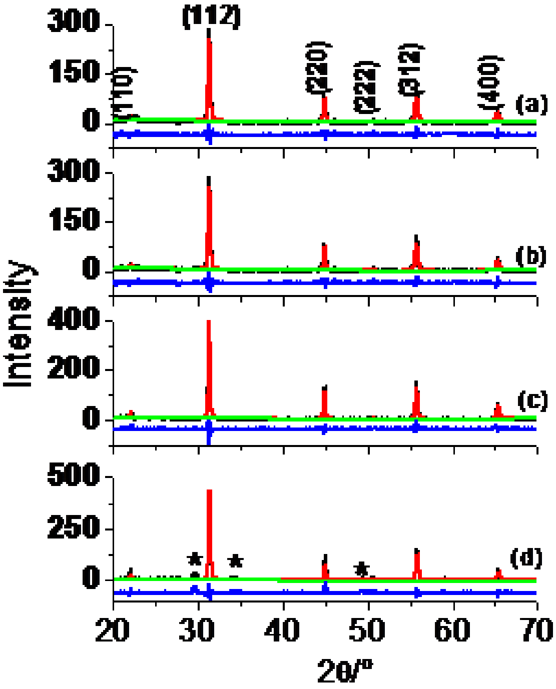

Figure 4.8 XRD patterns of $SrSnO_3$ samples containing (a) 0 at% (b) 1at% (c) 2 at% and (d) 4 at% of Eu^{3+} ions.

Table 4.2 Average bond length values of Sr-O and Sn-O linkages in $SrSnO_3$ samples containing different amounts of Eu^{3+} ions as obtained from XRD measurements.

Sample	Sr-O (Å)	Sn-O (Å)
$SrSnO_3$	2.871 ± 0.001	2.038 ± 0.002
$SrSnO_3$:Eu(1%)	2.883 ± 0.005	2.059 ± 0.006
$SrSnO_3$:Eu(2%)	2.891± 0.001	2.052 ± 0.003

Fig. 4.9 shows the emission spectra of $SrSnO_3$ nano-rods containing different amounts of Eu^{3+} ions. For $SrSnO_3$ sample containing 0.5 at % Eu^{3+} ions, the emission spectrum mainly consists of a sharp peak around 590 nm along with a very weak peak around 612 nm. The peak around 590 nm is characteristic of $^5D_0 \rightarrow {}^7F_1$ transition and that around 612 nm is characteristic of $^5D_0 \rightarrow {}^7F_2$ transition of Eu^{3+} ions. The relative intensity ratio of $^5D_0 \rightarrow {}^7F_2$ to $^5D_0 \rightarrow {}^7F_1$ transition, known as the asymmetric ratio of luminescence, is a measure of the symmetry of the local environment around Eu^{3+} ions in the lattice. Smaller the asymmetric ratio more symmetric is the environment around Eu^{3+} ions.

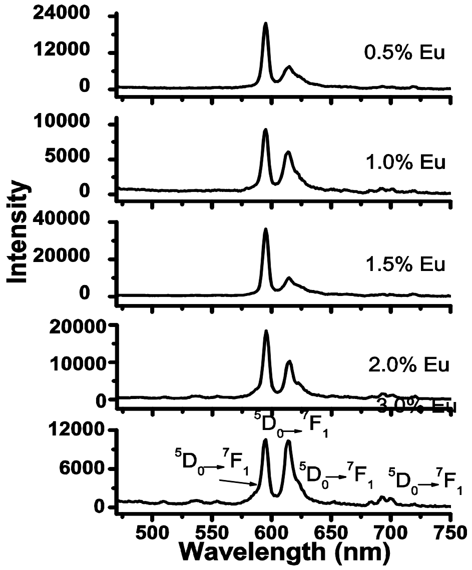

Figure 4.9 Emission spectra of $SrSnO_3$ nano-rods containing different amounts of Eu^{3+} ions.

The values of the asymmetric ratio fall in the range of 0.3 to 0.4 for samples containing up to 2 atom% Eu^{3+} ions. Appearance of intense emission peak around 590 nm in the emission spectra of the samples containing up to 2 at % Eu^{3+} ions substantiates the fact that, Eu^{3+} ions have a centro-symmetric environment. In the centro-symmetric environment, only the magnetic dipole transition ($^5D_0 \rightarrow {}^7F_1$) is allowed and the electric dipole transition ($^5D_0 \rightarrow {}^7F_2$) is forbidden. For sample containing 3 at % Eu^{3+} ions, asymmetric ratio is found to increase to a va1ue of 1.3, suggesting that Eu^{3+} ions are having significantly distorted environment. Possible reason for this could be the formation of a secondary phase containing Eu^{3+} ions. Hence from the emission spectrum, it is confirmed that for 3 and more than 3 at % Eu^{3+} incorporation, Eu^{3+} ions exist in more than one environment. These inferences are also supported by the XRD results reported above for these samples. Further it is also inferred from the luminescence studies that, Eu^{3+} ions are getting incorporated at Sr^{2+} site in the $SrSnO_3$ lattice up to 2 at%. Incorporation of Eu^{3+} ions at Sr^{2+} site is expected to have significant changes in the electronic nature of Sr-O/Eu-O bonds in the lattice.

To further check the effect of Eu^{3+} doping on Sr-O bonds lengths, Sr K-edge EXAFS studies were carried out on the samples at the Energy Dispersive EXAFS beamline (BL-08) described in *Chapter-2*. EXAFS spectrum of a commercial Y_2O_3 powder pellet has been used for calibration of the CCD channels in this case. Under the same setting of goniometer, both Sr and Y edges appeared at CCD channel nos. 588 and 1579 respectively and assuming the reported values of Sr K-Edge of 16105 eV and Y K-edge of 17038 eV, the CCD channels were calibrated in energy scale. Fig. 4.10 shows the experimental EXAFS ($k\chi(k)$ *vs* k) spectra of $SrSnO_3$ samples doped with varying concentrations of Eu^{3+} ions.

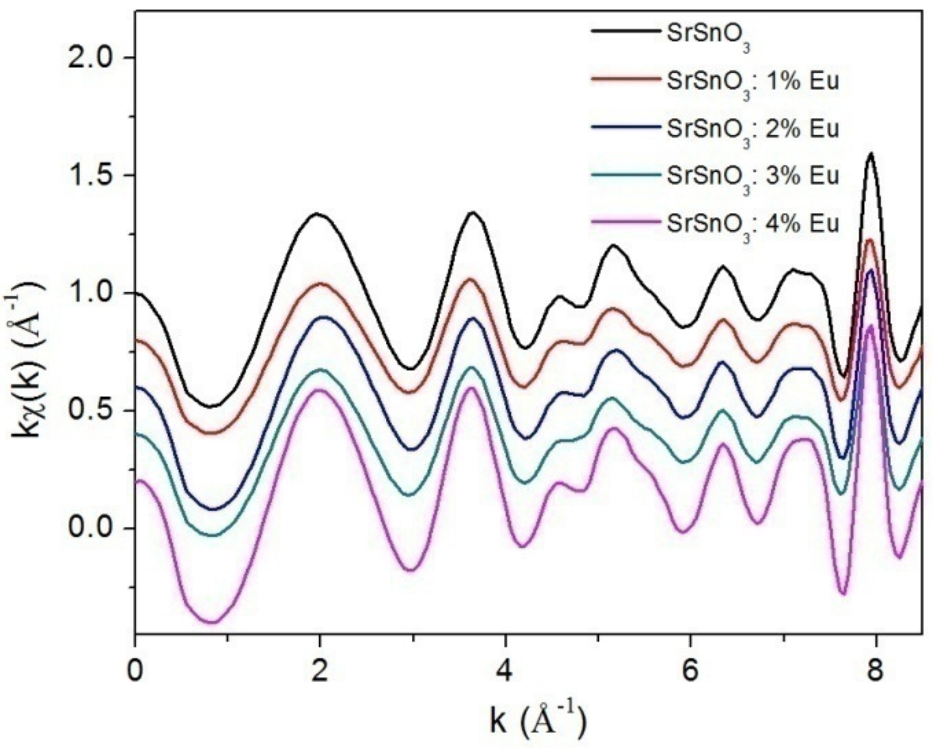

Figure 4.10 Experimental EXAFS spectra (*kχ(k) vs k)* of $SrSnO_3$ samples.

Further, the experimental $\chi(R)$ versus R spectra of the above $SrSnO_3$ samples doped with Eu^{3+} ions are fitted with theoretically generated spectra following the methodology described in *Chapter-2*. There exists some ambiguity in the literature regarding the structure of $SrSnO_3$. Glerup *et al.* [74] have reported that $SrSnO_3$ exhibits structural transition from space group *Pmcn* at 573 K to *Incn* at 973 K and then finally to *I4/mcm* at 1173 K. Mountstevens *et al.* [75] have reported a similar transition in the material when heated, progressing from room temperature *Pnma* cell to *Imma* at 905 K, to *I4/mcm* at 1062 K and finally to *Pm3m* at 1295 K [73], [75]**.** In a recent XRD study it was inferred that $SrSnO_3$ samples doped with Eu^{3+} ions, obtained by heating the precursor material at 1173 K, have a crystal structure that corresponds to *I4/mcm* space group [72]**.** However, another report claims that the XRD patterns for $SrSnO_3$ and its Er doped derivatives, which were also annealed upto 1173 K during preparation methods, match with the orthorhombically distorted perovskite structure having the space group *Pbnm* [76]**.** So it was only rational to investigate the two possibilities

(*Pbnm* and *I4/mcm*) and to determine the appropriate structure for modeling. In the present case, better fitting of the EXAFS data (lower χ^2 values) were obtained with the former space group (*I4/mcm*) which is in accordance with our earlier investigation by XRD measurements [72].

For fitting of EXAFS spectra of the samples, the structural data obtained from the Reitvield fitting of the X-ray diffraction data of undoped $SrSnO_3$, as described above, have been taken as the starting values. Based on the position coordinates obtained from the Rietveld refinement, the SrO_{12} and SnO_6 polyhedra are constructed and schematic diagrams of SrO_{12} and SnO_6 polyhedra from undoped $SrSnO_3$ sample is shown in Figs. 4.11(a) and (b).

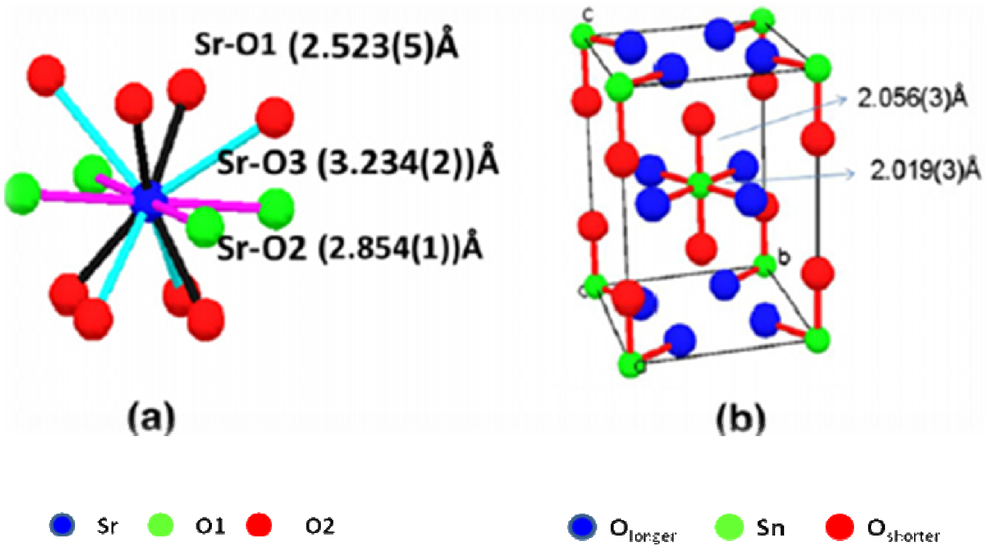

Figure 4.11 Schematic diagrams of (a) SrO_{12} and (b) SnO_6 polyhedra from undoped $SrSnO_3$.

The SrO_{12} polyhedron can be considered to consist of a central Sr atom with 4 oxygen atoms on a plane and 4 oxygen atoms each above and below the plane as can be seen from Fig. 4.11(a). The four atoms in the plane are equidistant from the central strontium atom. Unlike this the four atoms above and below are at different distances from the central Sr atom. Thus there exists three different Sr-O distances in the SrO_{12} polyhedron. The four Sr-O bonds, (shown as magenta colour in Fig. 4.11(a) and denoted as Sr-O2) are in a plane with Sr-O distance 2.854(1) Å. Among the remaining eight Sr-O bonds, four of them (black lines, indicated as Sr-O1 with Sr-O distance 2.523(5)Å) are shorter than Sr-O2 bonds and the remaining four (denoted as cyan colour) with Sr-O bond length 3.234(2) Å are longer than Sr-O2 bonds. The SnO_6 polyhedron, on the other hand, is characterized by four equidistant oxygen atoms (denoted as blue colour with Sn-O distance 2.019(3) Å) in the equatorial plane containing Sn atom and 2 oxygen atoms, one each above and below the plane (denoted as red colour with Sn-O distance 2.056(3)Å, as can be seen from Fig. 4.11(a).

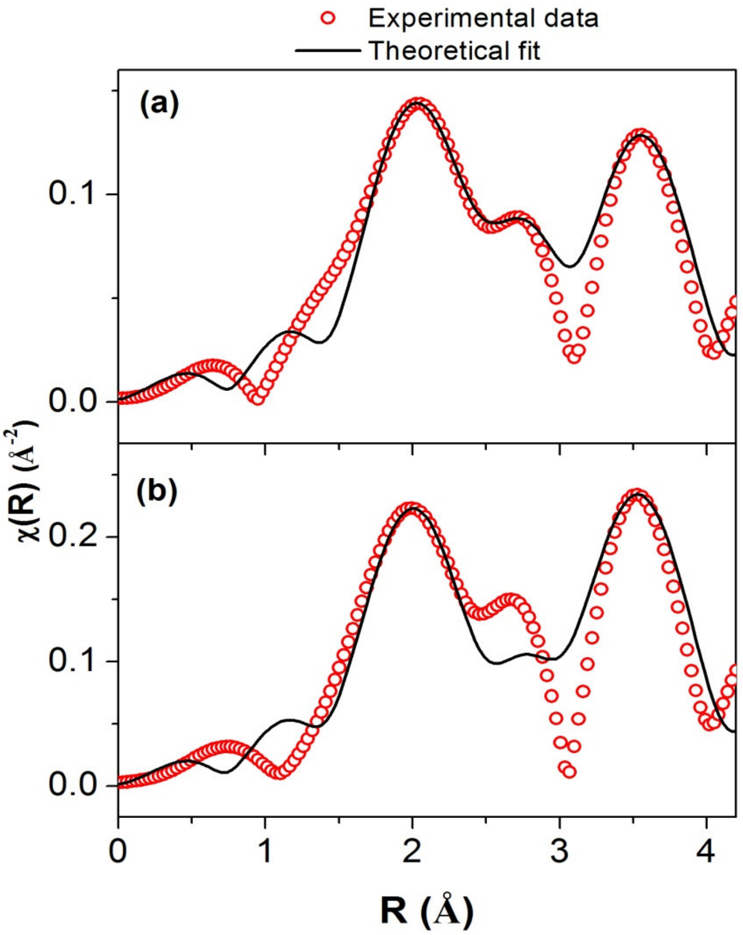

Figure 4.12 Experimental and theoretical $\chi(R)$ *vs* R spectra for $SrSnO_3$ nano-rods containing (a) 1 at% and (b) 2 at% Eu^{3+} ions.

The experimental data has been fitted in R space over the range of 1- 4 Å and the best-fit theoretical $\chi(R)$ versus R spectra have been shown in Fig. 4.12 along with the experimental data. The first peak at around 2 Å with another poorly resolved peak at ~ 2.5 Å correspond to the Sr-O shell with an oxygen coordination of 12, which itself comprises of three single scattering paths due to three distinct oxygen shells at different distances as mentioned above. The second distinct peak displayed in the experimental spectrum at ~ 3.5 Å is a consequence of the cationic (Sr-Sn) shell with a coordination of eight Sn atoms as scatterer.

Table 4.3 The different Sr-O bond lengths obtained from Sr K edge EXAFS studies on $SrSnO_3$ nano rods doped with europium ions.

Sample	Sr-O1 (Å)	Sr-O2 (Å)	Sr-O3 (Å)	Average Sr-O (Å)
$SrSnO_3$	2.59	2.91	3.27	2.923
$SrSnO_3$: Eu (1%)	2.61	2.91	3.29	2.936
$SrSnO_3$: Eu (2%)	2.61	2.91	3.28	2.933
σ^2 (Å^2)	0.003	0.001	0.001	0.002

Typical error bars involved are ±0.02 Å in R and ±10% in σ^2.

The best fit values of the bond distances (R), co-ordination numbers N) and disorder (Debye-Waller) factors (σ^2), which give the mean-square fluctuations in the distances, have been summarized in Table 4.3. The bond distances of the undoped $SrSnO_3$ sample as obtained from EXAFS analysis, are found to be in agreement (within experimental errors) with the values obtained from Rietveld analysis reported earlier [72]. From the three Sr-O bond distances for each $SrSnO_3$ sample (shown in Table 4.3), the average Sr-O bond distances have been calculated which are found to be higher for Eu^{3+} containing samples compared to the undoped $SrSnO_3$. The increase in bond length can be described in terms of the substitution of a larger cation (Sr^{2+}) by a smaller one (Eu^{3+}). The Eu^{3+} being smaller (higher charge to radius ratio (z/r) as well as higher cationic field strength compared to Sr^{2+}), attract the oxygen atoms closer towards it, shortening the Eu-O bond and stretching the Sr-O bond. As there exists Sr-O-Sn linkages in the lattice, Sn-O bond length is also expected to increase with incorporation of Eu^{3+} at Sr^{2+} site. The observed increase in average Sr-O and Sn-O bond lengths shown in Table 4.2 and Table 4.3 supports this. The Sr-Sn bond length and coordination number around Sr atoms remained same within experimental errors for different Eu^{3+} concentrations.

Conclusions

From the steady state luminescence, it is confirmed that Eu^{3+} ions occupy more than one type of environment for ≥3 at.% Eu^{3+} doped samples. The polarizability or the covalent character of Eu-O bonds is less when it occupies only Sr^{2+} site in the lattice. Based on Sr K-edge EXAFS studies, supplemented by XRD measurements, it is confirmed that, average Sr-O and Sn-O bond lengths in SrO_{12} and SnO_6 polyhedra are higher in Eu^{3+} doped sample compared to undoped one and this has been explained based on the higher charge to radius ratio of Eu^{3+} compared to Sr^{2+}. Thus the above studies clearly establish that for doping concentration < 3%, Eu goes to Sr sites leading to a symmetric environment that gives rise to sharp $^5D_0 \rightarrow {}^7F_1$ transition in the luminescence spectra.

4.3 $CaWO_4$

$CaWO_4$ belongs to the family of alkaline earth tungstates having scheelite structure. Compounds of this family exhibit interesting characteristics like excitonic luminescence, thermo luminescence, electro-optical behaviour etc. [77]–[81] $CaWO_4$ is also a very promising material for applications based on scintillation phenomenon due to its very high light output [82], [83]**.** However, this light output is a strong function of the quality or nature of the samples as well as the synthesis conditions. In most of the luminescence studies involving $CaWO_4$, a blue emission around 420 nm and a weak green emission that strongly overlaps with the blue emission are observed. Based on time resolved spectroscopy, Leonelli and Brebner [84], [85] have confirmed that visible emission from such materials arises due to recombination of self trapped excitons. It is now generally accepted that the blue emission in $CaWO_4$ is a consequence of the recombination of self trapped excitons associated with WO_4^{2-} species in the lattice and weak green emission is due to defect levels present in the optical gap of $CaWO_4$ [84], [86], [87]**.** Campos *et al.* [88] have carried out detailed studies on the luminescent properties of both crystalline and amorphous $CaWO_4$ and $CaMoO_4$ powders. These authors have suggested that in the case of amorphous $CaWO_4$ or $CaMoO_4$, emission is due to the presence of localized bands in the optical gap. Such bands arise due to oxygen vacancy complexes of type $[MO_3 \cdot V_O^x]$, $[MO_3 \cdot V_O^\bullet]$ and $[MO_3 \cdot V_O^{\bullet\bullet}]$ (where M is Mo or W and V_O^x, $V_O^\bullet$, $V_O^{\bullet\bullet}$ represent oxygen vacancy with neutral, singly positive and doubly positive charges respectively). Unlike this, in the case of crystalline material, emission occurs due to slight distortion of WO_4 or MoO_4 tetrahedra. In another study, Hu *et al.* [89] prepared $Ca_{(1-x)}Zn_xWO_4$ nanocrystals at room temperature based on solution chemistry and characterized their structural and optical properties. It was observed that the isovalent substitution of Ca^{2+} by Zn^{2+} in $CaWO_4$ lattice leads to quenching of intrinsic blue emission. This has been explained based on the shorter Zn-O distance compared to Ca-O distance leading to lattice contraction and associated constraints in the generation of self trapped excitonic states (STEs). Emission due to defects observed along with the blue emission from $CaWO_4$ crystals has been found to be very sensitive to annealing temperatures and the atmospheres under which the annealing is carried out. [90] Thongtem *et al.* [91] prepared nano-crystalline $CaWO_4$ and $SrWO_4$ by microwave method using CTAB as stabilizing ligand. It was reported that, luminescence intensity increases with increase in ligand concentration in the synthesis medium. However, reason for improved luminescence with increase in ligand concentration is not clearly understood. Li *et al.* [92] observed an improved symmetry in terms of c/a ratio of the tetragonal unit cell of $CaWO_4$ by reducing size of the $CaWO_4$ nanoparticles to less than

5 nm. These authors have also observed that luminescence intensity decreases with decrease in particle size. Quantum confinement effects in the excitation spectrum corresponding to $^1A_1 \rightarrow {}^1T_1$ transition of W^{6+} ions has been reported for $CaWO_4$ nanoparticles by Su *et al.* [93]. In the present study, $CaWO_4$ particles having different average crystallite sizes have been investigated for their structural aspects using XRD, W L_1 edge XANES and W L_3 edge EXAFS techniques with a view to understand the effect of WO_4 structural units on the luminescence characteristics of $CaWO_4$ particles. Here, we have studied undoped $CaWO_4$ particles prepared at room temperature and subjected to different annealing temperatures.

For the synthesis of $CaWO_4$ particles, $Ca(NO_3)_2.4H_2O$ and $Na_2WO_4.2H_2O$ were used as starting materials. Around 0.5 g $Ca(NO_3)_2.4H_2O$ was dissolved in 20 ml of ethylene glycol while stirring. To this solution, 0.8 g of $Na_2WO_4.2H_2O$ was added and stirring was continued for two hours. A white precipitate was formed which was separated by centrifugation and then washed with methanol and acetone to remove un-reacted species. The samples thus obtained were dried overnight under ambient conditions. These samples were divided into five parts and heated at different temperatures in air for 5 hours each.

The lattice parameters, relevant bond angles and bong lengths were obtained from Rietveld refinement of the XRD patterns. Fig. 4.13 shows the Rietveld refined XRD patterns of $CaWO_4$ samples, as-prepared and heat-treated at different temperatures. The average crystallite size calculated from the linewidth of the diffraction patterns is shown in Table 4.4. All the diffraction patterns are characteristic of tetragonal structure of $CaWO_4$. For the as-prepared sample, lattice parameters are found to be a = b = 5.230(1) Å and c = 11.392(7) Å with c/a ratio of 2.178 (Table 4.4). With increase in heat treatment temperature to 300°C, c/a ratio slightly decreases (c/a=2.168) indicating an increase in the order in the lattice (c/a = 2.0 for ideal tetragonal lattice).

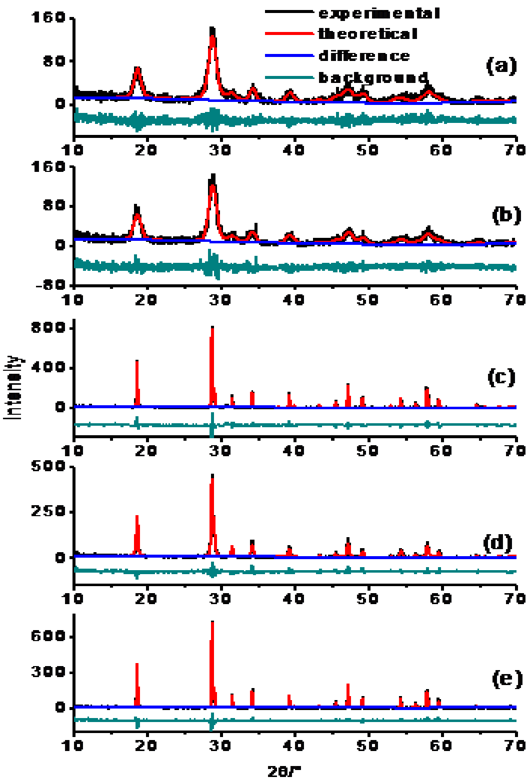

Figure 4.13 Rietveld Refined XRD patterns of $CaWO_4$ samples: (a) as prepared in ethylene glycol. The samples heated at 300, 500, 700 and 900°C are shown in Fig. 1(b-e) respectively.

Table 4.4 Crystallite size and c/a ratio in the samples as obtained from XRD measurements.

Sample	Average crystallite size (nm)	c/a ratio
$CaWO_4$ as prepared in ethylene glycol	7	2.178
$CaWO_4$ annealed at 300 ºC	8	2.168
$CaWO_4$ annealed at 500 ºC	26	2.170
$CaWO_4$ annealed at 700 ºC	90	2.169
$CaWO_4$ annealed at 900 ºC	99	2.171

On further increase in heat treatment temperature, c/a ratio remains the same (Table 4.4). The as-prepared $CaWO_4$ sample is found to have crystallite size in the range of 5-10 nm and the average crystallite size is found to be the same for both as-prepared and 300°C heat-treated sample, whereas for samples heat-treated above 300°C crystallite size increases as can be seen from Table 4.4. Fig. 4.14(a) shows the emission spectrum obtained after 250 nm excitation from the as-prepared $CaWO_4$ nanoparticles along with from those heat-treated at different temperatures, namely 300°C, 500°C, 700°C and 900°C. For the as-prepared sample, emission spectrum is found to have very poor signal to noise ratio with a peak maximum around 420 nm. The emission from $CaWO_4$ around 420 nm has been thoroughly investigated by different groups. [83]–[85], [87] Based on those extensive investigations, it is inferred that the peak at 420 nm arises due to the electronic transition $^3T_2 \rightarrow {}^1A_1$ of W^{6+} ions in WO_4 tetrahedron. To our surprise, it is observed that line widths and peak maxima of the emission spectra of the samples heat-treated at different temperatures are identical to that of the as-prepared sample, except that signal to noise ratio increases with increase in heat treatment temperatures.

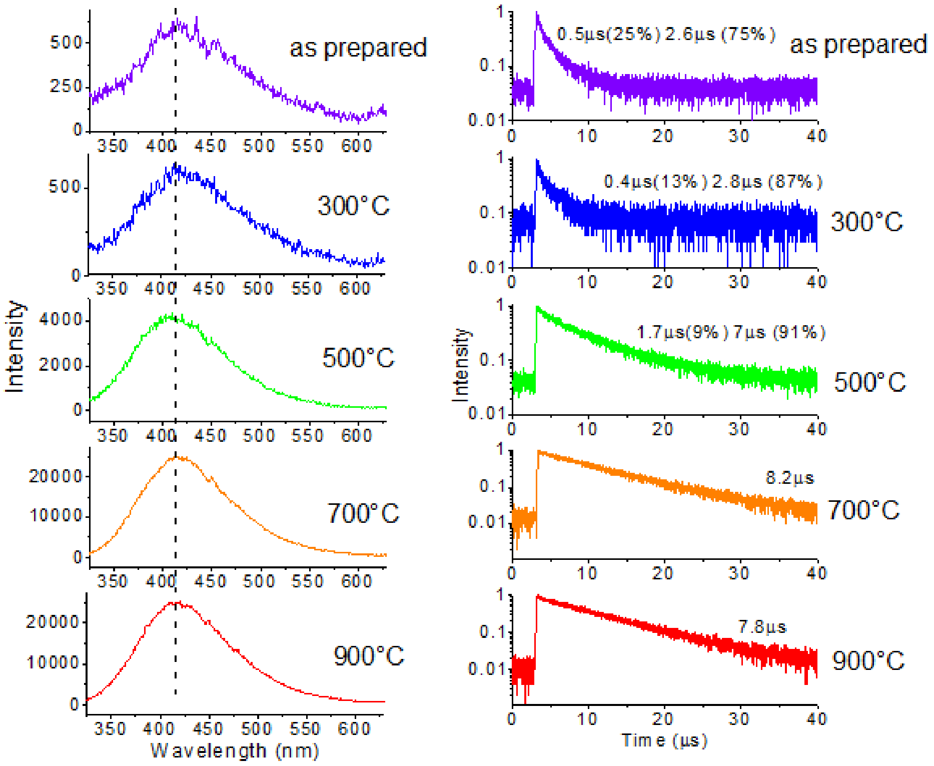

(a) (b)

Figure 4.14 Emission spectra (a) from $CaWO_4$ nanoparticles as prepared and annealed at different temperatures. Corresponding decay curves are shown in Fig. 4.14(b). Samples were excited at 250 nm and emission was monitored at 420 nm.

To get further insight regarding the nature of luminescent species existing in the samples, the decay curves corresponding to the blue emission from the samples were recorded and are shown in Fig. 4.14(b). For the as-prepared sample, the decay is found to be multi-exponential with an average lifetime value of 2.08μs. This is because WO_4^{2-} species feels a variety of environments in the nanoparticles due to the large surface to volume ratio. The situation is same in the case of the 300°C heat-treated sample. However for sample heat-treated at 500°C and above, decay curves are nearly single exponential type with higher average lifetime values. The lifetime values are found to be 6.5μs, 8.2 μs and 7.8μs for 500, 700 and 900°C heated samples respectively. In other words, the values remained nearly same with increase in heat treatment temperatures above 500°C. Increased lifetime values for the sample heated at 500°C and above can be attributed to the increase in the particle size and lack of distribution in the environment around WO_4^{2-} species compared to the nanoparticles.

To get insight into the origin of increased lifetime for samples heated above 300°C, further structural investigations were carried out on the samples by W-L_1 edge XANES and W-L3 edge EXAFS measurements. The measurements have been carried out at the Energy Scanning Beamline (BL-09) at INDUS-2 SRS in transmission mode, which has been described in *Chapter 2.*

To identify the chemical state of W atom in $CaWO_4$ samples, XANES measurements were performed at W L_1 edge (12100 eV) as shown in Fig. 4.15(a). The presence of the pre-edge peak of considerable intensity in all the samples, which is a characteristic of tetrahedral coordination, confirms that W in all the $CaWO_4$ samples exists as WO_4 tetrahedra. The EXAFS spectra of the as-prepared and the heat treated samples measured at room temperature at W L_3- edge are shown in fig. 4.15(b).

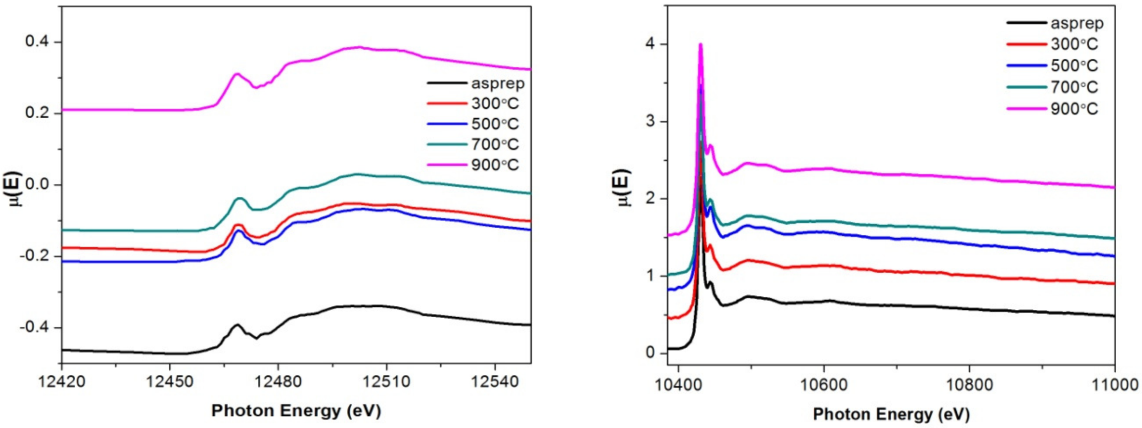

(a) (b)

Figure 4.15 XANES spectra (a) for $CaWO_4$ samples at W L1-edge ($\mu(E)$ *vs* E)
(b) Corresponding EXAFS spectra for the samples ($\mu(E)$ *vs* E) recorded at W L3-edge.

In the present study theoretical modelling for the samples has been carried out assuming tetragonal structure of $CaWO_4$ with lattice parameters a = b = 5.243 Å and c = 11.376 Å**.** The WO_4 and CaO_8 polyhedron are shown schematically in Fig. 4.16.

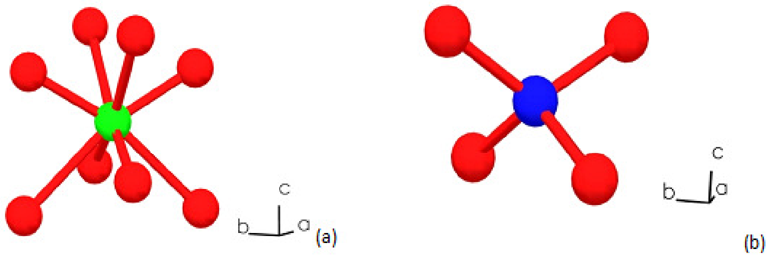

Figure 4.16 CaO8 polyhedron (a) and WO_4 tetrahedron (b) present in as prepared $CaWO_4$ nanoparticles. Colour codes: Green spheres represent Ca, blue spheres represent W and red spheres represent oxygen atoms.

Fig. 4.17 shows the best fit theoretical spectra along with the experimental $\chi(R)$ versus R data of the $CaWO_4$ samples. The bond distances, co-ordination numbers (including scattering amplitudes) and disorder (Debye-Waller) factors (σ^2), which give the mean-square fluctuations in the distances, for the W-O nearest neighbor shell of the WO_4 tetrahedra have been used as fitting parameters and the fitting has been performed in the R range of 0.9 - 2 Å as discussed above. The best fit parameters obtained are presented in Table 4.5 and Fig. 4.18

(a), (b) and (c). It can be seen from Table 4.5 that the W-O bond length remains almost same with increase in annealing temperature, except for the 300°C annealed samples where the bond length decreases slightly. However, the oxygen coordination number decreases gradually in the samples with increase in annealing temperatures as evident from Fig. 4.18(b) and Table 4.5, implying an increase in oxygen vacancies in the system with an increase in heat treatment temperature.

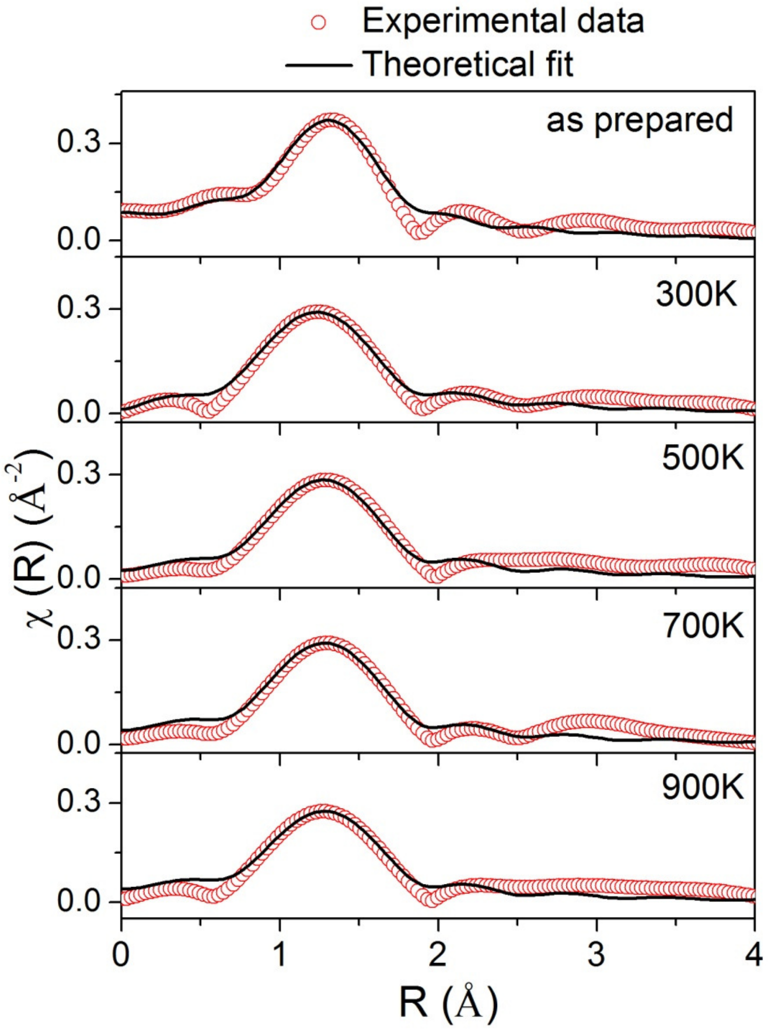

Figure 4.17 Experimental $\chi(R)$ versus R spectra of $CaWO_4$ samples along with the best fit.

As expected the disorder factor, decreases gradually with increase in annealing temperature which shows that the static disorder in the system is reduced with increase in annealing temperature. As has been discussed above, emission in $CaWO_4$ is attributed by various authors to localized bands arising due to oxygen vacancy complexes or distorted WO_4 tetrahedra. Here we have found from the WL1 XANES measurements that the pre-edge intensity does not change with annealing temperature, which shows that the WO_4 polyhedra does not get distorted. Thus the decrease in oxygen coordination or increase in oxygen vacancies as observed above from W L3 edge EXAFS measurements is found to be responsible for the increase in luminescence intensity in the samples with increase in annealing temperature.

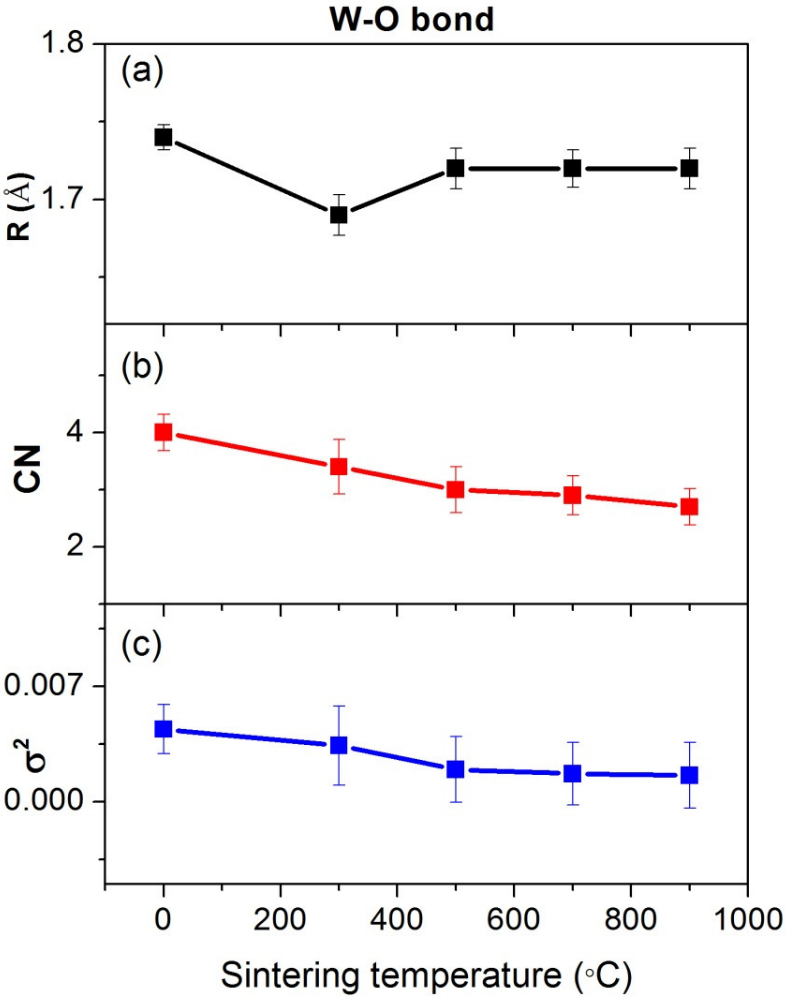

Figure 4.18 Variation of (a) W-O bond lengths (R), (b) nearest neighbour oxygen coordination (CN) and (c) W-O bond disorder factor of $CaWO_4$ samples annealed at different temperatures.

Table 4.5 Best fit parameters for $CaWO_4$ samples at W L3 edge.

	$CaWO_4$ as prepared in ethylene glycol	$CaWO_4$ annealed at 300ºC	$CaWO_4$ annealed at 500ºC	$CaWO_4$ annealed at 700ºC	$CaWO_4$ annealed at 900ºC
R (1.78 Å)	1.74	1.69	1.72	1.72	1.72
CN (4)	4	3.4	3	2.9	2.7
σ^2	0.004	0.003	0.002	0.002	0.002
R-factor	0.02	0.05	0.04	0.03	0.04

Typical error bars involved are ±0.02 Å in R and ±10% in CN and σ^2

Conclusions

$CaWO_4$ nanoparticles having size in the range of 5-10 nm have been synthesized at room temperature and heat treated at different temperatures viz., 300°C, 500°C, 700°C and 900°C . Based on XRD, W L_1 edge XANES and W L_3 edge EXAFS studies it is concluded that WO_4 tetrahedra in the samples remain unaffected by annealing. Further with increase in annealing temperatures, there is decrease in oxygen coordination surrounding W atoms, resulting in creation of oxygen vacancies in the lattice and this is responsible for the increase in luminescence intensity and associated increase in the lifetime values.

Chapter 5

EXAFS MEASUREMENTS ON MAGNETIC MATERIALS

(Transition Metal doped Dilute Magnetic semiconductors)

It has been more than a decade since Dietl *et al.* [94] proposed that 5 at.% Mn doped ZnO could exhibit room temperature (RT) ferromagnetism (FM) following which Sato and Katayama-Yoshida [95] employed local density approximation method to theoretically demonstrate that ZnO doped with transition metals like Fe, Co and Ni would show ferromagnetic ordering whereas Mn doped ZnO would manifest a stable antiferromagnetic state. Ever since transition metal doped ZnO has garnered a tremendous interest in the scientific community. These magnetic materials are called dilute magnetic semiconductors (DMSs) and can be fabricated by replacing a fraction of the parent cation by a 3d transition metal (TM) cation. Such tailor-made material which combines the characteristics of a semiconductor with tunable magnetic properties would generate a new genre of devices that would be indispensable to modern technology. Specifically the DMSs have potential application in spin-electronic devices [96], [97] operating at ambient conditions, provided their Curie temperature T_c is well above RT and hence it is necessary to understand the basis of the magnetism in order to design viable devices.

Thus there exists a substantial number of reports regarding the origin and value of the room temperature ferromagnetism (RTFM) in a variety of DMSs mainly focusing on TM ion (Ni^{2+}, Co^{2+}, Fe^{2+}, Mn^{2+} etc.) doping though ZnO has emerged out to be the most feasible for practical applications [98]–[102]**.** However, the reported results pertaining to the magnetic behavior (T_c, magnetic moment etc.) of these DMSs vary greatly ranging from RTFM to no magnetic ordering at all. A number of diverse theories have been put forward to explain the source of FM in these DMSs. The theoretical model of Dietl *et al.* [94] suggests that magnetic cations, which act as ionized acceptors in the semiconductor lattice, introduce holes in the valence band of the semiconductor, which in turn mediate FM exchange interaction between the magnetic cations giving rise to FM in p-type semiconductors. Coey *et al.* [98] explained FM in intrinsically n-type semiconductors and insulators by a model where shallow donor electrons, created due to intrinsic defects in the semiconductors, form bound magnetic polarons (BMPs) with magnetic cations, which finally gives rise to the FM interaction. Both of these theories suggest that FM arises due to uniform doping of the TM ions in the host and their interaction with the charge carriers generated due to extrinsic or intrinsic defects [103], [104]**.** However, there are still uncertainties, particularly in case of TM doped ZnO whether FM arises due to uniformly distributed TM cations in the semiconductor lattice or due to precipitation of metallic clusters in an otherwise homogeneous ZnO host matrix or presence of an entirely separate magnetic phase [105], [106]**.** To add to the confusion, several authors [99]–[101], [107] have proposed that the origin of FM in DMSs might be a consequence of targeted chemical perturbations facilitated by organic capping molecules present during the synthesis of ZnO nanocrystals through wet chemical route that may give rise to defects such as oxygen and/or Zn vacancies or Zn interstitials. Garcia *et al.* [102] argue that capping nanocrystals with organic molecules alters their electronic configuration and yields long range FM ordering in ZnO nanocrystals in absence of any kind of defects. Thus origin of FM in TM doped ZnO is still a fairly unresolved question and further experimental and theoretical studies are required particularly to explore the local environment around the host and the dopant cations carefully to obtain unambiguous results regarding the origin of FM in these systems.

In the present study, we put forward a systematic local structure investigation of Co and Mn doped ZnO nanocrystals (NCs) by synchrotron-based Extended X-ray Absorption Fine Structure (EXAFS) measurements at both Zn K edge and dopant (Co, Mn) K edges. Generally most of the other studies on these systems have been carried out on nanocrystals grown by conventional wet chemical route or sol-gel route. However, recently it has been shown that an alternative microwave-assisted non-aqueous route of synthesis can provide higher doping of TM ions in the nanocrystals [106], [108]**.** Hence the measurements have been carried out on samples prepared by three different methods, viz., high temperature wet chemical method, sol-gel route and the microwave-assisted method. The EXAFS results presented here have also been supported by the results of X-Ray Diffraction (XRD) measurements, optical absorption studies and magnetic measurements on the samples and are also confirmed by first principle calculations

In the wet chemical method, doped ZnO NCs were grown by thermal decomposition of zinc acetate [$(CH_3CO_2)_2Zn$]. Zinc acetate and cobalt(II) acetate tetrahydrate [$(CH_3CO_2)_2Co.4H_2O$] for Co^{2+}-doped samples and zinc acetate and manganese acetate tetrahydrate [$(CH_3CO_2)_2Mn.4H_2O$] for Mn^{2+}-doped samples are used as precursors in the mixture of HDA ($C_{16}H_{33}NH_2$) and TBPA [$C_4H_9PO(OH)_2$] at high temperatures (300°C). Nanocrystals were separated by centrifugation and washed several times with hexane and collected in the form of free-flowing powder ZnO samples with 7, 10 and 15 at% Co doping have been prepared by the above method. $Zn_{1-x}Co_xO$ ($0\leq x \leq0.04$) samples (named as Co0, Co0.5, Co1, Co1.5, Co2, and Co4 for Co concentration x = 0, 0.005, 0.01, 0.015, 0.02, and 0.04 respectively) were also synthesized by the sol-gel method. Appropriate proportions of analytical grade metal nitrates $Zn(NO_3)_2.6H_2O$ (99.9% purity) and $Co(NO_3)_2.4H_2O$ (99.9% purity) powders were thoroughly mixed and dissolved in aqueous solution of citric acid [$C_6H_8O_7$] (99.5% purity) while stirring to obtain a homogeneous precursor solution. Citric acid serves as fuel for the reaction. The precursor solution was dried at 80˚C for 3h to obtain xerogel and the swelled xerogel was kept at 130˚C for 12 h to complete it. The simplified exothermic reaction can be expressed as:

$$M(NO_3)_2 + C_6H_8O_7 + 4O_2 \rightarrow MO + 2NO_2 + 6CO_2 + 4H_2O; (M = Zn, Co).$$

After grinding, the xerogel powders were sintered at 600˚C for 10 h under air to obtain $Zn_{1-x}Co_xO$ nanoparticles.

Table 5.1 Description of Co and Mn doped ZnO samples.

Sl. No.	Sample name	Description	Method of preparation EXAFS measurements
1.	Co 7MW	ZnO NCs doped with Co 7%	Microwave method
2.	Co 10MW	ZnO NCs doped with Co 10%	Microwave method
3.	Co 15MW	ZnO NCs doped with Co 15 %	Microwave method
4.	Co 7WC	ZnO NCs doped with Co 7%	High temperature wet chemical method
5.	Co 10WC	ZnO NCs doped with Co 10%	High temperature wet chemical method
6.	Co 15WC	ZnO NCs doped with Co 15 %	High temperature wet chemical method
7.	Mn 7MW	ZnO NCs doped with Mn 7%	Microwave method
8.	Mn 10MW	ZnO NCs doped with Mn 10%	Microwave method
9.	Mn 15MW	ZnO NCs doped with Mn 15 %	Microwave method
10.	Mn 7WC	ZnO NCs doped with Mn 7%	High temperature wet chemical method
11.	Mn 10WC	ZnO NCs doped with Mn 10%	High temperature wet chemical method
12.	Mn 15WC	ZnO NCs doped with Mn 15 %	High temperature wet chemical method
13.	Co0 SG	Undoped ZnO NCs	Sol-gel method
14.	Co0.5 SG	ZnO NCs doped with Co 0.5 %	Sol-gel method
15.	Co1 SG	ZnO NCs doped with Co 1 %	Sol-gel method
16.	Co1.5 SG	ZnO NCs doped with Co 1.5 %	Sol-gel method
17.	Co2 SG	ZnO NCs doped with Co 2 %	Sol-gel method
18.	Co4 SG	ZnO NCs doped with Co 4 %	Sol-gel method

In the microwave-assisted method, Zinc acetate and cobalt(II) acetate tetrahydrate $(CH_3CO_2)_2Co \cdot 4H_2O]$ for Co^{2+} doped samples and zinc acetate and manganese acetate tetrahydrate $(CH_3CO_2)_2Mn \cdot 4H_2O$] for Mn^{2+} doped samples are used as precursors dissolved in 20 ml of benzyl alcohol and subjected to microwave irradiation for 5 minutes to obtain doped ZnO nanoparticles with crystal sizes of 8-9 nm. The sample details are compiled in Table 5.1 where the dopant concentration mentioned in each sample is based on the initial concentrations in the reaction solution. In the subsequent sections of the paper, the samples prepared by wet chemical method have been referred to as WC samples, sol-gel prepared samples as SG samples while the samples prepared by microwave-assisted route are referred to as MW samples.

In all the cases, the average crystal sizes in the samples have been determined from X-ray Diffraction measurements using Scherer formula. The EXAFS measurements on the doped ZnO samples in the present case have been carried out at the Energy Dispersive EXAFS beamline (BL-08) at INDUS-2 SRS, described in detail in *Chapter-2*. Measurements have been carried out at Zn, Co and Mn edges. In each case the bent crystal polychromator of the beamline has been set at proper Bragg angle so that a reasonable band of energy is obtained around Zn K edge of ~ 9659 eV, Co K edge of ~7709 eV or Mn K edge of 6539 eV. EXAFS spectra of standard filters of Zn and Ga have been used for calibration of the CCD channels at the Zn K edge, assuming the theoretical values of Zn K-edge of 9659 eV and Ga K edge of 10367 eV. Similarly a standard Co filter along with commercial HoO_2 powder, with theoretical energy values of 7709 eV (for Co K edge) and 8071 eV (for Ho L_3 edge) have been used for calibration of the CCD channels at the Co K edge. EXAFS spectrum of a standard Mn filter along with that of commercial Sm_2O_3, with reported energy values of 6539 eV (Mn K edge) and 6718 eV (Sm L_3 edge) were used to calibrate the CCD channels in energy scale at Mn K edge. Magnetization of the samples was studied in the temperature (T) range of 5 to 300 K and magnetic fields (H) of (-6 to +6) kOe.

5.1 Co doped ZnO

X-ray diffraction patterns of MW prepared undoped and 10% Co doped ZnO nanocrystals are shown in Fig. 5.1. The diffraction features match with wurtzite phase of ZnO which is consistent with what has been reported already for the WC samples [101]**.** No drastic change in d values of ZnO nanocrystals has been observed due to doping. Rietveld refinement of the X-ray diffraction (XRD) patterns for SG prepared $Zn_{1-x}Co_xO$ ($0\leq x \leq 0.04$) samples are shown in Fig. 5.2.

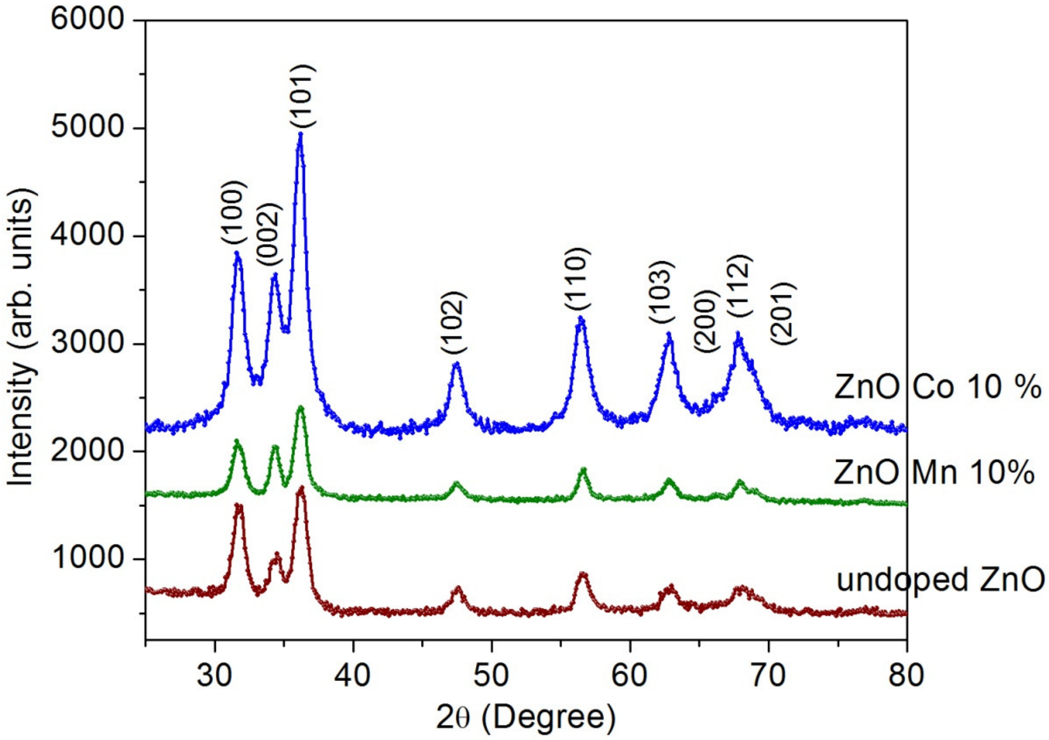

Figure 5.1 X-ray diffaraction patterns of undoped ZnO, 10% Mn doped ZnO and 10% Co doped ZnO nanoparticles.

Peak positions of Co-doped ZnO correspond to the standard Bragg positions of hexagonal wurtzite ZnO (space group *P63mc*) have been shown by the vertical bars in the above Fig. while the residue is shown by a line at the bottom of each XRD pattern.

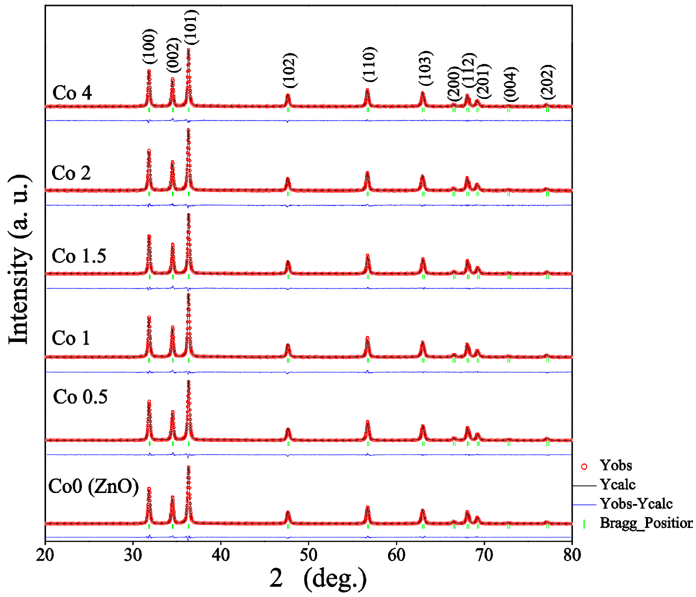

Figure 5.2 XRD pattern of Co doped ZnO nanoparticles prepared by sol-gel method.

Table 5.2 Estimated crystallite size and average strain developed in different samples.

Sample	Crystallite Size (nm)			Strain	
	Scherrer formula	Size-Strain Plot	W-H Plot	Size-Strain Plot	W-H Plot
ZnO	32.71	33.75	33.18	2.89×10^{-4}	4.94×10^{-5}
$Zn_{0.995}Co_{0.005}O$	34.08	35.69	30.32	1.10×10^{-3}	3.18×10^{-4}
$Zn_{0.99}Co_{0.01}O$	35.17	36.45	33.92	1.05×10^{-3}	2.03×10^{-4}
$Zn_{0.985}Co_{0.015}O$	35.86	36.64	32.47	1.71×10^{-3}	3.95×10^{-4}
$Zn_{0.98}Co_{0.02}O$	36.33	37.24	34.00	3.11×10^{-4}	2.12×10^{-4}
$Zn_{0.96}Co_{0.04}O$	39.18	39.49	36.54	1.05×10^{-3}	2.11×10^{-4}

In this case also, the Rietveld analysis of the XRD patterns show that the SG samples have hexagonal wurtzite structure belonging to the C^{4}_{6v} space group ($P6_3mc$) and indexed using the standard JCPDS file for ZnO (JCPDS 36-1451). Since no diffraction peaks corresponding to elemental Co or Co- related impurity phases are observed in the above samples, the formation of $Zn_{1-x}Co_xO$ solid solution is confirmed by either of the preparation technique, instead of any Co-precipitation or formation of any secondary phase. However, the presence of a secondary phase in the samples (viz. metallic nanoclusters or metallic oxides) cannot be ruled out completely. It may be localized near the dopant sites and is beyond the detection limit of XRD and will not express itself in the spectrum. To verify the presence or absence of such phases EXAFS measurements at Zn, Co and Mn edges have been carried out for all the samples prepared by different synthesis routes.

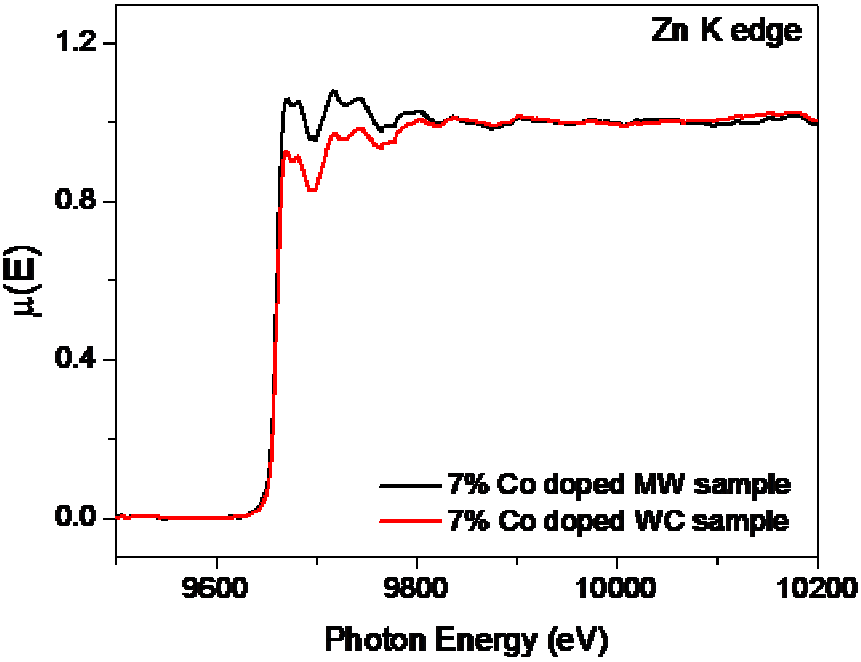

Figure 5.3 Experimental EXAFS spectra for 7% Co doped ZnO NCs at Zn K edge.

The experimental Zn K edge EXAFS spectra for two representative Co doped ZnO samples prepared by wet chemical and microwave-assisted method are shown in Fig. 5.3. To analyse the EXAFS spectra of the samples at Zn K edge, the structural parameters for the wurtzite ZnO used for simulation of theoretical EXAFS spectra have been obtained from reported values in the literature [109]. A model with the first oxygen shell (Zn-O1) at 1.98 Å (3), second oxygen shell (Zn-O2) at 1.99 Å (1) and a Zn shell (Zn-Zn) at 3.21 Å (12) is assumed corresponding to standard wurtzite structure of ZnO, the CN value of the respective shell given in parentheses following the bond length value. Due to their very close proximity, first two oxygen shells are generally combined together with an average bond length and total oxygen coordination of 4 in the fitting process. The first few peaks (in the k range of 3–10 Å^{-1} and up to 3.5 Å in R space) are fitted and shown in the $\chi(R)$ versus *R* spectra of the samples. Fig. 5.4 shows the experimental $\chi(R)$ versus *R* spectra of two representatives WC 7% Co and MW 7% Co doped ZnO samples at the Zn K edge along with the best fit theoretical spectra.

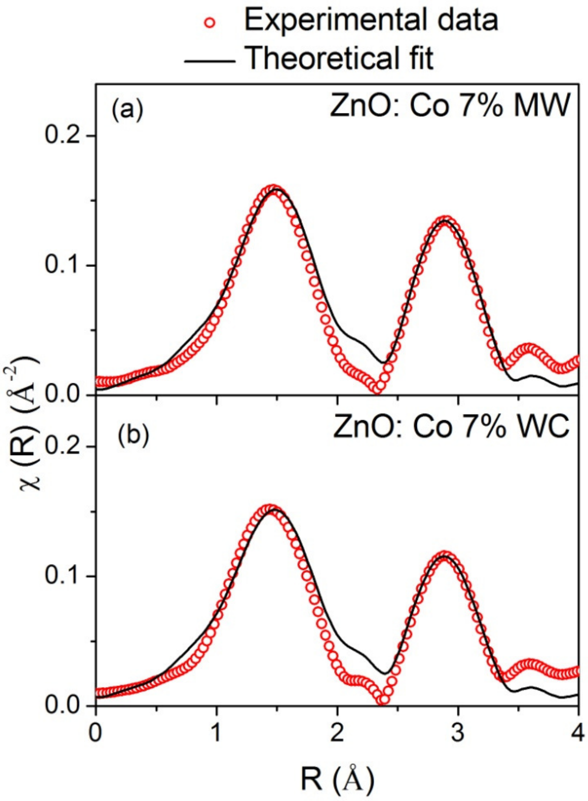

Figure 5.4 The experimental χ *(R) versus R* spectra and the theoretical fits of 7% Co doped ZnO prepared by (a) microwave method and (b) wet chemical method at Zn K-edge

It has been observed that values of the bond distances for both Zn-O and Zn-Zn shells for the Co-doped ZnO samples are similar to the distances in undoped bulk wurtzite ZnO within experimental error since substitution of Zn ions (ionic radius 0.6Å) by Co ions of almost similar size (ionic radius 0.58Å) does not cause any significant change in the host lattice. Hence it is logical to assume that Co goes into the ZnO lattice in the same oxidation state as

Zn (i.e., +2) with a tetrahedral coordination. However, as evident from Fig. 5.5, there is a significant reduction of CNs of both oxygen and zinc around the central zinc atom with increase in Co doping concentration.

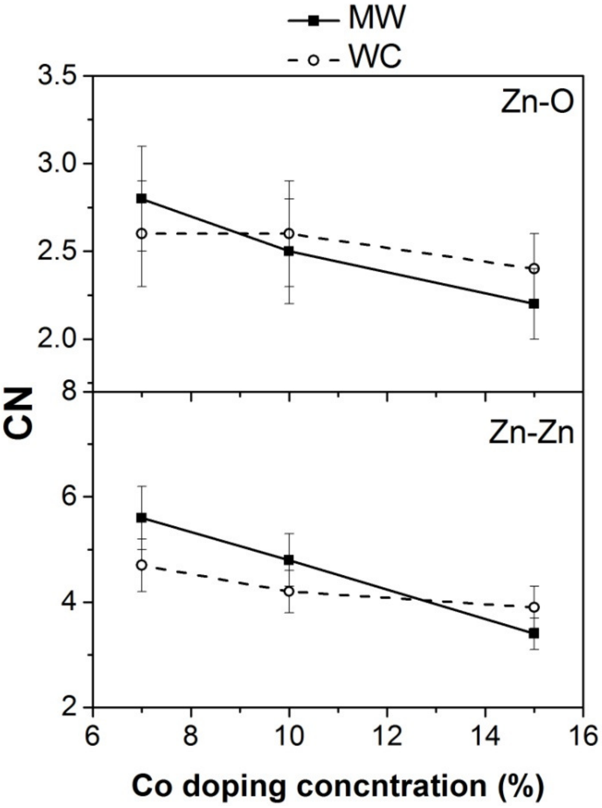

Figure 5.5 Variation of coordination number of (a) nearest Zn-O shell and (b) next nearest Zn-Zn shell prepared by both microwave method and wet chemical method with change in dopant concentration.

It should be noted that even at the lowest doping concentration, the CN's are less than that of theoretical values for wurtzite ZnO (which are 4 for Zn-O shell and 12 for Zn-Zn shell). It is known that n-type ZnO is prone to have significant amount of oxygen vacancies [110] as native defects and in the nanocrystals range, the Zn-Zn shell generally has a lower coordination which decreases with decrease in particle size [111]**.** The gradual decrease of Zn coordination with increasing Co concentration is attributed to the substitution of Zn ions by Co. The DW factor of the Zn-O bond is found to be quite high which also portrays a disturbed environment around the central atom due to the incorporation of a foreign cation in the lattice. Fig. 5.6 shows the Fourier transformed EXAFS (FT-EXAFS) $\chi(R)$ versus R spectra of SG prepared Co doped ZnO samples at Zn K-edge.

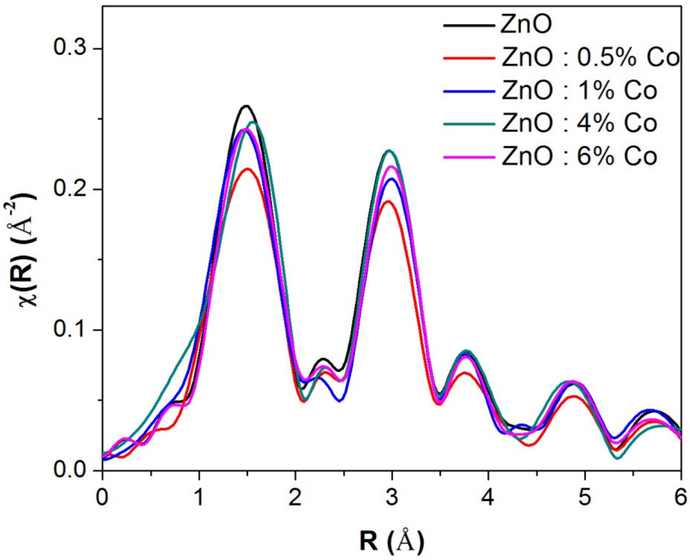

Figure 5.6 FT-EXAFS $\chi(R)$ *vs* R spectra of SG prepared Co doped ZnO samples at Zn K-edge.

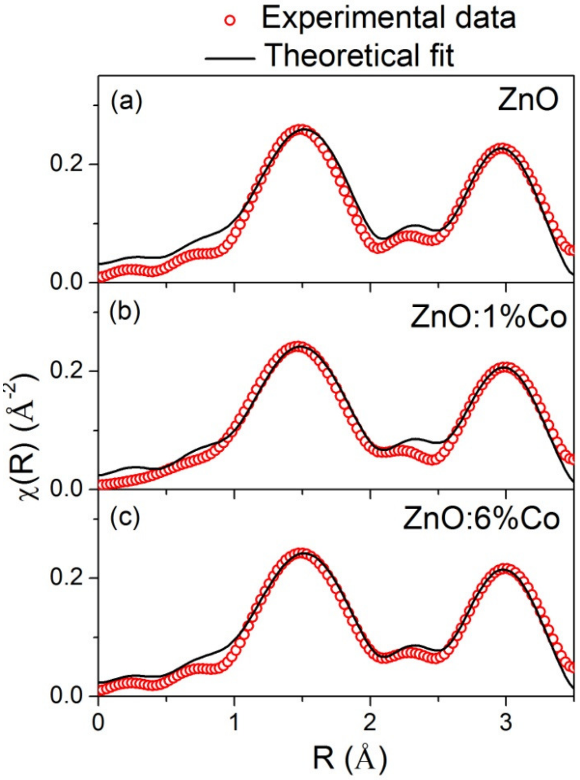

Figure 5.7 Experimental χ (R) versus R spectra of undoped, 1% and 6% Co doped ZnO NCs at the Zn K edge along with the corresponding best fit theoretical spectra of the SG samples.

Fig. 5.7 shows the experimental χ (*R*) versus *R* spectra of undoped, 1% and 6% Co doped ZnO NCs at the Zn K edge along with the corresponding best fit theoretical spectra of the above SG samples. Fig. 5.8(a) shows variation of coordination number of nearest Zn-O shell and next nearest Zn-Zn shell with the variation of the Co-concentration while Fig. 5.8(b) gives the variation of the XAFS Debye-Waller factors (σ^2). It should be noted the in the above Fig.s total CN's and average σ^2 factors are presented for the first two oxygen shells.

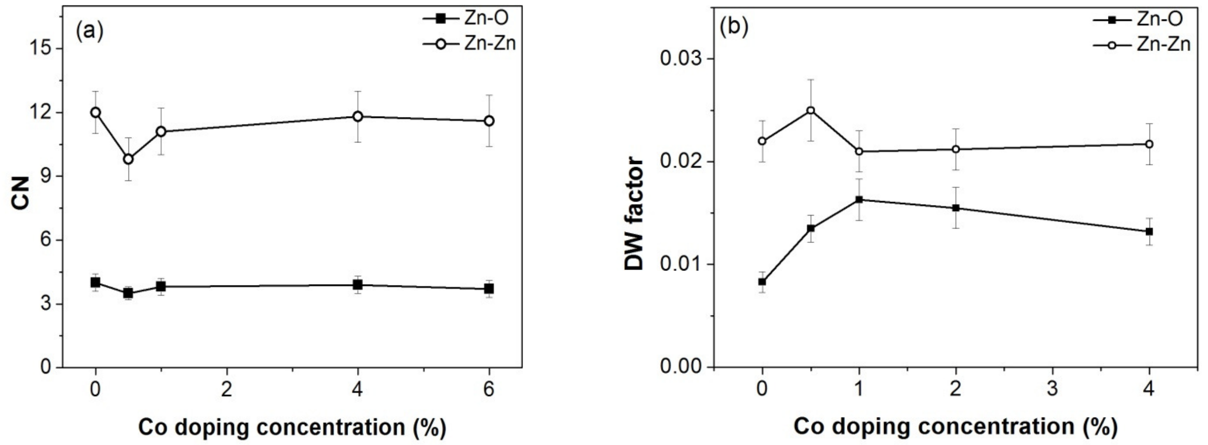

Figure 5.8 (a) Variation of coordination number (CN) and (b) Debye-Waller factor of nearest Zn-O shell and next nearest Zn-Zn shell with the variation of the Co-concentration.

Like the WC and MW samples described above, the peak positions for the SG samples which translate to bond length values does not change by Co doping, as it has been observed from Fig. 5.6, due to the reasons described above. Figs. 5.8(a) and (b) however, clearly show that over the whole Co doping range, the oxygen coordination remains lower and DW factor remains higher compared to their respective values in undoped ZnO, showing that doping takes place throughout the whole composition range. The oxygen vacancies present in the samples in the 1-6% Co doping concentration is found to be ~4-5%. Similar reduction in oxygen coordination and increase in oxygen vacancies due to doping has recently been observed by Chakraborty *et al* in Fe doped system [112]**.** It should be noted that the oxygen coordination is less than that of bulk value even for the undoped sample (with an estimated oxygen vacancy of ~2.5%) due to the fact that larger number of atoms are residing on the surface for the nanosized crystals being probed here.

However, as can be seen from both Figs. 5.8 (a) and (b), though the samples having doping concentration of 1% and above show a slow and gradual change, for the 0.5% Co doped sample, significant changes in the coordination and Debye-Waller factors are observed both at O and Zn sites. This might be due to larger strains generated in the lattice for this particular sample as obtained from the XRD measurements and shown in Table 5.2.

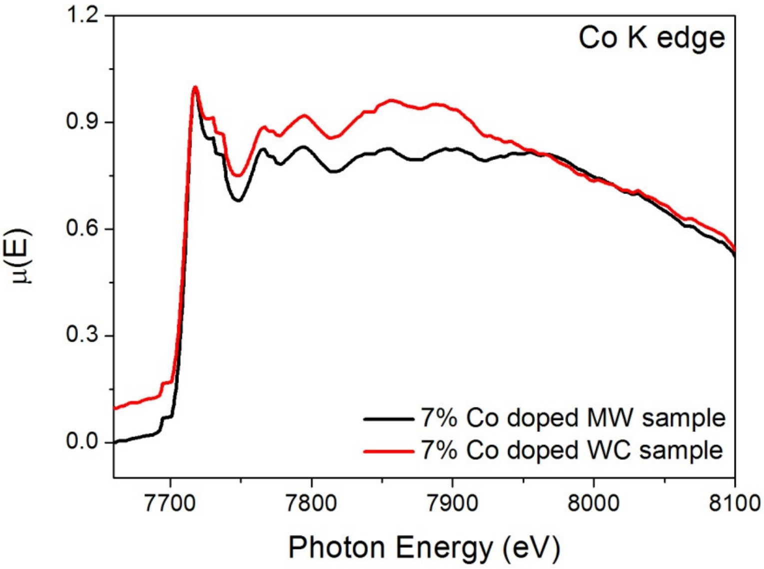

Figure 5.9 Experimental EXAFS spectra for 7% Co doped ZnO NCs at Co K edge.

Fig.5.9 shows the EXAFS spectra of two representative MW and WC 7% Co doped ZnO samples measured at the Co K edge and Fig. 5.10 shows the corresponding experimental $\chi(R)$ versus R spectra of the samples at the Co K edge along with the best fit theoretical spectra. At the Co K edge we explored the two possibilities of theoretical modeling to fit the experimental data: (a) starting with the basic wurtzite ZnO structure and replacing the central Zn atom with Co and (b) taking the initial model to be of cubic CoO.

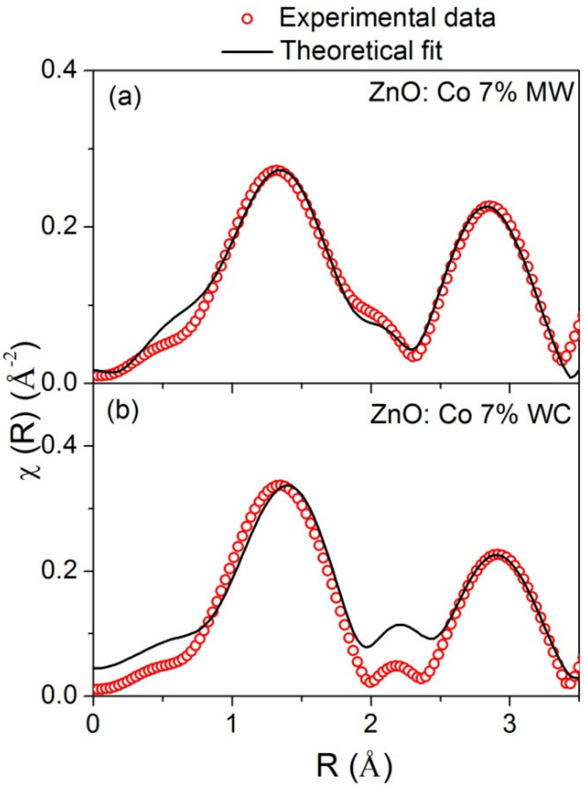

Figure 5.10 Experimental *χ(R)* versus *(R)* spectra of 7% Co doped ZnO sample prepared by MW and WC method at Co K edge along with the best fit theoretical spectra.

It was found from the χ^2 fitting of the data that the latter approach (b) is more suited to the measured data. The theoretical spectrum for CoO is generated assuming the model as described in [113] with the nearest oxygen shell at 2.13 Å and next nearest Co shell at 3.02 Å with CNs 6 and 12 respectively. The results of the best fit parameters are shown in Fig. 5.11(a) and (b).

It can be seen from Fig. 5.11(a) that Co-O first shell bond length values for both WC and MW samples are considerably less compared to the value in CoO (2.13Å) and is found to be closer to the Zn-O bond distance. This observation clearly establishes our previous supposition that Co ions indeed substitute Zn ions retaining the tetrahedral geometry of the parent lattice. However, the change in bond length values is not obvious from the Zn edge fitting results as the doping is low and only the local environment around the Co atoms gets distorted. The slightly lower values of Co-O bond lengths compared to ideal ZnO bond lengths as obtained here is also as expected since substitution of the Zn atom in tetrahedral coordination (ionic radius 0.6 Å) by a smaller Co atom (ionic radius 0.58 Å) would result in shortening of the nearest neighbor bonds. Similarly, the Co-Co/Zn bond lengths are found to be much longer than that expected for a perfect CoO system (3.02 Å) and are rather equal to the Zn-Zn bond in wurtzite ZnO.

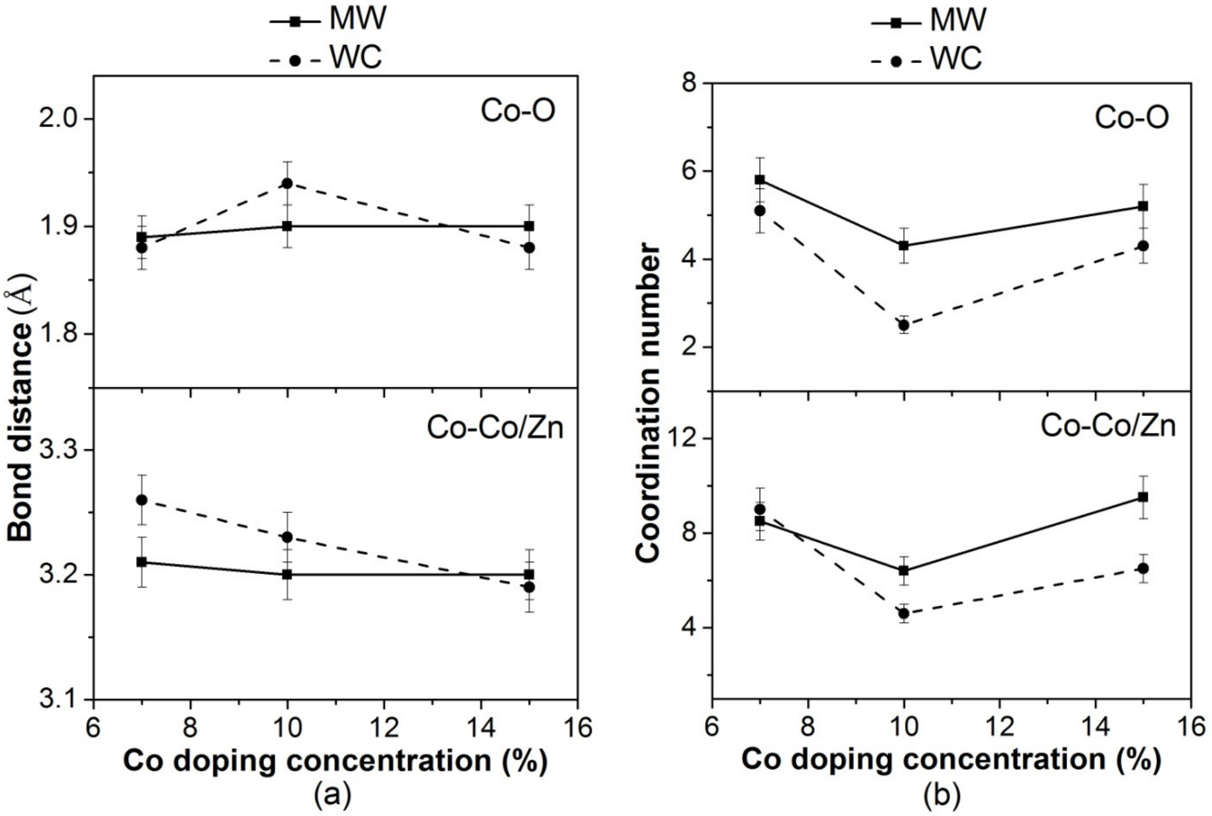

Figure 5.11 Variation of (a) bond length and (b) coordination number of nearest Co-O shell and next nearest Co- Co/Zn shell at Co K edge prepared by both microwave method and wet chemical method with change in dopant concentration.

As is evident from Fig. 5.11(b), starting from 7% Co doped ZnO, which has a CN of ~ 4 for Co-O, the CN value diminishes with increasing doping concentration from 7% to 10% but then shows an upward trend above 10% doping. The next nearest neighbor shell displays similar characteristics with the Co/Zn coordination less than the model value of 12 as seen previously at the Zn edge. Thus doping levels of ≤ 10% of Co can be assumed to be optimum for efficient doping in ZnO lattice and relatively higher Co concentration may lead to an onset of clustering of Co atoms manifested by an increase in CN of the Co-Co/Zn shell. Absence of Co clustering for low Co doping has also been reported by Han *et al*. [114] and Song *et al*. [104] by EXAFS measurements on their Co doped ZnO nanocrystals and thin film samples respectively. It should be noted that the results for the Co doped samples are fairly insensitive to the method of preparation since samples prepared by either method (wet chemical, sol-gel and microwave-assisted) have yielded similar results from EXAFS measurements.

Further, to ensure the oxidation state Co in ZnO matrix, we have carried out XANES measurements of the samples at Co K edge. Fig. 5.12 shows the XANES spectrum of a representative 6% Co doped ZnO SG sample along with that of a Co metal foil and a standard commercial sample of $Co(NO_3)_2$, which confirms the presence of Co in ZnO matrix in +2 oxidation state.

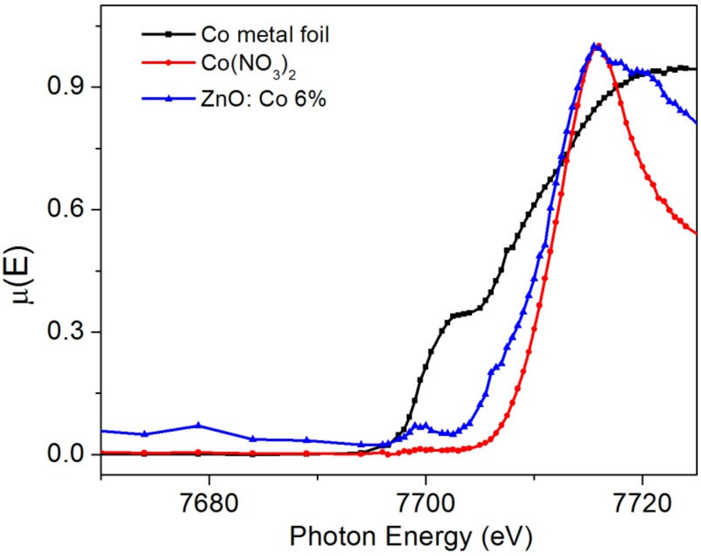

Figure 5.12 XANES spectra at Co K-edge.

5.2 Mn doped ZnO

X-ray diffraction patterns of Mn doped ZnO samples prepared by various synthesis routes match with those of phase pure hexagonal wurtzite ZnO similar to the Co doped ZnO samples. Fig. 5.13 shows representative experimental EXAFS ($\mu(E)$ versus E) spectra of 10% Mn doped ZnO at Zn K-edge, prepared by two different methods.

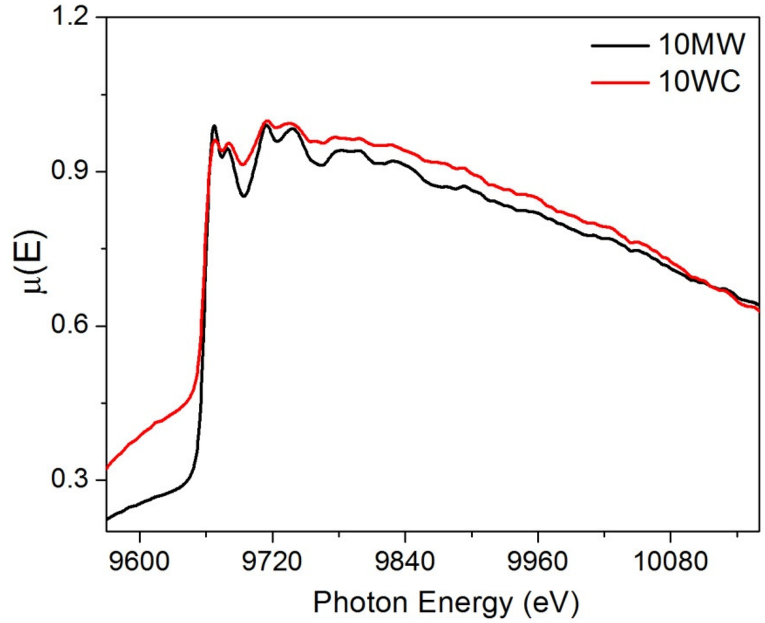

Figure 5.13 Normalized experimental EXAFS ($\mu(E)$ vs E) for 10% Mn doped ZnO NCs by two different synthesis routes at Zn K-edge.

Fig. 5.14 shows the experimental $\chi(R)$ versus R spectra for the representative 10% Mn doped MW and WC samples respectively along with the best fit theoretical spectra and the best fit results (coordination number and bond lengths) are shown in Fig. 5.15. It can be seen that the Zn-O bond length is less whereas the Zn-Zn bond distance is higher compared to the respective values of 1.98Å and 3.21 Å for undoped ZnO samples for all the samples.

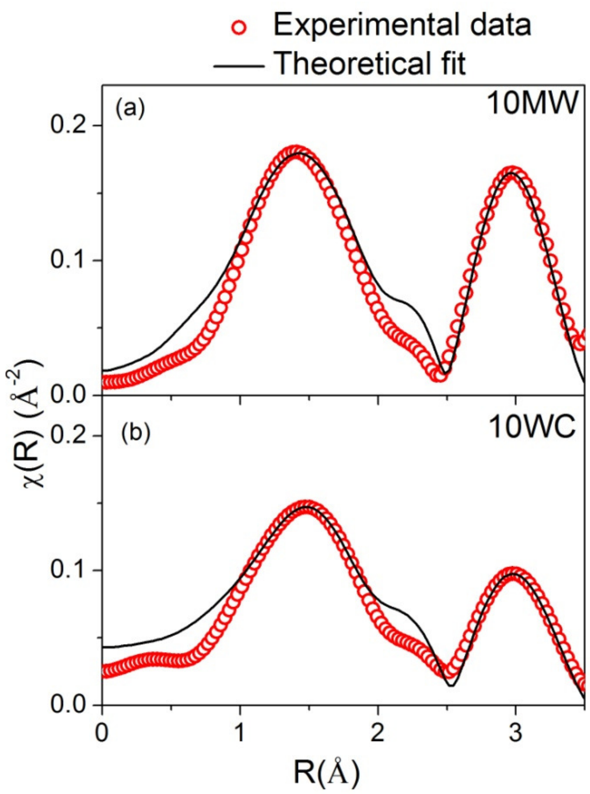

Figure 5.14 The experimental *χ(R) vs (R)* spectra and the respective theoretical fits of 10% Mn doped ZnO NCs prepared by (a) microwave assisted method and (b) wet chemical method at Zn K-edge.

This can be explained by the fact that the substitution of Zn atom in tetrahedral coordination (ionic radius 0.6 Å) by Mn atom (ionic radius 0.66 Å) would result in the shortening of the Zn-O bonds and elongation of Zn-Zn/Mn bond. For MW samples the first (oxygen) and second (zinc) shell co-ordination retain the values for undoped ZnO (4 & 12 respectively) for lower (<10%) Mn concentration as in Fig. 5.15 (c) and (d). This shows that Mn goes into the host with the same oxidation state of Zn i.e., as Mn^{2+}. The oxygen coordination decreases with increase in oxygen vacancies in the lattice only for significantly high Mn concentration (15%). In case of the WC samples, however, there is a monotonous decrease in coordination over the whole range of Mn concentration.

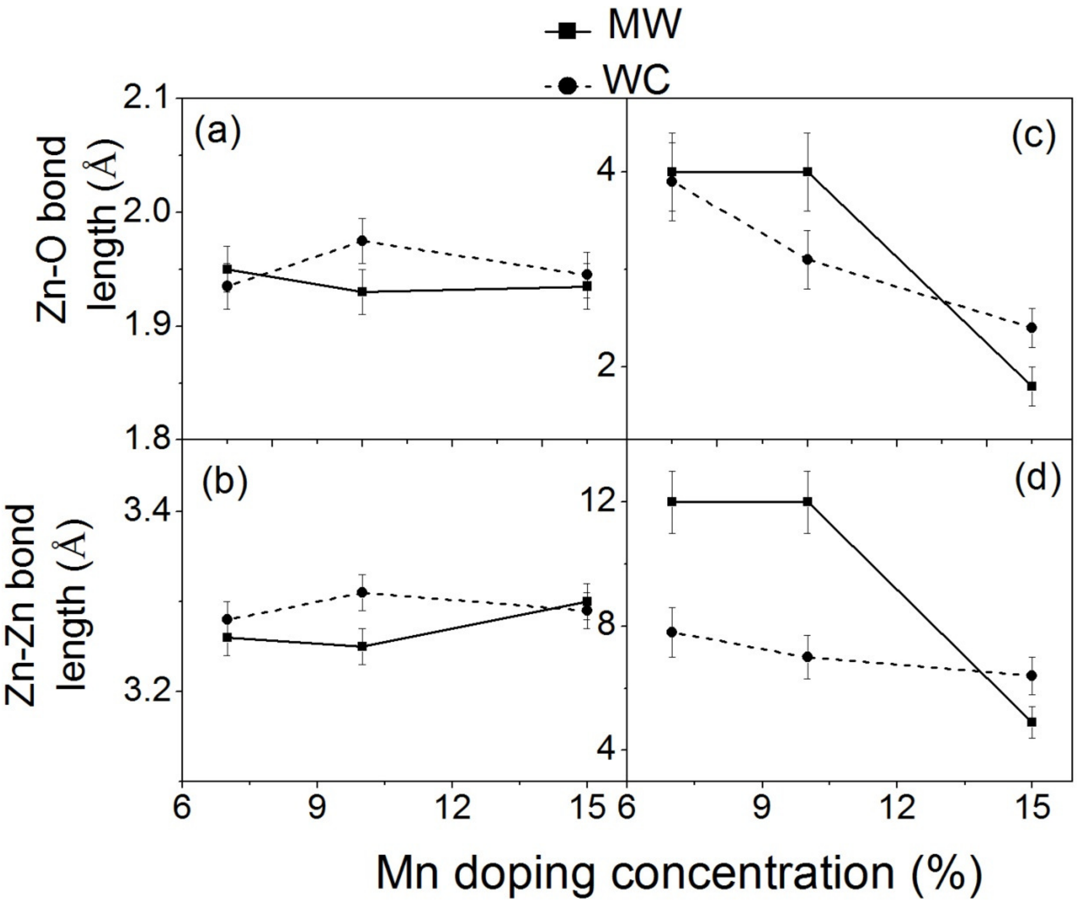

Figure 5.15 Variation of (a) nearest Zn-O shell bond length (b) next nearest Zn- Zn shell bond length (c) CN of nearest Zn-O shell and (d) CN of next nearest Zn- Zn shell prepared by both microwave method and wet chemical method with change in Mn dopant concentration at Zn K edge.

Similar difference between the Mn doped MW and WC samples in the nature of variation of bond lengths as a function of Mn concentration exists as evident from Figs. 5.15(a) and (b). One of the possible reasons for the reduced coordination in WC samples may be due to Mn going into the ZnO matrix in some other oxidation state, which has been probed further by the XANES measurements at Mn K edge of the samples. In order to have an idea regarding the oxidation state of Mn in ZnO, the XANES region of the Mn edge XAS spectrum was studied. Fig. 5.16 shows the representative XANES spectra of 10% Mn doped ZnO synthesized by two different routes along with the spectra of standard commercial Mn_2O_3 (Mn^{+3}) and MnO_2 (Mn^{+4}) samples.

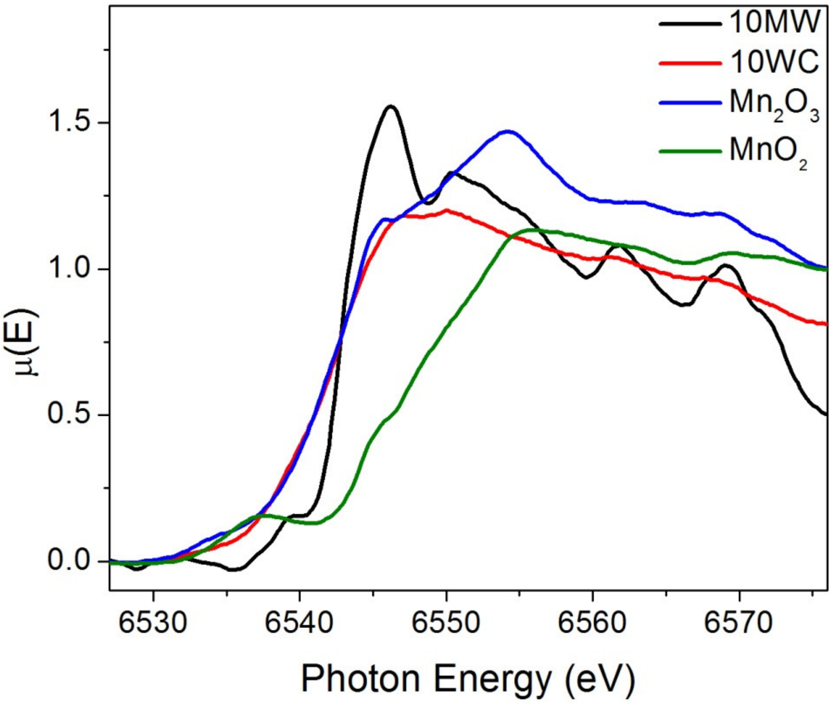

Figure 5.16 Normalized experimental XANES (*$\mu(E)$ vs E*) spectra for 10% Mn doped ZnO by two different synthesis routes with Mn_2O_3 and MnO_2 standards at Mn K-edge.

It is obvious that the spectrum of 10WC is similar to that of Mn_2O_3 whereas the 10MW spectrum is quite different implying presence of Mn_2O_3 phase in WC samples. The XANES spectra of the samples are also significantly displaced on the lower energy side from that of the MnO_2 sample, thus discarding the presence of Mn^{+4} in the lattice.

To fit the Mn edge data for the MW samples, two possibilities for theoretical modeling were explored to fit the experimental data such as (a) starting with the basic wurtzite ZnO structure and replacing the central Zn atom with Mn assuming uniform substitution of Zn by Mn and (b) taking the initial model to be the cubic MnO, Mn_2O_3 or Mn_3O_4. It was found from the χ^2 values of the fitting that for these samples the latter approach (b) is more suited, with cubic MnO as the initial modeling structure. Fig. 5.17 shows the experimental as well as the best fit theoretical $\chi(R)$ versus R spectra, including the magnitude, real and imaginary components of $\chi(R)$ for the representative MW 10% Mn doped ZnO sample.

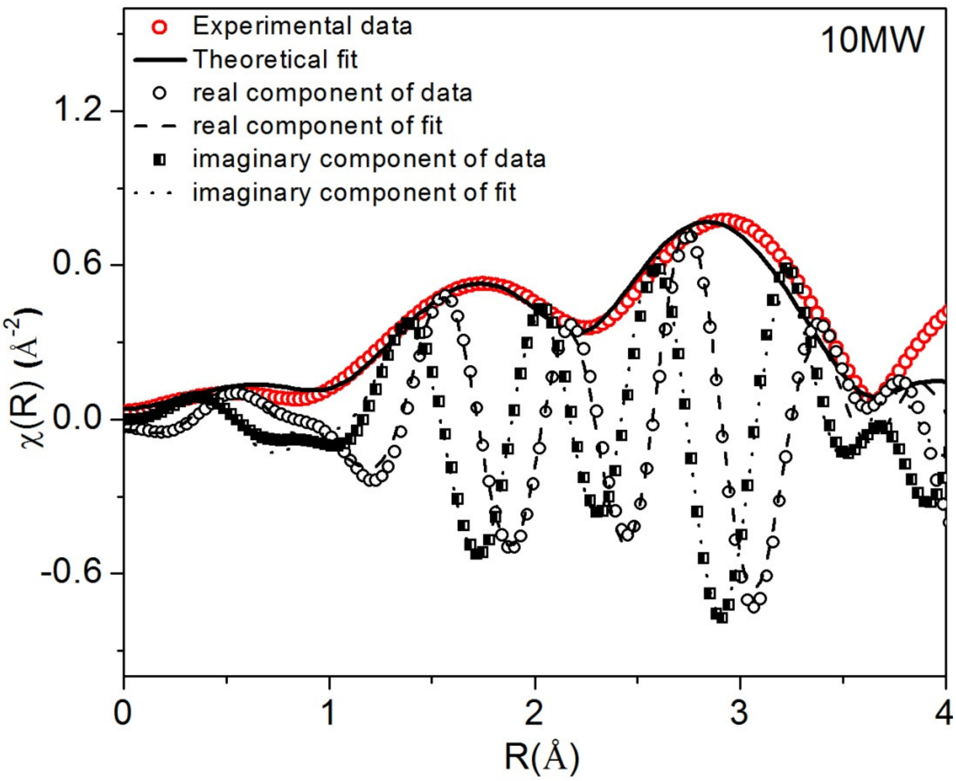

Figure 5.17 The experimental *χ(R) vs R* spectra (magnitude, real and imaginary components) and the respective theoretical fits of 10% Mn doped ZnO prepared by microwave method at Mn K-edge.

The theoretical spectra have been generated assuming Mn to be present as MnO, assuming the model as described in [115] with the nearest oxygen shell at 2.22 Å, next nearest Mn shell at 3.10 Å and the third oxygen shell at 3.85 Å with CNs 6, 12 and 8 respectively. Satisfactory fitting has been achieved up to 4.0 Å in R space following the same procedure as described previously and the best fit parameters have been presented in Fig. 5.18 for the MW samples. The nearest Mn-O shell bond length values are found to be less compared to the value in MnO (2.22 Å) and decreases with increase in Mn concentration which can be attributed to Mn being accommodated in the Zn-O structure, Zn-O bond length in ZnO being 1.98 Å. Similarly, the Mn-Mn/Zn bond lengths are much longer than that expected for a perfect MnO system and are rather comparable to the Zn-Zn bond lengths (3.21 Å) in wurtzite ZnO. However, the oxygen and Mn coordination in the 1st and 2nd shells respectively are in agreement with the standard ZnO values (4 and 12 respectively) for the sample with 7% Mn, whereas the coordination values are much higher for the samples having 10% and 15% Mn, indicating the onset of Mn clustering beyond 7% concentration of Mn.

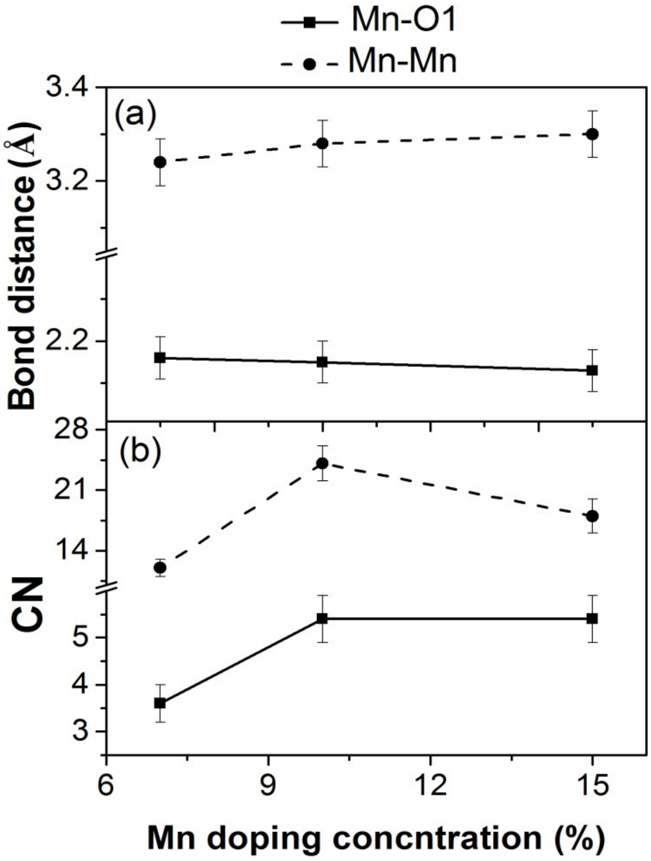

Figure 5.18 Variation of (a) bond length and (b) coordination number of nearest Mn-O shell and next nearest Mn-Mn/ Zn shell for the samples prepared by microwave-assisted method with change in dopant concentration at Mn K-edge.

The WC samples, on the contrary, were fitted with Mn_2O_3 as basic structure as had been implied by the XANES spectrum. The initial theoretical spectrum for Mn_2O_3 is generated assuming the model as described in [116] with the nearest oxygen shell at 1.99 Å, next nearest Mn shell at 3.56 Å and the third oxygen shell at 3.84 Å with CNs 6, 12 and 12 respectively. The fitting has been done up to 4.0 Å in R space and the results have been presented in Fig. 5.19(a) and (b).

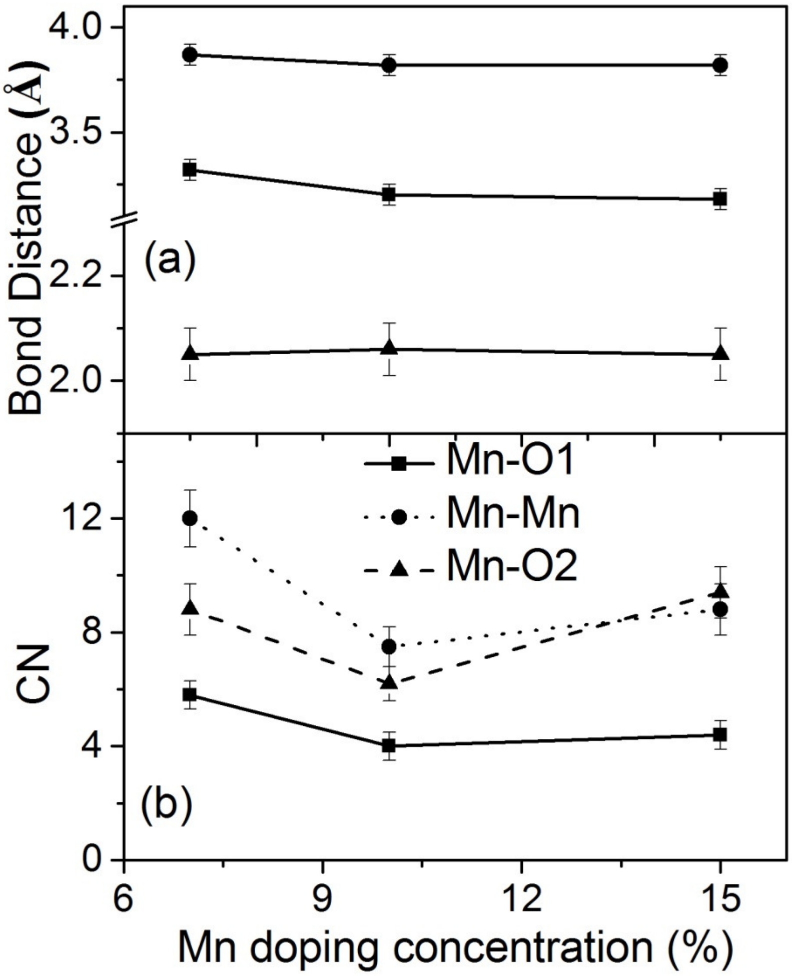

Figure 5.19 Variation of (a) bond length and (b) coordination number of nearest Mn-O shell, next nearest Mn- Mn/Zn shell and the third Mn-O shell for the samples prepared by wet chemical method with change in dopant concentration.

It can be seen from the above figure that for the 7% Mn doped sample best fit parameters closely resemble the Mn_2O_3 model parameters and it may be assumed that in this sample Mn exists as Mn_2O_3. However, the sample with higher Mn doping concentrations (~10%) shows more compatibility with the parent ZnO lattice though the Mn-O bond length values are slightly higher than that of standard ZnO values which may be due to higher size of Mn ions compared to Zn. The Mn-Mn/Zn bond lengths, are found to be smaller than that in Mn_2O_3 (3.56 Å) and closer to Zn-Zn bond length (3.21 Å) in ZnO lattice. The variation of 1st and 2nd shell coordination numbers as a function of Mn doping concentration, as shown in

Fig. 5.19(b), shows a decrease from the initial model structure value (6) of Mn_2O_3 to that of tetrahedral ZnO (4) for the Mn-O shell at 10% doping concentration and then a further increase. Hence a doping concentration of ~10% is optimum for the samples prepared by wet chemical route above which there is a possibility of Mn clustering.

5.3 Magnetic measurements

As the magnetic properties of DMS materials around or preferably above room temperature (RT) are important for their practical applications, we conducted a detailed study on the RT magnetization of Co and Mn doped ZnO systems. The magnetic measurement results on WC samples, observed by our group [101] show that with increase in Mn concentration, there is an increase in paramagnetic and decrease in ferromagnetic contribution. In case of Co doped WC ZnO nanocrystals, on the other hand, it has been observed that with increase in Co concentration ferromagnetic ordering increases at the cost of paramagnetic contribution. Fig. 5.20 shows the magnetization (M) vs applied field (H) curves of MW 10% Co and Mn doped ZnO samples measured at 300 K.

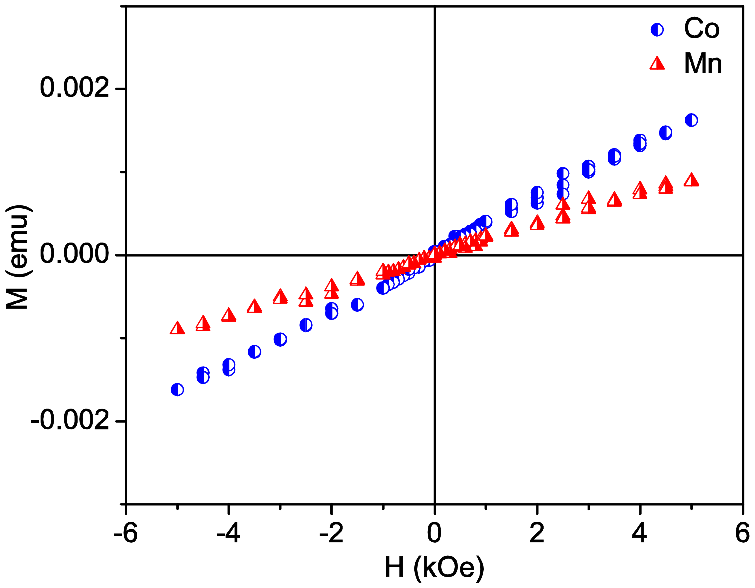

Figure 5.20 M vs H curve for 10% Co and Mn doped ZnO nanoparticles prepared by microwave-assisted method.

The samples do not show any ferromagnetic behavior as it is evident from the absence of any hysteresis in the above plots. Temperature dependent susceptibilities χ(T) has been recorded in the range 5K to 300 K at a constant magnetic field of 100 oersted and are shown in Fig. 5.21.

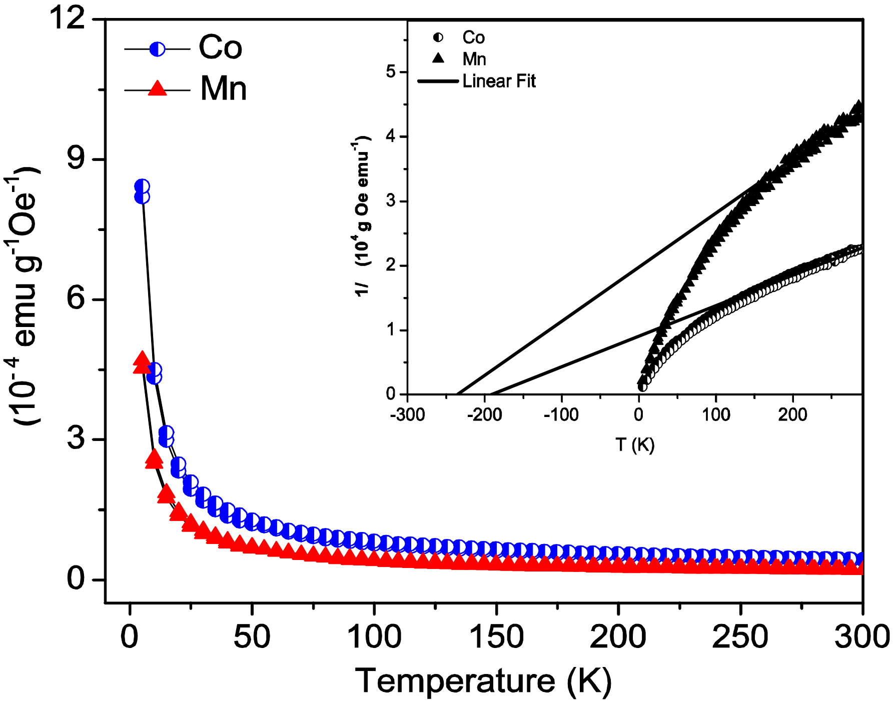

Figure 5.21 Temperature dependence of magnetic susceptibilities χ and inverse susceptibilities χ-1 (inset) measured in a dc field H = 100 Oe.

Both ZFC and FC measurements were carried out but no distinct splitting was observed in the χ vs T plots, a signature of paramagnetic samples. Inverse susceptibility χ^{-1}(T) curves of both 10% Co and Mn doped MW ZnO samples, as shown in the inset of Fig. 5.21, show a Curie-Weiss behaviour described by the following relation:

$$\chi = \frac{C}{T-\theta} \tag{5.1}$$

where, C is the material specific Curie constant, T is the absolute temp. and θ is the Weiss constant (in Kelvin). The Curie constants (*C*) have been calculated from the slope of the best fit line of the data points above 200 K to RT and subsequently the Curie temperature θ are calculated. The estimated value of θ is found to be negative for both the samples which indicates an antiferromagnetic interaction between the dopant TM ions. Similar results were obtained for 5% Co and Mn doped samples also. Thus it can be concluded that both Mn and Co doped MW samples with doping concentration ≥ 5% are not ferromagnetic at room temperature.

M-H curve of some of the SG samples are plotted in Fig. 5.22. The magnetization decreases with the increase in the field for Co0 and Co1 whereas it increases with the increase in the magnetic field for Co2 and Co4. The observed M-H behavior reveals that the samples Co0 and Co1 is a mixture of ferromagnetic (FM) and diamagnetic (DM) phases (where DM dominates) and the samples Co2 and Co4 are in weak ferromagnetic phase.

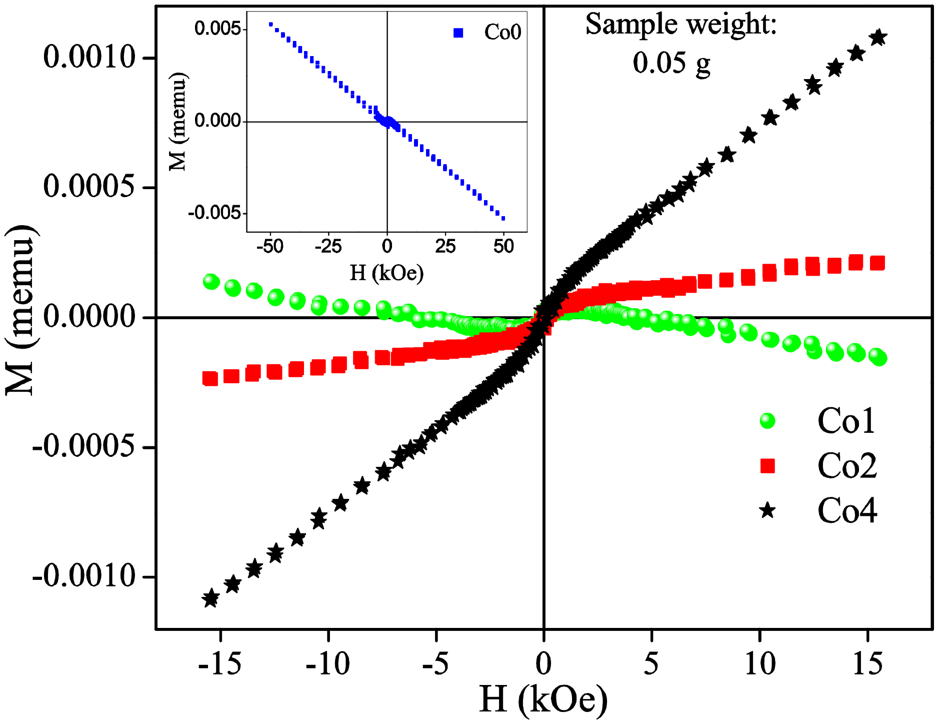

Figure 5.22 M-H curve of SG prepared Co doped ZnO samples.

In other words the magnetization increases with increasing Co-concentration and weak ferromagnetism arises gradually.

5.4 First Principle calculation

To support the experimental results of the Mn and Co-substituted ZnO systems, we have carried out first principles calculations for 6.25, 12.5, 18.75 and 25% Mn and Co substitutions in the ZnO system in the wurtzite structure. In the 2x2x2 super cell, which contains 16 Zn atoms, we replace 1, 2, 3 and 4 Zn atoms by the transition metal (TM) atoms for 6.25, 12.5, 18.75 and 25% substitutions, respectively. In cases of more than one TM atom per super cell, we have carried out calculations on substitutions created near and far from the other substituent atoms. Mn and Co being magnetic elements, we have probed the stability of all the three possible magnetic configurations: non-magnetic, ferromagnetic and anti-ferromagnetic, wherever possible. In Fig. 5.23 a typical structure is shown with two Mn substitutions near each other, which occupy the Zn sites.

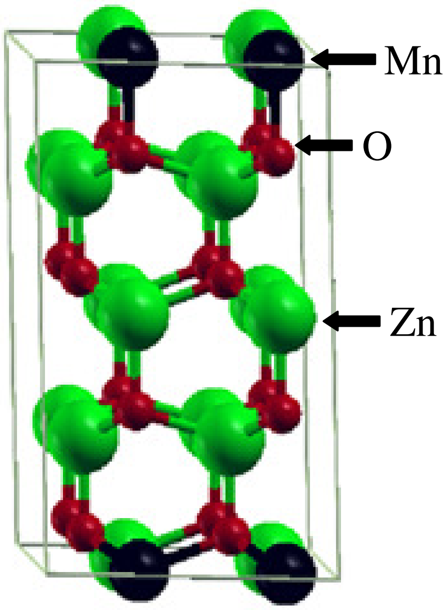

Figure 5.23 ZnO supercell (2x2x2) with 2 Mn atoms at Zn sites. Here the biggest spheres (green in color) correspond to Zn atoms, the smaller (black in color) and the smallest spheres (red in color) signify Mn and O atoms, respectively. This Fig. represents the case of two Mn atoms being near to each other.

We employ the Vienna Ab Initio Simulation Package (MedeA-VASP) [52]–[54] in combination with the projector augmented wave (PAW) method [55] and the generalized gradient approximation (GGA) over the local density approximation (LDA) for the exchange-correlation functional [47]. GGA is used because it accounts for the density gradients hence, it usually provides better agreement with experiment compared to LDA. For the planewaves, we have used an energy cutoff of 500 eV. A mesh consisting of about 300 K-points in the irreducible Brillouin zone has been used to calculate the total energies. The energy and force tolerance for our calculations were 10 μeV and 10 meV/Å, respectively. We have optimized the geometries for each system, with and without the substituted TM atoms, Co and Mn at the Zn site. To study and compare the stability of all the substituted systems, we have calculated the formation energy for each system after the geometry is optimized. The formation energy can be obtained by subtracting the total sum of the bulk energy of all the material components, E_i, weighted by its concentration c_i from the ground state energy of the total alloy system, E_{tot}

$$E_{mix} = E_{tot} - \sum_i c_i E_i \tag{5.2}$$

A negative mixing energy indicates that a system is stable and more negativity corresponds to increased stability of a system. Following the geometry optimization, we calculate the structural and magnetic properties. In addition to the pseudopotential calculations, we have carried out relativistic spin-polarized all-electron calculations of the properties of the optimized geometries as well. These calculations are performed using full potential linearized augmented planewave (FPLAPW) program, WIEN [46] with the generalized gradient approximation (GGA) for the exchange correlation functional [47]. The Brillouin zone (BZ) integration has been carried out onthe basis of tetrahedron method with Bloch corrections as given by the package WIEN. An energy cut-off for the plane wave expansion of about 19 Ry is used. The cut-off for charge density is G_{max}= 14. The numbers of k points for the self-consistent field (SCF) cycles in the reducible (irreducible) BZ are about 1500 (600). The convergence criterion for the total energy E_{tot} is about 0.1 mRy per atom. The charge convergence is set to 0.0001.

The detailed results of the above simulations are summarized in Fig. 5.24(a) and (b). Fig. 5.24(a) illustrates the variation of mixing energy with percentage of doping of Co atoms in the ZnO system for the non-magnetic case. As can be seen from the above-mentioned figure, the mixing energy of the system reduces with increase in percentage of Co substitution for both the cases, whether Co atoms are near or far from each other in the supercell.

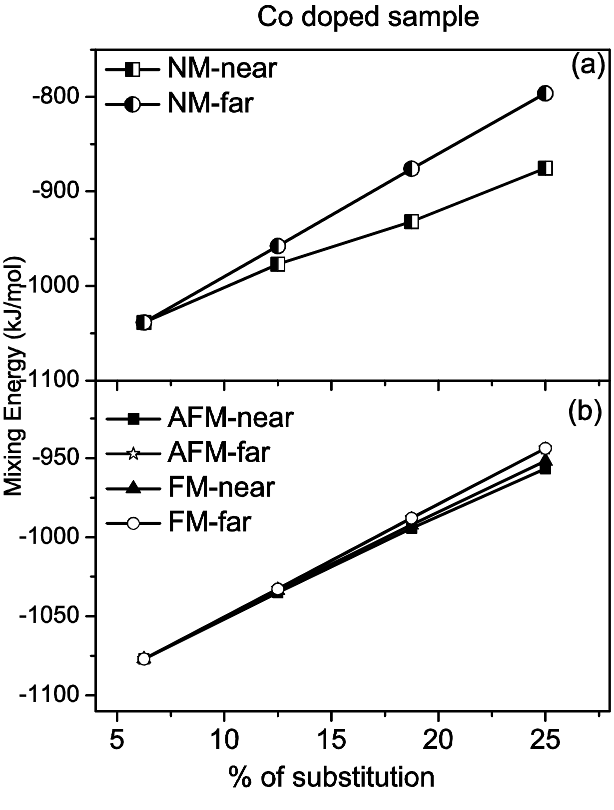

Figure 5.24 Plot of mixing energy versus percentage of substitution of Zn atoms by Co atoms in the 2x2x2 supercell for the (a) non-magnetic and (b) anti ferromagnetic and ferromagnetic cases.

This observation implies that the substitution leads to structural instability of the system. It can also be found that for higher Co concentration (>10%) the substituted system, where the

Co atoms are closer to each other, has significantly higher mixing energy compared to the case where two Co atoms are far from each other. This indicates that the Co atoms at higher concentration prefer to cluster together. Fig. 5.24b elucidates the variation of mixing energy as a function of percentage of substitution of Zn atoms by Co in the 2x2x2 supercell for the two magnetic cases, anti-ferromagnetic and ferromagnetic. It has been observed that for small concentration of Co doping (<15%) there is very small difference in energy or stability in the system for ferromagnetic or anti-ferromagnetic cases whether Co atoms are closer to each other or far away from each other. This indicates that both types of magnetic properties are possible in either of the above two cases.

Fig. 5.25(a) shows the variation of mixing energy with the percentage of substitution of Zn atoms by Mn atom in the 2x2x2 supercell for the non-magnetic case. As has been observed above, in case of Mn doping also, the mixing energy decreases with increase in percentage of substitution for both the cases, where Mn atoms are near or far from each other

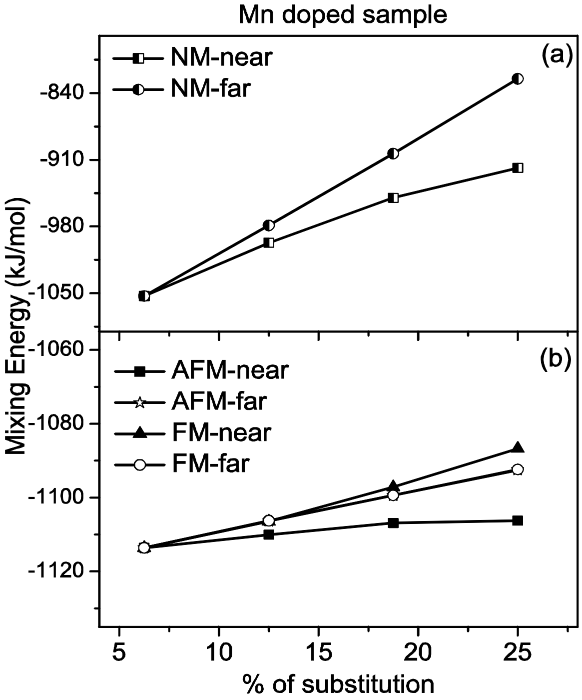

Figure 5.25 Plot of mixing energy versus percentage of substitution of Zn atoms by Mn atoms in the 2x2x2 supercell for the (a) non-magnetic and (b) anti ferromagnetic and ferromagnetic cases.

in the supercell. As has been observed in case of Co doped system, in this case also it is found that the system, where Mn atoms cluster together, has more stability at higher Mn concentration. The results of the magnetic cases are shown in Fig. 5.25(b), which shows that in the anti-ferromagnetic case, where the Mn atoms are closer to each other, has significantly higher mixing energy, specifically for relatively higher Mn concentration (>10%). This indicates that the anti-ferromagnetic behavior of the system is increasingly more likely when Mn atoms are situated closer to each other or in other words, form clusters. On the contrary, where Mn atoms are far away from each other, either ferromagnetic or anti-ferromagnetic behavior is possible.

Conclusions

Mn and Co doped ZnO NCs have been prepared following three different synthesis routes viz.,(i) high temperature wet chemical method (WC samples), (ii) sol-gel route (SG sample) and (iii) microwave-assisted method (MW samples). It is observed from EXAFS measurements on Co doped samples at Zn and Co edges that substitution of Zn ions by Co ions of almost similar size does not cause any significant change in the host lattice. Up to 10% concentration of Co appears to be optimum for efficient doping in ZnO lattice and relatively higher Co concentration may lead to an onset of clustering of Co atoms manifested by an increase in coordinations of the Co-Co/Zn shell. The samples prepared by both microwave-assisted method and wet chemical route show almost similar results in case of the Co doped samples. First principle calculations show that the ground state energies of Co doped ZnO NCs are almost similar in FM and AFM cases manifesting the fact that the system can either be ferromagnetic or anti-ferromagnetic. However, from magnetic measurements it has been observed that though the WC Co doped samples are ferromagnetic, MW samples show anti-ferromagnetic ordering. This observation suggests that the origin of magnetic properties for the Co doped ZnO NCs is probably due to surface modification related to the preparation process and not dependent on the bulk properties. Similarly Co doped SG samples which also shows weak ferromagnetism that increases with increase in Co concentration might also be attributed to surface modification of the nanoparticles related to preparation process. Capping by organic molecules during the wet chemical synthesis route might be a key factor in the origin of the observed ferromagnetism in the doped ZnO NCs. Our findings are analogous to a recent study which claims that intrinsic FM behavior in undoped ZnO NCs capped with different organic molecules is due to interface formation, preferably with Zn-O bonds on surface [107].

In case of Mn doped samples prepared by microwave method (MW samples) it has been found that for lower Mn concentration, Mn goes into the host with same oxidation state of Zn as Mn^{2+} and ~7% Mn concentration is optimum for efficient doping in ZnO lattice. Higher Mn concentration leads to clustering as is evidenced from EXAFS analysis. The magnetic measurements indicate that MW samples do not show ferromagnetism, rather show anti-ferromagnetic ordering as predicted by the first principle simulation of the energy of the system with Mn clustering. However, for samples prepared by wet chemical method (WC samples) there is an evidence of the presence of Mn_2O_3 phase i.e. Mn in Mn^{3+} oxidation state as observed by the XANES spectra and confirmed by EXAFS analysis. Hence the ferromagnetism observed in Mn doped WC samples is most likely due to the Mn_2O_3 phase unlike the Co doped samples where surface modification due to preparation process might have led to ferromagnetic properties. Ferromagnetism in Mn doped ZnO has been attributed to precipitation of separate phases viz., Mn_2O_3 and Mn_3O_4 by other authors also [117], [118]. The above conclusion is further supported by the fact that ferromagnetism in WC Mn doped samples decreases with increase in Mn doping concentration. At higher doping concentration

(>10%), EXAFS analysis suggests onset of Mn clustering and first principle calculations show that Mn clustering prefers anti-ferromagnetic ordering leading to a more stable structure. It is to be noted here that this is in contrast with the case of Co doped ZnO WC samples where ferromagnetism increases with increase in Co doping concentration, in agreement with the first principle calculations which show that Co clustering does not preferentially lead to antiferromagnetism.

Chapter 6

Multiferroic System

(Magnetic transition in Cr doped $GaFeO_3$)

In recent times multiferroic systems exhibiting magnetism and ferroelectricity simultaneously are being extensively investigated and have gained importance for their tremendous potential in technological applications. Gallium ferrite ($GaFeO_3$) is such a system demonstrating piezoelectricity [119] and ferrimagnetism [120] that has generated much interest in the scientific community. $GaFeO_3$ is more important since it has a magnetic transition temperature (T_c) around 210 K and has been extensively studied by various groups, though, most of the reported studies are on the magnetic properties and its possible explanation from the structural properties investigated by X-ray diffraction or first principles numerical simulations [121], [122]**.** $GaFeO_3$ is known to have an orthorhombic structure with one gallium atom (Ga1) in a tetrahedral site and the other gallium (Ga2) and the two iron atoms (Fe1 and Fe2) in octahedral sites.

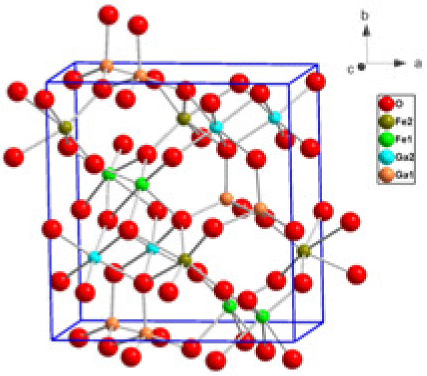

Figure 6.1 Crystal structure of $GaFeO_3$

The crystal structure of $GaFeO_3$ and schematic of the oxygen polyhedra surrounding Ga1, Ga2, Fe1 and Fe2 sites are shown in Fig. 6.1.

It has been observed by X-ray/neutron diffraction, Raman and Mössbauer spectroscopy studies that though no structural phase transition takes place in this system across the magnetic transition temperature, the magnetic properties of $GaFeO_3$ at low temperature is associated with cation site disorder, i.e. the presence of octahedral Fe ions predominantly in octahedral Ga sites [123]–[128]**.** Such site disorders can be best probed by an element specific local structure measurement tool such as EXAFS across the magnetic transition temperature which has not been reported so far in the literature. Further, there have been efforts to dope transition metal atoms (viz., Cr and Mn) in $GaFeO_3$ to explore the possibility of manipulating the magneto-electric effect of the system favourably [121], [122] and it has been observed that structural and magnetic properties of the system changes depending on Cr substitution at Fe or Ga sites [122]**.** However, no studies have so far been carried out to probe the local structure surrounding Ga or Fe sites on Cr doped samples. In the present study a systematic investigation has been conducted on the undoped, 10% and 20% Cr doped multiferroic $GaFeO_3$ by Synchrotron based EXAFS technique both at Ga K-edge (10367 eV) and Fe K-edge (7112 eV) over a wide temperature range from 25 K to 300 K.

The samples were synthesized by solid state reaction method following the procedure adopted by Saha *et. al.* [122] to ensure Cr substitution at the Fe site. Stoichiometric mixture of α-Fe_2O_3 and Cr_2O_3 were calcined at 1000^oC for 12 hours. This forms the intermediate compound $(Fe_{1-x}Cr_x)_2O_3$ which was then ground with stoichiometric amount of β-Ga_2O_3 and sintered at $1300^{\circ}C$ for 12 hrs. The phase purity of the final products was checked by X-ray powder diffraction.

Neutron diffraction patterns of the doped and undoped $GaFeO_3$ samples were recorded on a multi position sensitive detector based powder diffractometer (λ=1.2443Å) at the Dhruva reactor, Bhabha Atomic Research Centre, Mumbai, India at room temperature between 5°≤2θ≤140° range. Rietveld refinement of the neutron diffraction patterns were carried out using the FULLPROF program [129].

Fig. 6.2 shows the representative neutron diffraction pattern of $GaFeO_3$ and the Reitveld fit.

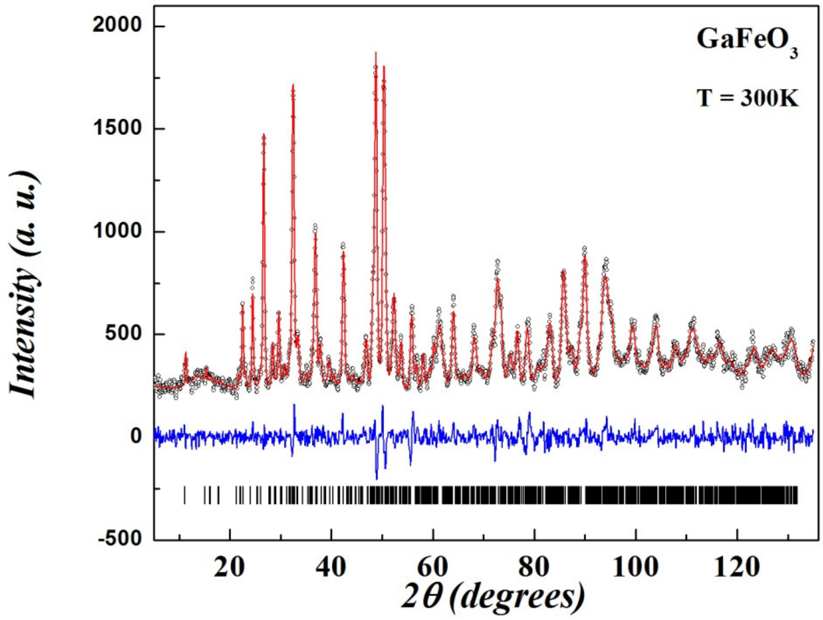

Figure 6.2 Neutron diffraction pattern of $GaFeO_3$ with Rietveld fit at 300K. Continuous line through data points is a fit to chemical structure. Continuous line at bottom is difference pattern and vertical bars indicate Bragg positions.

All the samples were found to be single phase, iso-structural and crystallize in space group $Pc2_1n$. In this space group, Ga and Fe ions are distributed among 4 crystallographic sites: one gallium atom (Ga1) in a tetrahedral site whereas the other gallium (Ga2) and the two iron atoms (Fe1 and Fe2) are in octahedral sites [127]. Refinement of neutron diffraction patterns indicates the cationic site disorder in the system with Ga atoms occupying Fe sites and vice versa. In Cr doped samples (x = 0.1, 0.2) the above analysis shows that Cr preferentially occupies Ga2 site despite the method of preparation followed to restrict its occupancy to Fe site. The lattice parameters and cation occupancies are summarized in Table 6.1.

Table 6.1 Structural parameters obtained from Reitveld analysis of the Neutron Diffraction data.

$GaFe_{1-x}Cr_xO_3$		x=0.0	x=0.1	x=0.2
a (Å)		8.7298(9)	8.7102(9)	8.7070(10)
b (Å)		9.3797(8)	9.3501(7)	9.3479(8)
c (Å)		5.0774(4)	5.0612(5)	5.0600(5)
V ($Å^3$)		415.7(1)	412.2(1)	411.8(1)
Occupancy	Ga1 (Ga/Fe)	0.96/0.04	0.94/0.06	0.98/0.02
	Ga2	0.54/0.46/0.0	0.57/0.32/0.11	0.
	Fe1	0.87/0.13/0.0	0.78/0.18/0.04	0.77/0.12/0.11
	Fe2	0.63/0.37/0.0	0.66/0.29/0.005	0.77/0.10/0.13

The magnetization measurements on the samples were carried out on a SQUID magnetometer. Fig. 6.3 shows the zero field cooled magnetization (ZFC) data of $GaFeO_3$. The compound undergoes a ferrimagnetic transition at 210K. With doping of Cr the T_C reduces to 160K and 100K for x=0.1, and 0.2, respectively.

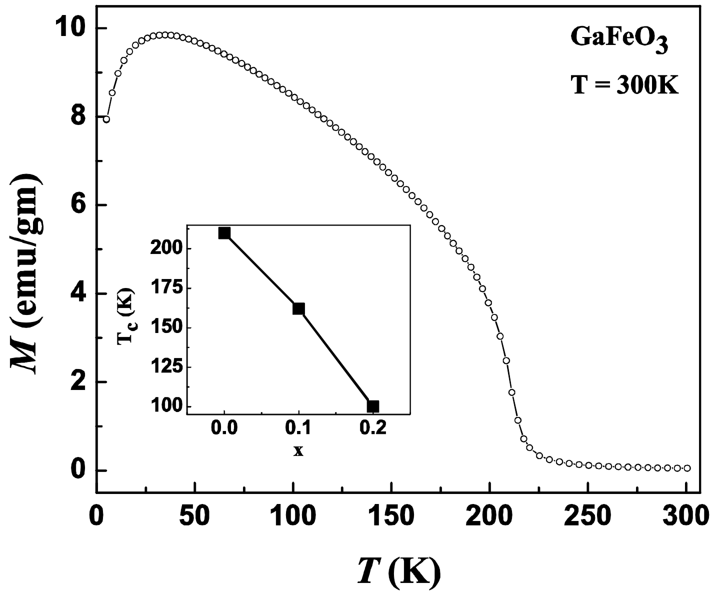

Figure 6.3 Temperature dependent magnetization of $GaFeO_3$ in zero-field-cooled (ZFC) condition under the field of 0.1 T. Inset shows the variation of Curie temperature with Cr content (x) in $GaFe_{1-x}Cr_xO_3$.

EXAFS measurements on the samples have been carried out at the Energy dispersive EXAFS beamline (BL-08) at INDUS-2 SRS, described in *Chapter 2.* For the EXAFS measurement at Ga K edge, the bent crystal polychromator of the beamline has been set at the proper Bragg angle so that a band of energy is obtained around Ga K edge of ~ 10367 eV. EXAFS spectra of a commercial Ga metal foil and commercial Lu_2O_3 powder has been used for calibration of the CCD channels in energy scale, assuming the reported values of Ga K-edge of 10367 eV and Lu L_3-edge of 10349 eV in Lu_2O_3. For the EXAFS measurements at Fe K edge similarly a band of energy is obtained around Fe K edge of ~ 7112 eV. EXAFS spectra of a commercial Fe metal foil and Gd_2O_3 pellet have been used for calibration of the CCD channels, assuming the reported values of Fe K-edge of 7112 eV and Gd L_3-edge of 7243 eV in Gd_2O_3. A closed cycle He based cryostat (Model no. DE-210 Cryo-cooler, Make: Advanced Research Systems) with two Kapton windows, described in *Chapter 2*, has been used for the EXAFS measurements of the samples over the temperature range of 25 K-300K.

Experimental EXAFS ($\mu(E)$ versus E) spectra of the undoped $GaFeO_3$ (GFO), 10% Cr doped $GaFeO_3$ (FCR-1) and 20% Cr doped $GaFeO_3$ (FCR-2) samples measured at Ga K edge and at various temperatures around the magnetic transition temperatures of the respective samples are shown in Figs. 6.4(a), while the corresponding FT-EXAFS spectra are depicted in Fig. 6.4(b) along with the best fit theoretical simulations. As explained previously in *Chapter 2*, for theoretical simulation of the FT EXAFS spectra, paths around a particular absorbing atom (either Ga1 or Ga2) have been generated using the FEFF code. In this case, the structural parameters of the samples obtained from the Rietveld fit of the neutron diffraction pattern as described above and given in Table 6.1 have been used for generating the starting structural model for EXAFS analysis. Fig. 6.5 shows the EXAFS data of undoped $GaFeO_3$ in k space.

It should be noted here that generally, under the IFEFFIT code, the crystallographic data is used as input in the ATOMS subroutine which then creates the different scattering paths of photoelectrons generated from an absorbing atom inside a lattice to finally yield the theoretical EXAFS spectrum. For example, in this case paths around a particular absorbing atom (either Ga1 or Ga2) can be generated using the ATOMS subroutine. However, since here the experimental spectra contain contributions from both the Ga atoms, the scattering paths have been manually generated around the Ga atoms (both Ga1 and Ga2) instead of using the ATOMS subroutine. The bond distances, co-ordination numbers (including scattering amplitudes) and disorder (Debye-Waller) factors (σ^2), which give the mean-square fluctuations in the distances, have been used as fitting parameters.

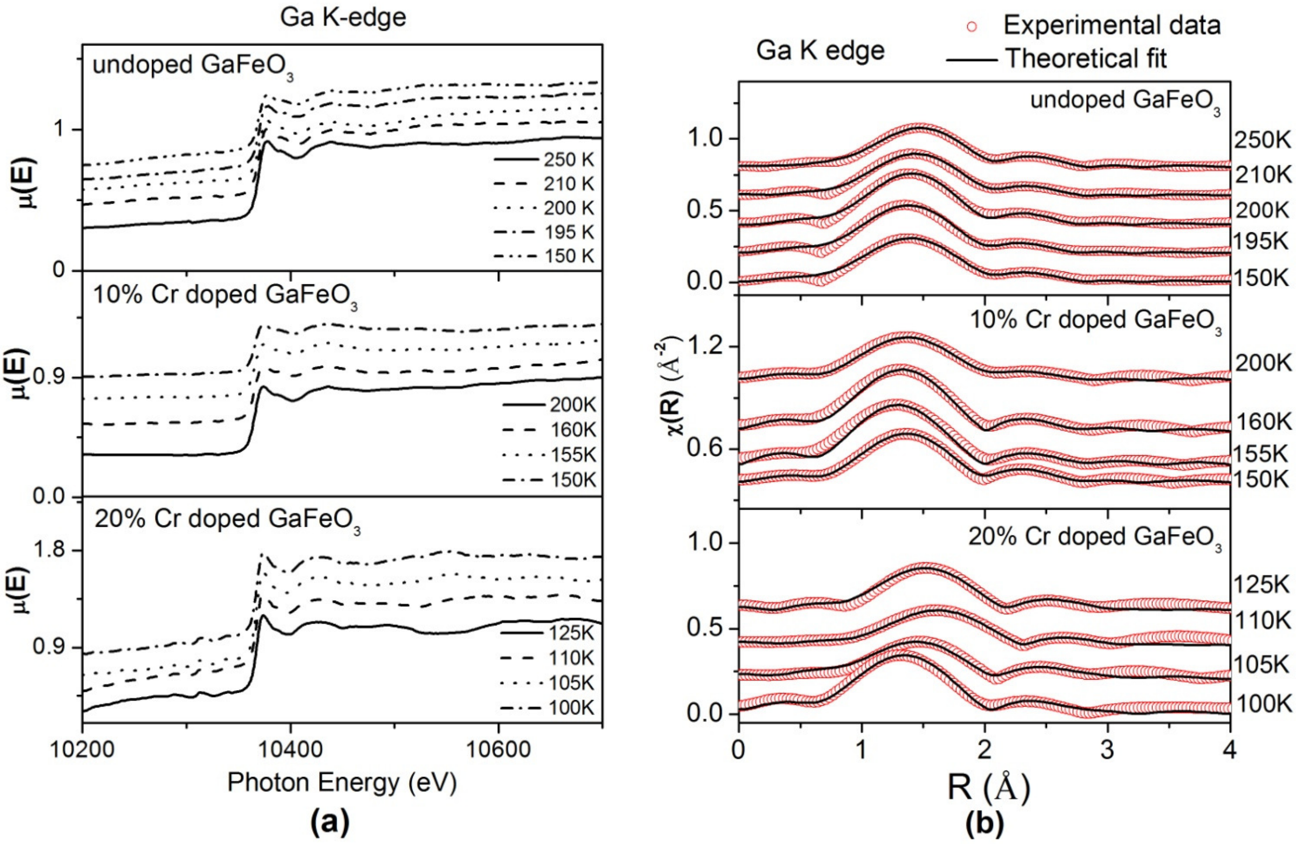

Figure 6.4 Temperature dependant experimental *μ(E) vs E* data at Ga K-edge and the corresponding FT-EXAFS spectra for undoped $GaFeO_3$, 10% Cr doped $GaFeO_3$ and 20% Cr doped $GaFeO_3$ respectively.

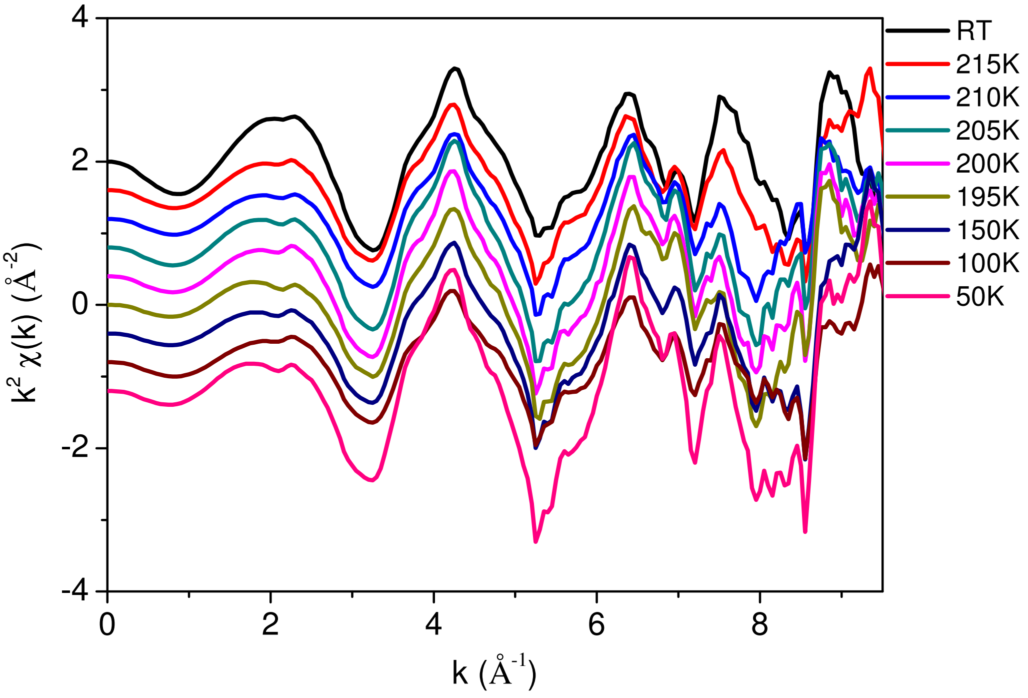

Figure 6.5 Temperature dependant experimental $k^2\chi(k)$ *vs k* data of undoped $GaFeO_3$ at Ga K-edge.

As evident from Fig. 6.4(b), a prominent peak is observed at ~ 1.5 Å (without phase correction) along with a smaller hump at ~ 2.5 Å (without phase correction) that can be fitted with the contributions from the six nearest single scattering (SS) paths around the central Ga atom as follows : Ga-O1 (1.86 Å), Ga-O2 (1.92 Å), Ga-O3 (2.02 Å), Ga-O4 (2.07 Å), Ga-Ga (2.95 Å) and Ga-Fe (2.98 Å) with coordination number (CN) of each path being 4, 1, 3, 2, 4 and 2 respectively. However, the Ga/Fe atoms have not been distinguished based on their positions as we have already incorporated that feature while modelling and we expect an average contribution of a single atom. The fitting has been performed in the R-range of 0 – 3.0 Å. The best fit room temperature bond length values at the Ga K edge are shown in Fig. 6.6 as a function of Cr doping concentration while in Fig. 6.7 the bond length values are shown for the GFO, FCR-1 and FCR-2 samples as a function of temperature.

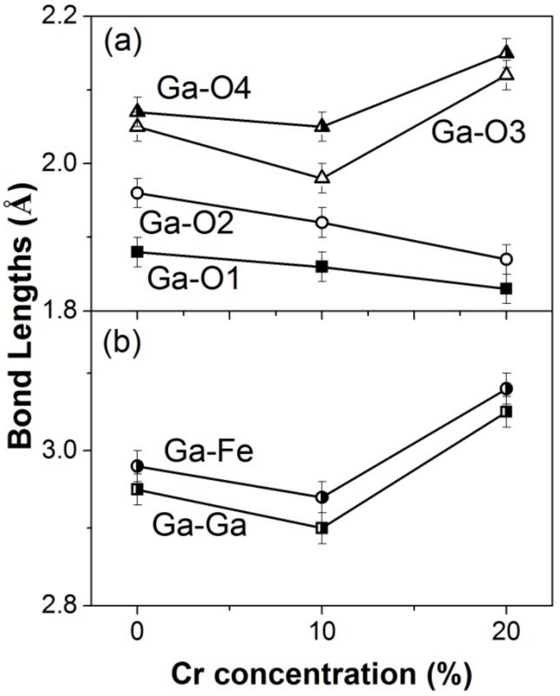

Figure 6.6 Variation of (a) Ga-O and (b) Ga-Ga/Fe bond lengths as a function of Cr doping concentration at Ga K edge as obtained from room temperature EXAFS data.

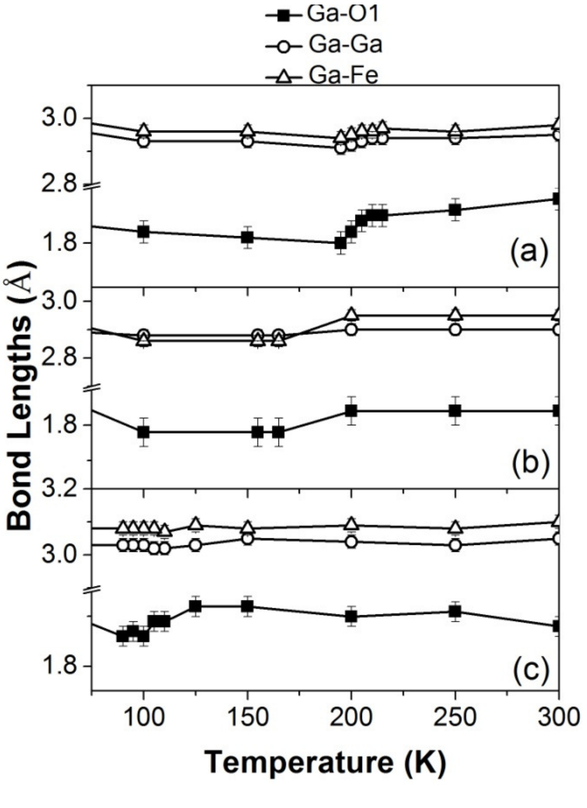

Figure 6.7 Variation of bond length around Ga sites for the (a) $GaFeO_3$ sample, (b) 10% Cr doped $GaFeO_3$ sample and (c) 20% Cr doped $GaFeO_3$ samples as a function of temperature at Ga K edge.

The temperature dependant experimental $\mu(E)$ vs E data at Fe K-edge for undoped $GaFeO_3$, 10% Cr doped $GaFeO_3$ and 20% Cr doped $GaFeO_3$ respectively are depicted in Fig. 6.8(a) whereas Fig. 6.8(b) shows the experimental $\chi(R)$ versus R spectra of the undoped $GaFeO_3$ (GFO), 10% Cr doped $GaFeO_3$ (FCR-1) and 20% Cr doped $GaFeO_3$ (FCR-2) samples at Fe K edge along with the best fit theoretical $\chi(R)$ versus R spectra.

Theoretical modelling for the data at Fe K edge has been carried out with the same crystallographic parameters as mentioned before [128] considering Fe to be the central atom. In this case also Fe has two different positions (both octahedrally coordinated) and this fact was taken into account while fitting the experimental data. In this case the paths have been generated assuming Fe1 and Fe2 separately as absorbing atoms and since it has been observed that the scattering paths generated around the Fe1 atom and the Fe2 atom are very close, the closely spaced paths are merged together combining their contribution towards the experimental data. The experimental data contains an average contribution due to both the Fe atoms which will be expressed eventually in the fitting parameters as will be explained later. The fitting region includes two peaks at ~ 1.5 Å and ~2.5 Å (without phase correction) in the R-range of 0 - 3.1 Å and incorporates the contribution of nine SS paths around the central Fe atom. The paths are Fe-O1 (1.98 Å), Fe-O2 (2.16 Å), Fe-O3 (2.30 Å), Fe-Ga1 (3.02 Å), Fe-Fe1 (3.05 Å), Fe-Ga2 (3.20 Å), Fe-Fe2 (3.25 Å), Fe-Fe3 (3.36 Å) and Fe-Ga3 (3.36 Å) with CN values 1, 1, 1, 2, 2, 2, 4, 1 and 4 as generated theoretically. The best fit room temperature bond length values at the Fe edge are shown in Fig. 6.9 as a function of Cr doping concentration while in Fig. 6.10 the bond length values are shown for the GFO, FCR-1 and FCR-2 samples as a function of temperature.

To support the experimental results, first principles calculations on the Cr doped $GeFeO_3$ system has also been carried out employing the Vienna Ab Initio Simulation Package (MedeA-VASP) [52]–[54] in combination with the projector augmented wave

(PAW) method [55] and generalized gradient approximation (GGA) [47]. For the planewaves, we have used an energy cut-off of 500 eV. A mesh consisting of about 500 K-points in the irreducible Brillouin zone has been used to calculate the total energies. The energy and force tolerance for our calculations were 10 meV and 10 meV per Angstrom, respectively.

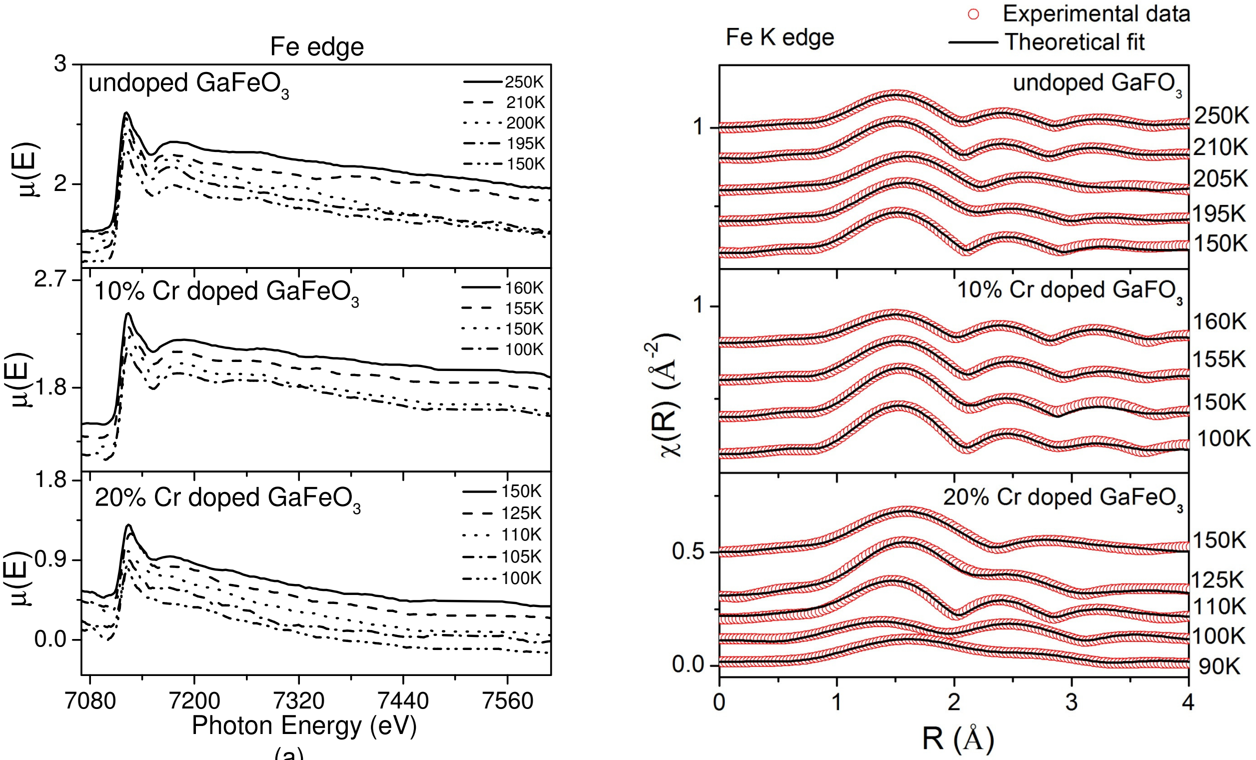

(a) (b)

Figure 6.8 (a) Temperature dependant experimental *μ(E) vs E* data at Fe K-edge and (b) the corresponding FT-EXAFS spectra for for undoped $GaFeO_3$, 10% Cr doped $GaFeO_3$ and 20% Cr doped $GaFeO_3$ along with the best fit theoretical curves respectively.

Geometries of the undoped $GaFeO_3$ as well as 12.5% and 25% Cr-coped $GaFeO_3$ systems have been fully optimized and the trends of change of volume and bond lengths as a result of Cr substitution have been obtained. The binding energies of these systems have subsequently been computed and shown in Table 6.2 for several cases of 12.5% Cr doped ($GaFe_{0.875}Cr_{0.125}O_3$) system viz., (i) Cr is substituted in Fe1 sites, (ii) Cr is substituted in Fe2 sites, (iii) Cr is substituted in Fe1 sites, where Ga1 and Fe1 have already been interchanged due to cationic site disorder and (iv) Cr is substituted in Fe1 sites where Ga2 and Fe1 are interchanged.

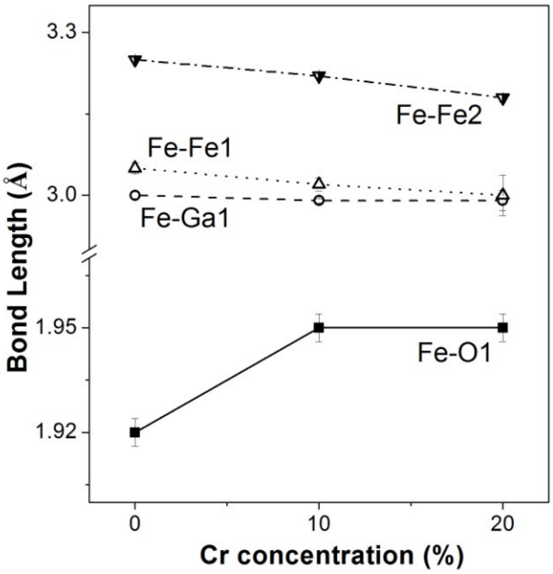

Figure 6.9 Variation of Fe-O and Fe-Fe/Ga bond lengths as a function of Cr doping concentration at Fe K edge as obtained from room temperature EXAFS data.

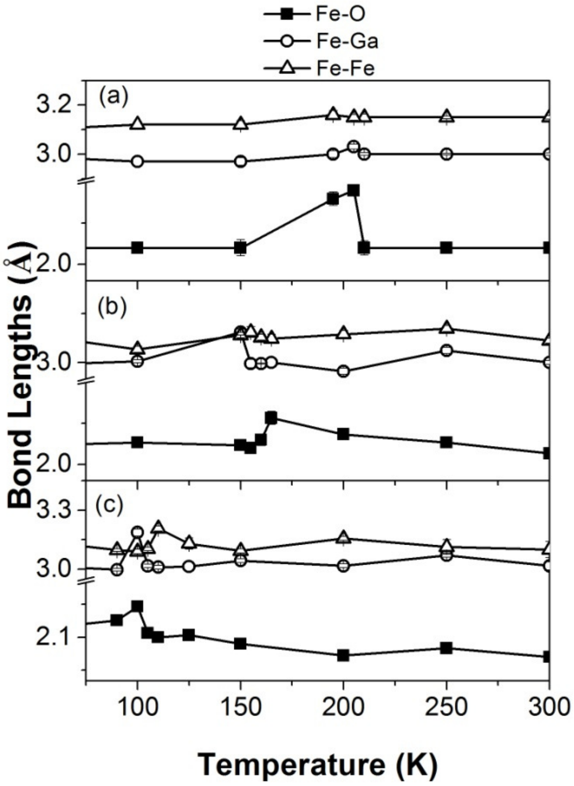

Figure 6.10 Variation of bond length around Fe sites for the (a) $GaFeO_3$ sample, (b) 10% Cr doped $GaFeO_3$ sample and (c) 20% Cr doped $GaFeO_3$ samples as a function of temperature at Fe K edge.

Table 6.2 Results of First Principle calculations on 12.5% Cr doped $GaFeO_3$ system.

Composition	Formation energy/atom(kJ/mol) obtained from VASP code	Binding or Cohesive energy/atom (eV)
$GaFe_{0.875}Cr_{0.125}O_3$	-154.76	-4.94
$GaFe_{0.875}Cr_{0.125}O_3$	-154.79	-4.94
$GaFe_{0.875}Cr_{0.125}O_3$	-151.77	-4.91
$GaFe_{0.875}Cr_{0.125}O_3$	-153.50	-4.92

In Cr doped samples (x=0.1, 0.2) neutron diffraction results (Table 6.1) show that volume contraction takes place. It has also been observed from the theoretical simulation that on 12.5% Cr-doping, $GaFeO_3$ system exhibits a contraction of volume from 437.34 Å^3 for the as-prepared system to 427.94 Å^3. The decrease in unit cell volume is consistent with the presumption that Cr occupies Fe sites in the $GaFeO_3$ lattice since octahedrally coordinated Fe^{3+} ion has an ionic radius of 0.65 Å whereas Cr^{3+} is smaller in size (0.62 Å). However, site occupancy results from neutron diffraction analysis (Table 6.1) show that Cr preferentially occupies Ga2 site despite the method of preparation followed, which should restrict its occupancy to Fe site. Though it contradicts the results presented by Saha *et al.* [122] obtained from X-ray diffraction data, however, as have been pointed out by Sharma *et al.* also [126] neutron diffraction data presented here should generally give better sensitivity in site occupancy due to better contrast in neutron scattering lengths between Fe and Ga atoms compared to their X-ray scattering strengths.

However, as in Fig. 6.6, the two nearest oxygen shells (named as Ga-O1 and Ga-O2) around the central Ga atoms, show a decrease in bond distance values as Cr doping concentration in the samples increases. This cannot be explained in terms of Cr occupancy in Fe sites. Since Cr is smaller than Fe, if Cr replaces Fe atoms, the Ga-O bond lengths would increase. However, the above results can be explained on the basis of the assumption that Cr doping enhances the cation site disorder i.e., more Fe atoms interchange positions with octahedral Ga2 atoms. Fe being larger than Ga, occupancy of Fe in Ga sites would reduce Ga-O bond lengths, and would increase Fe-O bond lengths, which is indeed observed from the EXAFS measurements (Fig. 6.9). This also causes decrease in the Fe-Fe1 and the Fe-Fe2 bonds as evident from Fig. 6.9, while Fe-Ga bonds remain unperturbed due to substitution of Cr atoms. Thus for the present Cr doped $GaFeO_3$ system, the EXAFS results indicate that Cr substitutes Fe atoms which occupy the Ga2 sites due to site disorder. From the energetics obtained by theoretical calculations also (Table 6.2), we observe that if we take the cohesive or binding energy for the $GaFe_{0.875}Cr_{0.125}O_3$ system, Cr substitution of Fe atoms which occupied the Ga2 sites is energetically possible. Thus the above results clearly establish the phenomenon of cationic site disorder i.e., interchanging of Fe1 and Fe2 atoms with Ga2 sites and vice-versa in the $GaFeO_3$ system and Cr doping enhances the site disorder. However, it is not possible from the above study to comment on preference of Cr substitution of Fe1 or Fe2 atoms since EXAFS measurement gives an average result over the all Fe atoms. Theoretical simulation (Table 6.2) shows both the cases are energetically similar and hence almost equally possible.

However, for the next two shells Ga-O3 and Ga-O4 in Fig. 6.6, the Ga-O bond length decreases upto 10% Cr doping, beyond which it again increases. This is probably due to the fact that at higher Cr doping concentration Cr is also replacing Ga atoms directly. It has been predicted by Saha *et. al.* [122] from their DFT calculations. Cr preferably occupies Ga2 site than Ga1 site and the octahedral Ga^{3+} (at Ga2 site) has a similar ionic radius (0.62 Å) as Cr^{3+}. Similar trend of variation is also observed in case of Ga-Fe and Ga-Ga bond lengths as shown in Fig. 6.6. Upward variation in lattice parameters with increase in Cr concentration has also been observed by Saha *et. al.* [122] for their $Ga_{1-x}Cr_xFeO_3$ samples where Ga is substituted by Cr atoms. It should be noted that the coordination number (CN) values for the above shells are mostly in accordance with the expected theoretical values upto 20% Cr doping which shows that Cr gets incorporated in the Fe or Ga sites in the 3+ state.

From the temperature dependence of the bond length values surrounding the Ga site, as seen from Fig. 6.7, there is an obvious effect at the magnetic transition temperature as evident from the changes in bond length values corresponding to each of the neighbouring shells. In case of undoped $GaFeO_3$, as can be seen from Fig. 6.7(a), the bond length values suffer significant reduction around the magnetic transition temperature of 200K. This trend is observed in the nearest neighbour oxygen and distant gallium and iron shells around the central Ga atom. It is to be noted here that in the above figures the average of the four Ga-O bonds viz., Ga-O1, Ga-O2, Ga-O3 and Ga-O4 has been given as Ga-O bond. Similar sudden decrease in the bond length values for the Ga-O, Ga-Ga and Ga-Fe bond lengths near the magnetic transition temperatures of 150 K and 100 K have also been observed in Figs. 6.7(b) and (c) also for the 10% Cr doped $GaFeO_3$ (FCR-1) and 20% Cr doped $GaFeO_3$ (FCR-2) samples respectively. Fig. 6.10 shows that for all the samples viz., undoped $GaFeO_3$, 10% Cr doped $GaFeO_3$ and 20% Cr doped $GaFeO_3$, the Fe bond lengths increase at the magnetic transition temperature below which they again gradually reduce.

Thus the above results clearly indicate a change in local structural parameters around Ga and Fe atoms across the magnetic transition temperature in $GaFeO_3$ though it has been reported by various authors that there is no long range structural phase change in these systems across T_c. Sharma *et al.* [126] have recently reported changes in phonon spectrum corresponding to Fe atoms around the magnetic transition temperature in $GaFeO_3$ from their Mössbauer studies. The EXAFS results suggest that the appearance of ferrimagnetism in $GaFeO_3$ systems below T_c is related to cationic site disorder i.e., higher occupancy of Fe in Ga2 sites and since Fe^{3+} has a higher ionic radius compared to Ga^{3+}, Fe in Ga sites leads to decrease in bond lengths in Ga sub lattice and increase in bond length in Fe sub lattice.

Further, decrease in T_c as Cr doping increases shows that Cr doping enhances site disorder in the system which agrees with our room temperature results discussed earlier. Finally, it should be noted that the change in the bond lengths near Ga and Fe sites at the magnetic transition temperature might be the reason for the dielectric anomaly observed at the magnetic transition temperature in $GaFeO_3$.

Conclusions

EXAFS measurements have been carried out on undoped and Cr doped $GaFeO_3$ samples both at Ga and Fe K edges at various temperatures in the regime of 25-300 K, to explore the changes in local structure surrounding the cations (viz., Ga and Fe) in $GaFeO_3$ due to Cr substitution and across its magnetic transition temperature. Neutron diffraction results show decrease in unit cell volume on Cr doping which indicates substitution of Fe atoms by Cr while site occupancy results show preferred occupancy of Ga sites by Cr. Analysis of FT-EXAFS spectra however show decrease in Ga-O bond lengths and increase in Fe-O bond lengths on Cr doping which clearly indicate higher occupancy of Fe atoms in octahedral Ga2 sites on Cr substitution. Thus the above results help to establish the mechanism of Cr doping in a microscopic scale where Cr preferentially substitutes Fe atoms which are in Ga2 sites or in other words Cr substitution enhances the cationic site disorder in the $GaFeO_3$ system. The results have also been supported by the first principles calculations on the Cr doped $GaFeO_3$ system, which shows that the system with Cr substituting Fe with a cationic site disorder, between octahedral Fe and Ga, is energetically similar to the cases of direct replacement of Cr at the Fe1 or Fe2 site.

Analysis of the temperature dependent EXAFS data on the undoped $GaFeO_3$, 10% Cr doped $GaFeO_3$ and 20% Cr doped $GaFeO_3$ samples show decrease in the values for the Ga-O, Ga-Ga and Ga-Fe bond lengths near the magnetic transition temperatures of 200 K, 150 K and 100 K respectively. This undoubtedly establishes cation site disorder i.e., occupancy of

Fe ions at Ga2 site, as a reason for magnetic transition in $GaFeO_3$ systems. The above results also corroborate the results of EXAFS measurements at Fe edge which show increase in the bond length values at the Fe sites near the magnetic transition temperature.

Chapter 7

EXAFS MEASUREMENTS ON OPTO-ELECTRONIC THIN FILMS

Gallium–arsenide–nitride (GaAsN) is an important optoelectronic material, whose optical properties can be tailored from GaAs-like to GaN-like semiconductor, thus covering a wide optical region from near-infrared to ultraviolet [130]. However, unlike group III-nitride based alloy systems, GaN and GaAs have limited miscibility on either end of the composition axis and the miscibility gap has been attributed to large mismatch in their lattice constants. Weyers *et.al.* [131], who were the first to report the growth of arsenic rich GaAsN alloy films, containing 2% nitrogen by plasma assisted metal organic chemical vapour deposition (MOCVD) found a considerable red shift in absorption edge and photoluminescence with increasing nitrogen content, which was attributed to severe band gap bowing. Subsequent reports on arsenic rich side of GaAsN alloy films [132]–[134] have shown that though the bowing parameter was large (~20 eV) at small concentrations of nitrogen, the change of band gap was highly non-linear, which resulted in a reduction of the bowing parameter at larger nitrogen concentrations. The interest in Nitrogen-rich side of GaAsN alloys, which are attractive for devices functioning in the infrared region, has dealt with impurity issues like arsenic concentrations in GaN films [135]–[137]. It was also reported that the As-doped GaN films deposited by molecular beam epitaxy (MBE) show a strong blue emission [138].

In all the above mentioned reports, GaAsN alloy films have been deposited by MOCVD, MBE or their minor variations. Efforts have also been made to deposit GaAsN alloy films by sputtering of GaAs target at various ambient conditions, with either nitrogen [139] or nitrogen–argon mixture [140], [141]. The sputtered films were mostly nitrogen-rich, but were amorphous [139], nano-whickered [140], or polycrystalline [141]. It has been shown earlier that polycrystalline [142], nanocrystalline [143] or amorphous GaN_x film deposited by sputtering and ion beam assisted deposition [144], show good luminescence characteristics. Hence, the possibility of depositing polycrystalline $GaAs_xN_{1-x}$ alloy films by sputtering technique, which is inherently suited for the deposition of large area thin films on a variety of substrates at relatively lower temperatures, opens up enormous opportunities for this alloy system.

In a recent work from our group [141] it has been shown that nitrogen-rich, polycrystalline $GaAs_xN_{1-x}$ alloy films can be formed at a substrate temperature of $500^{\circ}C$, by sputtering of a GaAs target in a mixture of argon and nitrogen as the sputtering atmosphere. GaAsN films were deposited on quartz substrates by rf magnetron sputtering of a 3 in. wafer GaAs target in sputter down configuration and the arsenic to nitrogen ratio in the films was varied by changing the relative percentage of nitrogen in the argon–nitrogen sputtering atmosphere, from 0% to 100%. From our earlier studies [145] on these samples it had been observed that for films deposited with 12% or more nitrogen in sputtering ambient, films are polycrystalline GaN with their refractive index, extinction coefficient and band gap values resembling that of hexagonal GaN. For films deposited with <5% nitrogen, As content increases significantly and the films are mostly amorphous with their optical parameters approaching that of amorphous GaAs. Films deposited with 5–12% nitrogen in the sputtering atmosphere, however, clearly show effects due to the incorporation of arsenic in the lattice and the consequent formation of polycrystalline $GaAs_xN_{1-x}$ alloy films. As the nitrogen percentage in the sputtering atmosphere is decreased from 12% to 5%, the As fraction (x) in the lattice increases from 0.01 to 0.08 and consequently the optical band gap decreases from 3.39 eV to 2.57 eV in a non-linier fashion with a bowing parameter of 15.5 eV.

Here, we have probed the changes in the local structures in these alloy films as a function of nitrogen percentage by Extended X-ray Absorption Fine Structure (EXAFS) measurements carried out both at Ga and As edges. EXAFS, which probes the local structure around a particular species of atom in a sample does not depend on the long range order in the samples, is particularly important for this system since at low nitrogen concentration the films are mostly amorphous and X-Ray Diffraction fails to give any useful information for the samples. Since EXAFS measurement on these thin films at the Energy Dispersive EXAFS beamline (BL-09) by the normal transmission mode was not possible due to the presence of thick quartz substrates of the films, the measurements were carried out in fluorescence mode in a slightly modified configuration of the beamline, called the "Turbo-EXAFS" configuration as described in detail in *Chapter 2*.

7.1 Measurement at Ga K-edge

At Ga K-edge the normalized experimental EXAFS spectra depicts obvious changes in the local environment around the central Ga atom. From Fig. 7.1 it is evident that with an increase in the nitrogen concentration during sputter deposition, the peaks denoted by A, B and C, become more prominent. In addition to that, on closer inspection as shown in the inset of Fig. 7.1, it is observed that there is a clear shift in the position of absorption edge towards higher energy with increase in nitrogen concentration. Shift in absorption edges of cations, known as the *chemical shift*, takes place due to a change in oxidation state of an element.

The absorption edge shift is governed by many other factors also viz., nature of the ligands to the metal ion, coordination numbers, covalent character of the bond, electronegativity of the anion, etc. i.e. the chemical environment of the metal ion. All these effects can be quantitatively described by a hypothetical parameter known as the '*effective charge' (q)*.

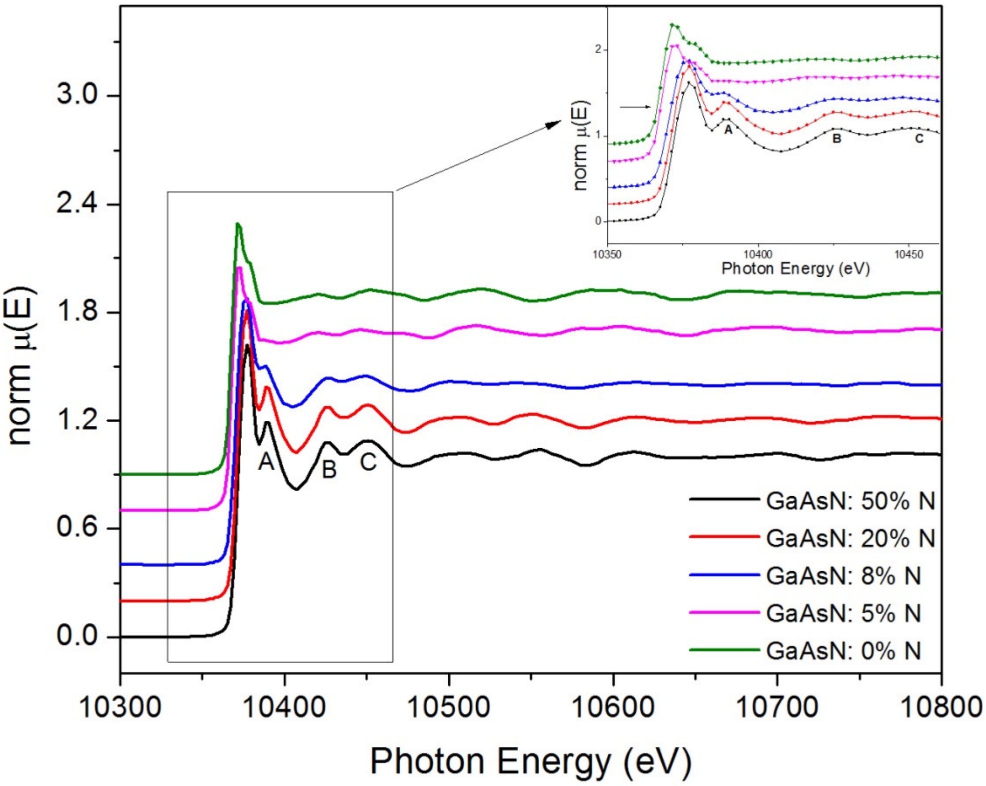

Figure 7.1 Normalized EXAFS spectra of $GaAs_{1-x}N_x$ thin films at Ga K-edge. (The spectra are shifted vertically for clarity).

Formation of chemical bond in a compound involves redistribution of valence electrons of the constituent atoms and effective charge gives a measure of the charge residing over the cation when it forms a bond with a ligand. In case of both GaN and GaAs compounds, the Ga atom is in +3 oxidation state thus implying that in this case the chemical shift definitely arises due to a change in its chemical environment. Several empirical relations [146]–[149] have been proposed in the literature to estimate the effective charge on a metal cation in a compound. According to Suchet's method [150] the effective charge on a cationic species involved in formation of a chemical bond is given by:

$$q = n\left[1 - 0.01185\left(\frac{z}{r'} + \frac{z'}{r}\right)\right] \tag{7.1}$$

where Z, r, and n are, respectively, the total number of electrons, the ionic radius and the oxidation number of the cation and the primed symbols refer to the anion in the compounds. The Pauling's method to estimate effective charge on the other hand, is represented by the following relation [151]**:**

$$q = nI \tag{7.2}$$

where n is the valence of the absorbing cation and I is the ionicity of the metal–ligand bond calculated as below

$$I = 1 - \frac{n}{c}\exp\left[-\frac{(X_1 - X_a)^2}{4}\right] \tag{7.3}$$

where X_l and X_a are the electronegativities of the ligand and the absorbing atom, respectively, and c is the coordination number of the absorbing atom. The above expression for ionicity of a partially covalent bond is found to agree with experimentally observed electric dipole moment of many standard molecules [151]**.** The electronegativity values for Ga, As and N are 1.81, 2.18 and 3.04 respectively which implicates that Ga-As bonding would be less ionic (more covalent in nature) than Ga-N bonding. Thus in the present case the effective charge on Ga atom in GaN has been calculated using Suchet's formula whereas for the Ga atom in GaAs, Pauling's method has been employed and the values obtained are 1.56 and 0.83 respectively. As a consequence of higher effective charge on Ga in GaN, more energy is required to extract a core shell electron from the Ga atom and thus explains the shift in the absorption edge towards higher energy values at higher nitrogen concentrations.

The gradual structural changes in the $GaAs_{1-x}N_x$ thin film samples are displayed in Figs. 7.2 and 7.3. The $\chi(k)$ spectra, depicted in Fig. 7.2, shows the appearance of new peaks with increase in nitrogen concentration. The FT-EXAFS $\chi(R)$ spectra, as shown in Fig.7.3, also depicts the gradual transformation of a single peak at ~ 2.2 Å for 0-5% nitrogen concentration to two peaks at ~ 1.6 Å and ~ 2.7 Å, as in Fig. 7.3, with the amplitude of the latter peaks increasing as nitrogen concentration increases from 8-50%. These observations suggest that these thin films undergo a conversion from cubic GaAs to hexagonal GaN.

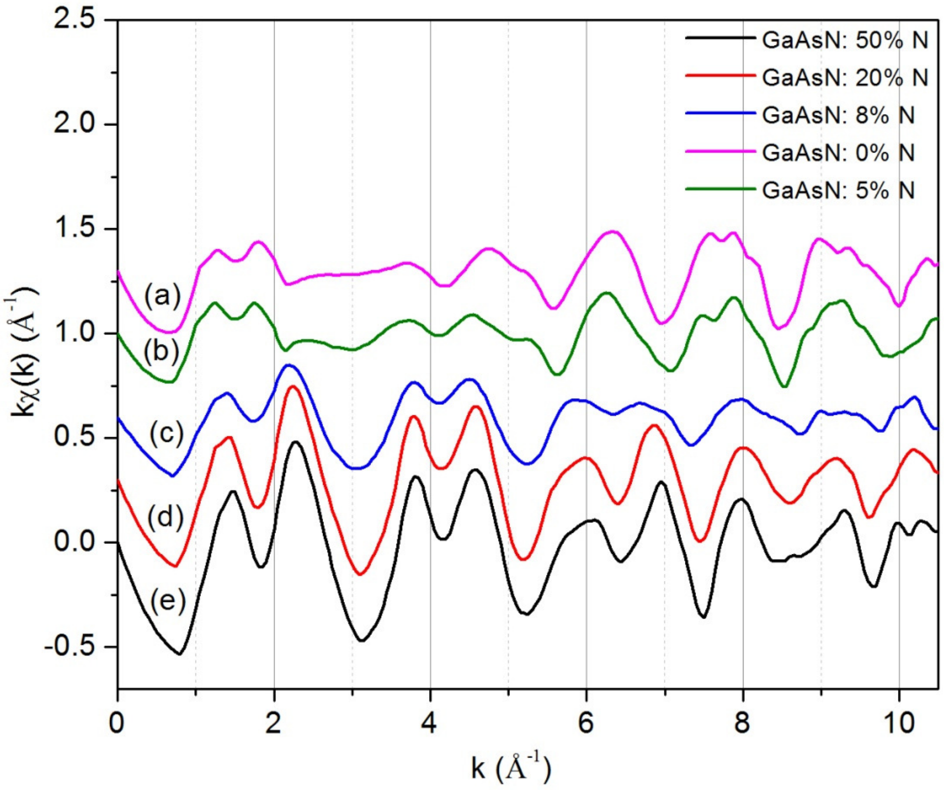

Figure 7.2. The $\chi(k)$ *vs k* spectra for $GaAs_{1-x}N_x$ thin films at Ga K-edge.

To fit the experimental FT-EXAFS spectra of the samples, the $GaAs_{1-x}N_x$ thin film samples have been modelled with a standard structure of GaN [152] or GaAs [153] or a combination of both, depending on the sputtering atmosphere i.e. the amount of nitrogen concentration present during film deposition. The crystallographic parameters were used as input in the ATOMS program as has been mentioned in *Chapter 2*. The data fitting has been performed in the *R*-range of ~ 0 – 3.8 Å at Ga K edge and *R*-range of ~ 0 – 4.5 Å at As K edge. The best fit parameters are presented in Table 7.1 which shows that there is no significant deviation in the Ga-As and Ga-Ga bond length values as nitrogen concentration is increased from 0-8% or Ga-N and Ga-Ga bond length values as nitrogen concentration is increased from 8-50%. However, there are definite changes in the respective coordination numbers around the probed Ga atom as represented in Fig. 7.4. Arsenic co-ordination decreases rapidly while nitrogen coordination increases around Ga atoms as the nitrogen concentration is increased beyond 8% in the sputtering atmosphere.

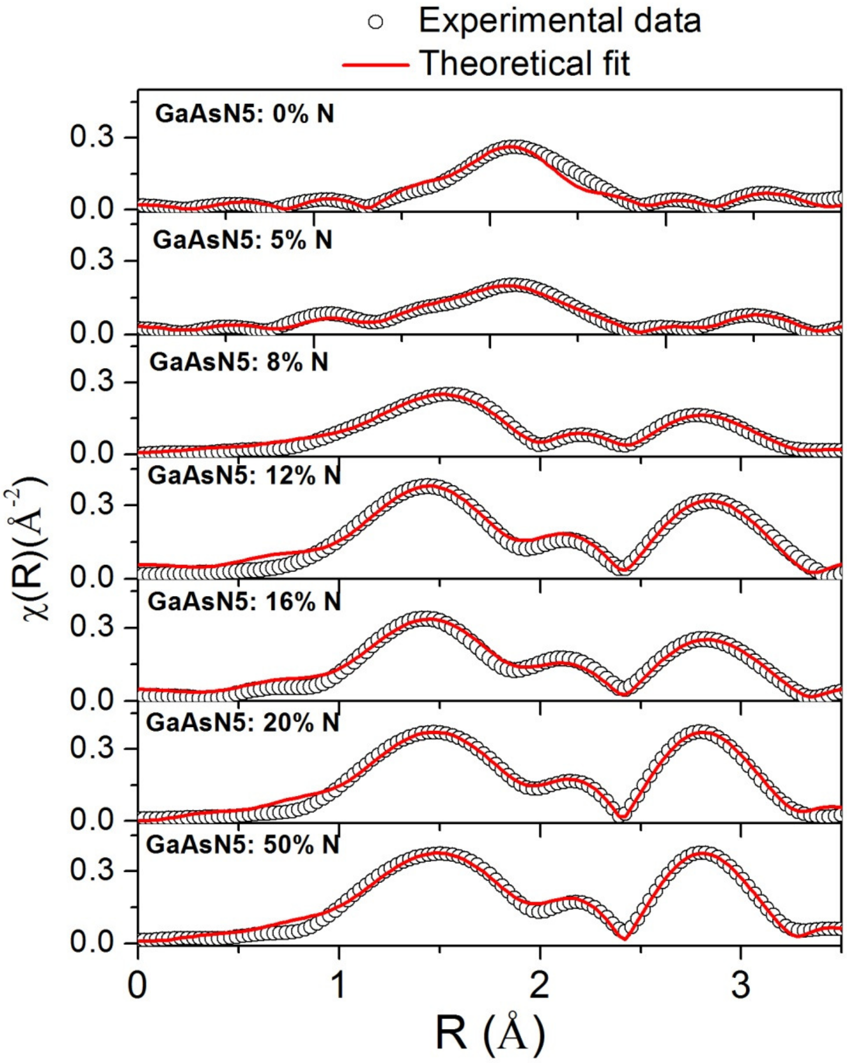

Figure 7.3 The experimental *$\chi(R)$ versus R* spectra of $GaAs_{1-x}N_x$ thin films at Ga K-edge along with the best fit theoretical spectra.

The above observations imply the realization of $GaAs_{1-x}N_x$–type films prepared in the nitrogen concentration range of 0-12%, where contribution of GaAs decreases whereas that of GaN increases as the nitrogen concentration is increased in the sputtering atmosphere. This has been further confirmed by As-edge EXAFS measurements of the samples. It can also be seen from Fig. 7.3 that the FT-EXAFS spectra of the films grown at 12% or more nitrogen in sputtering atmosphere resemble the spectrum of pure GaN sample prepared at 50% nitrogen atmosphere.

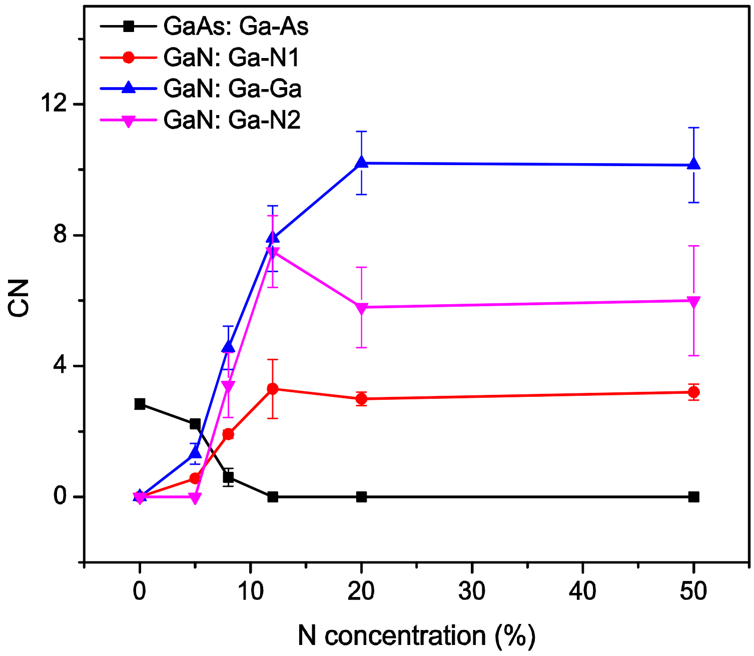

Figure 7.4 Variation of coordination numbers of the neighbouring shells surrounding the central Ga atom in the $GaAs_{1-x}N_x$ thin films at Ga K-edge.

7.2 Measurement at As K-edge

The measurement at As K edge has given reliable spectra for the samples prepared in the sputtering atmosphere containing upto 8% nitrogen beyond which the edge jump value at As edge was significantly low to get a reasonably good EXAFS spectrum. The normalized experimental EXAFS spectra of the samples, as in Fig. 7.5, for the films deposited at 0, 5 and 8% nitrogen concentration in sputtering ambient depict no prominent changes as nitrogen concentration is increased. The $\chi(k)$ spectra of the three samples are similar though the sample prepared under 8% nitrogen shows some subtle difference as can be seen from Fig. 7.6. The FT-EXAFS $\chi(R)$ spectra, however, shows that a new peak appears at ~ 2.8 Å for the sample prepared under 5% nitrogen and its amplitude increases for the next sample that has been prepared under 8% nitrogen while the amplitude of the first peak at ~ 2.1 Å decreases with increase in nitrogen concentration. To consider the possible contribution of both GaAs and GaN structure, the nitrogen atom in GaN was replaced by As atom and the theoretical modeling of the experimental data was performed.

Table 7.1 Best fit parameters at Ga-K edge

Ga K-edge								
		GaAs			GaN			
		Ga-As	Ga-Ga	Ga-As	Ga-N	Ga-Ga	Ga-N	Ga-N
Theoretical R		2.44	3.99	4.69	1.95	3.18	3.22	3.74
Theoretical CN		4	12	12	4	12	1	9
GaAsN: 0% N	σ^2	0.0005 ± 0.0005	0.006 ± 0.004					
	R	2.42	3.93					
	CN	2.8 ± 0.2	2.4 ± 1.1					
	R-factor	0.039						
GaAsN: 5% N	σ^2	0.001 ± 0.0004	0.008 ± 0.002	0.01 ± 0.002	0.001 ± 0.003	0.01± 0.003		
	R	2.40	3.94	4.59	1.89	2.88		
	CN	2.2 ± 0.1	5.0 ± 1.0	7.7 ± 1.3	0.6 ± 0.07	1.3 ± 0.3		
	R-factor	0.019						
GaAsN: 8% N	σ^2	0.005 ± 0.004			0.0003 ± 0.002	0.007 ± 0.002	0.006 ± 0.01	0.012 ± 0.01
	R	2.45			1.96	3.18	3.18	3.68
	CN	0.6 ± 0.3			1.9 ± 0.1	4.6 ± 0.7	1.4 ± 0.6	3.4 ± 1.0
	R-factor	0.035						
GaAsN: 10% N	σ^2				0.002 ± 0.002	0.006 ± 0.002	0.006	0.009 ± 0.007
	R				1.93	3.18	3.19	3.65
	CN				2.9 ± 0.2	7.1 ± 1.0	1.0 ± 0.8	5.8 ± 1.2
	R-factor	0.029						
GaAsN: 12% N	σ^2				0.0015	0.006 ± 0.001	0.009 ± 0.02	0.005 ± 0.004
	R				1.93	3.17	3.17	3.63
	CN				3.3 ± 0.9	7.9 ± 1.0	1.5 ± 0.8	7.5 ± 1.1
	R-factor	0.02						
GaAsN: 16% N	σ^2				0.001 ± 0.003	0.006 ± 0.002	0.003	0.008 ± 0.006
	R				1.93	3.17	3.18	3.64
	CN				2.9 ± 0.2	3.2 ± 0.5	1	5.6 ± 1.2
	R-factor	0.031						
GaAsN: 20% N	σ^2				0.002 ± 0.002	0.006 ± 0.001	0.006 ± 0.014	0.008 ± 0.007
	R				1.93	3.17	3.19	3.65
	CN				3.0 ± 0.2	10.2 ± 1.0	1.6 ± 0.8	5.8 ± 1.2
	R-factor	0.029						
GaAsN: 50% N	σ^2				0.004 ± 0.002	0.006 ± 0.001	0.006 ± 0.02	0.013 ± 0.009
	R				1.93	3.16	3.16	3.67
	CN				3.2 ± 0.2	10.1 ± 1.1	1.1 ± 0.8	6.0 ± 1.7
	R-factor	0.036						

Fig. 7.7 shows the experimental $\chi(R)$ versus R spectra of $GaAs_{1-x}N_x$ thin films at As K-edge along with the best fit theoretical spectra and the best-fit results have been shown in Table 7.2**.** It was indeed found that for samples prepared under 5% and 8% nitrogen concentration there was a contribution from the GaN structure. The variation of coordination numbers around As is presented in Fig. 7.8. and it shows that with an increase in nitrogen concentration the contribution from GaN structure increases.

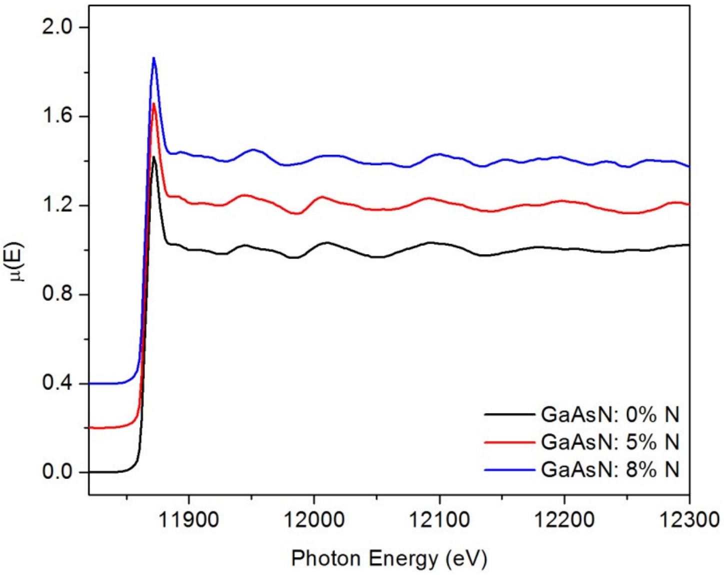

Figure 7.5 Normalized EXAFS spectra of $GaAs_{1-x}N_x$ thin films at As K-edge.

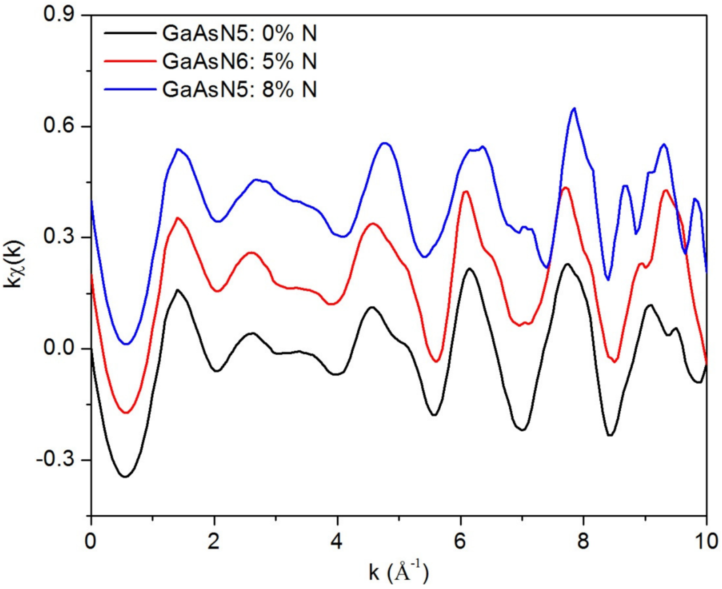

Figure 7.6 The $\chi(k)$ *vs k* spectra for $GaAs_{1-x}N_x$ thin films at As K-edge.

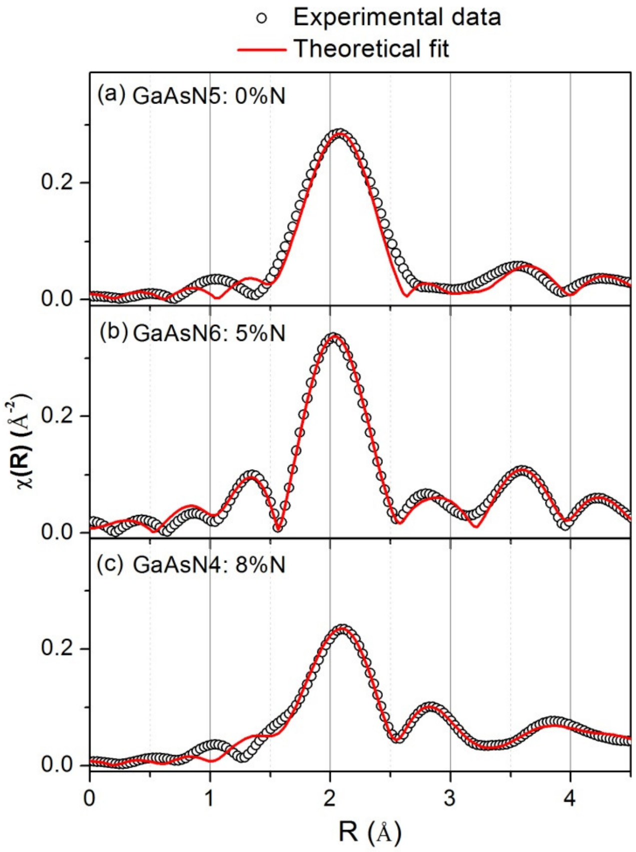

Figure 7.7 Experimental *$\chi(R)$ versus R* spectra of GaAs$_{1-x}$N$_x$ thin films at As K-edge along with the best fit theoretical spectra.

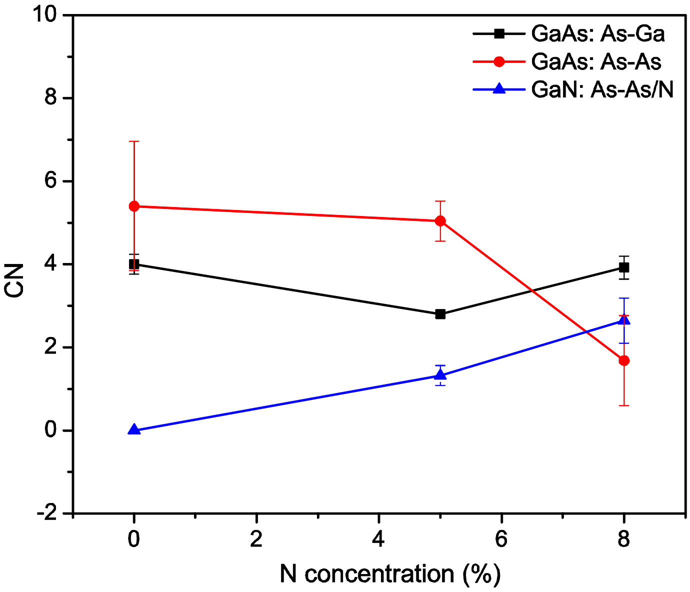

Figure 7.8 Variation of coordination numbers of the neighboring shells surrounding the central As atom in the GaAs$_{1-x}$N$_x$ thin films at As K-edge.

Table 7.2 Best fit parameters at As-K edge

As K-edge									
		GaAs			GaN : N replaced by As				
		As-Ga	As-As	As-Ga	As-Ga	As-As	As-As	As-As	As-Ga
Theoretical R		2.45	3.99	4.68	1.95	3.18	3.19	4.5	4.53
Theoretical CN		4	12	12	3(3+1)	6	6	6	6
GaAsN: 0% N	σ^2	0.005 ± 0.0004	0.011 ± 0.008	0.019 ± 0.005					
	R	2.42	3.93	4.64					
	CN	4.0 ± 0.2	5.4 ± 1.6	11.0 ± 5.2					
	R-factor	0.04							
GaAsN: 5% N	σ^2	0.0007 ± 0.0002	0.005± 0.0008	0.014 ± 0.002	0.016 ± 0.001	0.003 ± 0.001			
	R	2.39	3.94	4.57	1.73	3.30			
	CN	2.8 ± 0.1	5.0 ± 0.5	10.8 ± 1.9	1.3 ± 0.2	1.3 ± 0.2			
	R-factor	0.007							
GaAsN: 8% N	σ^2	0.006 ± 0.001	0.002± 0.003			0.005± 0.002	0.022 ± 0.005	0.01 ± 0.004	0.009 ± 0.004
	R	2.42	3.99			3.11	3.49	4.34	4.74
	CN	3.9 ± 0.3	1.7 ± 1.1			2.6 ± 0.5	10.0 ± 2.8	5.3 ± 2.5	6.3 ± 2.3
	R-factor	0.06							

Conclusion

A series of GaAsN thin films have been prepared by reactive magnetron sputtering of GaAs targets in the mixed ambient of Ar and nitrogen at different Ar to nitrogen ratios. In an earlier communication, we have presented our results on the optical properties of these opto-electronically important samples by spectroscopic ellipsometry technique. To give further insight into the above macroscopic observation, we have carried out fluorescence EXAFS measurements on these samples in Turbo-EXAFS configuration at the Energy Dispersive EXAFS beamline (BL-08) of INDUS-2 SRS at both Ga and As K edges. The above observations support our earlier findings on this system that the properties of these films, prepared with more than 12% nitrogen in the sputtering ambient, are GaN-like, with their refractive index, extinction coefficient and band gap values resembling that of hexagonal GaN, while for nitrogen concentration in the range of 5-12%, $GaAs_xN_{1-x}$ alloy films are realized where contribution of GaAs decreases whereas that of GaN increases rapidly as the nitrogen concentration is increased beyond 8% in the sputtering atmosphere.

Chapter 8

SUMMARY

The initial chapters of this thesis establish the motivation for using the XAS technique as an experimental tool and a basic introduction of its theory and relevant experimental setup. This technique, though in principle is possible with a laboratory-based source with an X-ray tube, EXAFS data is more realiable and accurate when measured with a tunable and bright x-ray source such as a synchrotron light source. With the advent of modern bright synchrotron radiation sources, EXAFS technique has emerged out to be very powerful for local structure determination.

INDUS-2 at RRCAT, Indore, India is the national hard X-ray synchrotron facility accessible to all researchers from national laboratories, academic institutions and industries in India. The Energy dispersive EXAFS beamline (BL-08) which has been utilized extensively in this thesis work is one of the first beamlines to be commissioned/operational at this synchrotron facility. The wide variety of samples studied in this thesis have potential applications in varied fields of technological importance such as solid oxide fuel cells, spintronics, optoelectronics, as luminescent materials, mulitiferroics etc. These samples have been studied by EXAFS as a part of the user support program to demonstrate the applicability of this technique in explaining the macroscopic behaviour of the respective samples. The EXAFS technique provides accurate information concerning the immediate environment of the probed element which is not accessible by other characterization techniques. This technique also has less number of constraints in terms of sample morphology or environment. In all the cases described in this thesis the various subroutines available under the IFEFIT programme module has been used for the analysis of the EXAFS data. This includes data reduction and Fourier transform to derive the $\chi(R)$ versus R spectra from the absorption spectra (using ATHENA software), generation of the theoretical EXAFS spectra starting from an assumed crystallographic structure and finally fitting of the experimental data with the theoretical spectra using the FEFF 6.0 code (using ARTEMIS software). The best fit results data have been chosen by the minimum R-factor obtained as described in *Chapter -2* and the errors involved in the whole procedure have been estimated in all the cases.

The first study deals with the identification of the most effective dopant for oxygen vacancy generation in zirconium oxide samples doped with trivalent rare earth ions, as a possible ion conducting electrolyte, to be used in solid oxide fuel cells. Structural information obtained from XRD was confirmed by EXAFS theoretical modelling. On careful analysis of the EXAFS data obtained from experimental measurements, Gd was identified as the most appropriate among the possible contenders of Gd, Nd and La primarily because Gd is found to cause the maximum reduction of oxygen coordination at Zr sites. The most effective Gd concentration for optimum vacancy creation was estimated to be ~9%. The measurements were carried out with Zr as well as Gd being the probed atom and the results were found to be consistent.

The next chapter is focussed on the study of luminescence properties of three different systems having different applications. The first set of samples was Eu doped gallium oxyhydroxide (GaOOH) nanorods which form the precursors for obtaining Ga_2O_3 based luminescent devices. However, even the presence of a small amount of Eu ions during the synthesis process is found to lead to a complete destruction of its crystalline structure. The XRD peaks clearly portrayed the amorphisation of the sample from the initial crystalline structure. Interestingly, EXAFS spectra at the Ga K-edge were identical for each sample, and even with a Eu doping of 3 at.% concentration there was no change in bond length values around Ga sites. It suggests the fact that the local environment around Ga was not perturbed and the Eu ions might be going to inter layer spacing. This was confirmed from supporting vibrational studies which showed that Eu ions interacted with hydroxyl groups to form europium hydroxide that finally led to the destruction of long range order in the system. Hence, the reason for the amorphisation of these samples upon Eu incorporation was accurately determined.

The second set of samples is $SrSnO_3$ nanorods which have potential applications in lithium-ion batteries, high-temperature humidity sensors, capacitor components with a small temperature coefficient of capacitance, etc. However, we are particularly interested in the luminescence property of this material. Lanthanide ion (viz., Eu^{3+}) doping in such materials is an option for making efficient luminescent materials**.** For $SrSnO_3$ sample containing 0.5 at % Eu^{3+} ions, the emission spectrum mainly consists of a sharp peak around 590 nm which is a characteristic of $^5D_0 \rightarrow {}^7F_1$ transition along with a very weak peak around 612 nm which is a characteristic of $^5D_0 \rightarrow {}^7F_2$ transition of Eu^{3+} ions. In the centro-symmetric environment, only the magnetic dipole transition ($^5D_0 \rightarrow {}^7F_1$) is allowed and the electric dipole transition ($^5D_0 \rightarrow {}^7F_2$) is forbidden. For these samples, the relative intensity ratio of $^5D_0 \rightarrow {}^7F_2$ to $^5D_0 \rightarrow {}^7F_1$ transition, known as the *asymmetric ratio of luminescence*, is a measure of the symmetry of the local environment around Eu^{3+} ions in the lattice. Smaller the asymmetric ratio more symmetric is the environment around Eu^{3+} ions. Thus a study of the short range structure around the host Sr atom is crucial to understand the luminescence property of these samples as the amount of Eu in the lattice is varied. Based on XRD and Sr K-edge EXAFS studies it is confirmed that, average Sr-O and Sn-O bond lengths in SrO_{12} and SnO_6 polyhedra of $SrSnO_3$ are higher in upto 2% Eu^{3+} doped sample compared to undoped one and this has been explained based on the higher charge to radius ratio of Eu^{3+} compared to Sr^{2+}. This study clearly establishes that for doping concentration < 3%, Eu goes to Sr sites leading to a symmetric environment that gives rise to sharp $^5D_0 \rightarrow {}^7F_1$ transition in the luminescence spectra.

The last set of luminescent materials discussed in this thesis is as-prepared and heat trated Calcium Tungstate ($CaWO_4$) nanoparticles. $CaWO_4$ is a promising material for applications based on scintillation phenomenon in medical and industrial radiology. However, its light output is heavily dependent on the structure of the samples which in turn depends on the synthesis and post synthesis treatment conditions. It is observed that line widths and peak maxima of the emission spectra of the $CaWO_4$ nanoparticles heat-treated at different temperatures are identical to that of the as-prepared sample, except that signal to noise ratio of the luminescence yield increases with increase in heat treatment temperatures. Our main goal in this study was to resolve the ambiguity regarding the cause of the observed luminescence from these samples. The two widely reported theories for this luminescence property is either the presence of oxygen vacancies or the distortion of the WO_4 tetrahedra. Both of these possibilities were explored by XAFS technique. High resolution XANES measurement at W L1-edge confirmed retention of perfect WO_4 tetrahedral in the samples even after heat treatment upto 900°C, while thorough analysis of the W L3 EXAFS data validated the presence of oxygen vacancies in the lattice which increases with increase in heat treatment temperature and gives rise to the observed luminescence yield.

The next chapter is concerned with magnetic properties and involves the study of the very contemporary and crucial problems of transition metal doped dilute magnetic semiconductors which have massive potential for applications in the modern technological field, with the useful properties of semiconductors and magnetic materials amalgamated into one. Thus it has generated tremendous interest in the scientific community and a huge number of studies have been reported, mostly on transition metal doped ZnO in various forms such as bulk, nanoparticles, thin films etc. However, the results of these studies are highly inconclusive regarding the origin of magnetic properties in these systems and are dependent on a number of variables. In this thesis work, ZnO nanoparticle samples were prepared with two different transition metal dopant atoms (Co and Mn) and by three different preparation methods viz. the wet chemical method, the microwave assisted route and the sol-gel method, with a range of doping concentrations, and each of these variable parameters were taken into account while explaining the outcome of the experimental results. It is observed from EXAFS measurements on Co doped samples at Zn and Co edges that up to 10% concentration of Co appears to be optimum for efficient doping in ZnO lattice and relatively higher Co concentration may lead to an onset of clustering of Co atoms manifested by an increase in coordination of the Co-Co/Zn shell. The samples prepared by all the three routes show almost similar results in case of the Co doped samples. First principle calculations show that the ground state energies of Co doped ZnO NCs are almost similar in FM and AFM cases manifesting the fact that the system can either be ferromagnetic or anti-ferromagnetic. However, from magnetic measurements it has been observed that though the WC and SG Co doped samples show ferromagnetism, MW samples show anti-ferromagnetic ordering and thus it was concluded that the ferromagnetism arises due to surface modification related to the preparation process and not dependent on the bulk properties. In case of Mn doped samples prepared by microwave method (MW samples) ~7% Mn concentration is found to be optimum for efficient doping in ZnO lattice. Higher Mn concentration leads to clustering as it is evidenced from EXAFS analysis. The magnetic measurements indicate that MW samples do not show ferromagnetism, rather show anti-ferromagnetic ordering as predicted by the first principle simulation of the energy of the system with Mn clustering. However, for samples prepared by wet chemical method (WC samples) there is an evidence of the presence of Mn_2O_3 phase i.e. Mn in Mn^{3+} oxidation state as observed by the XANES spectra and confirmed by EXAFS analysis. This suggest that ferromagnetism observed in Mn doped WC samples is most likely due to the Mn_2O_3 phase. The above conclusion is further supported by the fact that ferromagnetism in WC Mn doped samples decreases with increase in Mn doping concentration due to onset of anti-ferromagnetic ordering.

The next chapter deals with temperature dependent EXAFS measurements on undoped and Cr doped multiferroic sample of $GaFeO_3$. These materials exhibit magnetism and ferroelectric properties simultaneously and are very significant from the functional point of view. These systems are reported to be ferrimegnatic as a consequence of a cationic site disorder, i.e. a fraction of octahedral Ga atoms occupy the octahedral Fe atom positions and vice versa below the magnetic transition temperature a phenomenon which is also enhanced by Cr doping. However, this hypothesis had only been supported so far by theoretical models and indirect characterization techniques. Our EXAFS investigation of the short range order in the samples around the Ga and Fe atoms, across the magnetic transition temperature, has established the hypothesis more firmly for the first time in the literature. These findings have also been supported by neutron diffraction results, magnetic measurements and first principle calculations.

Finally the seventh chapter describes XANES and EXAFS measurements on thin film samples of GaAsN having applications in optoelectronic devices where tunable optical properties in the wide optical region from near-infrared to ultraviolet can be obtained, by varying the compositional ratio of GaAs and GaN in these films. In the present thesis work, a series of GaAsN thin films have been prepared by reactive magnetron sputtering of GaAs targets in the mixed ambient of Ar and nitrogen at different Ar to N ratios. In an earlier communication, we have presented our results on the optical properties of these opto-electronically important samples by spectroscopic ellipsometry technique. To give further insight into the above macroscopic observation, we have carried out EXAFS measurements on these samples. The studies mentioned in earlier chapters were concerned with mostly bulk or nanoparticle samples in powdered form and the experiments were carried out in transmission mode. However, for thin film samples the measurements needed to be performed in the fluorescence mode due to the presence of thick substrates which are non-transparent to X-rays. Thus the experimental station of the Energy Dispersive Beamline (BL-08) was modified and measurements were carried out on these samples in TURBO-EXAFS mode as described in details in *Chapter 2*. The XANES and EXAFS measurements on these samples at Ga and As K edges support our earlier findings on this system that the properties of the films, prepared with more than 12% nitrogen in the sputtering ambient, are GaN-like, with their refractive index, extinction coefficient and band gap values resembling that of hexagonal GaN, while for nitrogen concentration in the range of <12%, $GaAs_xN_{1-x}$ alloy films are realized where contribution of GaAs decreases whereas that of GaN increases rapidly as the nitrogen concentration is increased beyond 8% in the sputtering atmosphere.

The work described in this thesis thus covers a broad area demonstrating X-ray Absorption Spectroscopy (XAS) technique can be applied for successful characterization of materials. Samples in different morphology such as bulk, nanoparticles, nanorods, amorphous, thin films etc. and with diverse technological applications based on their catalytic, optical, opto-electronic and magnetic properties have been studied. Different sample environments have also been explored in terms of temperature dependent studies. The two possible modes of experimentation, viz. energy dispersive and energy scanning modes have been used for the experiments. In addition to that, both transmission and fluorescence mode of measurements have been carried out. However, one aspect of EXAFS measurements has not been tried in this thesis work viz., the time-resolved EXAFS. This can be carried out using the normal transmission mode measurements in an Energy Dispersive set-up or using Quick EXAFS mode measurement in an Energy Scanning set-up. In the future work, time-resolved aspect of the EXAFS technique will be explored to carry out structural investigation of various technologically important systems. The two important systems that have been planned to study include temperature or photon induced in-situ nucleation and growth of nanostructures (viz., Au and Pt nanoparticles or core-shell structures) in various matrices like glass or mesoporous materials and in-situ characterization of supported nanostructure based heterogenous catalysts (viz., Rh, Pt or Pd based supported metal catalysts) in chemical reactions. Since other techniques suitable to monitor initial nucleation and growth of nanostructures, viz., Transmission Electron Microscopy (TEM) needs special sample environment, they cannot be employed for in-situ characterisation. EXAFS does not need any special sample environment and can be conveniently employed in the actual condition of the growth process. EXAFS will also be a suitable technique for the structural analysis of active sites under reaction conditions because the reaction gases present in the catalytic systems do not interference with hard X-rays.

References

[1] R. de L. Kronig, “Zur Theorie der Feinstruktur in den Röntgenabsorptionsspektren.,” *Zeitschrift für Phys.*, vol. 1931, pp. 317–323, 1931.

[2] R. de L. Kronig, “Zur Theorie der Feinstruktur in den Röntgenabsorptionsspektren. II.,” *Zeitschrift für Phys.*, vol. 75, no. 3–4, pp. 191–210, 1932.

[3] R. de L. Kronig, “Zur Theorie der Feinstruktur in den Röntgenabsorptionsspektren. III.,” *Zeitschrift für Phys.*, vol. 75, pp. 468–475, 1932.

[4] D. E. Sayers, E. A. Stern, and F. W. Lytle, “New technique for investigating noncrystalline structures: Fourier analysis of the extended x-ray absorption fine structure,” *Phys. Rev. Lett.*, vol. 27, no. 8, pp. 1204–1207, 1971.

[5] E. A. Stern, “Theory of the extended x-ray-absorption fine structure,” *Phys. Rev. B*, vol. 10, no. 8, pp. 3027–3037, 1974.

[6] A. L. Robinson, “X-Ray Data Booklet Section 2 . 2 HISTORY of SYNCHROTRON RADIATION,” pp. 1–9, 1947.

[7] “http://www.lightsources.org/regions.” .

[8] D. D. Bhawalkar, G. Singh, and R. V. Nandedkar, “Synchrotron Radiation Sources INDUS 1 & 2,” *Pramana-Journal Phys.*, vol. 50, pp. 467–484, 1998.

[9] F. W. Lytle, D. E. Sayers, and E. A. Stern, “Extended x-ray absorption fine-structure technique. II. Experimental practice and selected results,” *Phys. Rev. B*, vol. 11, no. 12, pp. 4825–4835, 1975.

[10] E. A. Stern, D. E. Sayers, and F. W. Lytle, “Extended x-ray absorption fine-structure technique. III. Determination of physical parameters,” *Phys. Rev. B*, vol. 11, no. 12, pp. 4836–4846, 1975.

[11] A. I. Kostarev, *Zh. Eksp. Teor. Fiz.*, vol. 11, p. 60, 1941.

[12] T. Shiraiwa, T. Ishimura, and M. Sawada, “Fine Structures of X-ray Absorption Spectra of Crystalline and Amorphous Germanium,” *J. Phys. Soc. Jpn.*, vol. 12, p. 788, 1957.

[13] V. V Schmidt, *Bull. Acad. Sci. USSR, Phys. Ser.*, vol. 25, p. 998, 1961.

[14] P. A. Lee, and J. B. Pendry, “Theory of the extended x-ray absorption fine structure,” *Phys. Rev. B*, vol. 11, p. 2795, 1975.

[15] J. J. Rehr and R. C. Albers, “Scattering-matrix formulation of curved-wave multiple-scattering theory: Application to x-ray-absorption fine structure,” *Phys. Rev. B*, vol. 41, no. 12, pp. 8139–8149, 1990.

[16] D. C. Koningsberger, and R. Prins, *X-ray Absorption: Principles, Applications, Techniques of EXAFS, SEXAFS, and XANES*. New York: Wiley, 1988.

[17] G. Bunker, *Introduction to XAFS A Practical Guide to X-ray Absorption Fine Structure Spectroscopy*. New York: Cambridge University Press, p. 268, 2010.

[18] E. A. Stern and S. M. Heald, “Anisotropic x-ray absorption in layered compounds,” *Phys. Rev. B*, vol. 16, pp. 5549–5559, 1977.

[19] E. A. Stern and S. M. Heald, “Basic principles and applications of EXAFS, in Handbook of Synchrotron Radiation,” 1983, pp. 955–1014.

[20] L. M. Murphy, B. R. Dobson, M. Neu, C. A. Ramsdale, R. W. Strange and S. S. Hasnain, “Quick Fluorescence-EXAFS: an Improved Method for Collection of Conventional XAFS Data and for Studying Reaction Intermediates in Dilute Systems,” *J. Synchrotron Radiat.*, vol. 2, pp. 64–69, 1995.

[21] J.D. Grunwaldt, D. Lutzenkirchen-Hecht, M. Richwin, S. Grundmann, B.S. Clausen and R. Frahm, “Piezo X-ray Absorption Spectroscopy for the Investigation of Solid State Transformations in the Millisecond Range,” *J. Phys. Chem. B*, vol. 105, pp. 5161–5168, 2001.

[22] Rachel O_Malley, Antje Vollmer, Jonathan R.I. Lee, Ian Harvey, Jon Headspith, Sofia Diaz-Moreno and Trevor Rayment, “Time-resolved studies of diffusion via energy dispersive X-ray absorption spectroscopy,” *Electrochem. commun.*, vol. 5, no. 1–5, 2003.

[23] Y. Iwasawa, “In-situ characterization of supported metal catalysts and model surfaces by time-resolved and three-dimensional XAFS technique,” *J. Catal.*, vol. 21, no. 216, pp. 165–177, 2003.

[24] S. Pascarelli, T. Neisius, and S. De Panfilis, “Turbo-XAS: dispersive XAS using sequential acquisition,” *J. Synchrotron Rad.*, vol. 6, p. 1044, 1999.

[25] S. Basu, C. Nayak, A. K. Yadav, A. Agrawal, A. K. Poswal, D. Bhattacharyya, S. N. Jha and N. K. Sahoo, “A comprehensive facility for EXAFS measurements at the INDUS-2 synchrotron source at RRCAT, Indore, India,” in *J. Phys.: Conf. Ser*, 2014, p. 012032.

[26] D. Bhattacharyya, A. K. Poswal, S. N. Jha, and S. C. Sabharwal, “Nuclear Instruments and Methods in Physics Research A First results from a dispersive EXAFS beamline developed at INDUS-2 synchrotron source at RRCAT , Indore , India,” *Nucl. Inst. Methods Phys. Res. A*, vol. 609, no. 2–3, pp. 286–293, 2009.

[27] P. L. Lee, M. A. Beno, G. Jennings, M. Ramanathan, G. S. Knapp, K. Huang, J. Bai, P. A. Montano, “An energy dispersive x-ray absorption spectroscopy beamline, XGA, at NSLS,” *Rev. Sci. Intrum*, vol. 65, p. 1, 1994.

[28] A. K. Poswal, A. Agrawal, A. K. Yadav, C. Nayak, S. Basu, S. R. Kane, C. K. Garg, D. Bhattachryya, S. N. Jha, and N. K. Sahoo, “Commissioning and first results of

scanning type EXAFS beamline (BL-09) at INDUS-2 synchrotron source," in *AIP Conference Proceedings*, vol. 649, pp. 649–651, 2014.

[29] B. Ravel and M. Newville, "ATHENA, ARTEMIS, HEPHAESTUS: data analysis for X-ray absorption spectroscopy using IFEFFIT.," *J. Synchrotron Radiat.*, vol. 12, pp. 537–541, 2005.

[30] B. Ravel, "ATOMS : crystallography for the X-ray absorption spectroscopist," *J. Synchrotron Radiat.*, vol. 8, no. 2, pp. 314–316, 2001.

[31] M. Newville, "IFEFFIT : interactive XAFS analysis and FEFF fitting," *J. Synchrotron Radiat.*, vol. 8, no. 2, pp. 322–324, 2001.

[32] S. I. Zabinsky, J. J. Rehr, A. Ankudinov, R. C. Albers, and M. J. Eller, "Multiple-scattering calculations of x-ray-absorption spectra," *Phys. Rev. B*, vol. 52, no. 4, 1995.

[33] A. L. Ankudinov, B. Ravel, J. J. Rehr, and S. D. Conradson, "Real-space multiple-scattering calculation and interpretation of x-ray-absorption near-edge structure," vol. 58, no. 12, pp. 7565–7576, 1998.

[34] E. A. Stern, "Number of relevant independent points in x-ray-absorption fine-structure spectra," *Phys. Rev. B*, vol. 48, no. 13, pp. 9825–9827, 1993.

[35] M. Newville, P. Līviņš, Y. Yacoby, J. J. Rehr, and E.A. Stern, "Near-edge x-ray-absorption fine structure of Pb: A comparison of theory and experiment," *Phys. Rev. B*, vol. 47, p. 14126, 1993.

[36] M. Newville, B. Ravel, D. Haskel, J. J. Rehr, E. A. Stern, and Y. Yacoby, "Analysis of multiple-scattering XAFS data using theoretical standards," *Phys. b*, vol. 209, pp. 154–156, 1995.

[37] B. Ravel, "EXAFS Analysis Using FEFF and FEFFIT," *http://feff.phys.washington.edu/~ravel/course/*, 2000.

[38] P. D. L. Mercera, J. G. van Ommen, E. B. M. Doesburg, A. J. Burggraaf, and J. R. H. Roes, "Stabilized tetragonal zirconium oxide as a support for catalysts Evolution of the texture and structure on calcination in static air," *Appl. Catal.*, vol. 78, p. 79, 1991.

[39] R. M. Ormerod, "Solid oxide fuel cells," *Chem. Soc. Rev.*, vol. 32, no. 1, pp. 17–28, Dec. 2003.

[40] C. J. Howard, R. J. Hill, and B. E. Reichert, "Structures of ZrO_2 polymorphs at room temperature by high-resolution neutron powder diffraction," *Acta Crystallogr. Sect. B Struct. Sci.*, vol. 44, no. 2, pp. 116–120, 1988.

[41] M. O. Zacate, L. Minervini, D. J. Bradfield, R. W. Grimes, and K. E. Sickafus, "Defect cluster formation in M_2O_3-doped cubic ZrO_2," *Solid State Ionics*, vol. 128, pp. 243–254, 2000.

[42] O. Yamamoto, “Solid oxide fuel cells : fundamental aspects and prospects,” *Elctrochimica Acta.*, vol. 45, pp. 2423–2435, 2000.

[43] V. A. Sadykov, V. V. Kriventsov, E. M. Moroz, Y. V. Borchert, D. A. Zyuzin, V. P. Kol’ko, T. G. Kuznetsova, V. P. Ivanov, S. N. Trukhan, A. I. Boronin, E. M. Pazhetnov, N. V. Mezentseva, E. B. Burgina, and J. R. H. Ross, “Ceria-Zirconia Nanoparticles Doped with La or Gd: Effect of the Doping Cation on the Real Structure,” *Solid State Phenom.*, vol. 128, pp. 81–88, 2007.

[44] P. Li, I.W. Chen, and J. E. Penner-Hahn, “Effect of Dopants on Zirconia Stabilization—An X-ray Absorption Study: I, Trivalent Dopants,” *J. Am. Ceram. Soc.*, vol. 77, p. 118, 1994.

[45] M. Cole, “EXAFS Studies of Doped-ZrO_2 Systems,” *J. Phys. Chem. Sol*, vol. 51, no. 6, 1990.

[46] P. Blaha, K. Schwartz, G. K. H. Madsen, D. Kvasnicka, and J. Luitz, “WIEN97, An Augmented Plane Wave Plus Local Orbitals Program for Calculating Crystal Properties.” Wien, Austria, 2002.

[47] J. P. Perdew, K. Burke, and M. Ernzerhof, “Generalized Gradient Approximation Made Simple,” *Phys. Rev. Lett.*, vol. 77, no. 3, pp. 3865–3868, 1996.

[48] G. Teufer, “The crystal structure of tetragonal ZrO_2,” *Acta Crystallogr.*, vol. 15, no. 11, pp. 1187–1187, 1962.

[49] D. K. Smith and W. Newkirk, “The crystal structure of baddeleyite (monoclinic ZrO_2) and its relation to the polymorphism of ZrO 2,” *Acta Crystallogr.*, vol. 18, no. 6, pp. 983–991, 1965.

[50] A. M. Pires, M. R. Davolos, C. O. Paiva-Santos, E. B. Stucchi, and J. Flor, “New X-ray powder diffraction data and Rietveld refinement for Gd_2O_3 monodispersed fine spherical particles,” *J. Solid State Chem.*, vol. 171, no. 1–2, pp. 420–423, 2003.

[51] S. Basu, S. Varma, A. N. Shirsat, B. N. Wani, S. R. Bharadwaj, and A. Chakrabarti, “X-ray absorption spectroscopy of doped ZrO_2 systems,” *J. Appl. Phys.*, vol. 053532, pp. 1–9, 2012.

[52] G. Kresse and J. Furthmüller, “Efficient iterative schemes for ab initio total-energy calculations using a plane-wave basis set ¨,” *Phys. Rev. B*, vol. 54, no. 16, p. 11169, 1996.

[53] G. Kresse and D. Joubert, “From ultrasoft pseudopotentials to the projector augmented-wave method,” *Phys. Rev. B*, vol. 59, no. 3, p. 1758, 1999.

[54] “VASP 5.2.” .

[55] P. E. Blochl, “Projector augmented wave method,” *Phys. Rev. B*, vol. 50, no. 24, p. 17953, 1994.

[56] L. Binet, D. Gourier, and C. Minot, “Relation between Electron band Structure and Magnetic Bistability of conduction electrons in β-Ga_2O_3,” *J. Solid State Chem.*, vol. 113, p. 420, 1994.

[57] N. Ueda, H. Hosono, R. Waseda, and H. Kawazoe, “Anisotropy of electrical and optical properties in beta-Ga_2O_3 single crystals,” *Appl. Phys. Lett.*, vol. 71, pp. 933–935, 1997.

[58] A. C. Taş, P. J. Majewski, and F. Aldinger, “Synthesis of Gallium Oxide Hydroxide Crystals in Aqueous Solutions with or without Urea and Their Calcination Behavior,” *J. Am. Ceram. Soc.*, vol. 85, pp. 1421–1429, 2002.

[59] P. Gollakota, A. Dhawan, P. Wellenius, L. M. Lunardi, J. F. Muth, Y. N. Saripalli, H. Y. Peng, and H. O. Everitt, “Optical characterization of Eu-doped beta-Ga_2O_3 thin films,” *Appl. Phys. Lett.*, vol. 88, p. 221906, 2006.

[60] B. Sanyasi Naidu, M. Pandey, J. Nuwad, V. Sudarsan, R. K. Vatsa, R. J. Kshirsagar, and C. G. S. Pillai, “Lanthanide-ion-assisted structural collapse of layered GaOOH lattice,” *Inorg. Chem.*, vol. 50, pp. 4463–4472, 2011.

[61] M. F. Pye, J. J. Birtill and P.G. Dickens, “α-Gallium oxide deuteriohydroxide: a powder neutron diffraction investigation,” *Acta Crystallogr. Sect. B Struct. Sci.*, vol. 33, no. 10, p. 3224, 1977.

[62] Y. Hu, X. Liu, and Z. Xu, “Role of crystal structure in flotation separation of diaspore from kaolinite, pyrophyllite and illite,” *Miner. Eng.*, vol. 16, p. 219, 2003.

[63] M. Uchida, and A. Ukowaki, “Solubility of gallium(III) oxyhydroxide in aqueous NaCl solutions at 100°C,” *J. Solution Chem.*, vol. 26, p. 699, 1997.

[64] S. Wang, Y. Zhao, J. Chen, R. Xu, L. Luo, and S. Zhong, “Self-assembled 3D $La(OH)_3$ and La_2O_3 nanostructures: Fast microwave synthesis and characterization,” *Superlattices Microstruct.*, vol. 47, pp. 597–605, 2010.

[65] V. A. Kolesova, and Y. I. Riskin, “Infrared absorption spectra of diaspore (α-AlOOH). Boehmite (γ-AlOOH) and GaOOH,” *J. Struct. Chem.*, vol. 3, p. 656, 1962.

[66] A. Vegas, M. Vallet-Regí, J.M. Gonzalez-Calvet, and M. A. Alario-Franco, “The $ASnO_3$ (A=Ca,Sr) perovskites,” *Acta Crystallogr. Sect. B Struct. Sci.*, vol. 42, p. 167, 1986.

[67] G. Prathiba, S. Venkatesh, and N. Harish Kumar, “Structural, magnetic and semiconducting properties of Fe doped $SrSnO_3$,” *Solid State Commun.*, vol. 150, no. 31–32, pp. 1436–1438, 2010.

[68] W. Zhang, J. Tang, and J. Ye, “Structural, photocatalytic, and photophysical properties of perovskite $MSnO_3$ (M = Ca, Sr, and Ba) photocatalysts,” *J. Mater. Res.*, vol. 22, p. 1859, 2007.

[69] A. L. Goodwin, S.A. T. Redfern, M. T. Dove, D. A. Keen, and M. G. Tucker, "Ferroelectric nanoscale domains and the 905K phase transition in $SrSnO_3$: A neutron total-scattering study," *Phys. Rev. B*, vol. 76, p. 174114, 2007.

[70] H. Mizoguchi , H. W. Eng, and P. M.Woodward, "Probing the Electronic Structures of Ternary Perovskite and Pyrochlore Oxides Containing Sn^{4+} or Sb^{5+}," *Inorg. Chem.*, vol. 43, p. 1667, 2004.

[71] D. K. Patel, A. Sengupta, B. Vishwanadh, V. Sudarsan, R. K. Vatsa, R. Kadam, and S. K. Kulsreshtha, "Local Environments Around Eu^{3+} and Eu^{2+} Ions in Dual Light-Emitting $BaSnO_3$:Eu Nanomaterials," *Eur. J. Inorg. Chem.*, vol. 2012, no. 10, p. 1609, 2012.

[72] D. K. Patel, B. Rajeswari, V. Sudarsan, R. K. Vatsa, R. M. Kadam, and S. K. Kulshreshtha, "Structural, luminescence and EPR studies on $SrSnO_3$ nanorods doped with europium ions," *Dalton Transactions*, vol. 41. p. 12023, 2012.

[73] E. H. Mountstevens, J. P. Attfield, and S. A. T. Redfern, "Cation-size control of structural phase transitions in tin perovskites," *J. Phys. Condens. Matter*, vol. 15, pp. 8315–8326, 2003.

[74] M. Glerup, K. S. Knight, and F. W. Poulsen, "High temperature structural phase transitions in $SrSnO_3$ perovskite," *Mater. Res. Bull.*, vol. 40, pp. 507–520, 2005.

[75] E. H. Mountstevens, S. A. T. Redfern and J. P. Attfield, "Order-disorder octahedral tilting transitions in $SrSnO_3$ perovskite," *Phys. Rev. B*, vol. 71, p. 220102, 2005.

[76] S. Ouni, S. Nouri, J. Rohlicek, and R. Ben Hassen, "Structural and electrical properties of the sol–gel prepared $Sr_{1-x}Er_xSnO_{3-\delta}$ compounds," *J. Solid State Chem.*, vol. 192, pp. 132–138, 2012.

[77] Hong-Wei Liao, Yan-Fei Wang, Xian-Min Liu, Ya-Dong Li, and Y.T. Qian, "Hydrothermal Preparation and Characterization of Luminescent $CdWO_4$ Nanorods," *Chem. Mater.*, vol. 12, p. 2819, 2000.

[78] H. Wang, F. D. Medina, Y. D. Zhou, and Q. N. Zhang, "Temperature dependence of the polarized Raman spectra of $ZnWO_4$ single crystals," *Phys. Rev. B*, vol. 45, p. 10356, 1992.

[79] S. H. Yu, M. Antonietti, H. Cölfen, and M. Giersig, "Synthesis of Very Thin 1D and 2D $CdWO_4$ Nanoparticles with Improved Fluorescence Behavior by Polymer-Controlled Crystallization," *Angew. Chemie Int. Ed.*, vol. 41, p. 2356, 2002.

[80] G. Zhang, R. Jia, and Q. Wu, "Preparation, structural and optical properties of AWO_4 (A=Ca, Ba, Sr) nanofilms," *Mater. Sci. Eng. B*, vol. 128, no. 1–3, pp. 254–259, 2006.

[81] B. Liu, S.H. Yu, L. Li, Q. Zhang, F. Zhang, and K. Jiang, *Angew. Chemie Int. Ed.*, vol. 43, 2004.

[82] F. Zhang, Y. Yiu, M. C. Aronson, and S. S. Wong, "Exploring the room-temperature synthesis and properties of multifunctional doped tungstate nanorods," *J. Phys. Chem. C*, vol. 112, pp. 14816–14824, 2008.

[83] V. B. Mikhailik and H. Kraus, "Cryogenic scintillators in searches for extremely rare events," *Journal of Physics D: Applied Physics*, vol. 39. pp. 1181–1191, 2006.

[84] R. Leonelli and J. L. Brebner, "Time-resolved spectroscopy of the visible emission band in strontium titanate," *Phys. Rev. B*, vol. 33, pp. 8649–8656, 1986.

[85] R. Leonelli and J. L. Brebner, "Evidence for bimolecular recombination in the luminescence spectra of $SrTiO_3$," *Solid State Commun.*, vol. 54, no. 6, pp. 505–507, May 1985.

[86] V. Mürk, M. Nikl, V. Mihokova, and K. Nitsch, "A study of electron excitations in $CaWO_4$ and $PbWO_4$ single crystals," *J. Phys. Condens. Matter*, vol. 9, p. 249, 1997.

[87] V. B. Mikhailik, H. Kraus, D. Wahl, M. Itoh, M. Koike, and I. K. Bailiff, "One- and two-photon excited luminescence and band-gap assignment in $CaWO_4$," *Phys. Rev. B*, vol. 69, p. 204110, 2004.

[88] A. B. Campos, A. Z. Simoes, E. Longo, J. A. Varela, V. M. Longo, A. T. De Figueiredo, F. S. De Vicente, and A. C. Hernandes, "Mechanisms behind blue, green, and red photoluminescence emissions in $CaWO_4$ and $CaMoO_4$ powders," *Appl. Phys. Lett.*, vol. 91, 2007.

[89] W. Hu, W. Tong, L. Li, J. Zeng. and G. Li, "Cation non-stoichiometry in multi-component oxide nanoparticles by solution chemistry: a case study on $CaWO_4$ for tailored structural properties," *Phys. Chem. Chem. Phys.*, vol. 13, p. 11634, 2011.

[90] V. Yakovyna, Y. Zhydachevskii, V. B. Mikhailik, I. Solskii, D. Sugak, and M. Vakiv, "Effect of thermo-chemical treatments on the luminescence and scintillation properties of $CaWO_4$," *Opt. Mater. (Amst).*, vol. 30, no. 10, pp. 1630–1634, 2008.

[91] T. Thongtem, S. Kaowphong, and S. Thongtem, "Influence of cetyltrimethylammonium bromide on the morphology of AWO_4 (A=Ca, Sr) prepared by cyclic microwave irradiation," *Appl. Surf. Sci.*, vol. 254, no. 23, pp. 7765–7769, 2008.

[92] L. Li, Y. Su. and G. Li, "Size-induced symmetric enhancement and its relevance to photoluminescence of scheelite $CaWO_4$ nanocrystals," *Appl. Phys. Lett.*, vol. 90, p. 054105, 2007.

[93] Y. Su, G. Li, Y. Xue, and L. Li, "Tunable Physical Properties of $CaWO_4$ Nanocrystals via Particle Size Control," *J. Phys. Chem. C*, vol. 111, p. 6684, 2007.

[94] T. Dietl, "Zener Model Description of Ferromagnetism in Zinc-Blende Magnetic Semiconductors," *Science*, vol. 287, no. 5455, pp. 1019–1022, 2000.

[95] K. Sato and H. Katayama-Yoshida, “Ferromagnetism in a transition metal atom doped ZnO,” *Phys. E Low-dimensional Syst. Nanostructures*, vol. 10, no. 1–3, pp. 251–255, 2001.

[96] S. Wolf, D. Awschalom, R. Buhrman, J. M. Daughton, S. von Molnár, M. L. Roukes, Y. Chtchelkanova, and D. M. Treger, “Spintronics: a spin-based electronics vision for the future.,” *Science*, vol. 294, no. 5546, pp. 1488–95, 2001.

[97] F. Pan, C. Song, X. J. Liu, Y. C. Yang, and F. Zeng, “Ferromagnetism and possible application in spintronics of transition-metal-doped ZnO films,” *Mater. Sci. Eng. R Reports*, vol. 62, no. 1, pp. 1–35, 2008.

[98] J. M. D. Coey, M. Venkatesan, and C. B. Fitzgerald, “Donor impurity band exchange in dilute ferromagnetic oxides.,” *Nat. Mater.*, vol. 4, no. 2, pp. 173–9, 2005.

[99] K. Kittilstved, N. Norberg, and D. Gamelin, “Chemical Manipulation of High-TC Ferromagnetism in ZnO Diluted Magnetic Semiconductors,” *Phys. Rev. Lett.*, vol. 94, no. 14, p. 147209, 2005.

[100] Q. Wang, Q. Sun, and P. Jena, “Ligand induced ferromagnetism in ZnO nanostructures.,” *J. Chem. Phys.*, vol. 129, no. 16, p. 164714, 2008.

[101] D. Y. Inamdar, A. D. Lad, A. K. Pathak, I. Dubenko, N. Ali, and S. Mahamuni, “Ferromagnetism in ZnO Nanocrystals: Doping and Surface Chemistry,” *J. Phys. Chem. C*, vol. 114, no. 3, pp. 1451–1459, 2010.

[102] M. Garcia, J. M. Merino, E. Fernández Pinel, Quesada, J. de la Venta, M. L. Ruíz González, G. R. Castro, P. Crespo, J. Llopis, J. M. González-Calbet, and A. Hernando, “Magnetic properties of ZnO nanoparticles.,” *Nano Lett.*, vol. 7, no. 6, pp. 1489–94, 2007.

[103] W. Yan, Z. Sun, Q. Liu, Z. Li, Z. Pan, J. Wang, S. Wei, D. Wang, Y. Zhou, and X. Zhang, “Zn vacancy induced room-temperature ferromagnetism in Mn-doped ZnO,” *Appl. Phys. Lett.*, vol. 91, no. 6, p. 062113, 2007.

[104] C. Song, S. N. Pan, X. J. Liu, X. W. Li, F. Zeng, W. S. Yan, B. He, and F. Pan, “Evidence of structural defect enhanced room-temperature ferromagnetism in Co-doped ZnO.,” *J. Phys. Condens. Matter*, vol. 19, no. 17, p. 176229, 2007.

[105] J. H. Park, M. G. Kim, H. M. Jang, S. Ryu, and Y. M. Kim, “Co-metal clustering as the origin of ferromagnetism in Co-doped ZnO thin films,” *Appl. Phys. Lett.*, vol. 84, no. 8, p. 1338, 2004.

[106] I. Bilecka, L. Luo, I. Djerdj, M. D. Rossell, M. Jagodi, Y. Masubuchi, S. Kikkawa, and M. Niederberger, “Microwave-Assisted Nonaqueous Sol - Gel Chemistry for Highly Concentrated ZnO-Based Magnetic Semiconductor Nanocrystals,” *J. Phys. Chem. C*, pp. 1484–1495, 2011.

[107] C. Guglieri, M. Laguna-Marco, M. García, N. Carmona, E. Céspedes, M. García-Hernández, A. Espinosa, and J. Chaboy, “XMCD Proof of Ferromagnetic Behavior in ZnO Nanoparticles,” *J. Phys. Chem. C*, vol. 116, no. 11, pp. 6608–6614, 2012.

[108] I. Bilecka and M. Niederberger, “Microwave chemistry for inorganic nanomaterials synthesis.,” *Nanoscale*, vol. 2, pp. 1358–1374, 2010.

[109] E. H. Kisi and M. M. Elcombe, “u parameters for the wurtzite structure of ZnS and ZnO using powder neutron diffraction,” *Acta Crystallogr. Sect. C Cryst. Struct. Commun.*, vol. 45, no. 12, pp. 1867–1870, 1989.

[110] A. Janotti and C. G. Van de Walle, “Fundamentals of zinc oxide as a semiconductor,” *Reports Prog. Phys.*, vol. 72, no. 12, p. 126501, 2009.

[111] E.S. Jeong, H. J. Yu, Y. J. Kim, G. C. Yi, Y. D. Choi, and S. W. Han, “Local Structural and Optical Properties of ZnO Nanoparticles,” *J. Nanosci. Nanotechnol.*, vol. 10, no. 5, pp. 3562–3565, 2010.

[112] T. Chakraborty, C. Meneghini, G. Aquilanti, and S. Ray, “Microscopic distribution of metal dopants and anion vacancies in Fe-doped BaTiO3−δ single crystals,” *J. Phys. Condens. Matter*, vol. 25, p. 236002, 2013.

[113] “http://cars9.uchicago.edu/atomsdb/CoO.inp.” .

[114] A. R. Han, S.-J. Hwang, Y. Zhao, and Y.-U. Kwon, “X-ray absorption spectroscopic and magnetic characterization of cobalt-doped zinc oxide nanocrystals prepared by the molten-salt method,” *J. Magn. Magn. Mater.*, vol. 320, no. 8, pp. 1591–1596, 2008.

[115] “http://cars9.uchicago.edu/atomsdb/MnO.inp.” .

[116] “http://cars9.uchicago.edu/atomsdb/Mn_2O_3.inp.” .

[117] D. C. Kundaliya, S. B. Ogale, S. E. Lofland, S. Dhar, C. J. Metting, S. R. Shinde, Z. Ma, B. Varughese, K.V. Ramanujachary, L. Salamanca-Riba, and T. Venkatesan, “On the origin of high-temperature ferromagnetism in the low-temperature-processed Mn–Zn–O system,” *Nat. Mater.*, vol. 3, p. 709, 2004.

[118] R. K. Zheng, H. Liu, X. X. Zhang, V. A. L. Roy, and A. B. Djurii, “Exchange bias and the origin of magnetism in Mn-doped ZnO tetrapods,” *Appl. Phys. Lett.*, vol. 85, pp. 2589–2591, 2004.

[119] J. P. Remeika, “$GaFeO_3$: A Ferromagnetic-Piezoelectric Compound,” *J. Appl. Phys.*, vol. 31, no. 5, p. S263, 1960.

[120] R. B. Frankel, N. A. Blum, S. Foner, A. J. Freeman, and M. Schieber, “Ferrimagnetic Structure of Magnetoelectric $Ga_{2-x}Fe_xO_3$,” *Phys. Rev. Lett.*, vol. 15, p. 958, 1965.

[121] M. Bakr Mohamed and H. Fuess, “Effect of Mn doping on structural and magnetic properties of $GaFeO_3$,” *J. Magn. Magn. Mater.*, vol. 323, no. 15, pp. 2090–2094, 2011.

[122] R. Saha, A. Shireen, S. N. Shirodkar, U. V. Waghmare, a. Sundaresan, and C. N. R. Rao, "Effect of Cr and Mn ions on the structure and magnetic properties of $GaFeO_3$: Role of the substitution site," *J. Solid State Chem.*, vol. 184, no. 9, pp. 2353–2359, 2011.

[123] M. Han, T. Ozaki, and J. Yu, "Magnetic ordering and exchange interactions in multiferroic GaFeO3," *Phys. Rev. B*, vol. 75, no. 6, p. 060404, 2007.

[124] J. Y. Kim, T. Koo, and J. H. Park, "Orbital and Bonding Anisotropy in a Half-Filled $GaFeO_3$ Magnetoelectric Ferrimagnet," *Phys. Rev. Lett.*, vol. 96, no. 4, p. 047205, 2006.

[125] M. B. Mohamed, A. Senyshyn, H. Ehrenberg, and H. Fuess, "Structural, magnetic, dielectric properties of multiferroic GaFeO3 prepared by solid state reaction and sol–gel methods," *J. Alloys Compd.*, vol. 492, no. 1–2, pp. L20–L27, 2010.

[126] K. Sharma, V. Raghavendra Reddy, D. Kothari, A. Gupta, A. Banerjee, and V. G. Sathe, "Low temperature Raman and high field ^{57}Fe Mossbauer study of polycrystalline $GaFeO_3$," *J. Phys. Condens. Matter*, vol. 22, no. 14, p. 146005, 2010.

[127] S. C. Abrahams, J. M. Reddy, and J. L. Bernstein, "Crystal Structure of Piezoelectric Ferromagnetic Gallium Iron Oxide," *J. Chem. Phys.*, vol. 42, no. 11, p. 3957, 1965.

[128] S. Mukherjee, A. Garg, and R. Gupta, "Probing magnetoelastic coupling and structural changes in magnetoelectric gallium ferrite.," *J. Phys. Condens. Matter*, vol. 23, no. 44, p. 445403, 2011.

[129] J. Rodríguez-Carvajal, "Recent advances in magnetic structure determination by neutron powder diffraction," *Phys. B Condens. Matter*, vol. 192, no. 1–2, pp. 55–69, 1993.

[130] J. W. A. III and W. Walukiewicz, "Current status of research and development of III–N–V semiconductor alloys," *Semicond. Sci. Technol.*, vol. 17, pp. 741–745, 2002.

[131] M. Weyers, M. Sato, and H. Ando, "Red Shift of Photoluminescence and Absorption in Dilute GaAsN Alloy Layers," *Jpn. J. Appl. Phys.*, vol. 31, pp. L853–L855, 1992.

[132] W. G. Bi and C. W. Tu, "Bowing parameter of the band-gap energy of GaN_xAs_{1-x}," *Appl. Phys. Lett.*, vol. 70, pp. 1608–1610, 1997.

[133] R. Chtourou, F. Bousbih, S. Ben Bouzid, F. F. Charfi, J. C. Harmand, G. Ungaro, and L. Largeau, "Effect of nitrogen and temperature on the electronic band structure of $GaAs_{1-x}N_x$ alloys," *Appl. Phys. Lett.*, vol. 80, pp. 2075–2077, 2002.

[134] U. Tisch, E. Finkman, and J. Salzman, "The anomalous bandgap bowing in GaAsN," *Appl. Phys. Lett.*, vol. 81, pp. 463–465, 2002.

[135] K. Iwata, H. Asahi, K. Asami, R. Kuroiwa, and S. Gonda, "GaN-rich side of GaNAs grown by gas source molecular beam epitaxy," *Japanese J. Appl. Phys. Part 1 Regul. Pap. Short Notes Rev. Pap.*, vol. 37, pp. 1436–1439, 1998.

[136] Y. Zhao, “Effects of arsenic in gas-source molecular beam epitaxy,” *J. Vac. Sci. Technol. B Microelectron. Nanom. Struct.*, vol. 16, p. 1297, 1998.

[137] X. Li, S. Kim, E. E. Reuter, S. G. Bishop, and J. J. Coleman, “The incorporation of arsenic in GaN by metalorganic chemical vapor deposition,” *Appl. Phys. Lett.*, vol. 72, pp. 1990–1992, 1998.

[138] C. T. Foxon, T. S. Cheng, S. V. Novikov, D. E. Lacklison, L. C. Jenkins, D. Johnston, J. W. Orton, S. E. Hooper, N. Baba-Ali, T. L. Tansley, and V. V. Tret’yakov, “The growth and properties of group III nitrides,” *J. Cryst. Growth*, vol. 150, pp. 892–896, 1995.

[139] J. Bandet, K. Aguir, D. Lollman, A. Fennouh, and H. Carchano, “Raman and electrical characterizations of a-$GaAs_{1-x}N_x$ thin films grown on c-Si(p) substrates by N_2 reactive sputtering,” *Japanese J. Appl. Phys. Part 1 Regul. Pap. Short Notes Rev. Pap.*, vol. 36, pp. 11–18, 1997.

[140] X. M. Teng, H. T. Fan, S. S. Pan, C. Ye, and G. H. Li, “Optical properties of amorphous $GaAs_{1-x}N_x$ film sputtering with different N_2 partial pressures,” *J. Vac. Sci. Technol. A Vacuum, Surfaces, Film.*, vol. 24, no. 5, p. 1714, 2006.

[141] B. S. Yadav, S. S. Major, and R. S. Srinivasa, “Reactively sputtered $GaAs_xN_{1-x}$ thin films,” *Thin Solid Films*, vol. 515, pp. 1043–1046, 2006.

[142] N. Preschilla, S. Major, N. Kumar, I. Samajdar, and R. S. Srinivasa, “Nanocrystalline gallium nitride thin films,” *Appl. Phys. Lett.*, vol. 77, pp. 1861–1863, 2000.

[143] T. Miyazaki, K. Takada, S. Adachi, and K. Ohtsuka, “Properties of radio-frequency-sputter-deposited GaN films in a nitrogenhydrogen mixed gas,” *J. Appl. Phys.*, vol. 97, 2005.

[144] Y. Kang and D. C. Ingram, “Properties of amorphous GaN_x prepared by ion beam assisted deposition at room temperature,” *J. Appl. Phys.*, vol. 93, pp. 3954–3962, 2003.

[145] A. Biswas, B. S. Yadav, D. Bhattacharyya, N. K. Sahoo, S. S. Major, and R. S. Srinivasa, “Spectroscopic ellipsometry studies of reactively sputtered nitrogen-rich GaAsN films,” *J. Non. Cryst. Solids*, vol. 357, no. 18, pp. 3293–3300, 2011.

[146] A.R. Chetal, P. Mahto, P. R. Sarode, “Chemical-shift of the X-ray K-absorption edge of Co in some compounds, complexes and minerals,” *J. Phys. Chem. Sol*, vol. 49, p. 279, 1988.

[147] C. Mande, and M. Y. Apte, “Correlation between the magnetic properties and the chemical shifts in x-ray absorption spectra of some transition metal compounds,” *Bull Mat sci*, vol. 3, p. 193, 1981.

[148] V. K. Kondawar and C. Mande, “Chemical shifts of the K absorption discontinuity of cobalt in some binary and ternary intermetallic systems,” *J. Phys. C Solid State Phys.*, vol. 9, p. 1351, 1976.

[149] S. K. Pandey, A. R. Chetal, and P. R. Sarode, “Chemical Shift of the X-Ray K-Absorption Edge of Cu in Some of Its Compounds, Complexes and Superconductors,” *J. Phys. Soc. Jpn*, vol. 59, p. 1848, 1990.

[150] J. P. Suchet, *Chemical Physics of Semiconductors*. London: Van Nodstrand, 1965.

[151] L. Pauling, *The Nature of the Chemical Bond*. New York: Cornell Univ. Press, 1960.

[152] H. Schulz and K. H. Thiemann, “Crystal structure refinement of AlN and GaN,” *Solid State Commun.*, vol. 23, pp. 815–819, 1977.

[153] A. W. Stevenson, “Thermal vibrations and bonding in GaAs: an extended-face crystal study,” *Acta Crystallogr. Sect. A Found. Crystallogr.*, vol. 50, pp. 621–632, 1994.